eman ta zabal zazu

Universidad del País Vasco | Euskal Herriko Unibertsitatea

Characterization of environment-related endophenotypes in pulmonary hypertension

Doctoral Thesis

Lucía Fadón Padilla

Directors: Dr. Jesús Ruiz-Cabello & Dra. Edurne Berra

2023

eman ta zabal zazu

Universidad
del País Vasco

Euskal Herriko
Unibertsitatea

Characterization of environment-related endophenotypes in pulmonary hypertension

Lucía Fadón Padilla

Index

Figures

Tables

Abbreviations

^{18}F-FDG: ^{18}F-Fluorodeoxyglucose

2DG: 2-Deoxyglucose

3D: Three-Dimensional

ANOVA: Analysis of Variance

ATP: Adenosine Triphosphate

BCA: Bicinchoninic Acid

BSA: Body Surface Area

cFLFLF: N-cinnamoyl-F-(D)L-F-(D)L-F

CMR: Cardiac Magnetic Resonance

CO: Cardiac Output

COi: Cardiac Output Index

COPD: Chronic Obstructive Pulmonary Disease

CT: Computed Tomography

CTEPH: Chronic Thromboembolic Pulmonary Hypertension

CTL: Control (corresponds normally to control Wild type mice in normoxia)

DAPI: 4',6-diamidino-2-phenylindole

DCA: Dichloroacetate

DLS: Dynamic Light Scattering

DMSO: Dimethyl Sulfoxide

DNA: Deoxyribonucleic Acid

DUB: Deubiquitinating Enzyme

EC: Endothelial Cell

ECM: Extracellular Matrix

EDV: End-Diastolic Volume

EDVi: End-Diastolic Volume Index

EF: Ejection Fraction

ESV: End-Systolic Volume

ESVi: End-Systolic Volume Index

EtBr: Ethidium Bromide

FDG: Fluorodeoxyglucose

FPR1: Formyl Peptide Receptor 1

GPI: Glucose-6-Phosphate Isomerase

HIF: Hypoxia Inducible Factor

HK: Hexokinase

HU: Hounsfield Units

IHC: Immunohistochemistry

IONP: Iron Oxide Nanoparticles

IP: Intraperitoneal

IPA: Ingenuity Pathway Analysis

iPAH: Idiopathic Pulmonary Arterial Hypertension

IV: Intravenous

KO: Knockout

LCOi: Left-Ventricle Cardiac Output Index

LDHA: Lactate Dehydrogenase A

LEDVi: Left-Ventricle End-Diastolic Volume Indexed

LESVi: Left-Ventricle End-Systolic Volume Indexed

LSVi: Left-Ventricle Stroke Volume Indexed

LV: Left Ventricle

MCT: Monocrotaline

mPAP: Mean Pulmonary Arterial Pressure

MPO: Myeloperoxidase

MRI: Magnetic Resonance Imaging

mRNA: Messenger Ribonucleic Acid

NAD: Nicotine Adenine Dinucleotide

NET: Neutrophil Extracellular trap

PAEC: Pulmonary Arterial Endothelial Cell

PAH: Pulmonary Arterial Hypertension

PASMC: Pulmonary Artery Smooth Muscle Cell

PAWP: Pulmonary Arterial Wedge Pressure

PBS: Phosphate-Buffered Saline

PDH: Pyruvate Dehydrogenase

PDK: Pyruvate Dehydrogenase Kinase

PER: Peak Ejection Rate

PET: Positron Emission Tomography

PFKFB3: 6-phosphofructo-2-kinase 3

PFR: Peak Filling Rate

PH: Pulmonary Hypertension

PhA: Physical Activity

PHD2: Prolyl Hydroxylase Domain-2

PKFM: Muscle Phosphofructokinase

PVR: Pulmonary Vascular Resistance

qPCR: Quantitative Polymerase Chain Reaction

RCOi: Right-Ventricle Cardiac Output Index

REDVi: Right-Ventricle End-Diastolic Volume Indexed

RESVi: Right-Ventricle End-Systolic Volume Indexed

RNA: Ribonucleic Acid

ROI: Region of Interest

ROS: Reactive Oxygen Species

rplp0: Acidic Ribosomal Phosphoprotein P0

RSVi: Right-Ventricle Stroke Volume Indexed

RT: Room Temperature

RV: Right ventricle

RVSP: Right Ventricle Systolic Pressures

SC: Subcutaneous

SD: Standard Deviation

SIRT: Sirtuin

SLC2A1: Solute Carrier Family 2, Facilitated Glucose Transporter Member 1

SLC2A4: Solute Carrier Family 2, Facilitated Glucose Transporter Member 4

SMC: Smooth Muscle Cell

SPECT: Single Photon Emission Computed Tomography

Sugen/Sugen 5416: Vascular Endothelial Growth Factor type 2 receptor antagonist

SuHx: Hypoxia Plus Sugen

SUV: Standard Uptake Values

SV: Stroke Volume

SVi: Stroke Volume Index

TEM: Transmission Electron Microscopy

TGFβ: Transforming Growth Factor-Beta

Tom20: Translocase of the Outer Membrane of Mitochondria 20

Ub: Ubiquitin

USP: Ubiquitin-Specific Protease

Usp11$^{-/-}$: USP11 Knockout

VEGF: Vascular Endothelial Growth Factor

VOI: Volume of Interest

WB: Western Blot

WHO: World Health Organization

WT: Wild Type

WU: Wood Units

XPS: X-Ray Photoelectron Spectroscopy

αSMA: α-Smooth Muscle Actin

Abstract

Pulmonary hypertension (PH) is a complex condition characterized by increased pressure in the arteries of the lungs, which can damage the right side of the heart. PH is classically defined by mean pulmonary artery pressure values ≥25 mmHg. Most often, PH appears as a sequel to another disease, except in the case of group I-PH, pulmonary arterial hypertension (PAH), which courses with pulmonary vascular remodeling and increased resistance. The right ventricle (RV) increases the force of contraction to maintain blood flow, leading to hypertrophy, and ultimately heart failure. Worldwide, it is estimated that almost 1% of the population suffers from PH. Nonetheless, PH remains a fatal disease. Symptoms include shortness of breath, fatigue, chest pain, increased heart rate, and in more advanced cases, dizziness, syncope and edema. The main diagnostic methods include echocardiography as a non-invasive screening tool and RV catheterization to establish a definitive diagnosis. Given the importance of early diagnosis in the management of the disease, further research is needed to refine a non-invasive and specific technique capable of detecting PH at an early stage. As there is still no cure, therapy is aimed at palliating symptoms and delaying disease progression. In this regard, lifestyle interventions are gaining relevance as a supportive treatment for the disease, including physical exercise. However, there are many unknown aspects of PH and, despite advances, the lack of understanding of some aspects of the disease can make it challenging to find a cure. We have focused on some key elements of PAH pathogenesis, such as inflammation, hypoxia, and metabolic alterations, to analyze how they affect the pathology. The thesis is divided into 5 chapters in which different interventions have been carried out in preclinical rodent models: (i) the influence of physical activity on the phenotype of PH has been assessed, and it was observed that physical activity protects against some of the typical manifestations of PH; (ii) the use of ^{68}Ga-IONP-citrate-cFLF, a specific radiolabeled probe targeting neutrophilic inflammation was evaluated in two models of PH, concluding that it is able to detect the differential presence of neutrophils *in vivo* in different PH models; iii) the effects of 2-deoxyglucose (2DG) have been investigated through a proteomic study, and it was determined that 2DG treatment attenuates biomarkers associated with PH, possibly through the preservation of myocardial energy metabolism; iv) the phenotypic consequences (pulmonary and cardiac) of modulating mitochondrial function by chemical agents were determined, observing that altered mitochondrial function impacts key PH markers; v) and finally the effects of manipulating hypoxia signaling through ubiquitin-specific protease 11 (USP11) were assessed, determining that USP11 inhibition may offer some sex-specific protection against the development of the PH-associated phenotype.

Resumen

La hipertensión pulmonar (HP) es una condición compleja caracterizada por un incremento de la presión en las arterias de los pulmones, que puede dañar el lado derecho del corazón. Clásicamente se define por unos valores de presión arterial pulmonar media ≥25 mmHg. Con mayor frecuencia, la HP aparece como secuela de otra enfermedad, excepto en el caso de la HP del grupo I, hipertensión arterial pulmonar (HAP), que cursa con remodelación vascular pulmonar e incremento de la resistencia. El ventrículo derecho (VD) aumenta la fuerza de contracción para mantener el flujo sanguíneo, lo que acaba provocando su hipertrofia, y finalmente insuficiencia cardíaca. A nivel mundial se estima que casi el 1% de la población sufre de HP. A pesar de ello, sigue siendo una enfermedad mortal. Los síntomas incluyen dificultad respiratoria, fatiga, dolor en el pecho, aumento de la frecuencia cardíaca, y en casos más avanzados, mareos, síncopes y edema. Los principales métodos de diagnóstico comprenden el ecocardiograma como herramienta de cribado no invasiva y el cateterismo cardíaco derecho para establecer un diagnóstico definitivo. Dada la importancia del diagnóstico precoz en el manejo de la enfermedad, se necesita más investigación para refinar una técnica no invasiva y específica, capaz de detectar la HP en una etapa temprana. Como aún no hay cura, la terapia se dirige a paliar los síntomas y retrasar la progresión de la enfermedad. En este sentido, las intervenciones en el estilo de vida están ganando relevancia como tratamiento de apoyo de la enfermedad, entre las que se incluye la práctica de ejercicio físico. Sin embargo, sigue habiendo muchos aspectos desconocidos de la HP, y, a pesar de los avances, la falta de comprensión de la enfermedad puede obstaculizar la cura. Nos hemos centrado en algunos elementos clave de la patogénesis de la HAP, como la inflamación, la hipoxia y las alteraciones metabólicas, con el fin de analizar cómo afectan a la patología. La tesis se divide en 5 capítulos en los que se han llevado a cabo diferentes intervenciones en modelos preclínicos de roedores: i) se valoró la influencia de la actividad físicas en el fenotipo de la HP, y se observó que protege frente algunas de las manifestaciones típicas de la HP; ii) se evaluó el uso de que ^{68}Ga-IONP-citrato-cFLF, una sonda radiomarcada con afinidad por los neutrófilos en dos modelos de HP, concluyendo que es capaz de detectar la presencia diferencial de inflamación neutrofílica *in vivo* en distintos modelos de HP; iii) se indagó en los efectos de la 2-deoxyglucosa (2DG) mediante un estudio proteómico, y se determinó que el tratamiento con 2DG atenúa los biomarcadores asociados a la HP, posiblemente a través de la preservación del metabolismo energético del miocardio; iv) se determinaron las consecuencias fenotípicas (pulmonares y cardíacas) de la modulación de la función mitocondrial mediante agentes químicos, observando que las alteraciones de la función mitocondrial impactan en los principales marcadores de HP; v) por último, se valoraron los efectos de la manipulación de la señalización de hipoxia a través de la peptidasa específica de la ubiquitina 11 (USP11), determinando que la inhibición de USP11 podría ofrecer cierta protección específica del sexo contra el desarrollo del fenotipo asociado al HP.

INTRODUCTION

I)   Introduction

I.1 General description

I.1.1 Definition

Pulmonary hypertension (PH) is a type of exacerbated blood pressure in the lungs' arteries that can damage the right side of the heart. PH is a complex condition classically defined by an increase in mean pulmonary arterial pressure (mPAP) (≥25mmHg), measured by right heart catheterization in the supine position at rest [1]. Although this threshold has prevented overdiagnosis and overtreatment, it has been conservative and arbitrary [1]. Based on data from healthy subjects, scientific evidence has recently revealed that mPAP above 20 mmHg is already outside the healthy range. On this basis, resting mPAP >20 mmHg sets a more accurate limit for abnormal pulmonary arterial pressure [1].

Nevertheless, the resting mPAP value is insufficient to define pulmonary vascular disease since additional factors impact this pathology [1]. Further invasive hemodynamic parameters have begun to be considered, particularly pulmonary vascular resistance (PVR) and pulmonary arterial wedge pressure (PAWP) [1]. PAWP evaluated together with the left ventricular filling, left atrial pressure, and mitral valve function, helps to differentiate pre- and post-capillary PH [2]. PVR describes the resistance that blood must deal with to pass through the pulmonary vasculature. PVR functions as a static index to assess the hemodynamics of pulmonary circulation. Mathematically it is calculated as PVR=((mPAP-PAWP)/cardiac output (CO)), measured in Wood Units (WU, mmHg·min/L) [3].

Classically, this pre-capillary/post-capillary distinction has been used to differentiate between PH related to the remodeling of the arterial part, from the PH that occurs as a consequence of an increase in pulmonary venous pressure in left heart diseases, respectively. PAWP differentiates between post-capillary and pre-capillary PH [4]: high values of PAWP are normally indicators of post-capillary PH. Pre-capillary PH is hemodynamically defined by the concomitant presence of mPAP >20 mmHg, PAWP ≤15 mmHg, and PVR ≥3 WU at rest [1].

I.1.2 PH classification

According to the World Health Organization (WHO), PH is classified depending on the underlying cause. The first group, pulmonary arterial hypertension (PAH or group I-PH), presents as a primary alteration in the pulmonary vasculature. PAH is further divided into idiopathic pulmonary arterial hypertension (iPAH), familial PAH, or associated with previous disorders (i.e., congenital heart disease, connective tissue diseases, human immunodeficiency virus infection, portal hypertension, drugs and toxins, hemoglobinopathies, pulmonary venous or capillary abnormalities). Group II-PH (PH due to left heart disease) arises from heart failure, valvular heart

disorders, or cardiovascular conditions leading to post-capillary PH. The third group of PH is a complication of obstructive lung disease, restrictive lung disease, hypoxia without lung disease, or developmental lung disorders. Group IV-PH, due to pulmonary artery obstructions, is mainly represented by chronic thromboembolic pulmonary hypertension (CTEPH), a rare and progressive form of PH caused by non-dissolving blood clots in the lungs. Finally, a fifth group, PH group V, encompasses miscellaneous PH, with unclear or multifactorial causes. [1], [5]

Healthy   **Pulmonary Arterial Hypertension**
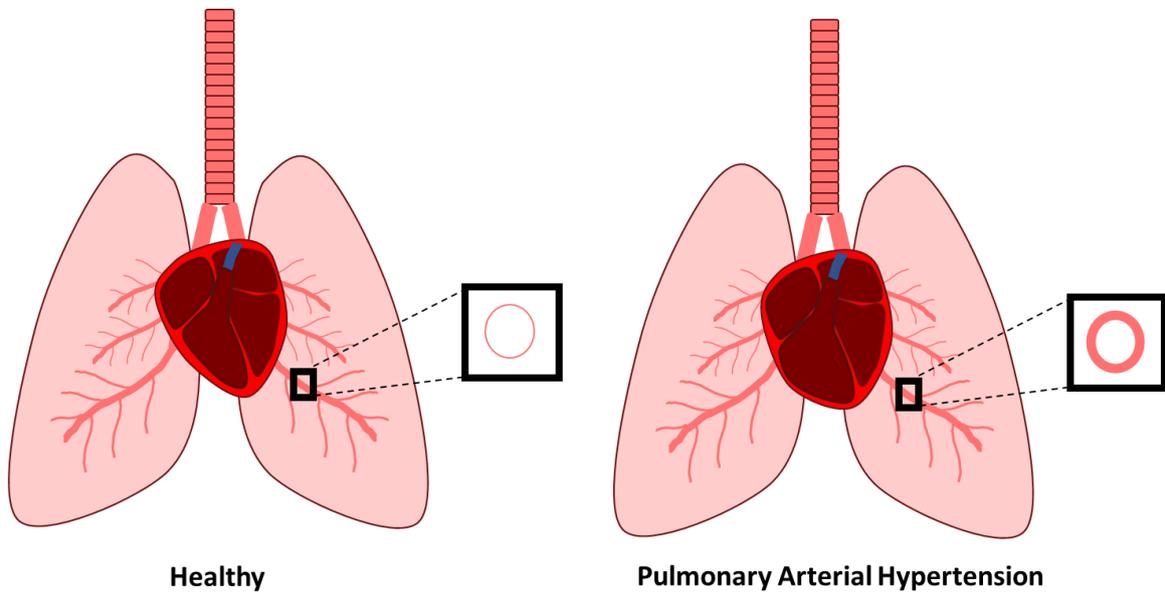
Figure 1. Illustration of the cardiorespiratory system in healthy patients and those with PAH.

Most frequently, PH appears as a sequel of another disease, except in the case of group I-PH non associated with previous disorders. PAH involves pulmonary vascular remodeling, characterized by a thickening of the arterial walls. Obliteration of the lumen and stiffening of the pulmonary vasculature cause increased resistance to blood flow. In the early stages of the disease, during the cardiac adaptation period, the right ventricle (RV) wall adjusts to increased pressures to maintain blood flow. RV must exert greater force in the contraction, causing hypertrophy of the right heart muscle mass. If high pressures are maintained for a long time, or the pressure increases excessively, it finally leads to heart failure. [5]

I.1.3 Prevalence and incidence

The epidemiology of PH is challenging to study because, currently, reliable diagnosis requires RV catheterization, an invasive procedure. Carrying out an epidemiological study based on invasive tests is not recommendable; thus, large-scale population-based studies rely on alternative diagnostic techniques, such as echocardiography. For this reason, one must be cautious when interpreting epidemiological results because data may not be entirely accurate [6].

Table 1. Prevalence of PH among the distinct groups.

	PREVALENCE
PH	Almost 1% of the world's population [6]. 3260 cases per 1 million inhabitants [7].
GROUP I	6.6-151 cases per 1 million inhabitants [7]–[10].
GROUP II	2500 cases per 1 million inhabitants [7]. Heart failure: 1000-2000 cases per 1 million adult inhabitants [11]. PH is present in more than 50% of heart failure patients [6].
GROUP III	370 cases per 1 million inhabitants [7].
GROUP IV	3.2-50 per 1 million inhabitants [12].

Globally, it is estimated that almost 1% of the world's population suffers from PH, and that after the age of 40, the lifetime risk of developing PH could be one in ten [6]. A community-based study in Western Australia between 2003-2009 revealed a minimum prevalence for all forms of PH, around 3260 cases per 1 million inhabitants [7].

Regarding PAH, in this same study, they report a prevalence of 151 cases per 1 million inhabitants [7]. However, this number is higher than that identified in other cohorts. In French hospitals, between 2002-2003, the prevalence was estimated at 15 cases per 1 million inhabitants, and the incidence was 2.4 cases per 1 million adult inhabitants/year [10]. In contrast, an UK/North Ireland cohort from 2001 to 2009 estimated a prevalence of 6.6 cases per million and an incidence of 1.1 cases per million/year [8]. In Scotland, between 1986–2001, 52 cases per million inhabitants and 7.1 cases per 1 million inhabitants/year were the numbers corresponding to the prevalence and the incidence, respectively [9].

Group II-PH, left heart disease-associated PH, was the most common form in the Western Australia cohort, with 2500 cases per 1 million inhabitants [7]. The prevalence of heart failure in high-income countries is generally estimated at 1000-2000 cases per 1 million adult inhabitants [11], and the incidence ranges from 100 to 900 cases per million inhabitants/year [11]. These records are mainly reached in Asia, Africa, and Latin America [6]. PH is a frequent complication of heart failure, affecting more than 50% of these patients [6]. In the United States, between 1997-2000, 83% of heart failure with preserved ejection fraction (EF) patients coexist with PH [13]. Moreover, in other cardiac pathologies, such as aortic valve disease or severe mitral valve disease, PH incidence is around 65% and nearly 100%, respectively [14].

Related to lung diseases, group III-PH affected 370 cases per 1 million inhabitants in Western Australia population [7]. More specifically, the global prevalence of chronic obstructive pulmonary disease (COPD) in adults aged older than 40 years is around 6.2%. Among COPD patients, the incidence of PH is reported to be between 30% and 70% of patients [15]. The most common form of interstitial lung disease, idiopathic pulmonary fibrosis, is in the range of 9-49

cases per 1 million adult inhabitants in Europe or 33-451 per million globally [16]. In these patients, 15-66% manifest mPAP ⩾25 mmHg, depending on seriousness [17].

CTEPH prevalence is difficult to assess in the general population, as it tends to be underdiagnosed [12]. Estimated CTEPH prevalence in different countries ranges from 3.2 per 1 million inhabitants in Spain, 19 per 1 million inhabitants in Japan, 47 per 1 million inhabitants in France, 38 per 1 million inhabitants in the United Kingdom, and 30–50 per 1 million inhabitants in the United States [12].

In group V-PH, the prevalence varies widely depending on the sub-phenotype [1[17].

Over recent years the age of diagnosis has shown a general trend toward an increase [18]. Concerning PAH, back in the 1980s, the National Institutes of Health registry reported 36 years as the mean age at diagnosis of PAH [18]. However, more recent studies, such as the United States PAH registry published in 2012, reported an average mean age of newly diagnosed patients of 53 years [19], and New Zealand PAH registry reported a median age of 58 years in a cohort of patients diagnosed from 2004 to 2017 [20]. This delay may be due to various factors, including that PAH in the elderly could have been misdiagnosed previously [18].

In other types of PH, the mean age at diagnosis in recent years is close to these epidemiological data. Age at COPD onset has been reported to be 57.2 years [21], while different studies state that the mean age was 51.6 in the United States [22] and 56 in Japan [23].

An essential feature of PH, especially for PAH, is sexual dimorphism. Prevalence is predominantly female, although the sex ratio balances out at older ages. However, PAH has a worse prognosis in men [24]. The hemodynamic profile, RV adaptation, survival, and response to some treatments differ according to gender [24]. Based on this, the influence that sex can have on the development of PH must be considered.

I.1.4 From symptoms to prognosis

PH may remain asymptomatic for some time, and symptoms usually develop slowly, although, unfortunately, the disease progresses rapidly. The typical symptoms include respiratory distress (dyspnea) during routine activities, fatigue, chest pain, increased heart rate, loss of appetite, breathing difficulties at rest, dizziness or syncope, bluish color, and edema of the ankles, legs, and abdomen [5], [25]. Considering that most of these signs and symptoms are also displayed in other pathologies of the lungs and heart, a final diagnosis is often difficult to detect on routine examination. The patients commonly require to be analyzed in specialized multidisciplinary units. It must also be considered that various pathologies and physiological processes, such as aging, end up with PH, and that this condition can complicate most cardiovascular and respiratory conditions. An early and differential diagnosis is, therefore, crucial in the progress of the disease.

Still, nowadays, there is a 1.2-year diagnostic delay of PAH in New Zealand [20], 9.6 months in Poland [26], and 2.3-3.9 years in France, Germany, and Australia [26]. Other groups of PH, such as CTEPH, have a similar diagnosis delay [27]. Unfortunately, the time from symptom onset to diagnosis of PH has not significantly decreased in the past 20 years [25].

Despite advances, PH is still a fatal disease. The 1980s registry of the National Institutes of Health reported a median survival of 2.8 years [24]. More recently, in the western Australia cohort previously mentioned [7], the mean survival for patients with estimated Right ventricular systolic pressure (RVSP) >40 mmHg was 4.3 years.

I.1.5 Diagnosis

Given the importance of early diagnosis in managing the disease, simple and accessible diagnostic methods are required.

The patient should be examined when PH is suspected due to symptoms and physical findings. The preferred imaging technique is echocardiography [5]. However, other diagnostic tests can alternatively be performed, such as electrocardiography (not recommended as a screening tool since a normal electrocardiogram does not exclude PH), ventilation/perfusion lung scintigraphy, or computed tomography (CT) of the thorax [25]. Based on the results of these initial tests, if there is evidence of PH, it is necessary to search for the underlying cause in order to apply the appropriate treatment. That is, determine to which PH group the patient belongs. For example, to discriminate CTEPH, the screening test of choice is radionuclide perfusion scanning [5] and lately, dual-energy CT is being recommended for future studies [12]. Finally, for subjects considered "probable PAH patients," the next step is to confirm PH using an invasive approach, either hemodynamic evaluation or right heart catheterization [5].

To summarize, the transthoracic echocardiogram is the essential non-invasive screening tool, and right heart catheterization usually remains mandatory to establish a definitive diagnosis [25]. Since the first is imprecise and the second is an invasive technique, there is considerable interest in using novel imaging techniques in assessing and categorizing patients with PH [5].

Novel diagnostic modalities that comprise innovative imaging techniques are emerging, such as ventilation-perfusion single photon emission computed tomography (SPECT) or dual-energy CT to measure lung perfusion [12] and magnetic resonance imaging (MRI) as a tool for assessing ventilation [25]. Other imaging procedures include time-resolved three-dimensional (3D) phase contrast MRI (which visualizes and quantifies cardiovascular blood flow in three dimensions and along the cardiac cycle). Intravascular ultrasound and optical coherence tomography can demonstrate intimal fibrosis, a surrogate marker of pulmonary arterial remodeling [25]. Techniques are also being developed to infer subclinical RV dysfunction using magnetic resonance metrics, such as a ventricular mass index, to assess functional and structural changes in the RV. T1 mapping is a non-invasive technique for extracellular volume quantification, which facilitates early detection of myocardial damage [25]. Machine learning applications and reliable

imaging biomarker developments are complementary approaches to these new diagnostic modalities [25].

There are many diagnostic methods, but more research is needed to refine a highly-specific non-invasive technique to detect PH at an early stage.

I.1.6 Therapy

As there is no cure, pharmacological and non-pharmacological therapies aim to decrease pulmonary vascular resistance, palliate symptoms, improve exercise capacity, and delay disease progression. Therapeutic opportunities depend on the PH clinical group classification and must be personalized [17]. For PAH, the first agents introduced were the prostacyclin analogs, known as potent vasodilators [28]. Endothelin receptor antagonists and antimitotic substances that could specifically dilate and remodel the pulmonary arterial system [29] are also used, as well as phosphodiesterase type 5 inhibitors, dealing with the nitric oxide pathway. Iron supplementation may be required, as iron deficiency is common in PAH. The cornerstone of groups II- and III-PH is managing heart and lung diseases. Soluble guanylate cyclase stimulators and oral anticoagulants are used to treat CTEPH, though pulmonary thromboendarterectomy is the treatment of choice [28].

Lifestyle interventions are gaining relevance as supportive treatment of the disease. Exercise intolerance is probably one of the main consequences limiting the quality of life in PH patients [1]. Until 2009, physical exercise was discouraged in subjects with precapillary PH, for fear of further stress the RV and induce heart failure [30]. Today, this idea has been renewed. Two systematic reviews [31], [32], collecting the latest studies carried out in this field, conclude that supervised exercise-based rehabilitation is beneficial for patients with groups I, II, and III-PH (when medically stable). The benefits in group IV-PH and more severely diseased patients are unclear. Both reviews emphasize that more studies are needed to give a specific recommendation about the type, intensity, duration, degree of regulation, and optimal exercise environment. This last point is especially relevant if we take into account that, although the benefits of a personal training program have become evident, some types of exercise carry a risk for patients with PH [33]. An increase in physical activity shares some benefits of a structured exercise program while avoiding the hazards. A lower daily step count is associated with an increased risk of hospitalizations in patients with PH [34], and in patients with PAH and CTEPH, increased physical activity positively correlated with quality of life and survival [35].

Moreover, animal models help determine exercise's effects on PH development. In general, preclinical studies point to a disease improvement [36], [37] or a delay in the appearance of symptoms [38]. Most of these preclinical studies use a male rat model induced by monocrotaline (MCT) under a structured exercise protocol (3-5 weekly sessions of between half and one hour) and conclude that physical activity exerts a protective effect [38]–[41], although, in more advanced stages, represented by MCT-induced progressive PH, exercise training become

detrimental [42]. As in human patients, the animals starting the physical training before or in the very early stages of the disease demonstrated the preventive effects against the PH development.

I.2 Molecular mechanisms underlying PAH

Several factors can trigger an increase in RV muscle mass or pulmonary artery pressure. Accordingly, it is challenging to elucidate the mechanisms underlying the development of PH. Since in groups II to V, the increase in pulmonary artery pressure appears as a consequence of another previous pathology, we will focus on the mechanisms that trigger PH as a primary cause, mimicking PAH.

One of the pathological hallmarks of PAH progression is pulmonary vascular remodeling. In this process, the arterial lumen is reduced, thus producing an increase in flow resistance and augmented pressures [43]. It has been proposed that vasculature alterations involve extracellular matrix (ECM) remodeling and the subsequent rewiring of smooth muscle cells (SMCs) anchorage to ECM [43]. This pathological mark is associated in an advanced stage with increased vascular stiffness and reduced pulmonary arterial compliance [44].

Concomitant to these changes, the pathogenesis in the pulmonary vasculature includes: i) perivascular infiltration of macrophages, dendritic cells, T- and B-lymphocytes, and mast cells as a source of inflammatory factors; ii) vasoconstriction/vasodilation imbalance; and iii) dysregulation of cell apoptosis and proliferation [45], [46]. The combination of these factors results in the hypertrophy of the arterial medial, adventitial thickening, and the phenotypic switch of the pulmonary vascular cells from a contractile to a synthetic and proliferative phenotype [47]. More advanced stages of the disease involve the formation of complex cellular and fibrotic neointimal and plexiform lesions. Furthermore, intimal fibrosis is conspicuous in many forms of PAH [45] and may occur in the absence of plexiform lesions [48].

There are still gaps in understanding the disease severity, interaction with comorbidities, treatment response, and prognosis. We have focused on some key elements of the pathogenesis of PAH, such as inflammation, hypoxia, and metabolic alterations. We aim to provide some notions and tools that may be useful to guide the development of future diagnostic and/or therapeutic strategies.

I.2.1 Inflammation

Inflammation is a physiological defense mechanism that becomes detrimental when dysregulated [49]. Inflammatory processes are involved in all PH groups [50]–[52], although it is unknown the chronology and bulk of the disease development [53]. The pathophysiological inflammatory component underlying each group has not been entirely elucidated.

The role of inflammation in PAH is characterized by immune response dysregulation, which is consistent in animal models [48] and patients [54]. Clinically, some inflammatory conditions correlate with a higher incidence of PAH [53]. Furthermore, the magnitude of perivascular inflammation in PAH is related to pulmonary hemodynamics, vascular remodeling, and clinical

outcome [53]. Increased serum cytokine levels in PAH patients have been associated with increased mortality [55]. In human samples, an imbalance in various genes involved in inflammatory pathways, such as major histocompatibility complex molecules and transporter 1, has been identified [56], as well as an increase in cytokines and other markers, indicative of the occurrence of inflammatory processes [54], [57]. The role of inflammation is substantiated by the presence of perivascular inflammatory cells, mainly macrophages, dendritic cells, and T and B lymphocytes in the lungs [58], [59]. Experimentally, PAH can be induced in animals by exposure to immunogenic stimuli, including human immunodeficiency virus, schistosomiasis, and interleukin-6 overexpression [60]. Inflammation in other groups of PH is summarized in Figure 2.

1. PAH
- Human patients: imbalance in related genes and cytokines.
- Animal models (MCT, Hypoxia): increase in circulating MIF inflammatory cytokine levels

5. Multifactorial mechanisms
- Heterogeneous.

PH Inflammation

2. LV disease
- Human patients: faulty immune response.
- Animal models (TAC): leukocyte infiltration and high values of pro-inflammatory cytokines.

4. CTEPH
- Human patients: elevated inflammatory markers and peripheral blood lymphocytes.

3. Lungs disease
- Human patients: higher serum levels of inflammatory biomarkers.

Figure 2. Inflammation in the different groups of PH.

Upon the appearance of an inflammatory stimulus, the primary immune response is activated. Tissue macrophages are the first line of defense and attract neutrophils through chemotaxis. Macrophage infiltrations have been reported in patients and animal models of PH [61], [62]. However, the role of neutrophils in pathological angiogenesis and vascular dysfunction in PH has been recently suggested [63], [64]. Neutrophils act by secreting toxic reactive oxygen species (ROS) and proteolytic enzymes to destroy pathogens. However, upon pathological activation, these granulocytes can also damage the surrounding tissues [65]. There are three elements of these cells of particular relevance in the context of PH: i) neutrophil extracellular traps (NETs), associated with inflammatory angiogenesis and disordered vascular homeostasis; ii) neutrophil

proteases, which increased activity is linked to lung disease [66]; and iii) myeloperoxidase (MPO), that catalyze ROS formation [63], [64], [67].

Inflammation causes an increase in the secretion of matrix metalloproteinases and other pro-inflammatory factors, which, through a positive feedback loop, reactivate inflammation [44]. In a more complex way, PH can be understood as a systemic disease in which certain risk factors can produce a cascade of reactions, implying the interaction of different organs, such as the intestine, autonomic areas of the brain, the cardiorespiratory system, or the bone marrow, which could be connected through pro-inflammatory progenitors [68].

Due to the lack of knowledge of the precise mechanism, attempts to target inflammation in PH have not been successful. To solve this, monitoring inflammation *in vivo* can help investigate the pathology and support the diagnosis and management of PH. One of our objectives is to assess the role and value of different imaging modalities in evaluating inflammation in different PH animal models.

I.2.2 Metabolic rewiring

OXPHOS/Glycolysis and mitochondria

During the development of PH, crucial alterations appearing along with structural changes are related to energy metabolism. The metabolism must cover the energetic demands of the highly proliferating cells. Metabolic reprogramming in PH is context-specific [69], [70] and may depend on the state of the disease. In the early stages, the mitochondrial oxidative phosphorylation is reduced in favor of aerobic glycolysis [71]. At this point, pyruvate, an end-product of glycolysis, is oxidized into the mitochondria after being converted by the pyruvate dehydrogenase (PDH) into acetyl-CoA, a major entry point into the Krebs' cycle. In PH models, PDH activity is often inhibited by the pyruvate dehydrogenase kinase (PDK) [72]. Consequently, pyruvate is converted into lactate. Lactate production contributes to the acidification of the microenvironment and likewise affects neighboring cells for energy utilization [71]. This reprogramming of cells to preferentially use glycolysis over oxidative phosphorylation for adenosine triphosphate (ATP) production is called the Warburg effect [73] and is very well-known in the cancer literature. The glycolytic switch involves endothelial cells (ECs), SMC, fibroblasts, cells of the immune system, and the sympathetic nervous system [74]. The cells of the pulmonary arteries increase the expression of glycolytic enzymes and glucose uptake while mitochondrial metabolism is repressed. This has the additional effect of suppressing the catabolic reactions in the mitochondria and providing the cells with the anabolic intermediates necessary for synthesizing amino acids, lipids, and nucleotides [74]. To try to alleviate these metabolic decompensations, therapy with glycolysis inhibitors has been tried. In animal models, both 3-bromopyruvate, a hexokinase (HK) 2 inhibitor [71], and dichloroacetate (DCA), a metabolic modulator and a pyruvate analog that inhibits mitochondrial PDK and enhances oxidative phosphorylation [75], attenuated the development of PH. DCA is even being tested to treat human patients with iPAH

[76]. DCA also upregulates the potassium channels Kv 1.5 in the mitochondrial membrane, leading to depolarization and subsequent caspase activation, which trigger apoptosis in pulmonary artery smooth muscle cells (PASMCs) [77]. Administration of DCA in PH rats induced by chronic hypoxia reversed the disease in these animals [77]. Thus, the results found in classic models of PH have demonstrated that, when DCA regulates the disturbed PASMC bioenergetics by preventing the metabolic shift from cellular respiration to glycolysis; PASMC hyperplasia, pulmonary artery vessel remodeling and hypertrophy are significantly reduced. This opens the way for the use of glycolysis inhibitors with therapeutic potential in PH.

In some cases, following these metabolic switches produced at early PH stages, a general decrease in glucose metabolism characterized by down-regulated glycolysis has been observed [70]. Mitochondria occupy a central role in metabolic rewiring processes.

Mitochondria are cytoplasmic organelles of eukaryotic cells formed by a double membrane whose primary function is the production of ATP, the major source of cellular energy. They also carry out part of the fatty acid metabolism through β-oxidation, and act as calcium storage [78]. Over the past two decades, new mitochondrial functions have been discovered. They act as mediators between different compartments (for example, with the endoplasmic reticulum) in communication with the cytosol to initiate biological responses in different homeostatic and stress conditions. Moreover, mitochondria are also involved in complex crosstalk with the nucleus [79]. Furthermore, mitochondria participate in the biosynthesis of iron-sulfur, heme- and lipid groups. Due to their capacity to produce energy, they integrate and converge anabolic and catabolic processes, playing an essential role in cell differentiation, proliferation, apoptosis, death, and adaptation mechanisms under stress conditions [79].

Structural and functional mitochondrial abnormalities have been described in the pulmonary arteries and RV of both patients and experimental models of PH [80], [81]. Results have shown the hyperpolarization of the SMCs mitochondria in human and animal pulmonary arteries with PH [82]. Such hyperpolarization is associated with increased pore opening limit and resistance to apoptosis [81]. In this regard, the role of mitochondria triggering SMCs and ECs to an apoptosis-resistant phenotype has been postulated as a PH driver. The development of PH is also associated with major mitochondrial metabolic changes such as electron transport chain dysfunction, mitochondrial deoxyribonucleic acid (DNA) damage, and alterations in the biogenesis and mitophagy coupling processes. In addition, mitochondria undergo phenotypic and structural modifications impacting the mitochondria network through fusion and fission processes [83]. In RV, mitochondrial dysfunctions have been associated with the progression of PH. Mitochondria play a critical role in maintaining cardiac function, as evidenced by a larger number of mitochondria in the heart muscle than in other tissues [84]. In PH, it has been observed that in the various stages of the disease, RV cardiomyocytes show distinct metabolic phenotypes. Demonstrated in a rat model MCT from three to six-weeks exposure to this toxin, in the hypertrophic compensated phase (rats before the 4th week exposure), the glucose oxidation to glycolysis ratio decreases, but in decompensated RV, the glycolytic phenotype is

reversed, contributing to ischemia and RV failure [85]. Mitochondrial dysfunction could be behind these changes [69]. Furthermore, the loss of physical and functional communication between the endoplasmic reticulum and mitochondria is a key structural event in developing pathological cardiac hypertrophy [86]. The Sugen 5416-hypoxia (SuHx) rat model of PH courses with mitochondrial hyperpolarization, structural and functional abnormalities of this organelle, along with increased ROS synthesis [87]. A metabolic shift from fatty acid oxidation to glycolysis in cardiomyocytes from PH subjects that developed myocardial hypertrophy and failure has also been reported [88].

On this basis, we can affect the phenotype associated with PH by modifying mitochondrial biogenesis and function. In this sense, results obtained with DCA have opened a new therapeutical window to treat this disease.

Choline metabolism

Additional metabolic pathways are altered in PH, including choline metabolism [89]. Choline is a quaternary ammonium base, an ubiquitous metabolite, and an essential constituent of cell and mitochondrial membranes. Choline participates in four major pathways. First, choline can be phosphorylated to produce phosphatidylcholine and further phospholipids, which are an integral part of the cell membranes. Choline can also be oxidized in the liver and kidney mitochondria to betaine, a compatible osmolyte, and a methyl donor. Furthermore, choline is a precursor of acetylcholine, which acts as a neurotransmitter [90]. An additional role of choline is in one-carbon metabolism, which is crucial for multiple physiological processes, including cellular biosynthesis, amino acid homeostasis, methylation, and regulation of the redox state [91].

Studies suggest a role for choline metabolism in PH. Metabolic analysis of blood and plasma samples from PH human patients found elevated choline [92] and enrichment of the acyl choline pathway [93]. Besides, lung tissue samples from a SuHx- induced mice model of PAH presented higher levels of phosphocholine and glycerophosphocholine [89].

^{18}F-Fluorodeoxyglucose (^{18}F-FDG) and ^{11}C-Choline as positron emission tomography (PET) metabolic tracers to study the metabolic shift in PH

An efficient way to monitor metabolism *in vivo* is by administering specific radiotracers and measuring their uptake by PET.

^{18}F-FDG is the most widely used radiotracer. Fluorodeoxyglucose (FDG) is a glucose analog bound to the radioactive isotope fluorine-18, whose uptake in different tissues reflects glucose metabolism [74].
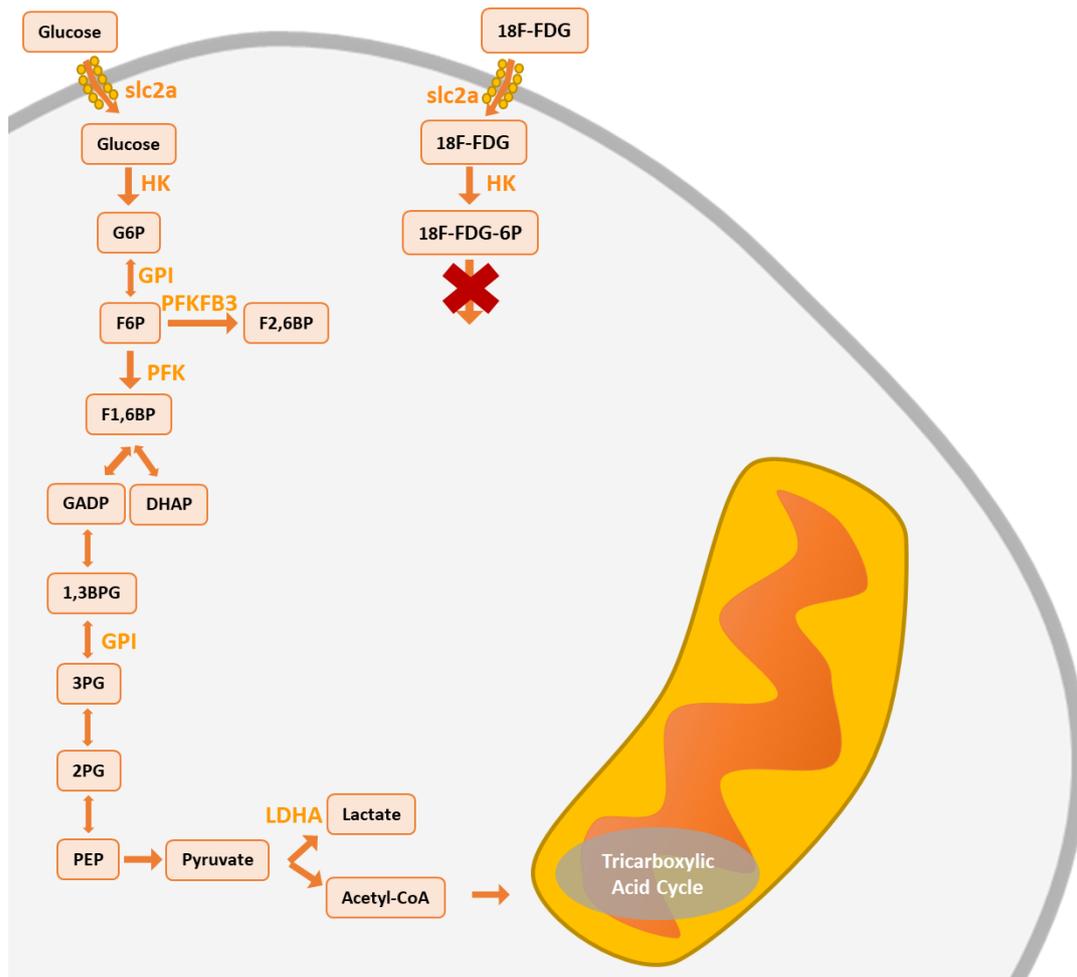
Figure 3. Scheme of the metabolism of glucose and its radioactive analogue, ^{18}F-FDG.

Higher ^{18}F-FDG uptake has been detected in lung parenchyma and RV of patients with iPAH than in controls, while uptake in large pulmonary arteries was similar [94]. In RV, ^{18}F-FDG accumulation is associated with RVSP elevation, although it failed to dictate severity [95].

These manifestations have also been reported in animal models, although critical aspects were not considered to reduce variability (e.g., fasting periods and use of left ventricle (LV) as reference). In MCT and SuHx rat models, pulmonary ^{18}F-FDG uptake was observed to increase in the PH animals [96], and RV/LV ratio was also increased in MCT rats with a difference between compensated and decompensated RV [85]. A mild increase in ^{18}F-FDG uptake appeared in RV of PH mouse models [89].

Similar to glucose, to monitor alterations in choline metabolism *in vivo*, this molecule can be labeled with a radioactive isotope similar to ^{18}F-FDG. Choline can indeed be labeled with ^{11}C or ^{18}F.

Although many studies have demonstrated the value of using ^{18}F-FDG in a PH context, as far as we know, no previous studies explored the potential role of ^{11}C-Choline as an imaging biomarker of cell proliferation in the context of PH.

I.2.3 Hypoxia

Hypoxia is defined as oxygen deficiency, an abnormal condition caused by a decrease in the oxygen supply and/or oxygen consumption. At the cellular level, hypoxia triggers adaptive responses [97].

The main orchestrators of hypoxia adaptation are the hypoxia-inducible factors (HIFs), involved in both acute and chronic responses to hypoxia [98]. HIFs, composed of HIF-1, HIF-2, and HIF-3, are heterodimeric proteins consisting of an oxygen-sensible α-subunit and a stable β-subunit constitutively expressed [99]. In the presence of oxygen, HIF-α is hydroxylated, ubiquitinated, and degraded into the proteasome [99]. HIF-1α half-life in normoxia is less than 5–10 minutes [100]. Upon hypoxia, the enzymes catalyzing HIF-α hydroxylation are no longer active, and thus, HIF-1α remains stable [99]. Once stabilized, HIF-α translocases into the nucleus, where it binds HIF-β, giving rise to the active form of the transcriptional complex HIF. This molecule binds the hypoxia-responsive elements, regulating the expression of the target genes [99]. Most of these genes' functions aim to promote cell survival under hypoxic conditions by causing molecular changes that allow cells to adapt to stress by reducing oxygen consumption or increasing oxygen availability [98]. Among the adaptive responses, HIF-1 upregulates genes encoding glucose transporters and enzymes of the glycolytic pathway and suppresses oxidative phosphorylation to promote an increased glycolytic flux [100].

Hypoxia is an environmental factor closely related to PH [101]. Although aerobic organisms usually cope with hypoxia, inappropriate adaptation causes devastating effects, especially in chronic situations. PH and hypoxia are associated in a bidirectional way. On the one hand, it has been observed that hypoxia causes PH in residents at high altitudes and patients with pathologies such as COPD or sleep apnea [102]. On the other hand, in animal models [103] and patients with PH, hypoxemia has been reported [104]. Furthermore, chronic hypoxia alone or double-hit chronic hypoxia plus an anti-angiogenic treatment are standardized models of PH in small mammals [48].

Adaptations to oxygen deprivation in the cardiopulmonary system may reinforce a link with the PH development. In pulmonary arterioles, hypoxia increases ROS levels, which inhibits the activity of voltage-gated K^+ channels and allows Ca^{2+} influx, leading to the depolarization of the PASMCs [105] and, consequently, pulmonary vascular constriction. Different concentrations of ROS affect the vascular tone and the balance between cell proliferation and apoptosis, which promote the development of PH [106]. Pulmonary arterial endothelial cells (PAECs) try to compensate for pulmonary vasoconstriction by releasing vasodilators that act locally on the smooth muscle layer. In patients with PH, the secretion of vasodilators is inhibited, favoring endothelial dysfunction, vascular remodeling, obliteration of pulmonary arteries, and further hypoxia, which again induces vasoconstriction, restarting the cycle and accelerating the process [104]. Moreover, adventitial fibroblasts perform a symphony of events that lead to changes in the function and structure of the vessel wall [107]. A wide heterogeneity has been identified

among fibroblasts derived from the adventitia of pulmonary arteries. Under hypoxic conditions, pathogenic fibroblasts are selectively imposed, with an increased proliferative capacity [108].

In summary, in hypoxic conditions, PAECs present deregulated proliferation, abnormal behavior, and release factors that stimulate the proliferation of PASMCs and the increased deposition of ECM components [109]. All these changes can lead to PH.

The effects of hypoxia on the heart are specific. Under normal conditions, cardiac tissue obtains 60-90% of ATP from the oxidation of fatty acids. In PH, the heart tackles an increased demand for oxygen but a decreased supply. Thus, the activation of the transcription factor HIF-1α becomes notably relevant. Up-regulation of glycolytic enzymes and glucose oxidation suppression derived from HIF-1 activation precipitate a glycolytic phenotype [110]. Acute hypoxic exposure is associated with mild PH, characterized by increased heart rate, decreased stroke volume (SV), and altered diastolic filling patterns of both ventricles [111].

Indeed, HIF has been directly implicated in PH [101]–[103]. HIF is a crucial mediator in regulating the mechanisms underlying PH, including metabolism rewiring, erythropoiesis, angiogenesis, and vascular remodeling [112]. Both *HIF-1α$^{+/-}$* [113], [114] and *HIF-2α$^{+/-}$* mice [115] exposed to normobaric hypoxia are protected against RV hypertrophy and PH development. In addition, when exposing conditional knockout (KO) mice to hypobaric hypoxia, inhibition of HIF-2α but not HIF-1α attenuated the development of PH [116]. Targeted deletion of HIF-1α in PAECs of mice maintained in normobaric hypoxia did not cause variations in RVSP or pulmonary arterial wall thickness compared to wild type (WT). However, the deletion of HIF-2α in the pulmonary endothelium improved markers of hypoxia-induced PH [117]. A different situation was reported in the case of HIF-1α deletion in SMCs of mice exposed to hypoxic conditions. In this case, pulmonary vascular remodeling and pulmonary pressure were reduced, though RV hypertrophy was not affected [118]. However, once exposed to hypoxia, myeloid-specific HIF-α KO mice exhibited a minor increase in PVR, RV hypertrophy, muscularization of small pulmonary arteries, and macrophage infiltration into the lungs and RV compared with WT mice [104]. Likewise, intratracheal instillation of lentivirus-carrying HIF-1α short hairpin ribonucleic acid (RNA) effectively reduced the hypoxia-induced elevation of RVSP, pulmonary vascular remodeling, and the muscularization of arterioles in rats [109].

The complex regulation of the hypoxia-mediated response by HIF has opened the field to many areas of study. As explained, ubiquitination is central in regulating the hypoxia signaling pathway. The regulation of this process could impact the response to hypoxia of the organism and can be an exciting and novel therapeutic target.

Ubiquitin (Ub) conjugation triggers changes in protein activity or stability [119]. Ubiquitination is a reversible process, which can be reversed by Ub proteases called deubiquitinating enzymes (DUBs). These enzymes can remove polyubiquitin chains from their specific target proteins. DUBs can be classified into distinct families based on their catalytic domains. The ubiquitin-

specific protease (USP) subclass accounts for the most prominent family of DUBs [120]. USP11 is a member of the USP family.

USP11 has been related to tumorigenesis, both promoting tumor initiation and progression through the deubiquitination and stabilization of implied enzymes [121]–[124] and functions as a tumor suppressor through the stabilization of protective proteins against tumors [125]. USP11 also plays a crucial role in regulating the cell cycle and DNA damage responses [126]–[129], inflammation, cellular growth, and apoptosis [130], [131]. More importantly, a role for USP11 has recently been reported as an activator of the hypoxia signaling pathway by regulating HIF-1α messenger ribonucleic acid (mRNA) stability [132]. Considering this last action, by modulating USP11, it is possible to investigate the effects of HIF regulation on the development of PH.

To sum up, PH is a widely unknown disease with high mortality, no cure, and triggers a substantial decrease in the patient's quality of life. In this thesis, different interventions have been conducted in rodent models to determine the manifestations of the development of the disease and expand the imaging tools for a comprehensive characterization of the PH phenotype.

II)   HYPOTHESIS AND OBJECTIVES

II) Hypothesis and objectives

We expected that modulation of physical activity, mitochondrial function and hypoxia signaling would lead to alterations in vascular remodeling and cardiac hypertrophy.

1. Preclinical study to evaluate the influence of environmental factors such as patients' quality of life in the phenotype of PH: physical activity. Physical activity can serve as an adjuvant therapy for PH.
2. Evaluation of the value of different PET nanoradiotracers for PH diagnosis in different animal models.
    2.1. PET nanoradiotracers targeting specific neutrophilic inflammation.
    2.2. PET-^{11}C-Choline and ^{18}F-FDG as biomarkers of cell proliferation and inflammation.
3. Multi-scale analysis of the phenotypic (lung and heart) consequences of interventions in rodent models of PH.
    3.1. Mitochondrial function.
    3.2. Manipulating hypoxia signaling through USP11.

MATERIAL AND METHODS

III) Material and methods

Animal models

Animal handling was conducted under the European Council Directive 2010/63/UE. The Ethical Committee at CIC biomaGUNE and local authorities *Diputación Foral de Guipuzcoa* (projects authorization number: PRO-AE-SS-152, PRO-AE-SS-181, and PRO-AE-SS-112) approved all the animal experiments of this thesis.

PH is a complex disease and, although various increasingly accurate small rodent models have been developed, none faithfully recapitulates all the aspects of the pathology in human patients [133]. We have used different animal models in rats and mice, depending on the needs of the study.

<u>Rats</u>

*MCT-induced model: R*ats received a single intraperitoneal (IP) injection of 60 mg/kg of MCT (C2401, Sigma-Aldrich), dissolved in HCl 1M and neutralized with NaOH. Control rats (CTL) were IP injected with the vehicle (saline serum). Although the study could be extended up to six-seven weeks after injection, we limited it to three weeks, at which the rats developed PH, in some cases severe, and the mortality is low.
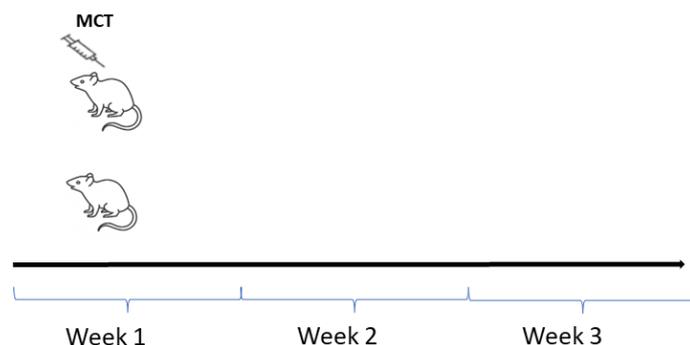
Figure 4. MCT-induced model in rats.

SuHx model: The combination of chronic hypoxia and vascular endothelial growth factor (VEGF) receptor inhibition in rats results in structural remodeling of pulmonary arterioles and progressive hemodynamic worsening not seen in any other PH model.

Rats were once injected subcutaneously (SC) at the beginning of the experiment with 20 mg/kg of the VEGF inhibitor (Sugen 5416 or Sugen; 3037, Tocris) dissolved in the vehicle (polysorbate 80 0.4% [v/v], P4780, methyl cellulose 0.5% [w/v], M6385; benzyl alcohol 0.9% [v/v],24122-1L-M in saline solution) and exposed to normobaric hypoxia at 10% O_2 inside a hypoxic workstation (BioSpherix) for three weeks, followed by a week in normoxia (20% O_2). The CTL group received an SC injection of the vehicle and stayed four weeks in normoxia.
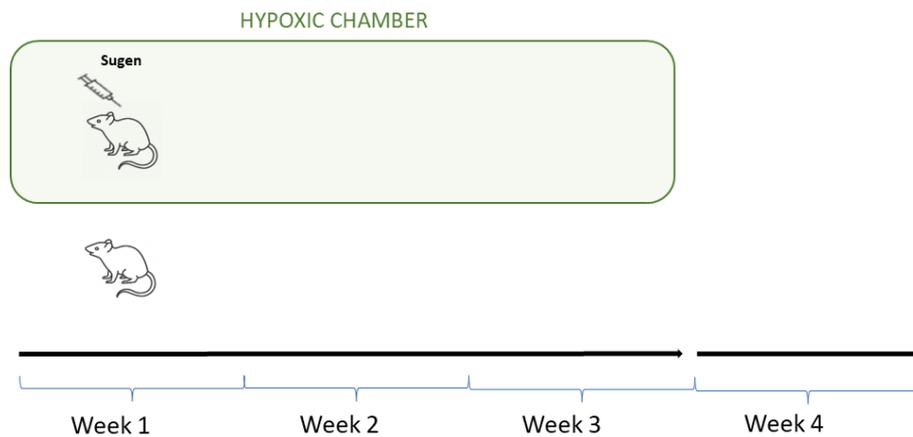
Figure 5. SuHx model in rats.

Mice

Given the anatomical and physiological characteristics of the species studied, in general, the SuHx-induced disease in mice is less severe [133]. As in rats, we used the combination of VEGF receptor inhibition (using Sugen 5416, from now on just Sugen) in concert with chronic hypoxia (10% O_2) as a model of PH to mimic the right ventricular hypertrophy and heart failure observed in PAH patients [134]. Mice were injected IP with 20 mg/kg of Sugen (3037, Tocris) once a week (three injections in total) dissolved in the vehicle described above and exposed to normobaric hypoxia at 10% O_2 inside a hypoxic workstation (BioSpherix) for three weeks, followed by 2-4 days in normoxia (20% O_2). CTL group received an IP injection of the vehicle and stayed four weeks in normoxia.

As even at very low concentrations, Ethidium Bromide is known to be potentially toxic and harmful, it is worth noting that in the case of the Ethidium Bromide and Physical Activity models, due to the unpredictable consequences that this intervention could have on the animals, the mice only received a single IP injection of Sugen in the first week of the experiment.
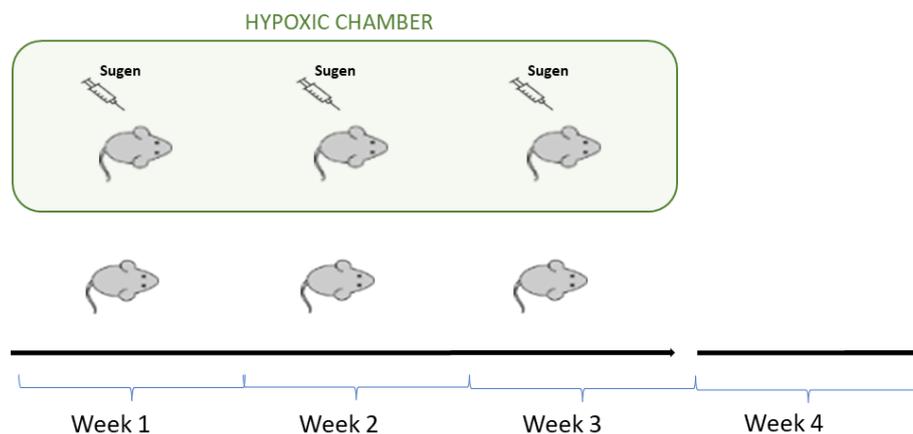
Figure 6. SuHx model in mice.

Study design

Chapter IV.1: 6 weeks-old C57BL/6J male mice were divided into four groups (n=4/each group): normoxia (CTL), normoxia with physical activity (CTL-PhA), hypoxia plus Sugen (SuHx), and hypoxia plus Sugen with physical exercise (SuHx-PhA). In control and SuHx, physical activity groups had free access to a running or activity wheel (see Figure 7) capable of quantifying turn numbers (1284L, Tecniplast).

Figure 7. Activity wheel adapted for mouse cages used in the experiments performed in this doctoral thesis. Activity wheels were introduced in the cages inside the hypoxia chamber, working at low concentration levels (10%) or room air.

Subsequent to functionally characterize cardiac magnetic resonance (CMR) and ^{18}F-FDG/^{11}Choline PET imaging, RVSPs were measured, animals were perfused with heparinized saline, and the lungs and heart were harvested for pathological determination. The right lung and the apical part of the heart were placed in liquid nitrogen to be stored at -80°C, while the left lung and the basal part of the heart were processed to form paraffin blocks.

Chapter IV.2: 6-8 weeks old RjHan: Sprague Dawley female rats (Janvier Labs, Saint Berthevin CEDEX, France) were divided into four groups (n=4/each group): normoxia control injected with vehicle (CTL), MCT and hypoxia plus Sugen (SuHx).

Subsequent to functional characterization by CMR and ^{18}F-FDG/^{68}Ga-IONP-citrate-cFLFLF PET imaging, RVSPs were measured, and rats were sacrificed. One rat from each group was reserved for the quantification of the vasculature by perfusion with a microfil® suspension (MV-122/130, Flow Tech Inc.). The rest of the rats were perfused with heparinized saline, and the lungs and hearts were harvested to form paraffin blocks.

Chapter IV.3: 6-8 weeks old RjHan: Sprague Dawley female rats (Janvier Labs, Saint Berthevin CEDEX, France) were divided into 4 groups (n=6/each group): normoxia control (CTL), normoxia with 2-deoxyglucose (2DG) (CTL-2DG), hypoxia plus Sugen (SuHx) and hypoxia plus Sugen with 2DG (SuHx).

In the treated groups, drinking water was supplemented with 0.4% (w/v) of 2DG (D6134, Sigma-Aldrich).

Subsequent to the functional characterization by CMR and ^{18}F-FDG PET imaging, RVSPs were measured, rats were perfused with heparinized saline, and the lungs and heart were harvested for pathological determination. The heart ventricles were separated and placed in liquid nitrogen to be stored at -80°C, while the lungs were processed to form paraffin blocks.

Chapter IV.4: Ethidium Bromide (EtBr) cohort: 6 weeks-old C57BL/6J male mice (Janvier Labs, Saint Berthevin CEDEX, France) were divided into 4 sub-groups (n=4/each group): normoxia (CTL), normoxia with EtBr (CTL-EtBr), hypoxia plus Sugen (SuHx) and hypoxia plus Sugen with EtBr (SuHx-EtBr). Ethidium bromide was dissolved in drinking water (0.033 mg/mL) *ad libitum*.

2DG cohort: 6 weeks-old C57BL/6J male mice (Janvier Labs, Saint Berthevin CEDEX, France) were divided into 4 sub-groups (n=9/each group): normoxia (CTL), normoxia with 2DG (CTL-2DG), hypoxia plus Sugen (SuHx) and hypoxia plus Sugen with 2DG (SuHx-2DG). 2DG was similarly prepared in a 4 mg/mL aqueous solution and administered in drinking water.

Fluid intake was measured in all groups to control the final dosage applied per animal's weight.

After the functional characterization by CMR and PET imaging, RVSPs were measured, animals were perfused with heparinized saline, and the lungs and heart were harvested for a pathological determination as described below. The right lung and the heart apex regions were placed in liquid nitrogen to be stored at -80°C, while the left lung and the basal part of the heart were processed into paraffin blocks.

Chapter IV.5: 8-9 weeks-old C57BL/6N-Atm1Brd Usp11tm1$^{(KOMP)Wtsi}$ mice were divided into 8 groups: normoxia WT male (CTL-WT-male; n=3), normoxia *Usp11*$^{-/-}$ male (CTL-*Usp11*$^{-/-}$ male; n=3), normoxia WT female (CTL-WT female; n=3), normoxia *Usp11*$^{-/-}$ female (CTL-*Usp11*$^{-/-}$ female; n=3), hypoxia plus Sugen WT male (SuHx-WT male; n=5), hypoxia plus Sugen *Usp11*$^{-/-}$ male (SuHx-*Usp11*$^{-/-}$ male; n=5), hypoxia plus Sugen WT female (SuHx-WT female; n=5), hypoxia plus Sugen *Usp11*$^{-/-}$ female (SuHx-*Usp11*$^{-/-}$ female; n=5).

Following the functional characterization by CMR and ^{18}F-FDG PET imaging, mean RVSP values were measured, mice were sacrificed by cervical dislocation, left lungs were embedded in formalin for paraffin blocks, and the ventricles of the heart and right lung were snap-frozen by immersing them in liquid nitrogen.

Hemodynamic measurements

Systolic pulmonary arterial pressure measurement is the gold-standard technique for PH diagnosis. However, the small size of the mice vessels' lumen hampers reaching the pulmonary artery using floating catheters safely. For this reason, the closed-chest right intraventricular pressure was used as a surrogate biomarker.

Anesthetized (2% isoflurane) rats or mice were placed supinely on a warmed table. The right neck area was shaved, and a small incisure was opened. The jugular vein was carefully dissected, and a tiny surgical hole was prepared to introduce a mikro-catheter (SPR-671NR Millar Catheter, ADInstruments, Dunedin, New Zealand). Then, the catheter was advanced to reach the RV, and the measurements were rapidly performed. The RVSP was recorded by a PowerLab data acquisition system (ADInstruments, Sydney, Australia) and digitized by LabChart software (ADInstruments). The average RV pressure was measured during systole to determine the individual RVSP. This is an experimental endpoint procedure carried out just before the sacrifice of the animals.

MRI acquisition protocol and manual segmentation

Cardiac MRI acquisitions were performed on a 7 Tesla Bruker Biospec 70/30 USR MRI system (Bruker Biospin GmbH, Ettlingen, Germany), interfaced to an AVANCE III console and with a BGA12-S imaging gradient insert (maximal gradient strength 400 mT/m, switchable within 80 μs). A combination of a 72 mm Bruker volumetric quadrature coil for excitation and a Rapid Biomedical 20 mm rat brain 4x array coil for the reception was used.

Rats or mice were anesthetized (3% isoflurane in 30% oxygen for induction and 1-2% isoflurane for maintenance throughout the experiment). They were prone positioned in a corresponding customized-3D printed bed with a head holder. The temperature in all cases was kept with heated air pumped through an MRI-compatible system interfaced to a monitoring and gating Model 1025 (SA instruments). The experiment monitored anal temperature and respiration through an MRI-compatible thermocouple and respiratory pad. The total experimental time per animal was about one hour.

Pure axial and 4-chamber view scout images were used to set up the representative heart views. Short-axis images were acquired from the apex covering both ventricles for cardiac function measurements. 11-12 x 0.8 mm (mice) x 1.2 mm (rats) consecutive slices were acquired using a Bruker cine IntraGate gradient-echo FLASH sequence with the following parameters: effective echo time TE=2.82 ms; repetition time TR=6.87 ms; matrix=256 x 128 points; flip angle FA=300; field of view FOV=25 x 25 mm. All images were reconstructed in 15-20 phases of a single cardiac cycle using the retrospective Intragate Bruker software. These cine magnetic resonance images, a type of sequence acquired to capture motion, were split according to the trigger time, corresponding to each cardiac cycle period for data analysis. For image analysis, regions of

interest (ROIs) were manually delimited using the open-source software ITK-SNAP (Version 3.8.0). Endocardial and epicardial surfaces were manually contoured on short-axis imaging to obtain end-systolic (ESV) and end-diastolic volumes (EDV) for both ventricles, including papillary muscles and trabeculations in LV and RV cavities. The ESV and EDV were subsequently used to calculate all the characteristic parameters of the cardiac function, such as stroke volume (SV = EDV-ESV) and ejection fraction (EF=SV/EDV). Volumes were indexed for body surface area (BSA) (ESVi, EDVi, SVi). BSA was calculated using the following equations: BSA=9.83 x body weight(g)$^{2/3}$) [135] and BSA=20 x body weight (g)$^{0.42}$ [136] for rats and mice, respectively. By averaging the manually delimitated regions between the epicardium and endocardium in two end-systolic frames, we calculated the volume of the myocardium. Since MRI directly provides volumes, we used a clinically accepted 1.055 g/mL value of myocardial tissue density and the MRI volumes to estimate the myocardial masses. Using this data, we calculated the Fulton index (RV mass / (LV mass + septum mass)).
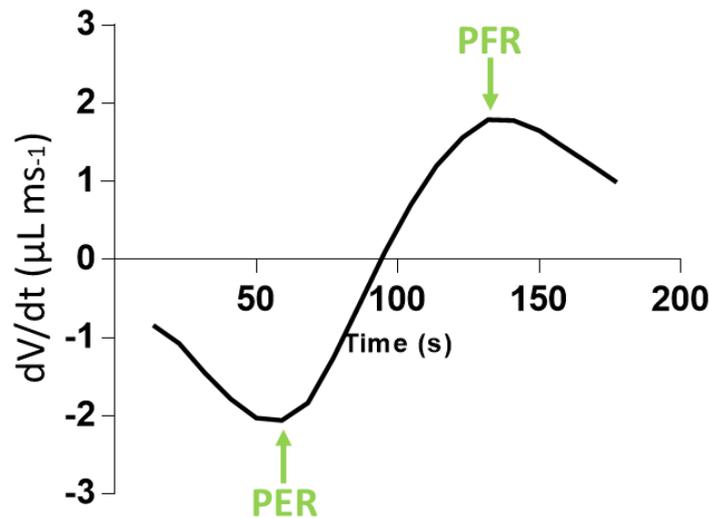
Figure 8. SuHx curves of the derivative of the ventricular volume with respect to time. Maximum ejection rate (PER) and maximum filling rate (PFR) are marked in green.

As described before [137], ventricular curves were obtained from the representation of the derivative of the ventricular volume with respect to time, that is, the slope at each point, such as the example in Figure 8. These curves provided precise information on systolic and diastolic function since additional functional parameters, such as the corresponding maximum or minimum filling (diastolic) or ejection (systolic) rates for each ventricle, can be obtained. Connected to the systolic function, we calculated the minimum amplitude, which is the negative peak during systole and represents the maximal ejection rate (PER). Regarding diastolic function, we calculated the maximum filling rate (PFR), defined as the maximum amplitude, which is the positive peak during diastole. For both ventricles, PER and PFR were normalized to EDV.

Positron emission tomography and computed tomography (PET/CT) imaging

PET and micro-CT imaging acquisitions were sequentially performed with β (PET) and X-cube (CT) microsystems of Molecubes® (MOLECUBES NV), respectively. Rats or mice were injected with the corresponding radiotracer. In each case, ^{18}F-FDG (100-180 µCi, after fasting overnight) or ^{68}Ga-IONP-citrate-cFLFLF (65-150 µCi) were intravenous (IV) injected through the tail vein and imaged 30 minutes post-administration by static 10 minutes scan whole-body images (1 bed). For ^{11}C-Choline, 150-200 µCi was injected IV through the tail vein. Whole body scans were acquired just after administration for 30 min. Dynamic scans were reconstructed with the frames: 5 x 30 s, 5 x 1 min, 5 x 1.5 min, 5 x 2 min, 1 x 5 min.

Anesthesia was induced by 4-5% isoflurane inhalation in pure O_2 and maintained with a 1.5-2% flow rate based on respiration-rate monitoring (60-80 bpm). Animals were maintained warm using the installed pad inside the equipment.

All the images (1 bed) were acquired in a 511 keV ± 30 % energetic window. CT acquisitions were also generally performed at the end of each PET scan for anatomic information and attenuation correction, providing unambiguous localization of the radioactive signal.

The reconstruction of the images was performed using the mathematic algorithm 3D-OSEM (3D Ordered Subset Expectation Maximization; 30 iterations).

For each animal, PET-CT images were co-registered and analyzed using PMOD image analysis software (PMOD Technologies Ltd, Zürich, Switzerland). The volumes of interest (VOIs) were manually outlined on the organs of interest on the CT images. VOIs were transferred to PET images, and activity values normalized to the initial amount of radioactivity were obtained as mean standard uptake values (SUV).

Quantitative polymerase chain reaction (qPCR) of heart and lung tissue

The apical heart and the right lung were excised and immediately snap-frozen in liquid nitrogen to analyze different mRNA levels by real-time quantitative polymerase chain reaction (RT-qPCR). RNA was extracted from tissues using the Maxwell® RSC simply RNA tissue kit (AS1340, Promega) described in the manufacturer's protocol. Briefly, tissue was embedded in 200 µL of chilled RNA latter (10584445, ThermoFisher) and kept at -20 °C until processed. Samples were then prepared by adding the tissue to 200 µL of chilled homogenization solution, including disrupting beads (Beads: Ceramic Bead Tubes 1.4 mm) and disrupted in a Precellys homogenizer (Bertin Technologies). 200 µL of Lysis Buffer was added to the homogenates, vortexed, and transferred to the cartridge into the Maxwell. Samples were processed, and the eluted RNAs were transferred to new tubes.

Approximately 1 µg of RNA was used as a template for reverse transcription using MaximaRT (Maxima™ H Minus cDNA Synthesis Master Mix finished, M1682, Invitrogen). 1/40th of the reaction was subsequently used for qPCR using specific primer sets (Table 2) and Taqman. qPCR

was performed in a ViiA 7 or QPCR QUANTSTUDIO 6 FLEX (Life Technologies) machine, and cycles were set as follows: 10 minutes at 95 °C, 40 cycles of 15 seconds at 95 °C, and 1 minute at 60 °C with a final cycle of 5 seconds at 55 °C and 50 seconds at 95 °C. All RT-qPCR data presented were normalized using acidic ribosomal phosphoprotein P0 *(rplp0)*. Table 2 includes the details of the primers used for the study.

Table 2. List of mouse oligos used for qPCR.

Gene	Enzyme	Forward primer sequence	Reverse primer sequence
rplp0	Acidic ribosomal phosphoprotein P0	actggtctaggacccgagaag	ctcccaccttgtctccagtc
hk1	Hexokinase 1	gtggacgggacgctctac	ttcactgtttggtgcatgatt
gpi	Glucose-6-phosphate isomerase	cctctttataatcgcctccaag	accactcctttgctgtctctg
pfkfb3	6-phosphofructo-2-kinase 3	acaggacaagtactactatcgctatcc	tggcgctctaattccatga
pgk1	Phosphoglycerate kinase 1	tacctgctggctggatgg	cacagcctcggcatatttc
ldha	Lactate dehydrogenase A	ggcactgacgcagacaag	tgatcacctcgtaggcactg
slc2a1	Solute carrier family 2, facilitated glucose transporter member 1	gaccctgcacctcattgg	gatgctcagataggacatccaag
slc2a4	Solute carrier family 2, facilitated glucose transporter member 4	gacggacactccatctgttg	gccacgatggagacatagc
pkfm	6-phosphofructokinase, muscle type	agatcgtagacgccatcacc	cggcccatcacttctaaca
tgfß	Transforming growth factor beta	tggagcaacatgtggaactc	gtcagcagccggttacca

Histological and immunofluorescence analysis

Lung and heart tissues were fixed with 10% formaldehyde for 24 h at room temperature (RT), dehydrated with alcoholic solutions, and embedded in paraffin. Lung and heart tissues were then cut into 5-µm sections and stained with an Elastic stain kit (HT25A-1KT, Sigma-Aldrich) and Picrosirius red, using Direct Red 80 (365548, Sigma-Aldrich), 0.5% acetic acid glacial solution (10304980, Fisher Scientific) and Weigert's Hematoxylin Solutions. Slides were digitalized using Cell Axio Observer microscopy (ZEN). 20x images were taken on a tile covering the entire lung and stitched together to identify the pulmonary arteries throughout the tissue.

Elastic Stain is used in vascular diseases because it stands out elastin, which is part of the connective tissue that is not well differentiated from other stains such as hematoxylin and eosin. This protocol stains the collagen in red while staining the elastic fibers in black and the muscle in yellow. This way, a clear identification of the pulmonary vasculature's SMC facilitates this layer's manual delimitation. Thickness quantification allows the measurement of vascular remodeling so that higher values are related to a stronger vascular reshape.

Five peripheral vessels adjacent to the airways in transverse orientation (the longest side did not exceed twice the length of the shortest side) were randomly taken from all the lung tissue. Medial wall thickness, lumen diameter, and medial wall cross-sectional area of small arteries (40–80 μm outer diameter) were determined using the open-source software ImageJ (Version 1.53). The diameter of the lumen on all occasions was delimited to the point of greatest length. These measurements have facilitated two indices to quantify the type and degree of vascular remodeling: percent medial wall thickness (medial wall thickness/inner diameter × 100) and percent wall area medial (medial wall cross-sectional area/total cross-sectional area × 100).

For immunofluorescence, five μm-thick sections of lung and heart tissues paraffin-embedded were deparaffinized with xylene and alcoholic solutions in decreasing concentrations. Antigen retrieval was performed with Sodium citrate buffer (pH 6) in a vegetable steamer on a 45-minute cycle and then allowed cooling down at RT for a total of 2 h. After washing in phosphate-buffered saline (PBS)-Triton 0,1% tissues were incubated with blocking solution (bovine serum albumin 1% + Goat serum 2% + PBS + Triton 0,1%) for 30 minutes at RT in a humid chamber. Subsequently, the slides were incubated with anti-ki67 (14-5698-82, ThermoFisher; 1/100), anti-alpha smooth muscle Actin (Abcam, ab7817; 1/500) and anti-tom20 (11802-1-AP, Proteintech; 1/100) antibodies overnight at 4 °C in a humid chamber. The next morning, after washing thoroughly with PBS-Triton 0.1%, the slides were incubated with Alexa Fluor 488 anti-Rat (10694383, ThermoFisher; 1/400), Alexa Fluor 555 anti-Rabbit (10082602, ThermoFisher; 1/400), Alexa Fluor 647 anti-Mouse (10739374, ThermoFisher; 1/400) or Alexa Fluor 647 anti-Rabbit (10123672, ThermoFisher; 1/400) secondary antibodies for 30 minutes RT in the humid chamber. Afterward, the nuclei were counterstained with 4',6-diamidino-2-phenylindole (DAPI) (10116287, ThermoFisher Scientific; 1/1000), and, finally, the slides were mounted with Fluorescence Mounting Medium (S302380-2, Agilent). Immune-stained slides were digitalized using Cell Axio Observer microscopy (ZEN).

Synthesis of ^{68}Ga-IONP-citrate-cFLFLF

Chapter IV.2

Synthesis of ^{68}Ga-IONP-citrate: ^{68}GaCl$_3$ (aq) precursor was eluted from the ^{68}Ge/^{68}Ga generator with 1 mL (from 2nd to 3rd mL in the elution) of HCl 0.05 M at 1mL/min rate and added directly to a microwave tube with 18.75 mg of FeCl$_3$·6H$_2$O (0.07 mmol) and 20 mg of sodium citrate dihydrate (0.068 mmol) dissolved in 1.25 mL of Milli-Q water, the mixture had an activity of 4.59

mCi. 0.25 mL of hydrazine hydrate was added, and the microwave was ramped to 100 °C for 1 min, and then the temperature was held for 10 min. The mixture was cooled to 60 °C and purified by a PD-10 column (previously activated with 25 mL of ultrapure Milli-Q water). The first drops were discarded, and the solution was recovered in a vial, obtaining 2 mL of nanoparticles solution. ICP-MS: [Fe]=1.28 mg/mL.

Synthesis of ^{68}Ga-IONP-citrate-cFLFLF (peptide): All previous solution (2.5 mL) with 2.75 mCi was added to a vial with 13.4 mg of 3-dimethylaminopropyl-N'-ethylcarbodiimide hydrochloride and 16.28 mg of N-hydroxysulfosuccinimide, the mixture was stirred 30 min. The purification was carried out by centrifugation (10.35 x g, 4 min) with six AMICON 30K filters. The retentate in each filter was resuspended in 150 µL of PBS (0.01M pH 8). This suspension was added to a vial with 1 mg of peptide (cFLFLF) in 50 µL of dimethyl sulfoxide (DMSO) and stirred for 1 h. Then, another centrifugation was carried out (10.35 x g, 4 min) with two AMICON 30K filters. The retentate was resuspended in 400 µL of saline solution (0.9%) of each filter (800 µL in total with 412 µCi). To prepare the final injectable doses, the appropriate amount of nanoparticles solution with the desired activity was taken with a syringe before proceeding to the administration. The total time of the synthesis from elution was around 140 min. ICP-MS: [Fe]=1.81 mg/mL in the final solution.

Microfil perfusion

In Chapter IV.2, to quantify and visualize the vascular (arterial and venous) remodeling *ex vivo*, we used a commercial alternative of casting agents, microfil® (MV-122/130, Flow Tech Inc.), that is used to fill and cast the vasculature. This is a colored resin containing a heavy atom (lead chromate) to act as a CT contrast agent. Anesthetized rats with 2% inhaled isoflurane were IV perfused with saline serum and subsequently with the MV122/130 microfil® solution and let sit for approximately 1 h RT until this fluid had polymerized. Lungs were extracted, fixed in formalin for 12-24 h, and stored in a 70° alcoholic mixture, deyhol 70 (610070, Lavolan), at 4 °C until CT scan. 3D data of the lungs with a complete vascular casting were generated by CT image acquisition, allowing a complete view and quantification of the lung vasculature. 3D VOIs were automatically delimited (-300 to -800 Hounsfield units, (HU)) in these images using the open-source software ITK-SNAP (Version 3.8.0) to provide quantitative values of the vascular remodeling.

Immunohistochemistry (IHC) analysis

In Chapter IV.2, five µm-thick sections of lung tissues paraffin-embedded were deparaffinized with xylene and ethanol in decreasing concentrations. Antigen retrieval was performed with sodium citrate buffer (pH 6) in a vegetable steamer on a 45 minute cycle and then allowed to cool for a total of 2 h RT. The next step was hydrogen peroxidase inhibition incubating with a

drop of endogenous blocking solution for 10 minutes RT. After washing in PBS-Triton 0.1%, the tissues were incubated with blocking solution (bovine serum albumin 1% + Goat serum 2% + PBS + Triton 0,1%) for 30 minutes RT in a humid chamber. Subsequently, the slides were incubated with an anti-Myeloperoxidase antibody (ab9535, Abcam) overnight at 4 °C in a humid chamber. The following day, after washing thoroughly with PBS-Triton 0.1%, the slides were incubated with secondary antibody for 30 minutes at RT in the humid chamber. Next, the signal amplification was carried out for 30 min. Peroxidase activity was developed with a DAB working solution and observed in a microscope. The reaction was stopped by rinsing the slides in de-ionized water and proceeded to hematoxylin counterstaining.

Proteomics

In Chapter IV.3, RV samples were digested following the filter-aided FASP protocol described by Wisniewski et al. [138] with minor modifications. Trypsin was added to a trypsin:protein ratio of 1:10, and the mixture was incubated overnight at 37 °C, dried out in an RVC2 25 Speedvac concentrator (Christ), and resuspended in 0.1% formic acid.

Samples were analyzed in a novel hybrid trapped ion mobility spectrometry – quadrupole time of flight mass spectrometer (timsTOF Pro with PASEF, Bruker Daltonics) coupled online to a nanoElute liquid chromatograph (Bruker). Sample (200ng) was directly loaded in an EVOSEP ONE chromatograph and acquired using the 30 spd protocol.

Protein identification and quantification were carried out using MaxQuant software [139] using default settings. Searches were carried out against a database consisting of *Rattus norvegicus* entries (Uniprot/Swissprot), with precursor and fragment tolerances of 20 ppm and 0.05 Da. Only proteins identified with at least two peptides at FDR <1% were considered for further analysis. Data (LFQ intensities) was loaded onto the Perseus platform [140] and further processed (log2 transformation, imputation).

Ingenuity pathway analysis (IPA) was used for enrichment analysis and detailed characterization of the molecular events behind the differential protein patterns. The calculated p-values for the different analyses determine the probability that the association between proteins in the dataset and a given pathway or upstream regulator is explained by chance alone, based on a Fisher's exact test (p-value <0.05 being considered significant). The activation z-score represents the bias in gene regulation that predicts whether the upstream regulator exists in an activated (positive values) or inactivated (negative values) state based on the knowledge about the relation between the effectors and their target molecules.

Western Blot (WB)

In Chapter IV.3, frozen RV tissues were manually pulverized using a mortar placed on dry ice. Liquid nitrogen assisted in maintaining the freezing temperature throughout the process.

For protein extraction, 150 µl of RIPA lysis buffer (1 mL RIPA (20-188, Merck) + 9 mL H_2O + inhibitors of proteases and phosphatases) were added to each sample. Subsequently, the tubes were incubated on ice for 30 min, shaking every 5 min. After this time, the samples were centrifuged at 13300 rpm for 10 minutes at 4 °C. The supernatants were transferred to a new tube.

The bicinchoninic acid assay (BCA) was performed on a 96-well plate for protein quantification. Serial dilutions of bovine serum albumin were prepared for the standard curve using RIPA as a diluent. The plate was loaded with 5 µL of each standard curve dilution in triplicate and then 1 µL of each sample in triplicate. BCA mix was added to a final volume of 100 µL in each well. The plate was incubated at 37 °C for 20 minutes in the dark. Then, the plate was read on the Epoch microplate spectrophotometer at 570 nm. The concentration of each sample was obtained by extrapolating measurements from the standard curve.

20 µg of protein extract was adjusted to a final volume of 15 µL with lysis buffer and 3 µL of loading buffer (0.6 mL 1 M Tris pH 6,8 (141940.1211, PanReac AppliChem) + 3.1 mL 80% glycerol (2143-01, J.T.Baker) + 2 mL 10% SDS (A2263,0100, PanReac AppliChem) + 0.5 mL Mercaptoethanol (M3148-25ML, Sigma) + 1 mL 1% Bromophenol blue (114391-5G, Sigma) + 2.8 mL H_2O). Heat shock treatment was completed at 95 °C for 10 min. These solutions were loaded into Mini-PROTEAN TGX Precast Protein Gels (4561096, BIORAD) and run at 100 V for 1.30 h.

Electroblotting was carried out in a Trans-Blot Turbo system with the pre-cut blotting transfer pack (1704158, BIORAD) following the MIXED MW protocol.

The membranes were stained with Ponceau reagent and incubated for 5 minutes to validate transfer efficacy. After taking photos, they were washed with 1X TBS-T until the red color disappeared.

The next step was to block the membrane for 1 h at RT while shaking with TBS-T 1X 0.1% + 5% milk (100 mL TBS-T 1X + 5 g milk). The primary antibody, anti-SIRT2 (S8447, Sigma-Aldrich; 1:1000), was then incubated overnight at 4 °C. The next day, after 3 washes of 5 minutes with TBS-T 0.1%, the secondary antibody was incubated (1:2000). 3 washes of 5 minutes were performed again with TBS-T 0.1% before the membrane was placed on parafilm and incubated for 1 minute with Novex™ ECL (WP20005, Invitrogen) (1:1), drained, and placed between 2 acetates. Finally, the membrane was revealed on iBright (chemiblots).

Since the molecular weight of sirtuin (SIRT) 2 and tubulin are very close, stripping was carried out with commercial Stripping Buffer: Restore™ Plus Western Blot Stripping Buffer (46430, Thermo-Fisher) following their protocol. The membrane was washed 4 times for 5 minutes in TBS-T in a roller and incubated for 30 minutes at 50 °C with shaking in stripping buffer. It was rewashed 6 times and 5 minutes in TBS-T on a roller. From this point, the process explained by the blockade of the membrane was repeated, using anti-tubulin (T9026, Sigma-Aldrich; 1:2000) as the primary antibody, which was maintained for 1 h at RT.

NAD$^+$/NADH ratio Measurement

In Chapter IV.3, a colorimetric measurement was performed using a NAD/NADH Assay Kit (65348, Abcam) according to the manufacturer's protocol. Briefly, around 20 mg of RV tissue were homogenized in NADH/NAD Extraction Buffer and filtered through a 10 kD Spin Column (ab93349, Abcam) to eliminate NADH-consuming enzymes. Half of the extracted samples were NAD$^+$ decomposed by heating at 60 °C for 30 minutes in a heating block (NADH sample), and the rest keep on ice (Total NAD samples). 50 μl of diluted NADH standards and samples (NADH and Total NAD samples) were loaded into 96-well microplates in duplicate. Consequently, 100 μL of the NAD cycling Reaction Mix was added to each standard and sample well. After 5 minutes incubation, NAD$^+$ in the samples was converted to NADH. Finally, 10 μL of NADH developer was added into each well, and multiple readings were taken over 3 h at OD 450 nm. The NADH concentration of the samples was extrapolated from the standard curve. The NAD$^+$/NADH ratio was calculated as (Total NAD − NADH)/NADH.

TEM: preparation of resins, images acquisition and quantification

In Chapter IV.4, mice reserved for TEM analysis were sacrificed by perfusion with a saline solution followed by a fixative medium (2.5% glutaraldehyde/2% formaldehyde in PB buffer (Na_2HPO_4/NaH_2PO_4 in water, adjusted with NaOH to pH 7.4)). Once extracted, organs were placed in the fixation medium for 5 h, washed 3 times for 5 minutes with PB buffer, and kept at 4 °C until processed in a storage medium (0.5% formaldehyde diluted in PB Buffer).

After washing with buffer PB for 10 minutes, organs were incubated in postfix solution (1% OsO4/1.5% $K_2Fe(III)(CN)_6$ in 0.1M PB) for 2 h at RT. Subsequently, samples were washed with distilled water, and dehydration began. Samples were immersed in water:acetone solutions of increasing acetone concentrations and incubated for 15 minutes RT on each solution. In the 100% acetone final solution, samples were incubated 3 times x 30 minutes at RT. With the dehydrated samples, we proceeded to the inclusion into the resin. Like the previous step, samples were immersed in resin:acetone solutions of increasing resin concentrations and incubated for 30 minutes RT on each solution. After 100% resin solution, samples were moved to the mold and polymerized at 70 °C for 3 days.

Ultrathin sections of the resins were made, mounted on grids, and stained with lead. Images were taken from the resin cuts with an ultra-high-resolution Transmission Electron Microscope, TEM, JEOL JEM-2100F UHR. This system is equipped with a field emission electron beam (Field Emission Gun) with variable acceleration between 80 and 200 kV, a 4-megapixel CMOS camera (TVIPS TemCam-F216), and two STEM detectors (BF & HAADF) in combination with an EDX detector (Oxford Ultim® Max) and has the GATAN 626 cryo-transfer system.

Statistical analysis

Statistical analysis was performed using GraphPad 9.0.2 software. One-way Analysis of variance (ANOVA), corrected for multiple comparisons using statistical hypothesis testing by Šidák correction. Values are presented as mean ± SD (SD) unless otherwise noted. p-values were represented by asterisks as follows: * $p < 0.05$; ** $p < 0.01$; *** $p < 0.001$; **** $p < 0.0001$. Differences were considered significant when $p < 0.05$.

CHAPTERS

IV) Chapters

IV.1 Consequences of physical activity on developing the phenotype associated with pulmonary hypertension in the lung and heart

IV.1.1 Rationale

Managing PH is essential to improve patients' health outcomes as a chronic disease. Physical activity is a simple, accessible, and safe intervention to improve PH patients' quality of life. A more active lifestyle reduces the risk of hospitalization [34] and improves survival [30] in PH patients.

The objective of the present study was to explore the effect of physical activity in a PH SuHx mouse model. Specifically, we aimed to analyze the influence of an increased daily movement on ventricular functional parameters and vascular dysfunction associated with PH. In our case, a well-planned physical exercise adapted to the hypoxia chamber was methodologically limited by the restricted access to this space. Thus, in this study, we evaluated the outcome of including exercise wheel-based stimulus inside the hypoxic chamber during the three-week exposure to low oxygen concentration. The practice of voluntary wheel-running physical activity in these animals was parallel to the disease's development. Voluntary exercise presents three main advantages [141] compared to forced patterns: the similarity to natural running, the absence of stress conditions, and no interference from the researcher. However, the results are not often individually recorded since several animals are included in the same cage, so exercise parameters are unavoidably averaged by the number of animals accessing the same device. Previous studies in MCT male rats undergoing similar voluntary exercise and starting before developing a PAH-liked phenotype revealed that this exercise regime delayed the development of severe arterial remodeling and RV failure [142].

Our study included four groups (CTL and SuHx with or without voluntary and open access to the running wheel) with four animals per cage. The four groups consisted of animals of the same age, diet, and sex (male). The number of rotations was registered daily as an end-point physical activity measure for each group during the first three weeks of the experiment.

Using imaging techniques, we obtained a comprehensive *in vivo* clinically relevant assessment. First, MRI evaluated cardiac function. Second, PET monitored different properties, such as glucose and choline metabolisms, through ^{18}F-FDG and ^{11}C-Choline uptake, and we evaluated these radiotracers as markers of glycolytic shift and cell proliferation, respectively. We also performed histological, immunofluorescence, and molecular biology tests to deepen the results.

IV.1.2 Results

Physiological repercussions of physical activity stimulation

All mice were visually inspected daily for any deterioration throughout the experimental conditions. Animals from different groups were healthy, without visual signs of physical or functional impairment. They did not display any adverse effects caused by the disease or any negative impact from physical activity. Besides, there were no casualties from any group. As expected, the weight gain (calculated as (final weight – initial weight) / initial weight) x 100) was smaller in the group with open access to wheels than that of the control groups (Figure 9A). The weight difference is significant when comparing SuHx versus CTL mice.
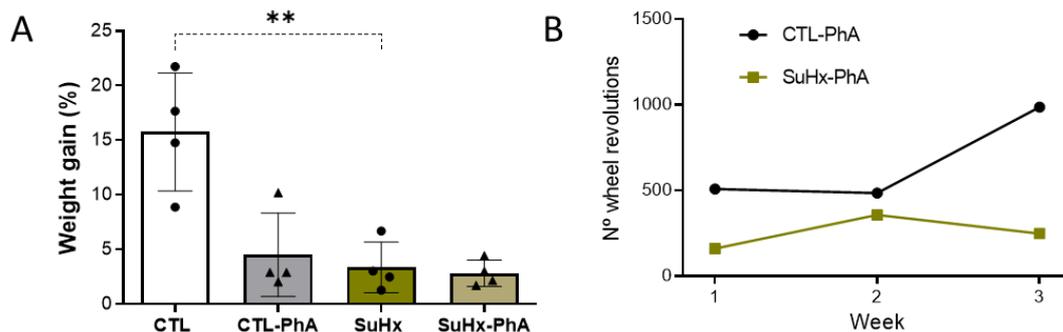
Figure 9. Tracking animal weight gain and animal-averaged wheel revolutions in the different hypoxic and normoxic groups recorded during the three week-experiment. (A) Graphic representation of the body variation weight throughout the experiment approach. Values are presented as mean ± SD, **p-value < 0.01 assessed by the One-way ANOVA test. (B) Representation of the number of revolutions on the activity wheel per week for each group. CTL: control or normoxia groups. CT-PhA: same as CTL but with free access to physical activity. SuHx: Hypoxia + Su5412 IP treatment. SuHx-PhA: same as SuHx but with free access to physical activity.

A summary of the physical activity of these animals is shown in Figure 9B. It represents the mean weekly rotation counts of the four animals from each group. The rotation counter in the activity wheel estimates the averaged, accessible, and spontaneous activity for the mice included in that cage. The average rotations in CTL groups were usually higher, indicating that these groups of animals performed more open and spontaneous activity than the diseased animals. The differences were much higher during the last week of hypoxia exposure when these mice were expected to already be in a more advanced stage of the disease. Healthy mice showed a continuous increase in physical activity during the experimental period. We also noticed a slight increase in activity in SuHx-PhA group during the first ten days in the hypoxic chamber.

Impact of physical activity on hemodynamics

As a gold-standard measure in the field (although not exempt from problems mainly in small animals due to the surgical procedure and miniaturized and fragile catheters), we performed and compared RVSP, measured by cardiac catheterization in CTL and SuHx animals. Due to technical problems with the catheter, we were unable to obtain measurements of the CTL-PhA

group. As expected, the control animals without physical activity demonstrated significantly lower RVSP than in both hypoxic groups (Figure 10). This data shows that physical activity did not prevent RVSP increase in hypoxia.

Figure 10. Tracking the RV hemodynamics. (A) Images of representatives RVSP curves. (B) Quantitative analysis of RVSP (Invasive measurement of RVSP at the end of the treatment). Values are presented as mean ± SD, *p-value < 0.05 assessed by the One-way ANOVA test.

Cell proliferation markers and pulmonary vascular remodeling

Pulmonary vascular remodeling is another classical and relevant parameter to characterize the phenotype associated with PH. The lungs were stained with elastic stain to investigate the pulmonary vascular remodeling in these animals. The percentages of medial wall thickness and medial wall area were measured to quantify vascular remodeling.

A significantly higher vascular remodeling is observed in the hypoxic groups, determined by variations in these parameters (Figure 11). Interestingly, the percentage of change in medial wall thickness was lower in the SuHx-PhA group, indicating a possible beneficial effect of physical activity on pulmonary vascular remodeling.
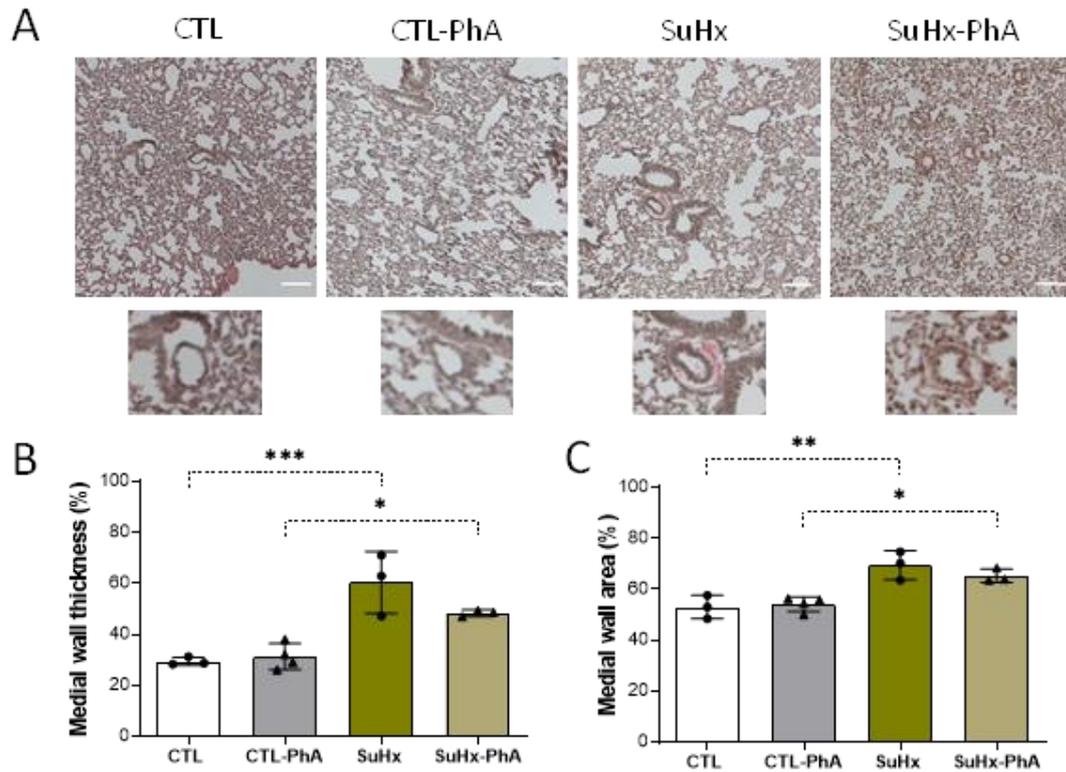
Figure 11. Assessment of pulmonary vascular remodeling. (A) Representative photomicrographs of the elastic staining of the whole lung (upper panel) and a representative pulmonary artery (bottom panel) for each lung section. Scale bars are 100 μm. Quantitative analysis of the (B) medial wall thickness and (C) medial wall area. Values are presented as mean ± SD, *p-value < 0.05, **p-value < 0.01, ***p-value < 0.005 assessed by the One-way ANOVA test.

The increase in the size of pulmonary vessels is linked to the rate of proliferation of their SMCs. Greater proliferation determines a more significant number of cells and, therefore, a higher vessel thickness. Additionally, Figure 12 summarizes the immunofluorescence analysis of pulmonary vascular SMCs proliferation and a read-out of proliferating cells using Ki67 and smooth muscle alpha-actin (αSMA), one isoform of actin, which is enriched in vascular SMCs and plays an essential role in tissue thickening.
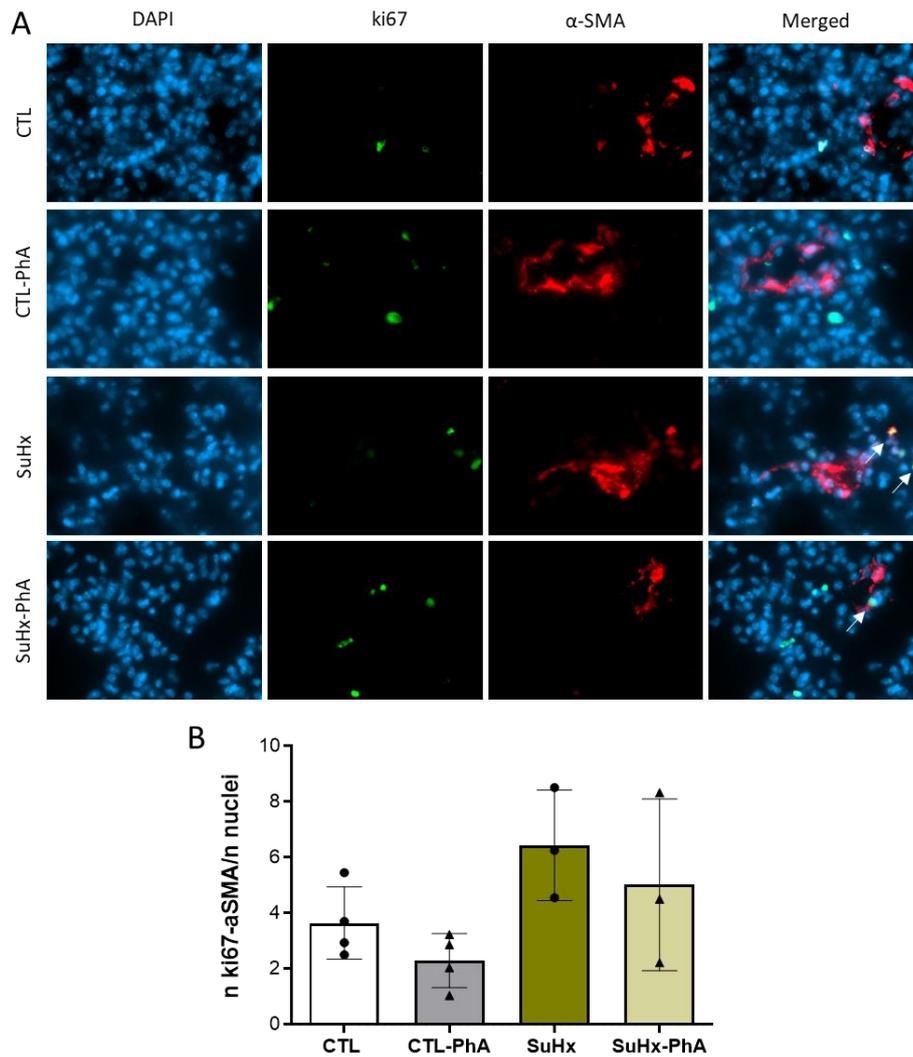
Figure 12. Immunofluorescence evaluation of pulmonary SMCs proliferation. (A) Photomicrographs of lungs stained with Ki67, αSMA, and nuclear DAPI staining. The white arrows point to the co-staining points in the image corresponding to "Merged". (B) Quantification of αSMA and Ki67 positive cells. Values are presented as mean ± SD.

Similar to the histopathological observations, a tendency toward a more proliferative vascular phenotype is observed in the SuHx and SuHx-PhA groups compared to controls (Figure 12). Nevertheless, physical activity shows a protective trend effect against this increased vascular proliferation.

Analysis of cardiac function by CMR

To analyze cardiac function, we followed the protocol for data acquisition presented in section III of Material and Methods.
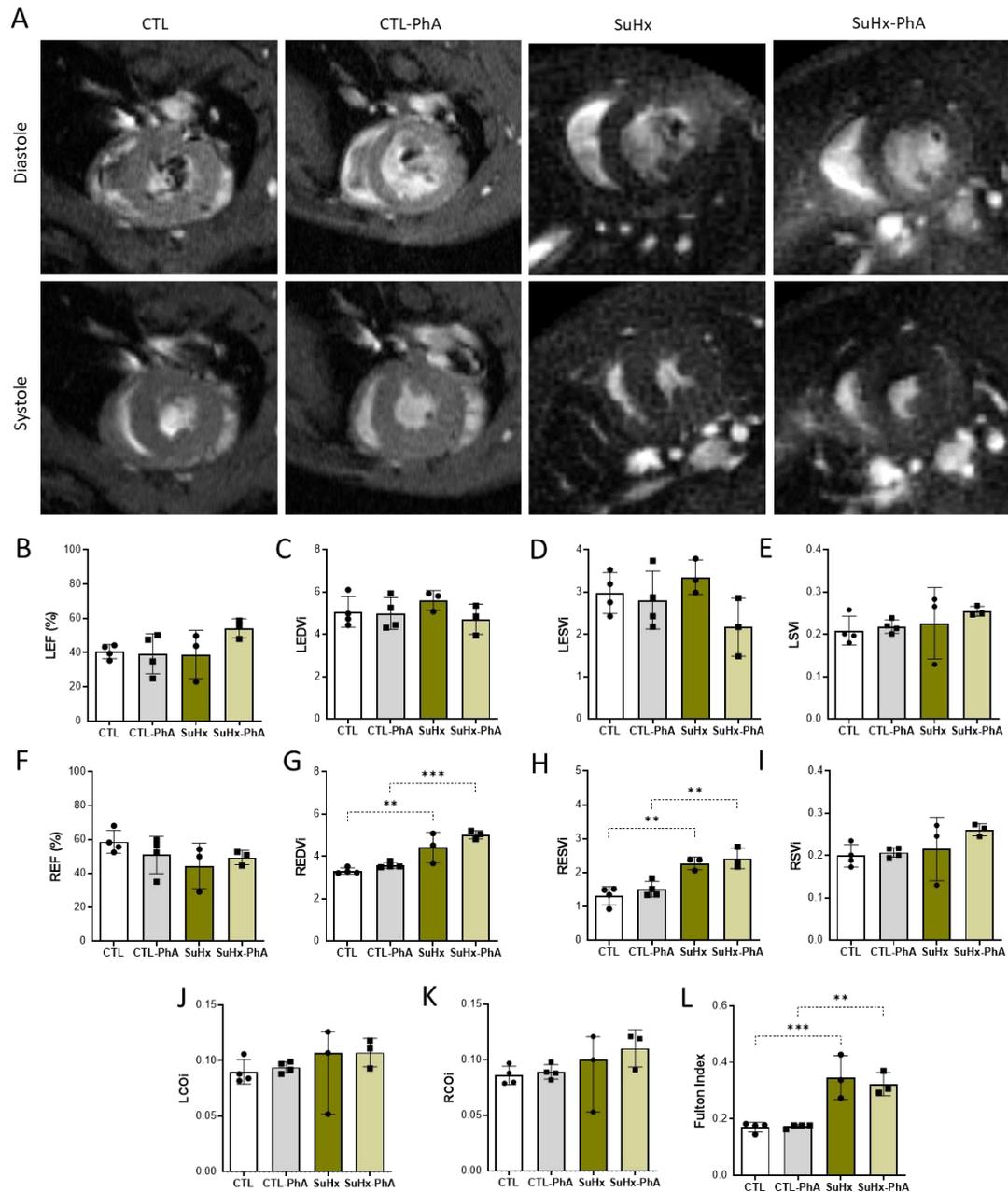
Figure 13. MRI images and quantitative analysis of cardiac remodeling of each group. (A) Cross-sectional representative images of the heart of a representative animal of each group acquired by MRI showing the myocardium and epicardium of both ventricles in systole (bottom image) and diastole (upper image). Measurement of the Left Ejection Fraction (LEF, B), the Left-ventricle End-Diastolic Volume Index (LEDVi, C), the Left-ventricle End-Systolic Volume Index (LESVi, D), the Left-ventricle Stroke Volume index (LSVi, E), the Right-ventricle Ejection Fraction (REF, F), the Right-ventricle End-Diastolic Volume Index (REDVi, G), the Right-ventricle End-Systolic Volume Index (RESVi, H), the Right-ventricle Stroke Volume index (RSVi, I), the Left-ventricle Cardiac Output index (LCOi, J), the Right-ventricle Cardiac Output index (RCOi, K), and the right ventricular hypertrophy calculated using the Fulton index (K). Values are presented as mean ± SD, **p-value < 0.01, ***p-value < 0.001 assessed by the One-way ANOVA test.

Typical cardiac function parameters of the LV, such as EF, EDVi, ESVi and SVi in LV measured by MRI (Figure 13B, C, D, E) were similar in all the experimental groups. In SuHx animals, EDVi and ESVi were significantly increased in the RV, markers of ventricular dilatation. As shown in Figure

13J, the Fulton Index, characteristic of right ventricular hypertrophy, increased in the SuHx groups. The exercise demonstrated slightly improved Fulton Index and Svi of the RV, consistent with a more physiological hypertrophy. The cardiac output of both ventricles tended to increase in SuHx groups.
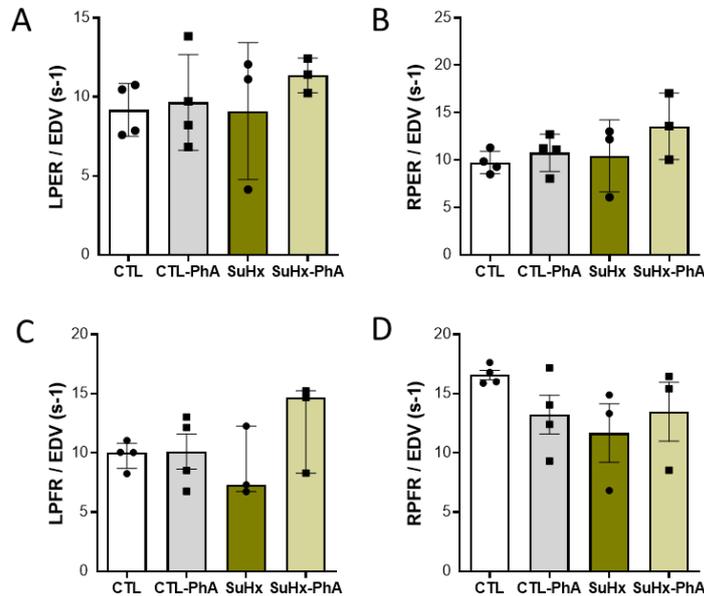
Figure 14. Analysis of the systolic and diastolic function. Measurement of the (A) Left-ventricle peak ejection rate (PER) normalized to End-Diastolic Volume (EDV), (B) Right-ventricle PER normalized to EDV, (C) Left-ventricle peak filling rate (PFR) normalized to EDV, (D) Right-ventricle PFR normalized to EDV. Values are presented as mean ± SD.

As indicated before, additional systolic and diastolic function parameters can be obtained from the analysis of the curves of the time derivative (rate) of each ventricular volume. We calculated the maximum or minimum filling (diastolic) or ejection (systolic) rates and corresponding times for each ventricle. No alterations were found in any of these parameters (Figure 14).

Influence of physical activity on the development of cardiac fibrosis

We also explored the non-pharmacological effect of physical activity on cardiac fibrosis development associated with this disease. Fibrosis is a characteristic feature that often accompanies PH, especially as a severe complication in the late stages of the disease. We quantified fibrosis by histological techniques, using Picrosirius red-stained heart sections and imaging with polarized light. We have also analyzed transforming growth factor beta (*tgfß*) mRNA cardiac expression, which has been described as the master regulator of fibrosis, by qPCR to complement these results.

A representative RV section from each group is shown in Figure 15A, in brightfield in the upper panel and the same sections under polarized light below. The quantification of these images (Figure 15B) revealed an increased fibrotic area in hearts associated with the SuHx model. The effect of physical activity seems to attenuate this increase in fibrotic tissues.
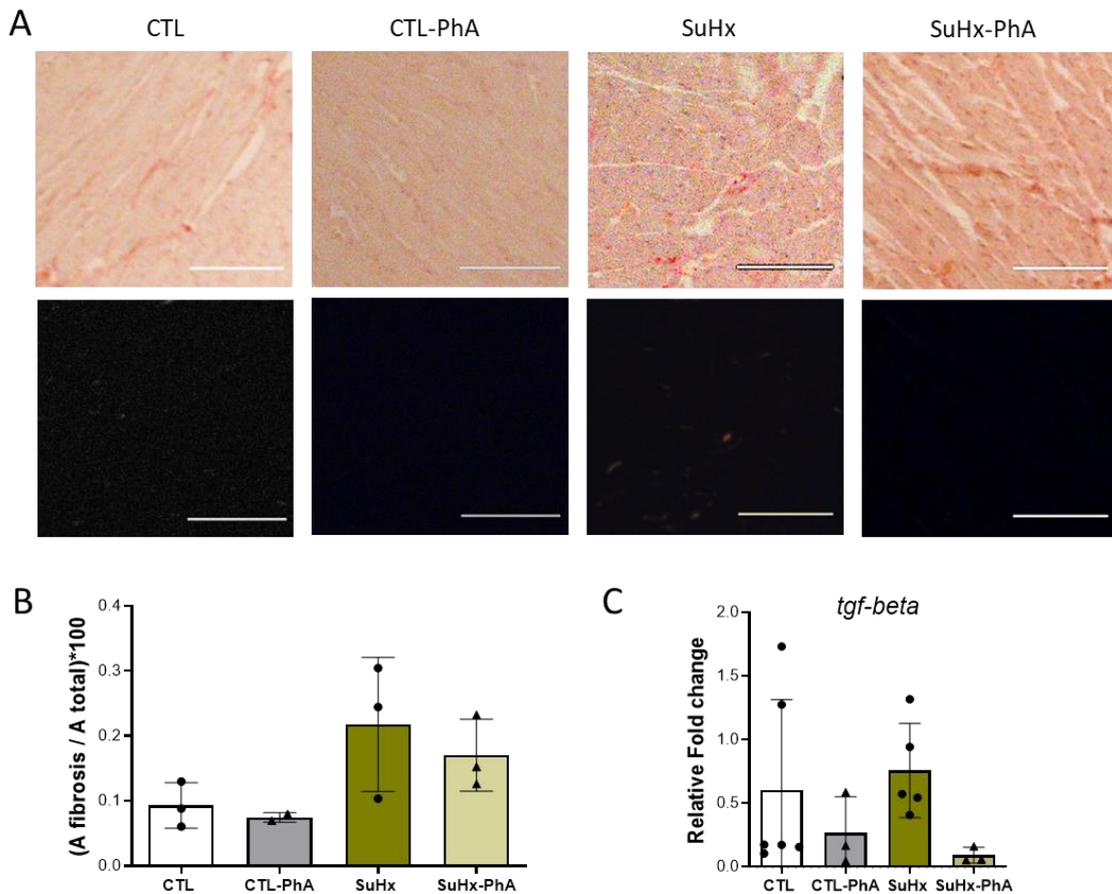
Figure 15. Picrosirius red staining and mRNA expression of *tgfβ*. (A) Representative 10× magnification images of the Picrosirius red-stained heart sections with brightfield microscopy (upper panel) and polarized light microscopy Picrosirius Red birefringence (bottom panel). Scale bars are 100 µm. (B) Quantification of Picrosirius Red signals. (C) mRNA levels of *tgfβ* in the heart tissues of mice. Values are presented as mean ± SD.

Concerning *tgfβ*, Figure 15C displays a tendency to reduce mRNA levels in the SuHx-PhA group compared to SuHx.

Evaluation of glycolytic and choline metabolism by PET

In vivo ^{18}F-FDG PET imaging evaluates glycolytic metabolism and possibly inflammation. Signal changes could reflect metabolic shift alterations in the pulmonary vascular cells or cardiomyocytes, or the presence of metabolically active inflammatory cells in these tissues. Despite its poor selectivity, this radiotracer has been used in previous human and animal studies and is increasingly used for different applications. In this context, we have included an analysis with ^{18}F-FDG to explore glucose metabolism alterations associated with the SuHx model and physical activity.

As summarized in Figure 16B, ^{18}F-FDG SUV did not change in the lungs of the different groups. In the heart (Figure 16C, D), increased glucose uptakes in the hypoxic groups are observed in both ventricles, without alterations associated with the practice of physical activity.
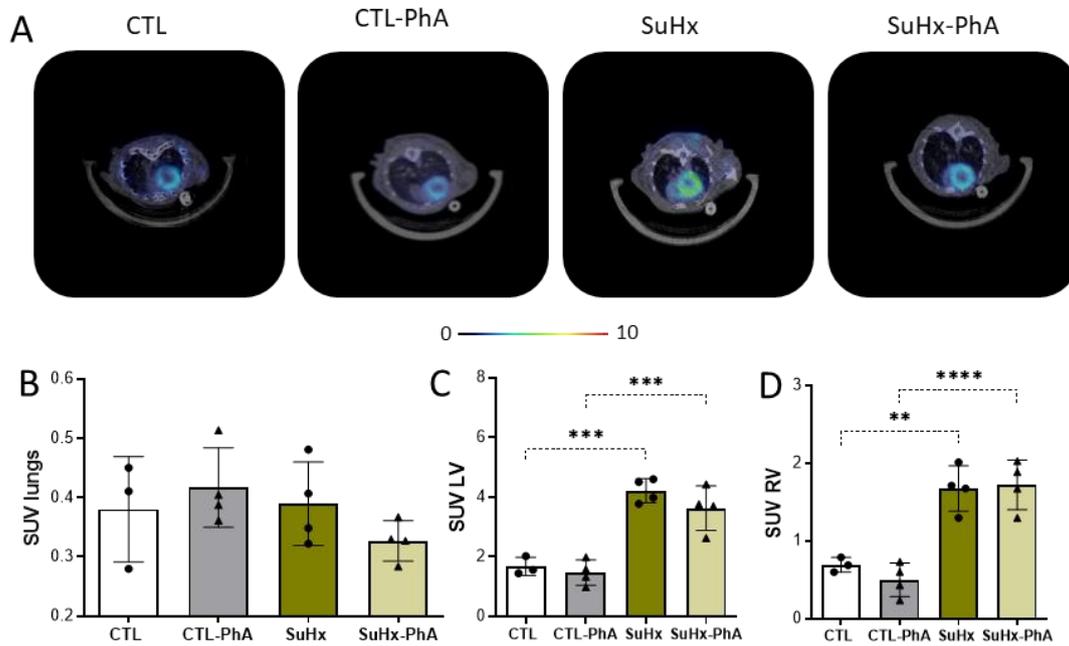
Figure 16. Evaluation of glucose metabolism by ^{18}F-FDG accumulation. (A) Overlay illustration of a representative image of the 3D reconstructions of CT (gray scale) and mid-ventricular axial PET images (color scale represented over the images). Measurement of the SUV uptake in the ((B) lungs, (C) LV, and (D) RV. Values are presented as mean ± SD, **p-value < 0.01, ***p-value < 0.001, ****p-value < 0.0001, assessed by the One-way ANOVA test.

In addition to ^{18}F-FDG, we explored changes in choline metabolism using ^{11}C-Choline, a radiolabeled choline derivative. This radiotracer has been mainly used in oncological studies but, as far as we know, never in the context of PH. We found it an exciting imaging biomarker to measure the presence of active metabolic cells in these tissues.
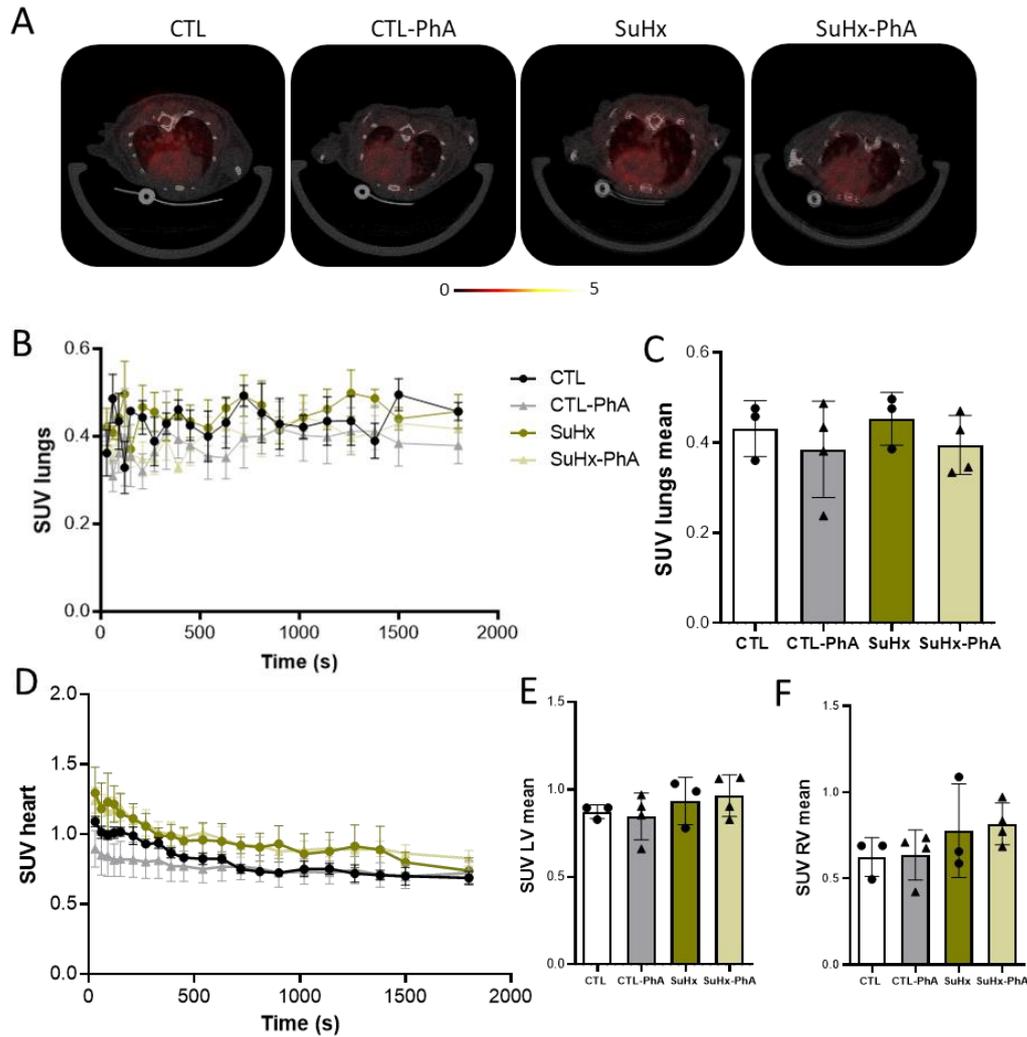
Figure 17. Analysis of ^{11}C-Choline uptake by PET imaging. (A) Representative images of each group of a dynamic PET scan of ^{11}C-Choline uptake in the lungs and heart. The images are a time uptake average of 7.5 to 30 minutes. Quantification of the SUV ^{11}C-Choline uptake in lungs (B) and in the heart (D) in each frame with respect to the time. SUV means in the lungs (C), LV (E), and RV (F), from minute 2 to the end of the acquisition. Values are presented as mean ± SD.

In order to establish an experimental protocol for ^{11}C-Choline, since we did not have previous experience with this tracer, we started the experiment using a dynamic list-mode data acquisition during the 30 minutes after injection, due to the shorter half-life of ^{11}C (around 20 minutes). The results are summarized in Figure 17. Figure 17A displays axial and coronal thoracic mid-ventricular views as an average of different times after injection. Figures 17B and 17C show that ^{11}C-Choline uptake in the lungs is similar in all groups, with no variations due to hypoxia or physical activity. In the heart (Figure 17D), after an initial fall, probably due to the radiotracer clearance from the blood circulation, the levels are maintained, with SUV values slightly higher in the SuHx groups. Although the differences in the heart were small, the main changes were observed between RV of SuHx and CTL mice (Figure 17F).

Physical activity impacts on the expression of glycolytic enzymes in the heart

The metabolic shifts hinted at by ^{18}F-FDG PET uptake within the heart were confirmed through the expression of different glucose transporters and enzymes in cardiac tissues of the different groups. mRNA expression of glucose transporter (solute carrier family 2, facilitated glucose transporter member 1, *slc2a1*) and relevant enzymes of the glycolytic pathway, *hk1*, glucose-6-phosphate isomerase (*gpi*), 6-phosphofructokinase, muscle type (*pkfm*) and phosphoglycerate kinase 1 *(pgk1),* were studied by RT-qPCR and normalized to the ribosomal protein lateral stalk subunit P0, *rplp0*. The fold change values are summarized in Figure 18.
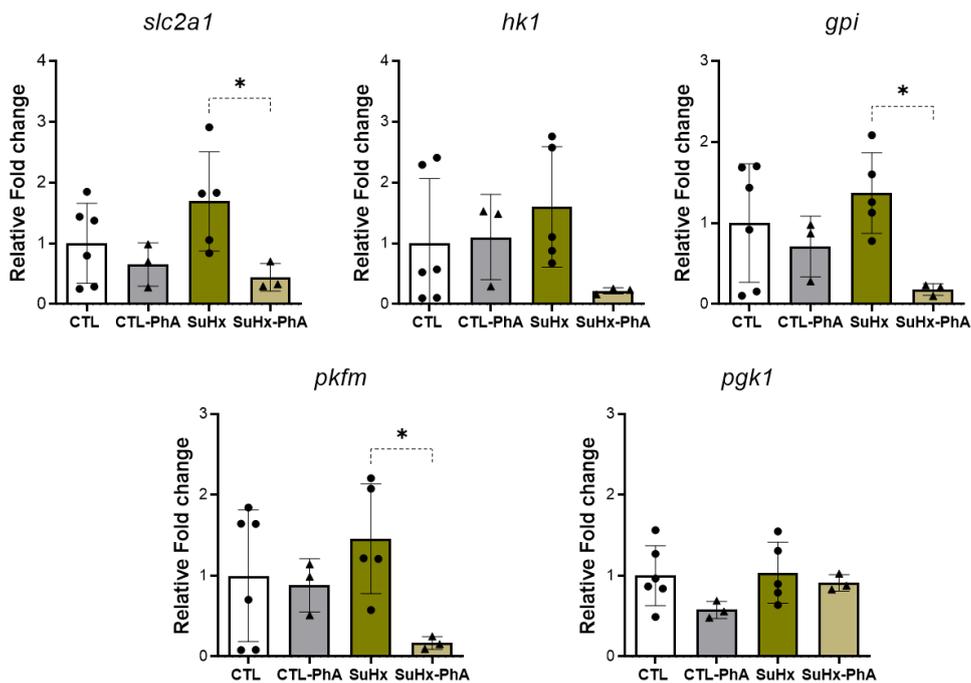
Figure 18. Expression of "glycolytic" enzymes into the heart. mRNA relative fold change of *slc2a1, hk1, gpi, pkfm* and *pgk1* in the heart tissues of mice normalized to *rplp0*. Values are presented as mean ± SD, *p-value < 0.05 assessed by the One-way ANOVA test.

Although there were no significant alterations between SuHx and CTL groups, the physical activity significantly reduced the expression of *slc2a1, hk1*, *gpi* and *pkfm*. Previous data with animals in normoxia has demonstrated a reduction of glucose utilization via glycolysis after exercise, stimulating cardiac remodeling (see [143]). Normoxic animals show this trend in our case after exercise, nevertheless, this was especially relevant in hypoxic animals.

IV.1.3 Discussion

PAH is a disease coursing with characteristic manifestations, such as pulmonary arterial wall thickening, which hinders the passage of blood flow and the consequent RV adaptation and enlargement to pump the blood efficiently. This study aimed to explore the effect of voluntary daily physical activity, organized without a specifically structured exercise program, on different functional, metabolic, and molecular biomarkers in mice. To perform this study, SuHx and control animals, at different times, remained in the same chamber with (exercised groups) and without free access to a running wheel, in groups of four animals per cage, thus trying to have similar experimental conditions. In normoxic (CTL) and SuHx groups unexposed to exercise, physical activity is limited to the intra-cage normal motion.

The effect of physical activity on the PH-phenotype

To assess how this murine model resembles the increase in pulmonary artery pressure, the gold-standard of the diagnostic techniques for PH, we measured RVSP as a surrogate value. We obtained augmented RVSP in the SuHx animals, with a slight tendency to increase in the group that performed physical activity (see Figure 10). This could be a physiological adaptation, since increased pressures have also been reported in humans in response to exercise [144]. Despite these hemodynamic changes, mice did not suffer from RV failure.

MRI results revealed preserved left ventricular function . In the RV, we observed a compensatory increase in indexed EDV and ESV values in SuHx animals, and a higher trend to increase these two parameters in SuHx-PhA mice (see Figure 13). This compensatory RV hypertrophy was also identified by the increase in MRI-derived Fulton indexes of both SuHx groups. The absence of reduced EF in any group described a hypertrophic phenotype without RV heart failure. We also represented PER normalized to EDV to characterize the systolic function and PFR normalized to EDV to characterize the diastolic function. The homogeneity of the results between the groups indicates the absence of evident diastolic and systolic dysfunctions in both ventricles.

Post-mortem pulmonary vascular analysis showing an increase in the percentage of medial wall thickness and medial wall area in the SuHx groups confirmed an early PH phenotype. In turn, the increase in SMC proliferation matches the detected increase in vessel thickness (see Figures 11, 12).

An increase in pulmonary artery pressure disproportionated to systemic arterial pressure associated with exercising has been observed in other animals, such as horses [145]. This pressure is finally exerted on the RV [146] and, in some cases, could lead to RV remodeling and justify the increase in RVSPs. Furthermore, CO is a measure of the volume of blood expelled by a ventricle in one minute, calculated as the heart rate per SV. CO is the result of the mechanisms involved in ventricular function, mainly the heart, arterial afterload and venous return. In our case, the increase in indexed CO in the SuHx groups, and specially in SuHx-PhA, matched the increase in RVSP in these animals. Mirea et al. [144] also stated that 12.9% of athletes presented RV enlargement and elevated pulmonary arterial pressures. This increase was not accompanied

by a significant reduction in RV strain, indicating preserved right ventricular function. In addition, exercise at high altitudes, a scenario similar to our experimental setup, led to increased RV systolic and pulmonary arterial pressures [147]. All this seems to indicate that in response to physical exercise physiological adaptations occur in the heart that may overlap with the remodeling of PH.

Our hemodynamic, histological, and functional CMR data corroborated an early development of this disease in all SuHx groups, with and without exercise practice, defining a *cor pulmonale* condition after three weeks in hypoxia. Cardiac failure was absent in all cases, regardless of the physical training.

Metabolic shift phenotype associated with PH and physical activity

Alterations in glucose metabolism in the lung and heart have been considered possible biomarkers of PH development and RV maladaptation [85], [148]. We evaluated *in vivo* glucose metabolism by PET imaging. ^{18}F-FDG showed different LV and RV uptake in SuHx animals (see Figure 16). The higher uptake values in SuHx hearts have also been related to compensated periods in hypertrophied RV [85], observed both in humans [149] and in animal models [89], [148]. This glycolytic phenotype is characteristic of ventricular hypertrophy and is associated with an up-regulation of glucose uptake. This higher glucose uptake has been associated with increased protein levels of HIF-1α and its downstream target slc2a1 [150]. In the present study, in cardiac tissues as a consequence of hypoxia, we have observed a trend to increase some glucose mediators, *slc2a1, gpi, hk1,* and *pkfm*, but without statistically significant differences due to the high variability.

Furthermore, as referenced before [143], exercise caused a reduction in the expression of *slc2a1*, *hk1*, *gpi* and *pkfm* (see Figure 18)*.* The expression of glucose transporter slc*2a1* is increased SuHx hearts but decreased in the case of SuHx-PhA. Meta-analysis studies in various PH models reported an increase in ^{18}F-FDG uptake and *slc2a1* in the RV [151]. Slc2a1 translocation and activation is the first step to ensure the supply of glucose into the cardiomyocytes [152]. Increased levels of *slc2a1* have been observed in cell cultures under hypoxic conditions [153], [154], pointing out that slc2a1 responds to situations of inhibition of oxidative phosphorylation caused by lack of oxygen.

Collectively, our results of the decrease in the expression of glycolytic enzymes in cardiac tissues associated with physical activity, the ^{18}F-FDG uptake (maintained in hypoxic animals with and without exercise) and the improved functional cardiac indices in physically active mice, are probably indicating a robust cardiac adaptation in these mice. Despite the remarkably lower levels of some glycolytic enzymes, the surprisingly high glucose uptake in hypoxic animals is only possible if the corresponding low glycolytic rate is sufficient to meet the increased cardiovascular demands of exercise. Further studies should be required to investigate long-term effects in a more advanced PH phenotype.

In the lungs, the main protective effect observed was the attenuation of the vascular remodeling demonstrated by the reduced proliferation of SMCs from the vessels. In this sense, the increase in RVSP in the exercised animals seems more physiological than a pathological response to the higher activity. In this SuHx mice model, we did not find differences between groups in ^{18}F-FDG uptake in the lungs.

Physical exercise and cardio-protection

Moderate and controlled physical exercise has the benefit of reducing some of the problems caused to the heart in different cardiovascular diseases [155]. In our case, voluntary/regular physical practice can help improve myocardial metabolism and prevent cardiac apoptosis and fibrosis in response to chronic afterload. Although, as indicated above, in none of the experimental groups, there were signs of heart failure (revealed by ventricular remodeling and reduced EF), our results showed a global tendency to cardio-protection in the exercised SuHx groups. This assumption was strengthened by relevant concomitant biomarkers such as increased left ventricular EF, RV adaptation to higher pulmonary vascular resistance without apparent differences in right ventricular EF and reduced fibrotic markers in exercised animals.

In the present work, fibrosis in the murine hearts was measured by total interstitial collagen obtained with picrosirius red staining. The reduction of collagen levels in exercised SuHx animals followed a similar pattern to the *tgfβ1* mRNA expression (see Figure 15). Fibrosis and remodeling of the RV are associated with RV dysfunction and mortality in PH patients [156]. Still, the role of fibrosis in developing the disease is not fully understood. TGFβ is by far the most investigated mechanism in cardiac fibrosis. The TGFβ complex remains latent in interstitial space and can be activated by mechanical stress in different cardiovascular diseases. Besides, cardiac fibroblasts activate the TGFβ1 signaling pathway under hypoxic conditions, promoting fibrosis [156]. TGFβ also contributes to cardiomyocyte hypertrophy [157]. In the MCT rat model [158], cardiac fibrosis through TGFβ1 signaling has been associated with RV pressures, so that the reduction found in SuHx with physical activity reveals healthier myocardial tissue.

Choline-based PET as a possible proliferation biomarker in PH

Another pathway involved in the metabolic alterations underlying PH is choline metabolism. Increased glycolysis, pathological cell hyperproliferation, and apoptosis resistance entail an aberrant choline metabolism characterized by exceeding choline phospholipids. Metabolic analysis of blood and plasma samples from PH human patients found elevated choline levels [92]. Former studies by our group also demonstrated that lung tissue samples from a similar mouse model had higher levels of phosphocholine and glycerol-phosphocholine [89].

As a possible imaging biomarker of cellular proliferation, we investigated ^{11}C-Choline uptake in the hearts and the lungs. However, we did not observe any difference in lung uptake, indicating that this radiotracer is not sensitive enough in this organ to detect small changes in vascular SMCs proliferation. In the heart of both hypoxic groups, there was a slight increase in ^{11}C-Choline uptake, mainly in the RV, without significant difference after physical activity.

Conclusion

In summary, physical activity seemed to exert beneficial effects against pulmonary vasculature remodeling, cardiac fibrosis, and the expression of some enzymes related to glucose metabolism. Some of these functional and pathophysiological biomarker improvements may reflect the benefit of a controlled exercise in delaying RV maladaptation to a permanent increase in RV afterloads.

^{18}F-FDG uptake was increased in the heart of hypoxic animals, as described in many studies. The fact that glucose uptake did not vary after exercise, although this physical practice significantly altered the expression of glycolytic enzymes, suggests that the glycolytic phenotype has been modified with this non-pharmacological treatment and has considerably and positively affected the ventricular adaptation. This exciting result will be further studied in the group with more extended exercise periods and a more severe PH phenotype.

IV.2 Comparison of neutrophil related inflammation between MCT and SuHx rat models by *in vivo* imaging

IV.2.1 Rationale

Inflammation has been recognized as a critical paradigm in PH pathogenesis, particularly in the case of PAH [58]. The association between inflammation and PAH comes in many forms. Inflammatory cells and mediators have been reported in pulmonary vascular lesions and correlated with pulmonary vasculature remodeling. In particular, an increased density of perivascular cells (macrophages, monocytes, mast cells, dendritic cells, and T lymphocytes) has been reported in plexiform lesions of PAH vessels [58], [59]. Furthermore, reduced levels of anti-inflammatory regulatory T cells, which control pulmonary artery endothelial function and inhibit pulmonary vascular remodeling, have been shown [58].

Our study aimed to bring new possibilities to characterize inflammation in PH. We have used two rat PAH models. In the first MCT-induced model, inflammation is part of the triggering events [159]. MCT is a toxic alkaloid from Crotalaria spectabilis, which causes PH by a mechanism dependent on the conversion of MCT to MCT-pyrrole by the cytochrome P450 system in the liver. Two weeks after administration, the endothelial barrier is lost, and fluid and inflammatory cells accumulate in the adventitial sheath of the small lung intracinar vessels [160]. Furthermore, MCT increases the rigidity of the vessels, and thus hinders correct vasodilation [159]. These events seem to have a significant role in the development of the characteristic of PH pathology (distal smooth muscle hypertrophy and obliteration of small pulmonary arteriole lumens) [161]. However, its acute toxicity is not limited to pulmonary circulation. Upon contact with other organs, MCT produces alveolar edema, pneumotoxicity [133], inflammation in the heart and acute damage of the peripheral vasculature [48].

On the other hand, in the SuHx model, the disease is caused by oxygen deficit with a second hit due to the inhibition of angiogenesis by blocking the VEGF receptor [162]. SuHx model causes vascular remodeling with medial wall thickening, EC hyperproliferation [48], and impaired pulmonary vascular contractility. In the SuHx model, only the pulmonary vasculature is affected [162] and recapitulates the concentric neointimal and complex plexiform-like lesions of human PH [163]. The development in the early stages of the disease differs between the sexes. In both cases, increased proliferation of pulmonary vasculature and adaptive RV hypertrophy has been reported, but in the case of females with no heart fibrosis [164]. In the present study we used female rats with these two well-established and cited animal models.

Apart from presenting the differential manifestations outlined in the literature, it has been described that circulating metabolites are also differentially expressed in the MCT and the SuHx models. The urea cycle and the methionine metabolism are the main pathways altered in MCT and the SuHx groups, respectively [165]. These disparities reveal the different inflammatory responses in these two PH models.

In particular, we aimed to compare disease progression and the recruitment or not of neutrophils using molecular imaging approaches. This characterization is important because neutrophils have a specific role in the innate immune response. Tissue macrophages are the first line of defense upon the appearance of an inflammatory stimulus, which attracts neutrophils by chemotaxis. Due to their quick and short action, neutrophils are linked to acute inflammation, while macrophages evidence a chronic situation [61], [62], [64].

Considering that the development of the PH is accompanied by metabolic dysregulation with structural RV and pulmonary vascular manifestations, imaging techniques provide a tool to characterize in a non-invasive way both the anatomical features and the functional/metabolic status of the two target organs. To this end, we conducted MRI and PET studies in our animal models. MRI enables the visualization of the RV, while PET imaging is considered an excellent tool to monitor pathophysiological processes *in vivo.*

^{18}F-FDG PET is the most widely used imaging technique to monitor pathophysiological inflammatory processes *in vivo,* though this technique lacks cellular specificity [166]. Other agents [167] currently used for inflammation imaging are autologous white blood cells labeled with ^{99m}Tc or ^{111}In, ^{99m}Tc-labeled bisphosphonates, [9m]Tc-labeled nanocolloids, and [99m]Tc- or ^{111}In-labeled proteins, such as IgG or albumin [168]. However, they also lack cell specificity and tend to give false-positive results [169]. In addition, antibodies have the potential risk of triggering and additional immune response, which may cause adverse effects [170]. For this reason, it is needed to find more selective radiotracers for inflammation. Among these are ligands of the somatostatin receptor SST2 [171], the translocator protein, the mannose receptor, C-X-C chemokine receptor type 4, the folate and interleukin receptors, and the cannabinoid receptor type 2 are some of them; as well as choline, and some inflammatory cytokines [169]. Targeting specific innate immunity cells is a strategy to acquire a deeper understanding of the process. In this sense, Jun-Bean Park et al. [172] measured macrophage infiltration in the lungs of an MCT rat model of PH using the radiotracer ^{68}Ga-NOTA-MSA, which binds the mannose receptor. We have used an analogous strategy for the differential detection of neutrophils.

Quiescent neutrophils constitutively express formyl peptide receptor 1 (FPR1) at the membrane, but the expression is upregulated in response to inflammatory stimuli [173]. As early as the 1980s, specific proteins produced by mitochondria isolated from human cells, formylated peptides, were noticed to induce neutrophil chemotaxis through FPR1 binding [174]. Today, the activation of this receptor has been validated and its implication in diverse inflammatory diseases is well established [173]. Peptide N-cinnamoyl-F-(D)L-F-(D)L-F (cFLFLF) is an antagonist of FPR1, which has been used in this study coupled to an iron oxide nanoparticle-based molecular imaging solution to modify and possibly enhance targetability. cFLFLF targets polymorphonuclear leukocytes and displays high neutrophil-binding affinity. cFLFLF has been tested in preclinical models of acute osteomyelitis [175], osteoarthritis [176], ischemia-reperfusion injury [177], disk herniation [178], type 2 diabetes mellitus [179], lung inflammation and abdominal aortic aneurysms [180].
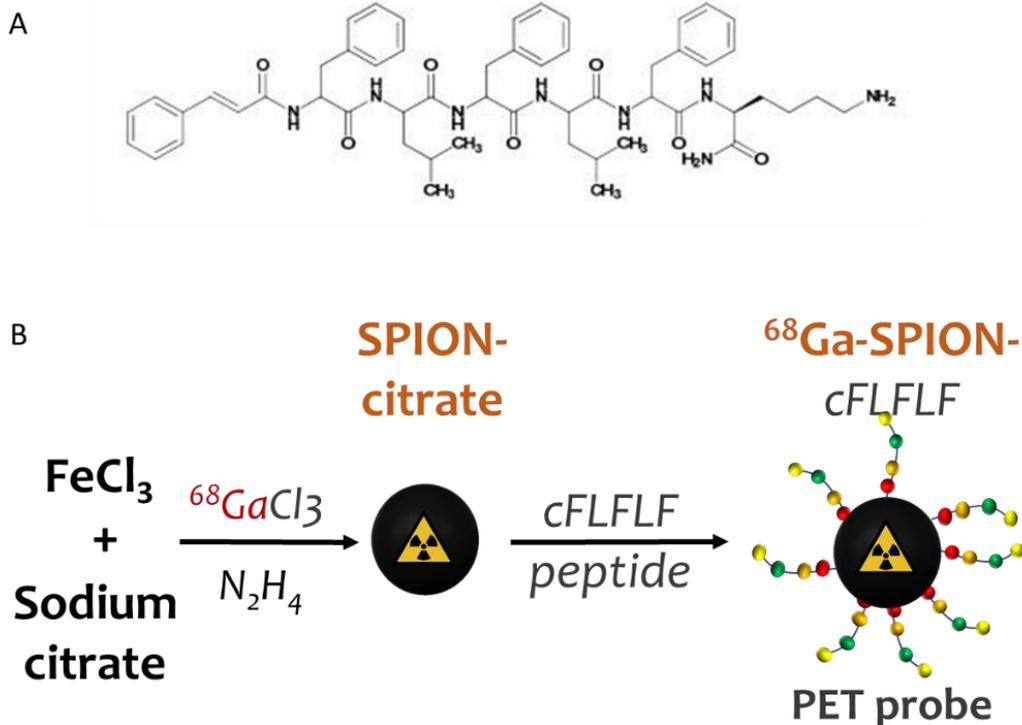
Figure 19. **Peptide N-cinnamoyl-F-(D)L-F-(D)L-F (cFLFLF) and radiolabeling**. (A) Chemical structure of peptide cFLFLF. (B) ^{68}Ga-NRT-cFLFLF tracer synthesis.

For intravenous administration, cFLFLF must be reformulated in an aqueous solution since this molecule is very hydrophobic. A widespread solution is through the conjugation with water-soluble molecules to enhance its hydrophilicity, mainly polyethylene glycol [176]. The present study incorporated the peptide into highly hydrophilic doped iron-oxide nanoplatforms for *in vivo* labeling and imaging applications [181]. The ^{68}Ga-NRT-cFLFLF tracer has been probed to enable *in vivo* detection of neutrophils [181].

Due to their magnetic properties, superparamagnetic iron oxide nanoparticles (IONPs) have been applied in nanomedicine as "negative" or T2 contrast agents for MRI. Nanotechnology-based contrast agents also allow the modification and relatively easy functionalization with targeting moieties to improve directionality. Additionally, a microwave-mediated synthetic approach allows an easy radiolabeling of IONP with PET radionuclides. Since these nanoparticles expected short biodistribution times, we have used a relatively short half-life radioisotope [68]Ga ($t_{1/2}$=68 min). These nano-radiotracers are composed of an iron oxide core, doped with this metallic radionuclide inserted in the crystalline structure of the iron oxide and coated with citrate. Citrate protects the inorganic core, and due to its hydrophilicity, this coating helps to maintain the colloidal stability of the nanoparticles, avoiding agglomerations. The citrate surface can be rapidly functionalized in a second step through the carboxylic groups of citric groups bound to different amine groups present in the FRP1 peptide used to target neutrophils via EDC/sulfo-NHS protocol [181], [182].

Previous results have shown an increased ^{18}F-FDG uptake in the cardiopulmonary system of MCT and SuHx rats [96], [183], but the cellular origin of this effect and the mechanisms underlying each model are not fully understood. In the present study, we investigated and compared PET tracers to decipher lung and heart neutrophil accumulation in the MCT and SuHx models of PH.

IV.2.2 Results

Animal weight and health status in MCT and SuHx rats

No visible alterations nor behavior changes were observed in any group of animals throughout the experimental procedure, except for both PH groups that exhibited more unsteady breathing under anesthesia in the consecutive experiments performed with these animals.
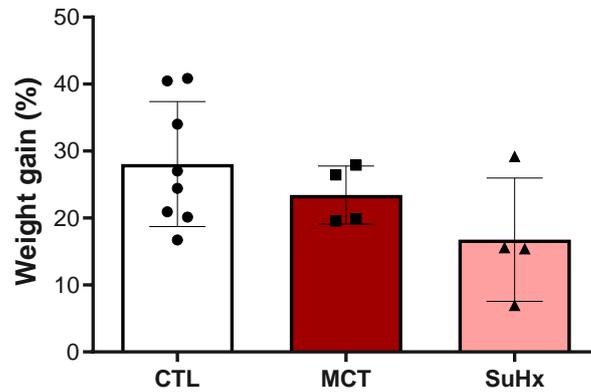
Figure 20. Tracking animal weight gain along the experiment. Graphic representation of the weight variation from the beginning to the end of the experiment. Values are presented as mean ± SD. CTL: control group. MCT: monocrotaline rats. SuHx: Hypoxia + Su5412 IP treatment.

Figure 20 shows that all animals gained weight during the four weeks of the experiment. Nevertheless, the proportion of this increase was lower in PH groups, especially in SuHx rats.

Characterization of hemodynamic and pulmonary vascular remodeling

RVSP was confirmed to be significantly elevated in both PH models compared to the control group, corroborating one of the most relevant indicators of the PH phenotype. This increase was most pronounced in the SuHx group (Figure 21).
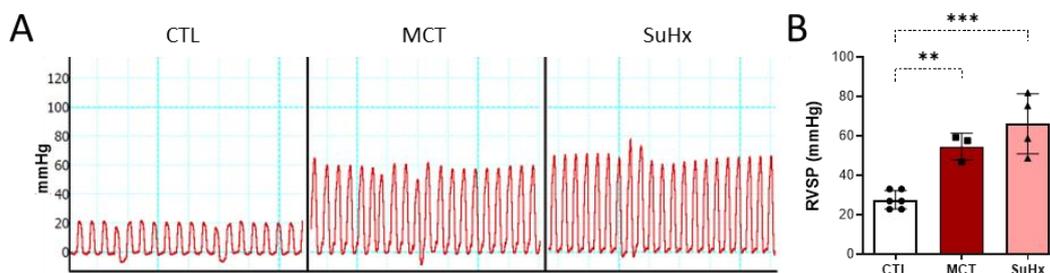
Figure 21. Tracking the RV hemodynamics. (A) Representative plots of the RVSP values of each group. (B) Invasive measurement of right ventricular pressure after disease development. Values are presented as mean ± SD, **p-value < 0.01, ***p-value < 0.001 assessed by the One-way ANOVA test.

As an additional central feature of PH development, the vessels were analyzed in the lung histological preparations from the two models. In particular, the percentages of medial wall

thickness and medial wall area have been calculated. As shown in Figure 22, significant differences were found in the treated groups compared with controls, reaching the highest values in the SuHx group.
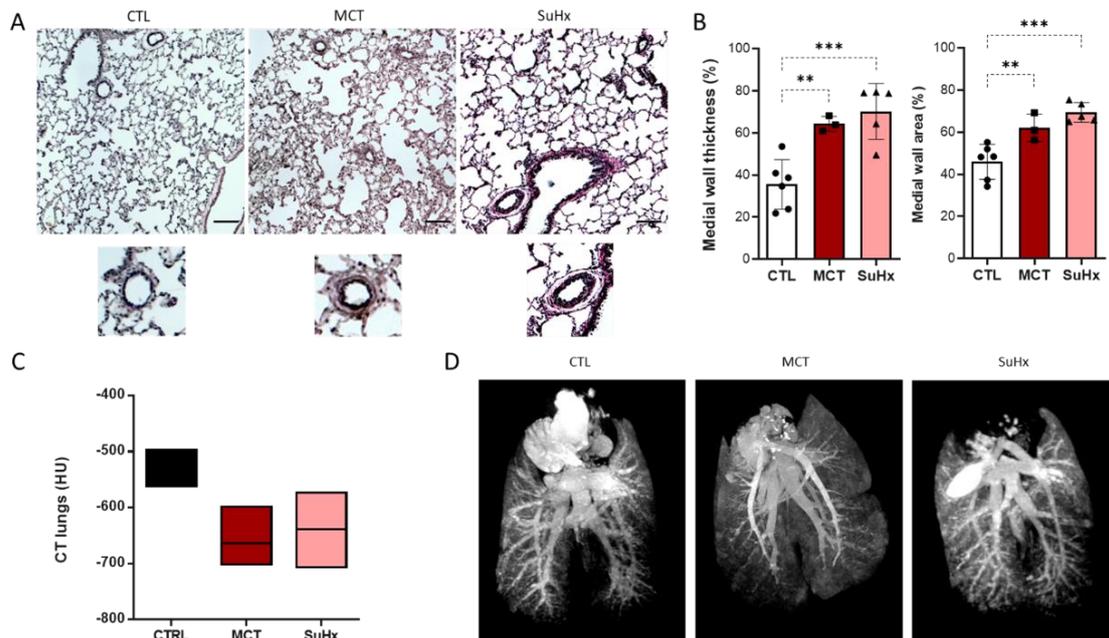
Figure 22. Assessment of pulmonary vascular remodeling. (A) Representative images of each group of elastic staining of arterioles in lung sections. (B) Differences in the remodeling of the pulmonary arteries calculated from the histological sections. Scale bars are 100 µm. Values are presented as mean ± SD, **p-value < 0.01, ***p-value < 0.001 assessed by the One-way ANOVA test. (C) Measurement of the Hounsfield Units (HU) in three VOIs of each lung image acquired by CT. (D) Three-dimensional reconstructions of CT images of the lungs. CT: computed tomography, HU: Hounsfield units.

Vascular remodeling was also revealed from lungs intravascularly perfused with microfilm®, which filled the pulmonary vasculature and acted as a CT contrast agent. Subsequently, 3D images of the lungs were generated by CT, which allowed the complete visualization and quantification of the pulmonary vasculature (Figure 22C, D).
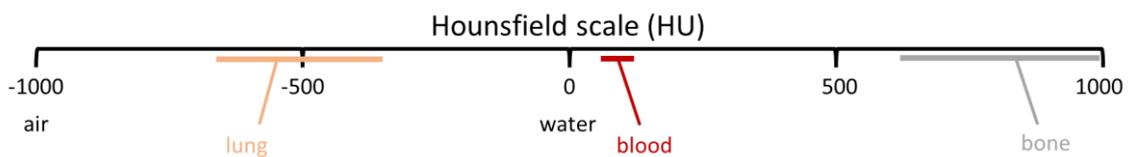
Diagram 1. X-ray attenuation of different tissues, quantified as Hounsfield Units (HU).

The quantitative CT scale in HU is used in these studies to describe the different levels of radiodensity of tissues and has, in many cases, diagnostic value. The low-density (e.g., lungs) and soft tissues appear with the lowest values or hypointense in CT images, while hard tissues (e.g., bone or the vasculature filled with a heavy atom or iodine-based contrast agent) appear hyperintense.

	HU	SD
Microfil	-345	10
CTL	-520	83
MCT	-664	102
SuHx	-638	91

In our application, a HU reduction revealed a reduction of the microvasculature in the MCT and SuHx models. Different causes could explain the reduction in the number of vessels we have reported, such as the increase in vasculature resistance due to changes in wall stiffness, vasoconstriction, or structural changes.

Assessment of cardiac function by CMR

To get an insight into the heart's function *in vivo*, cardiac MRI data were recorded before the sacrifice of the animals. Ventricular volumes and LV and RV masses were obtained from apical to base short-axis views along the cardiac cycle of the different animals. From here, parameters such as right and left end-diastolic or systolic volumes, SV, and EF were obtained to characterize the cardiac function. Values were indexed using the BSA of the animals. An MRI-based Fulton index was also generated, as explained previously. Figure 23 summarizes all these results.
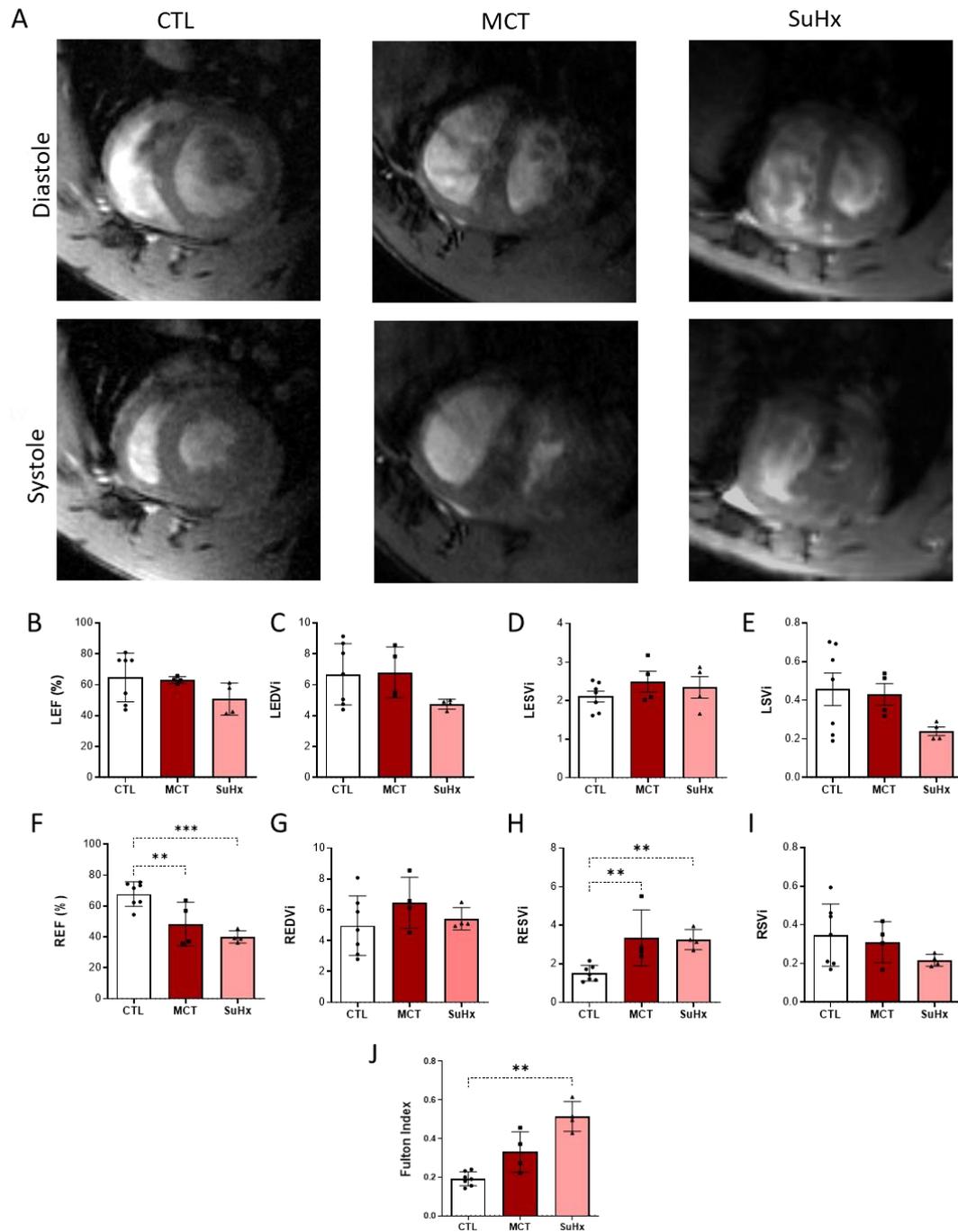
Figure 23. MRI images and quantitative analysis of cardiac remodeling of each group. (A) Cross-sectional representative images of the heart of a representative animal of each group acquired by MRI showing the myocardium and epicardium of both ventricles in systole (bottom image) and diastole (upper image). Measurement of the Left Ejection Fraction (LEF, B), the Left-ventricle End-Diastolic Volume Index (LEDVi, C), the Left-ventricle End-Systolic Volume Index (LESVi, D), the Left-ventricle Stroke Volume index (LSVi, E), the Right-ventricle Ejection Fraction (REF, F), the Right-ventricle End-Diastolic Volume Index (REDVi, G), the Right-ventricle End-Systolic Volume Index (RESVi, H), the Right-ventricle Stroke Volume index (RSVi, I), and the right ventricular hypertrophy calculated using the Fulton index (J). Values are presented as mean ± SD, **p-value < 0.01, ***p-value < 0.001 assessed by the One-way ANOVA test.

The analysis of the main functional parameters of LV revealed that this ventricle mostly kept its function in the MCT and the SuHx models. Only a tendency to decrease the SVi is observed in the SuHx group (Figure 23E). In the case of the RV, EF underwent a significant decrease, and ESVi was significantly increased in both MCT and SuHx groups compared to the CTL group. In the MCT model, this was accompanied by a tendency to increase EDVi. The Fulton Index tended to increase in both models but only significantly in the SuHx group.

Additional systolic and diastolic function parameters have been calculated from the analysis of the time derivative (frequency) curves of each ventricular volume (Figure 24). We obtained the previously described parameters from these curves, PER and PFR, normalized to EDV (Figure 24).
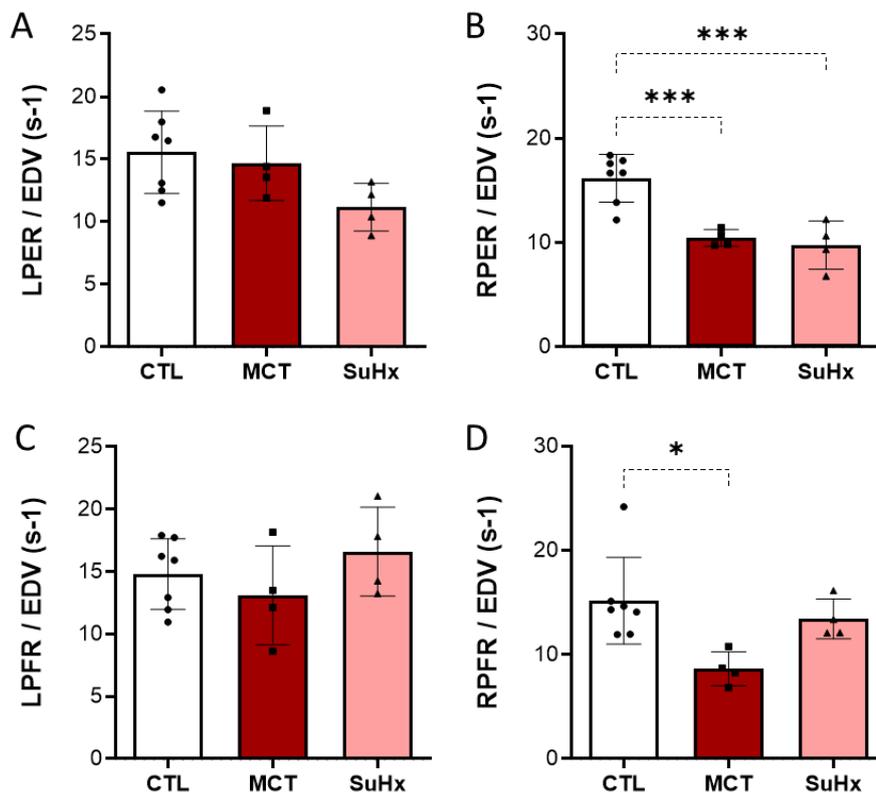
Figure 24. Analysis of the systolic and diastolic function. Measurement of the (A) left-ventricle peak ejection rate (LPER) normalized to end-diastolic volume (EDV), (B) right-ventricle PER (RPER) normalized to EDV, (C) left-ventricle peak filling rate (LPFR) normalized to EDV, (D) right-ventricle PFR (RPFR) normalized to EDV. Values are presented as mean ± SD, *p-value < 0.05, ***p-value < 0.001 assessed by the One-way ANOVA test.

PER/EDV remained unchanged in the LV (Figure 24A), according to the preserved left ventricular function. However, we found that the PER/EDV was significantly decreased in the MCT and SuHx groups (Figure 24B), confirming the alterations in the systolic function of the RV in these two groups. Moreover, PFR/EDV did not change in the LV of the animals (Figure 24C), although there was a significant decrease in the RV of MCT rats (Figure 24D), reflecting alterations in diastolic function in the MCT animal model.

18F-FDG PET imaging is not an accurate marker for inflammation

We have analyzed the ^{18}F-FDG accumulation by PET imaging since this radiotracer is the most widely used radiotracer to evaluate glucose metabolism and inflammatory processes and has previously been acknowledged as a good indicator of RV maladaptation and possible lung vascular remodeling.
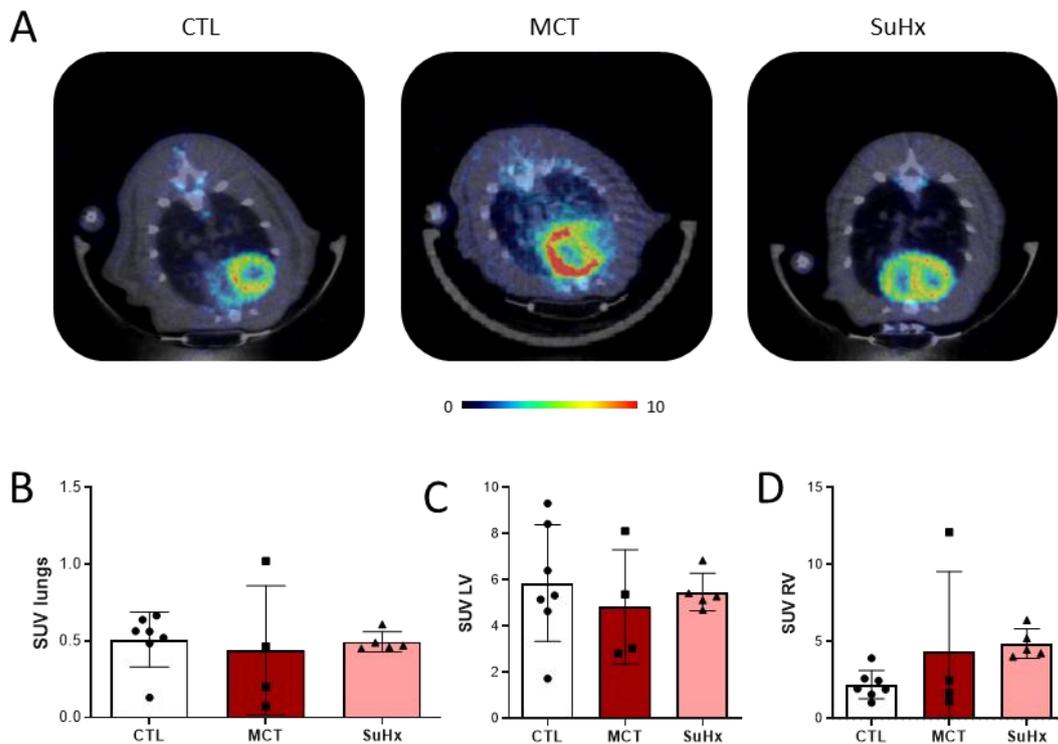
Figure 25. Evaluation of organ glucose metabolism by ^{18}F-FDG accumulation. (A) Overlay illustration of a representative image of the three-dimensional reconstructions of CT (grayscale) and mid-ventricular axial PET images (color scale represented over the images). Measurement of the SUV uptake in the (B) lungs, (C) LV and (D) RV. Values are presented as mean ± SD assessed by a One-way ANOVA test.

Curiously, our data show a tendency to increase ^{18}F-FDG uptake exclusively in the RV of the SuHx group compared to the control, although without statistical significance (Figure 25). Note the huge variability found mainly in the MCT group, in lung and cardiac tissues, with one extreme case (there is not enough data to consider it as an outlier) corresponding to the displayed animal in the central row of the upper panel, clearly showing much higher SUV values in both tissues. Although it is not representative of the average status of the disease at this period after disease induction, we include it as an illustration in Figure 25A. Note that the RV size in this animal is even larger than the LV and much higher than other animals from the same group. Note that this variability and ventricular hypertrophy was also observed by MRI in some cases (Figure 24A, also includes one case like this). It is relevant to say that, although the disease starts earlier, most studies with this model are obtained after four weeks of treatment. Based on our own experience with this MCT model, we tried to avoid these conditions since the animal losses were

higher after three weeks, and the disease phenotype of the animals was much more severe, such as those displayed in figures 24 and 25.

Synthesis and characterization of ^{68}Ga-IONP-citrate-cFLFLF for imaging of neutrophilic accumulation

Both ^{68}Ga-IONP-citrate and ^{68}Ga-IONP-citrate-cFLFLF were synthesized, stored for 24 hours to decay radioactivity, and characterized by transmission electron microscopy (TEM), dynamic light scattering (DLS), and X-ray photoelectron spectroscopy (XPS) in order to confirm the correct synthesis, main properties, and functionalization of the nanoparticles. Figure 26 shows the main results of such characterization before and after the cFLFLF conjugation. A team member, Ana Beatriz Miguel Coello, performed the chemical synthesis of these nanoparticles.
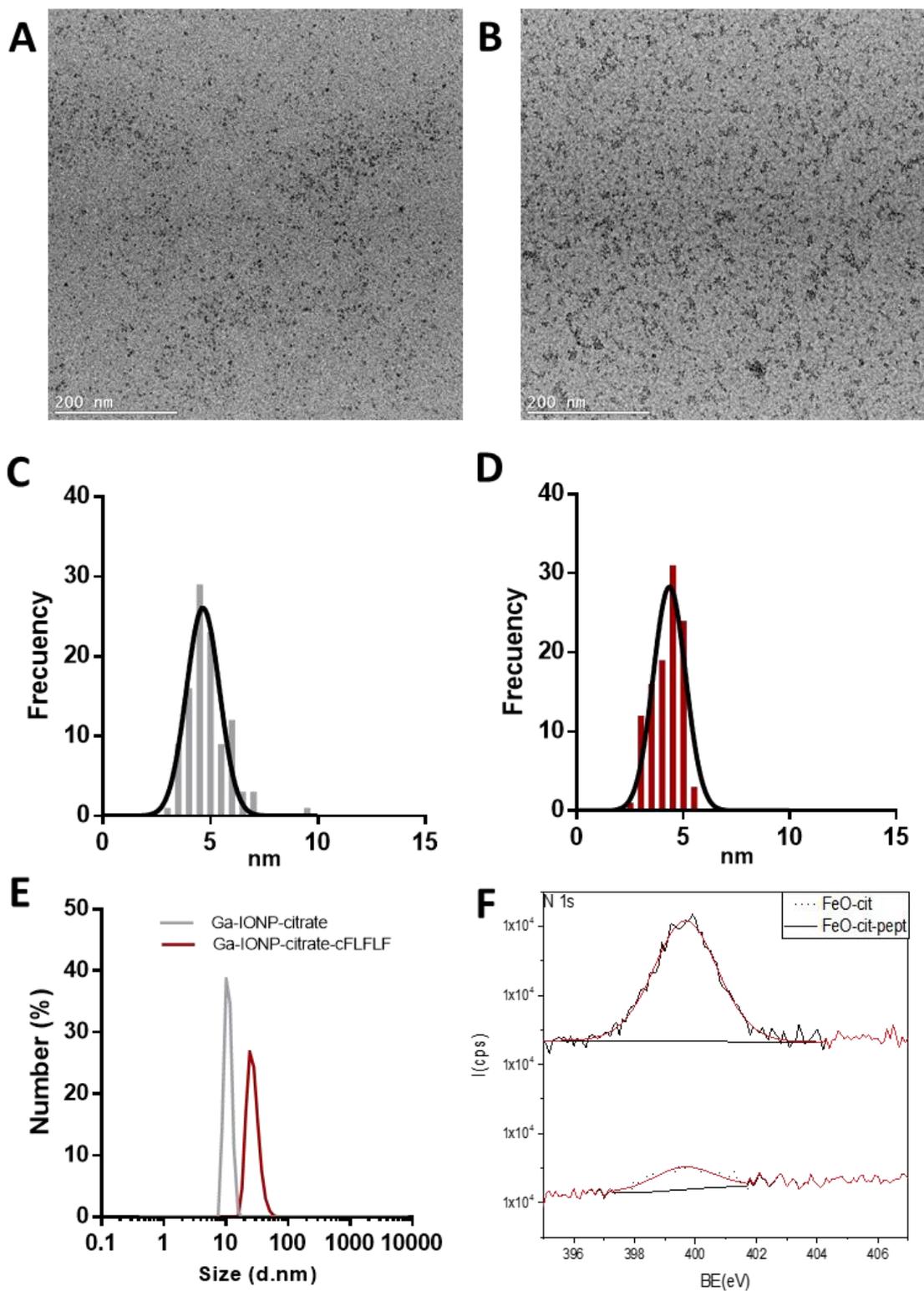
Figure 26. Nanoparticle's characterization. TEM images of IONP (A) before and (B) after cFLFLF functionalization. (C) TEM measured the frequency distribution of IONPs size (C) before and (D) after cFLFLF functionalization. (E) DLS measurements of hydrodynamic diameter of IONP before (grey line) and after cFLFLF functionalization (red line). (F) XPS peak of the core-level spectra of N 1s, before (bottom) and after cFLFLF functionalization (top) of IONP.

TEM shows negligible nanoparticle aggregation (Figures 26A and B). The diameter of the nanoparticles through TEM images followed a Gaussian distribution with an average value of 4.7±0.8 nm and 4.3±0.8 nm for Ga-IONP-citrate and Ga-IONP-citrate-cFLFLF nanoparticles, respectively (Figures 26C and D).

The hydrodynamic radius of the nanoparticles in water was measured by DLS analysis. Conjugation of cFLFLF peptide to IONPs increased its hydrodynamic size from 11.4±1.4 to 39.1±10.5 nm (Figure 26E) and shifted the zeta potential from -23.0±2.5 eV to -6.9±2.6 eV. The larger radius of IONP-peptide compared to IONP-citrate confirmed the number of hydrophobic cFLFLF peptides attached to the nanoparticle's surface. As expected, X-ray particle surface analysis obtained by XPS proved that nitrogen amount was significantly higher in the nanoparticles conjugated with the hydrophobic peptide (Table 4), only possible due to the presence of this peptide in the ^{68}Ga-IONP-citrate-cFLFLF coating and characterized by the N 1s binding energy that belongs to its amino acids. The N 1s peak is found at 399.8 eV, and the Fe 2p3/2 peak is found at 710 eV, as is reported in the literature for the FeO compound (Figure 26). The increase in size, change in superficial charge, and XPS results confirmed the conjugation of the peptide and the synthesis of ^{68}Ga-IONP-citrate-cFLFLF.

Table 4. XPS data for the atomic percentage of IONP-citrate and IONP-citrate-cFLFLF.

	C (at%)	O (at%)	N (at%)	Fe (at%)
FeO-cit	38.4	49.5	0.3	11.5
FeO-cit-pept	31.3	62.8	1.4	4.3

In vivo Imaging monitoring the presence of neutrophils

Once the two PH models were established, we evaluated the neutrophil accumulation in these animals. Gallium-doped IONPs conjugated with a neutrophil-specific peptide were administered to all rats following the same protocol as ^{18}F-FDG.
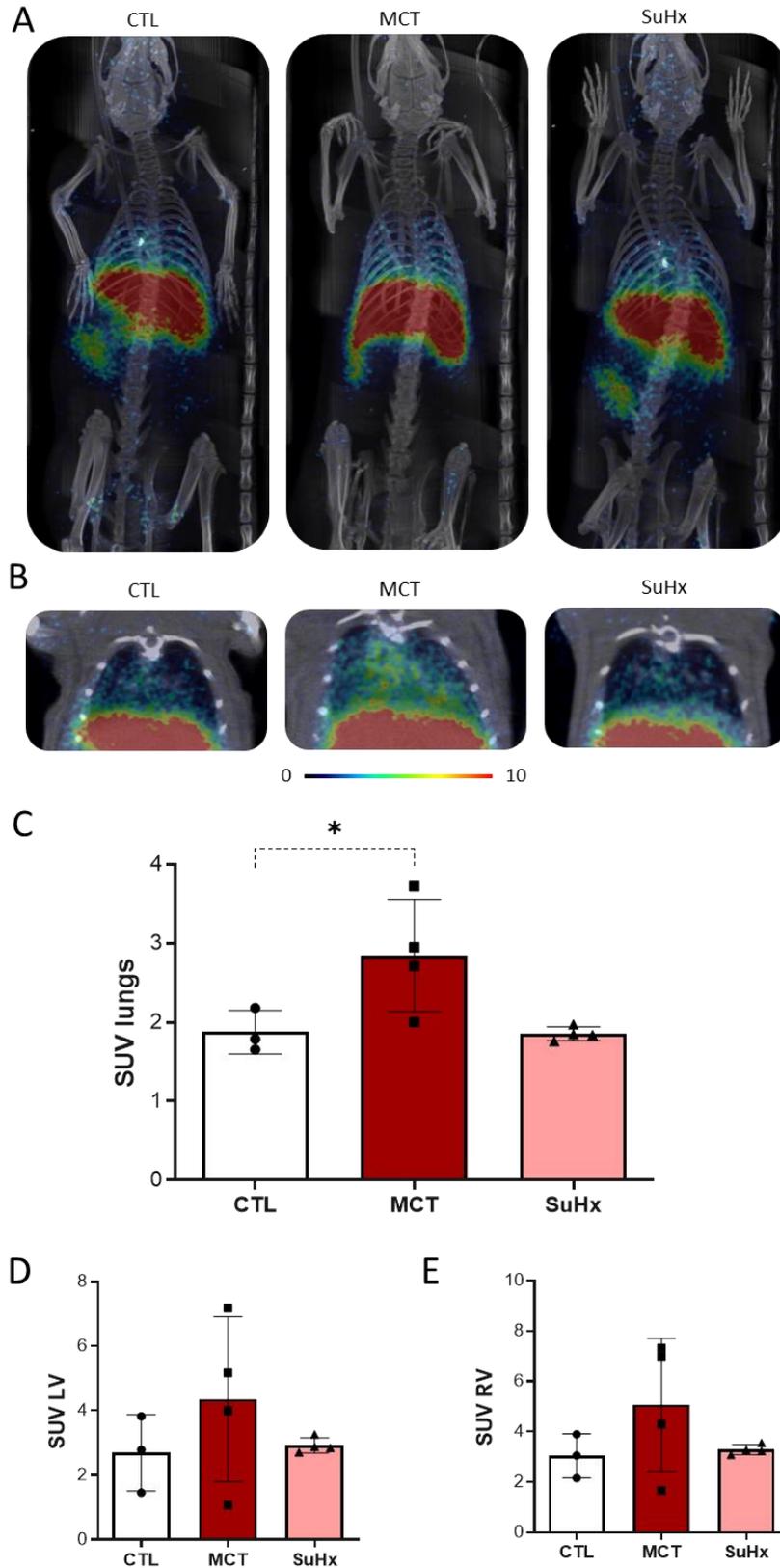
Figure 27. Neutrophil accumulation assessed by ^{68}Ga-NRT-cFLFLF. (A) Overlay representation of a representative image of the 3D reconstructions of CT (Maximum Intensity Projection, grayscale) and PET (color scale displayed over the CT images) images, coronal plane. (B) Representative coronal PET images for each group. Measurement of the SUV uptake in the (C) lungs and (D) LV, and (E) RV. Values are presented as mean ± SD, *p-value < 0.05.

As expected, PET images show the typical biodistribution results obtained with these nanoparticles (Figure 27A-B), with typical accumulation in clearance organs such as the liver and spleen. The specific activities in the lungs and the heart were measured by drawing VOIs of these areas. Results demonstrate that ^{68}Ga-NRT-cFLFLF uptake was higher in MCT-induced rats than in control and SuHx animals in the heart and significantly elevated in the lungs (Figure 27C-E). Despite the variability of the results, especially in the heart, our data seem to confirm that the neutrophil accumulation in the MCT model was higher than in the SuHx model.

Confirmation of the presence of neutrophils in lung sections by IHC

To corroborate the presence of neutrophils, paraffin-embedded sections of the lungs from different models were assessed for neutrophil accumulation using an anti-MPO antibody (Figure 28A).
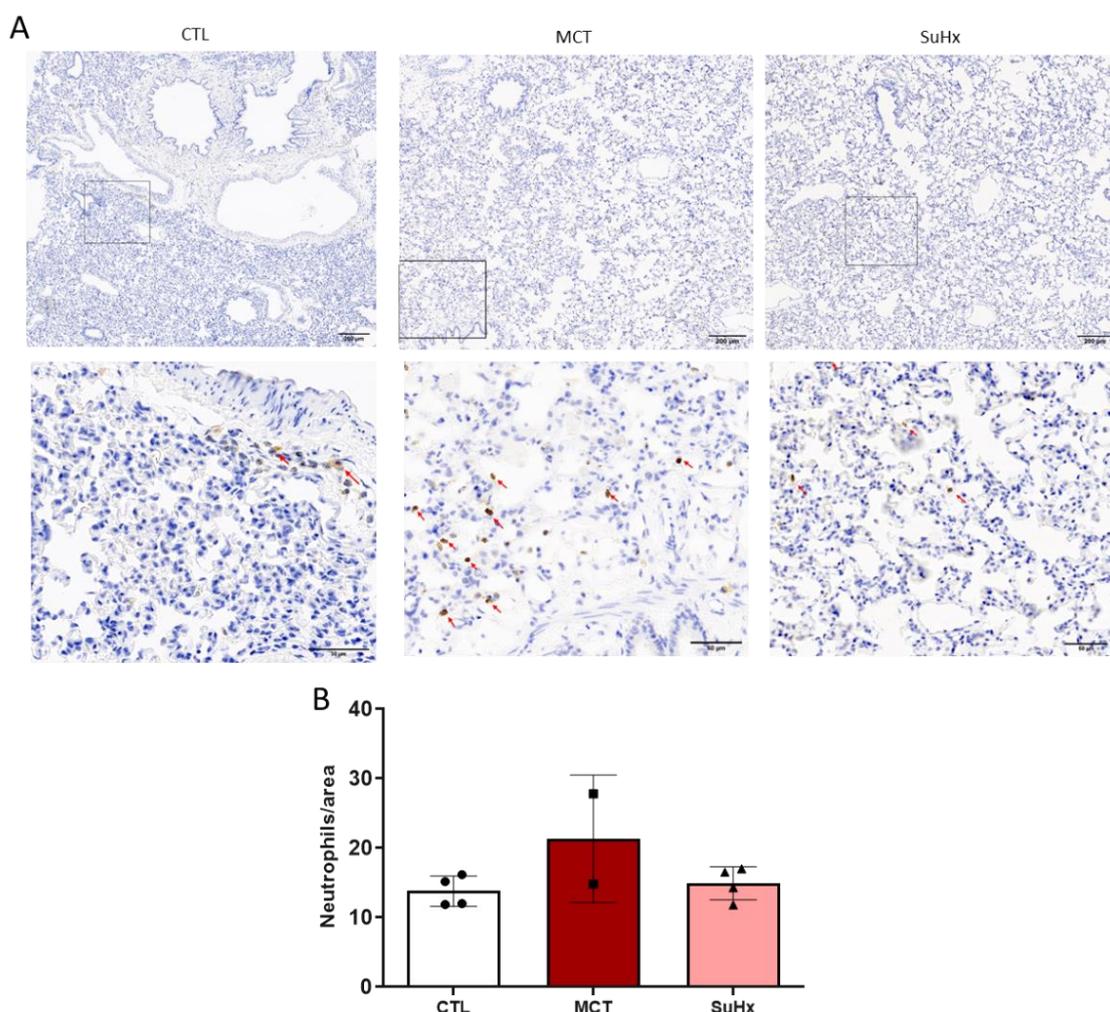
Figure 28. Detection of neutrophils in pulmonary tissue. (A) Representative images of lung tissue stained for MPO. Red arrows point to neutrophils. Scale bars are 200 μm at the top and 50 μm at the bottom. (B) Bar graphs showing the staining quantification. Values are presented as mean ± SD. Statistical analysis was not performed since we could only dedicate 2 samples for this analysis in the MCT model.

In clear concordance with the imaging data obtained with the neutrophil-specific radiotracer, we observed a tendency to increase the number of neutrophils per area in lung tissue sections in the MCT group determined by MPO immunostaining (Figure 28B). The values of the SuHx rats were similar to the controls.

IV.2.3 Discussion

Inflammation, which plays a central role in some types of PH, is recapitulated in animal models. This chapter intended to bring a possible non-invasive way to analyze *in vivo* the recruitment of a specific cell population in two models of PH, in this case, neutrophils, crucial effectors of acute inflammation that belong to the innate immune system. Thus, we intended to validate in these models ^{68}Ga-IONP-citrate-cFLFLF nanoradiotracer to measure the accumulation of these granulocytes in the lungs and compare these two models with the inflammation-related signal measured by the cell unspecific ^{18}F-FDG tracer. The chapter compares the results in these two well-established PH rat models to draw conclusions related to function and neutrophilic inflammation through a comprehensive comparison of molecular and functional imaging-based biomarkers.

Two distinct RV phenotypes in animal models of PH

CMR scanning provides an excellent tool to compare the status of the heart, in particular the RV dysfunction, which is especially relevant in PH, and thus to determine the prognosis of this disease. MRI is currently considered the gold standard technique to quantify RV function.

In the two PH rat models studied in this chapter, LV functional parameters did not show significant changes compared to control animals at the initial stages of the disease. Only a tendency to decrease the indexed left EDV and, consequently, SV was observed in the SuHx group. This reduction in LV performance has been previously observed in this SuHx model [137]. In the MCT model deterioration and failure were only observed at late stages and were preceded by RV remodeling [184].

As expected, we found significant decompensated RV failure in the SuHx rats, including a statistically significant reduction in EF. Indexed right end-systolic volumes were increased in both models. However, in MCT rats, the results are more consistent with heart failure with preserved EF phenotype, as previously reported [185]. In this model, signs of heart failure are found at later stages (more than six weeks of treatment) [186], and the intra-group differences observed in the MCT model were explained by the development of LV myocarditis and significant inflammatory infiltration [184]. The statistically insignificant variations and high variability in the PH phenotype need to be considered for further PH studies and display the relevance of imaging to personalize the diagnostic and possible therapy. Still, even at an early phase of the disease, both models demonstrated a significant decrease in some systolic indices, such as the normalized peak ejection rates, and MCT rats showed a reduction in diastolic normalized peak filling rates.

Altogether, the SuHx rat model shows a more severe RV hypertrophy phenotype than the MCT rats after three weeks of treatment. However, some MCT animals (e.g., the animals shown in Figures 23, 25 and 27) showed a severe phenotype, including flattened septum and dilated cardiomyopathy. In summary, each model, as it has been well described [184], [187], showed differential characteristics, and the response to MCT had a higher variability. Despite many other

factors contributing to the progression of the disease in both models, we aimed to characterize the role of inflammation and metabolic shift, and thus we did a comparison using two radiotracers for PET imaging.

Correlation of ^{18}F-FDG and neutrophilic accumulation in the two PH models

^{18}F-FDG PET imaging gave us insight into the inflammatory processes and the metabolic shift from mitochondrial oxidative phosphorylation to glycolysis that occurs in the heart and the lungs in both experimental groups. We also explicitly checked differences in the pathogenesis of both models associated with the neutrophilic inflammatory component using a targeted nano-radiotracer for the in vivo detection of these cells.

Clinical evidence established ^{18}F-FDG as a valuable tool for detecting metabolic switches and inflammatory processes. This is why countries such as Italy [188] or the United States [189] recommend PET imaging examinations to manage and monitor inflammation. In the cardiovascular field, ^{18}F-FDG has demonstrated a complementary value for the evaluation by PET-MRI of myocarditis [190].

Comparing ^{18}F-FDG uptake in the cardiorespiratory system between the MCT and SuHx models proved different metabolic alterations in both cases. According to the higher severity of RV hypertrophy in SuHx animals, RV glucose uptake was significantly upregulated in these animals. Additionally, ^{18}F-FDG uptake was unchanged or slightly decreased in the SuHx lungs, which can only be linked to an initial PH phenotype. Unlike previous observations, we did not observe a higher uptake in these animals' lungs, probably due to the absence of active inflammatory or high proliferative cells associated with vascular remodeling in the SuHx lungs.

We observe uneven results in the MCT group, with significant differences depending on the severity of the disease. The heterogeneity found in the ^{18}F-FDG uptake in the toxin-induced PH group is similar to the changes in the RV dysfunction observed by MRI and characteristics of the higher variability of this model. Holda et al. [184] found that the temporal evolution of PH in rats after injection of the toxin is not the same in all animals and that the expression of the disease could vary between rats with considerable differences depending on the presence of LV myocarditis. Although our histopathological evaluation of some rats did not confirm it, this fact may explain disparities that we found in the glucose uptake in this group. Interestingly, high ^{18}F-FDG uptake in the lungs and RV in these rats appeared only when a very pronounced and severe RV dilation was observed.

To further investigate the role of inflammation in the development of this disease and its correlation with the accumulation described in ^{18}F-FDG in these two models, we used ^{68}Ga doped IONPs coated with citrate and modified with cFLFLF, an antagonist of the FPR1, to add the neutrophil-specific capability to these nanoparticles and thus try to evaluate neutrophilic inflammation. The nanoradioprobe was administered intravenously and distributed accordingly to the normal biodistribution of nanoparticles with this kind of coating and size, with a strong signal in the liver and the spleen, normal clearance organs. Our group had previously

demonstrated that the increased uptake is a reliable marker of neutrophil accumulation in an acute inflammation model [181]. Thus, we tested this ^{68}Ga-IONP-citrate-cFLFLF in the two PH models studied in this chapter. As we anticipated, due to the pneumotoxicity of MCT, our results demonstrate that ^{68}Ga-IONP-cFLFLF uptake was higher in the lungs of these animals.

While the SuHx model gave the same PET signal as the controls in the two analyzed organs, we observed an increase in the uptake of this specific nanoradiotracer in the lungs and hearts of MCT-driven PH animals. This can be the consequence of a larger number of neutrophils and the inflammatory impact of MCT on these two organs. This is probably related to the known pneumotoxicity of this drug and, consequently, the development of acute lung respiratory distress [191] and some cases of myocarditis. In contrast, the pathological mechanisms of the SuHx model do not imply the recruitment of such immunological cells. Neutrophils were visualized on the IHC with MPO. The images showed a greater influx in the lungs of rats treated with MCT than in controls or in rats exposed to SuHx. The gender of the rats might have influenced these results, as it has been reported a significant increase in MPO levels in similar IHC studies with MPO in lung tissue from SuHx rats [164].

Our results display the different pathophysiology and how the combination of ^{18}F-FDG and another more specific radiotracer can reveal central and precise mechanisms of the disease evolution, in this case, to separate the contribution of the metabolic switch and inflammatory cell infiltration.

Conclusion

This study validated the use of ^{68}Ga-IONP-citrate-cFLFLF, as a nanoradiotracer functionalized probe to detect neutrophils. Although both SuHx and MCT models evidenced inflammation in these animals' lungs and hearts, we could determine that only the MCT coursed with the presence of neutrophils. This conclusion was validated with the IHC lung images of the neutrophil's MPO. Furthermore, this probe may be of great interest in different pathologies in which these leukocytes have clinical relevance and for monitoring some new anti-inflammatory therapies. Our results also illustrate the importance of imaging to have an individual/personalized evaluation of this disease.

IV.3 Proteomics analysis of the RV of the heart in a PH rat model treated with 2DG

IV.3.1 Rationale

It is well known that the alterations in metabolism contribute to PH, and the role of mitochondria is a critical hub in this process [69]. This chapter explored the consequences of modifying energy metabolism, and particularly the consequences of boosting mitochondrial biogenesis on PH development. PH is associated with chronic mitochondrial dysfunction, but at the same time, the inhibition of mitochondrial respiratory Complex III, induced by Antimycin A, causes the appearance of PH [192]. These data question whether mitochondrial dysfunction plays a critical role in genesis or as a consequence of the disease.

2DG is a synthetic glucose with hydrogen in the second carbon instead of an alcohol group. The first glycolysis enzyme, HK, recognizes and phosphorylates this molecule. However, the resulting product, 2-deoxy-D-glucose-6-phosphate, cannot be further metabolized, so it accumulates and finally inhibits HK by an allosteric feedback mechanism. In addition, 2-deoxy-D-glucose-6-phosphate competes with glucose-6-phosphate for binding to GPI [193].
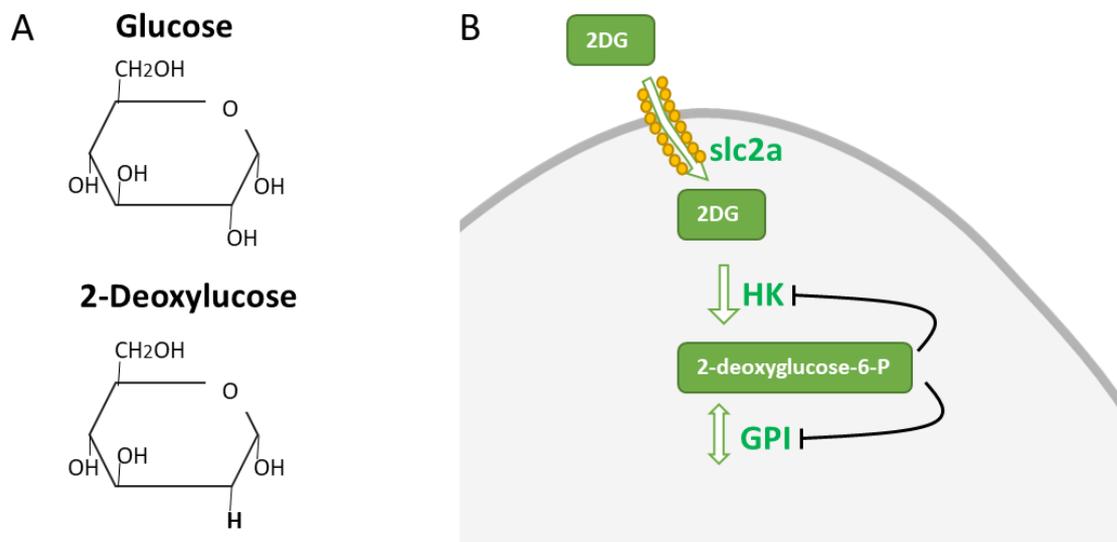
Figure 29. Molecular structure of glucose and 2DG, and 2DG action in the glycolytic pathway. (A) Structural comparison between glucose and 2DG. (B) Schematic diagram of 2DG mechanism of action in cells.

Thus, following 2DG treatment, the amount of glucose transformed into ATP is reduced, and accordingly, 2DG has been identified as a glycolytic inhibitor and a caloric restriction mimetic [194]. More importantly, glycolytic pathway inhibition forces a higher dependence on mitochondria as a source of energy, and, consequently, 2DG has been proposed as a potential enhancer of mitochondrial biogenesis. To delve into the role of variations in glucose and mitochondria metabolism, 2DG was chosen as a treatment for PH rats.

We hypothesized that the increase in mitochondrial biogenesis caused by 2DG treatment could reduce or protect the cardiomyocyte injury and, thus, impact the development of PH in a SuHx rat model. RVSP, pulmonary histology, MRI cardiac characterization, and ^{18}F-FDG PET imaging were investigated to obtain a comprehensive picture of the potential cardiac remodeling and the characterization of the disease. Finally, we tried to provide insights into the underlying mechanisms through RV proteomic analysis and further validation.

Implications of 2DG treatment on weight gain and water intake in normoxia and hypoxia

Rats were visually inspected daily for any sign of physical deterioration throughout the four weeks of the experimental approach. Animals from different groups progressed healthily, and no alterations in physical appearance were observed with the disease or 2DG treatment.

The percentage of weight gain at the end of the experiment was significantly lower in the rats subjected to the 2DG treatment, as shown in figure 30A. As expected, SuHx also tended to decrease weight gain.
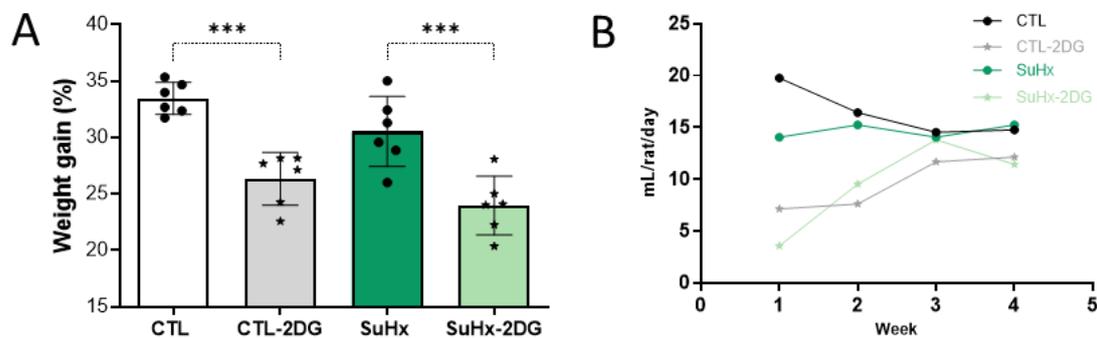
Figure 30. Changes in animal weight along the experiment and comparison of water consumption (and therefore, 2DGi intake in the treated groups). (A) Graphic representation of the weight variation (at the end of the experimental setting compared to the initial values). The graphic represents the Values are presented as mean ± SD, ***p-value < 0.001 assessed by the One-way ANOVA test. (B) Comparison of the water drunk in each group every week. CTL: control or normoxia group. CT-2DG: same as CTL but with 2-deoxyglucose treatment. SuHx: Hypoxia + Su5412 IP treatment. SuHx-2DG: same as SuHx but with 2-deoxyglucose treatment.

Compared to controls, the behavior in the 2DG groups evolved from a certain reluctance to drink water during the first two weeks to an equal fluid intake in the last weeks (Figure 30B).

2DG treatment effects on PH phenotype

As a gold-standard measure in the field, we performed and compared RVSP acquired by cardiac catheterization in control and SuHx animals. The data in the SuHx group demonstrated significantly higher RVSP (Figure 31). Interestingly, SuHx animals treated with 2DG show pressure values considerably lower than those of the SuHx group, pointing to a protective effect of 2DG against the development of PH-associated pathology.
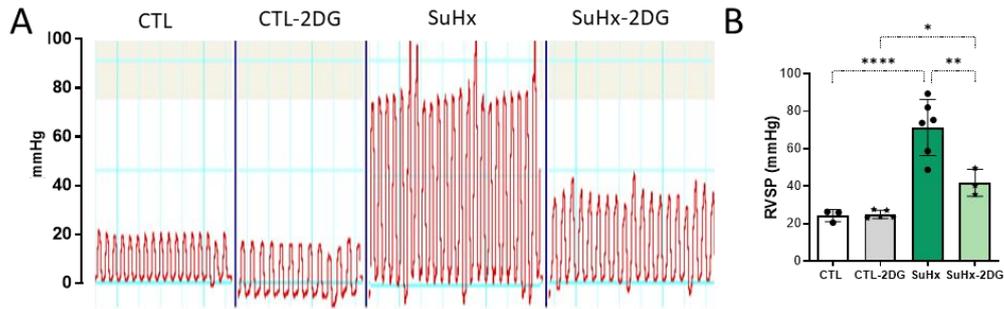
Figure 31. Tracking the RV hemodynamics. (A) Representative RVSP curves of each group. (B) Graphical representation of the invasive measurement of RVSP after four weeks of treatment. Values are presented as mean ± SD, *p-value < 0.05, **p < 0.01, **** p < 0.0001 assessed by the One-way ANOVA test.

The lungs from these animals were collected after the sacrifice, processed, and stained with an elastic stain to analyze the vascular remodeling (Figure 32).
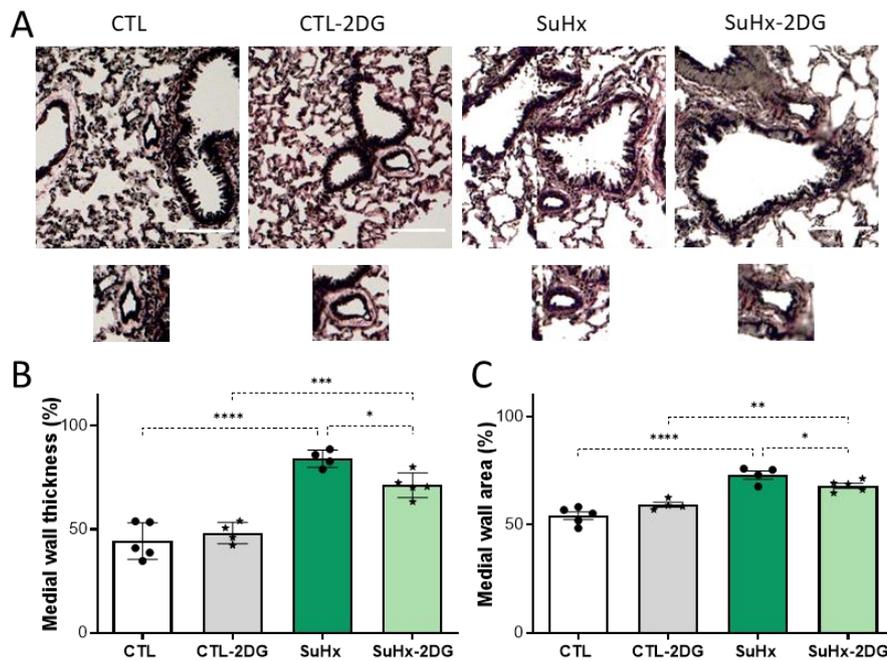
Figure 32. Assessment of pulmonary vascular remodeling. (A) Representative photomicrographs of each group of elastic staining of the whole lung (up) and a representative arteriole in each lung section (down). Scale bars are 100 µm. Representation of (B) the percentage of medial wall thickness and (C) the percentage of medial wall area. Values are presented as mean ± SD *p-value < 0.05, **p < 0.01, ***p < 0.001, ****p<0.0001 assessed by the One-way ANOVA test.

A greater pulmonary vascular remodeling was detected in the SuHx groups, measured by significantly higher values in the medial wall thickness and the medial wall areas (Figure 32). This remodeling was reduced in the group with the 2DG treatment, as shown by a statistically significant lower percentage of medial wall thickness and medial wall area in the SuHx-2DG group.

CMR functional characterization

Through MRI, cross-sectional images of different heart slices were taken and reconstructed in 20 frames throughout the cardiac cycle. As in all previous studies of this thesis, parameters were calculated from ventricular volume data to characterize cardiac function, such as EDVi, ESVi, SV, and EF. All of them are represented in Figure 33. No significant differences can be detected in LV function. However, in the RV, EF was reduced in the SuHx group compared to controls but not in the rats that received 2DG treatment. Besides, REDVi and RESVi were significantly increased in the SuHx groups compared to controls but ameliorated in the rats with 2DG treatment, indicating a protective effect. The Fulton Index obtained by MRI was increased in the SuHx groups compared to the controls and significantly lower in the SuHx-2DG group. This result seems to confirm the protection of 2DG against RV hypertrophy in rats.
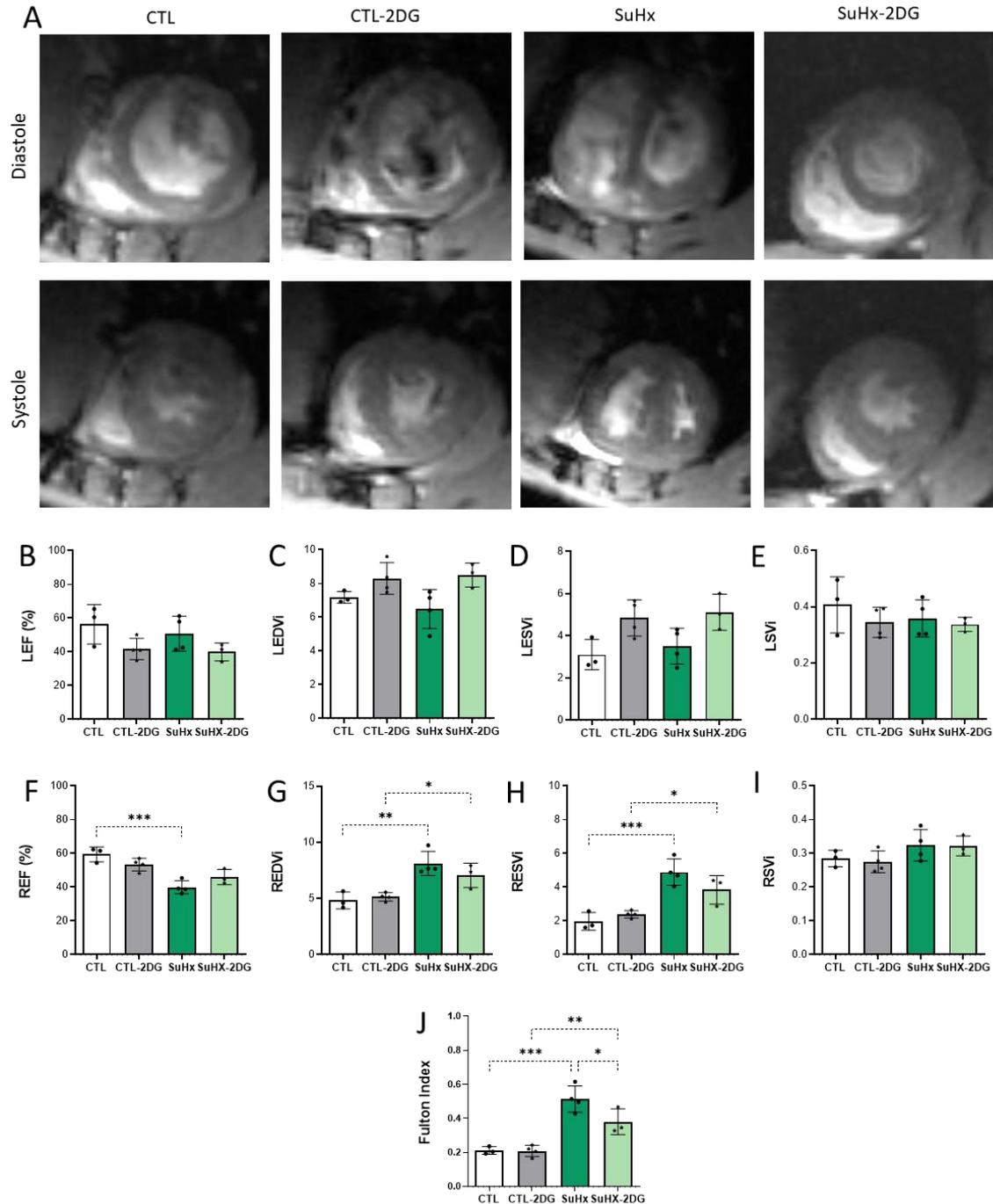
Figure 33. MRI images and quantitative analysis of cardiac remodeling of each group. (A) Cross-sectional representative images of the heart of a representative animal of each group acquired by MRI showing the myocardium and epicardium of both ventricles in systole (bottom image) and diastole (upper image). Measurement of the Left Ejection Fraction (LEF, B), the Left-ventricle End-Diastolic Volume Index (LEDVi, C), the Left-ventricle End-Systolic Volume Index (LESVi, D), the Left-ventricle Stroke Volume index (LSVi, E), the Right-ventricle Ejection Fraction (REF, F), the Right-ventricle End-Diastolic Volume Index (REDVi, G), the Right-ventricle End-Systolic Volume Index (RESVi, H), the Right-ventricle Stroke Volume index (RSVi, I), and the right ventricular hypertrophy calculated using the Fulton index (J). Values are presented as mean ± SD, *p-value < 0.05, **p-value < 0.01, ***p-value < 0.001 assessed by the One-way ANOVA test.

The same indices shown in previous chapters, used as a read-out of the systolic and diastolic function, have been calculated from the curves of the time derivative of the ventricular volume.
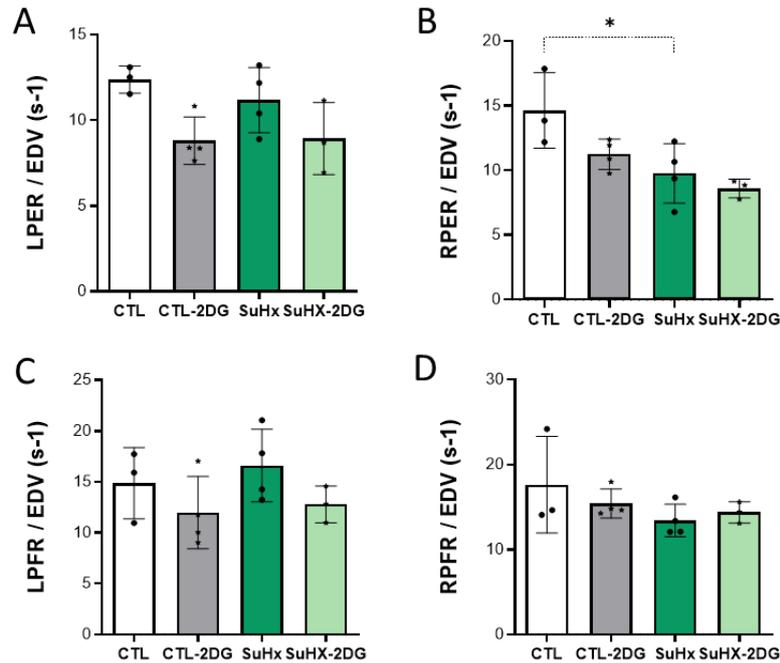
Figure 34. Analysis of the systolic and diastolic function. Measurement of the (A) Left-ventricle peak ejection rate (PER) normalized to end-diastolic volume (EDV), (B) Right-ventricle PER normalized to EDV, (C) Left-ventricle peak filling rate (PFR) normalized to EDV, (D) Right-ventricle PFR normalized to EDV. Values are presented as mean ± SD, *p-value < 0.05 assessed by the One-way ANOVA test.

Figure 34 exposes no variations in LV parameters. In the RV, SuHx rats presented a decreased PER/EDV, irrespective of the 2DG treatment, indicative of systolic dysfunction.

Exploring glucose metabolism by ^{18}FDG PET imaging

As 2DG inhibits the glycolytic pathway, one objective was to evaluate the glucose metabolism in the hearts and lungs of the experimental cohorts. Non-invasive ^{18}F-FDG PET imaging allowed us to conduct such *in vivo* analysis.
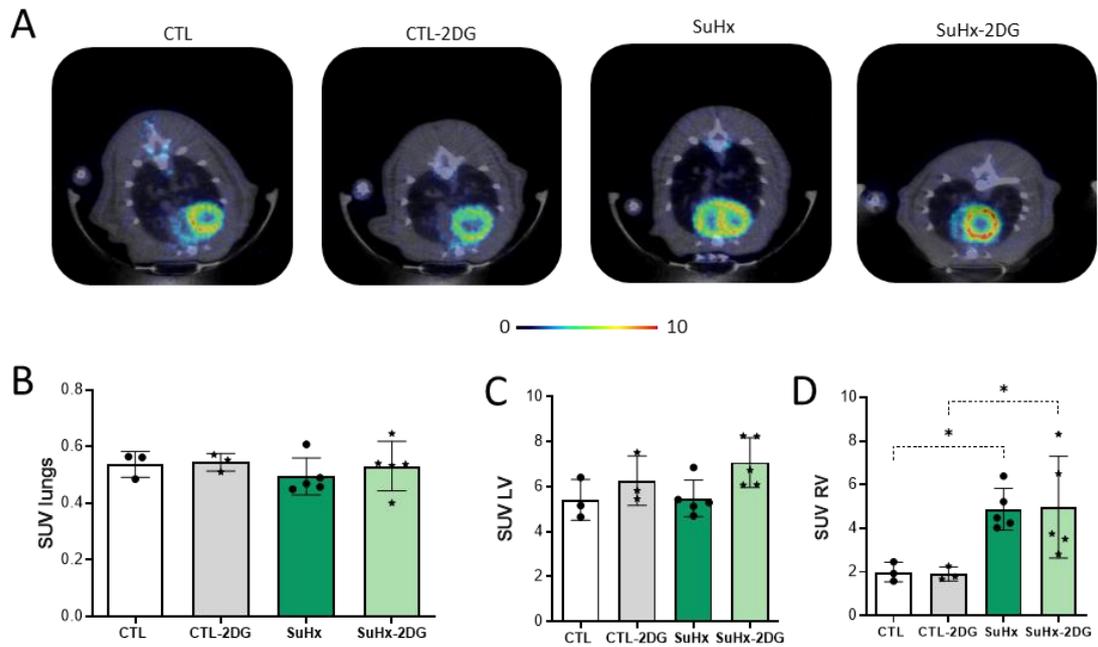
Figure 35. Evaluation of glucose metabolism by ^{18}F-FDG accumulation. (A) Overlay illustration of a representative image of the three-dimensional reconstructions of CT (MIP, gray scale) and PET (color scale represented over the images) images, transversal plane. Measurement of the SUV uptake in the (B) lungs, (C) LV and (D) RV. Values are presented as mean ± SD, *p-value < 0.05 assessed by the One-way ANOVA test.

Figure 35 shows no differences in glucose uptake in the lung between the different groups. However, the increase in the glucose uptake of both treated and untreated SuHx groups is worth noting compared to controls in the RV.

Alterations in the right ventricular proteomic profile

To try to understand the possible therapeutic effect of the continuous 2DG treatment and beneficial heart function, we studied the RV protein expression profile in control and SuHx experimental conditions (4 animals per group) using a nanoflow liquid chromatography system coupled to a tandem mass spectrometer. We aimed to identify variations within the proteome to understand the molecular mechanisms underlying the protective impact of 2DG in this complex disease.

Figure 36. Analysis of the differentially expressed proteins. (A) Venn diagram adaptation representing the number of the differentially expressed proteins between the four different groups. (B) Volcano plots of the different comparisons. Upregulated proteins appear in red and downregulated proteins in blue.

A total of 1304 proteins were identified and quantified by proteomic analysis of the hearts. Differentially expressed proteins were selected as those with a p-value < 0.05. Then we calculated the proteins that, among these, have a variation higher than 20%. A panel of 87 differentially expressed proteins was obtained by comparing CTL and CTL-2DG conditions. Among them, the expression of 36 and 44 proteins was increased or decreased, respectively, by more than 20%. From the comparison between CTL and SuHx groups, 215 proteins were differentially expressed, 102 upregulated, and 106 downregulated, more than 20%. In the case of the SuHx group compared to SuHx-2DG, 135 differentially expressed proteins were detected. Among them, the expression of 89 and 43 proteins was increased or decreased, respectively, by more than 20%. Finally, CTL-2DG and SuHx-2DG conditions were compared, and 98 differentially expressed proteins were identified. 75 upregulated and 24 downregulated, more than 20%.

Enrichment analysis using the IPA software

The proteomic datasets were uploaded onto the IPA software for insightful pathway analysis, integration, and a deeper understanding of the proteomic data. The output of IPA analysis illustrated that differentially expressed proteins were significantly related to specific pathways. We were first interested in studying the networks altered in our PH model and compared to healthy controls, and therefore directly linked to the disease. Afterward, we studied the differential alterations in cardiac tissues in 2DG-treated SuHx versus untreated SuHx rats to establish which mechanisms determine the different PH phenotypes between these two groups.

Accordingly, we evaluated the SuHx versus CTL group based on the z-score. The z-score value provides information about the activation/inhibition patterns of specific pathways or molecules based on the information within the IPA databases. Results (Table 5) show that NAD signaling pathway was significantly inhibited in SuHx RV, suggesting the central role of energetic metabolism and redox status in the development of PH.

Table 5. List of the canonical pathways arising from SuHx vs. CTL comparison, ordered by z-score.

Ingenuity Canonical Pathways	-log(p-value)	z-score	Proteins
NAD Signaling Pathway	1.94E+00	-2	GSK3B,NT5E,PARP1,SIRT2
EIF2 Signaling	4.31E+00	-1	ACTA1,EIF5,GSK3B,RPL22,RPL31,RPLP1,RPS21,RPS5
Integrin Signaling	2.10E+00	-1	ACTA1,CAPN1,Cdc42,GSK3B,PXN

We then assessed the effects of 2DG treatment in PH by comparing the SuHx-2DG vs. SuHx groups. The canonical pathways with the most significant z-scores are shown in Table 6. Notably,

the NAD signaling pathway was reversed after treatment and significantly increased in the group of 2DG-treated animals, with a z-score of 2.24. Interestingly, other highly scored activated pathways correspond to PPARα/RXRα, the white adipose tissue browning pathway, the sirtuin signaling pathway, and the insulin secretion signaling pathway, all related to energy metabolism, reaffirming the idea that these pathways, in our case modified by 2DG, can be an excellent target to minimize tissue remodeling and myocardial maladaptation in PH.

Table 6. List of the canonical pathways arising from SuHx-2DG vs. SuHx comparison, ordered by z-score.

Ingenuity Canonical Pathways	-log(p-value)	z-score	Proteins
Estrogen Receptor Signaling	3.16E+00	2.646	AKT1,EIF4E,GNB2,MT-ATP6,PRKAA1,PRKAB1,PRKACA,PRKAR2A
NAD Signaling Pathway	3.12E+00	2.236	AKT1,Hist1h2bg,PRKAA1,PRKAB1,SIRT2
PPARα/RXRα Activation	2.63E+00	2.236	INSR,PRKAA1,PRKAB1,PRKACA,PRKAR2A
CDK5 Signaling	2.68E+00	2	CAPN1,PPP2R2A,PRKACA,PRKAR2A
Nitric Oxide Signaling in the Cardiovascular System	2.61E+00	2	AKT1,PRKAA1,PRKACA,PRKAR2A
White Adipose Tissue Browning Pathway	2.40E+00	2	PRKAA1,PRKAB1,PRKACA,PRKAR2A
Cardiac Hypertrophy Signaling (Enhanced)	2.37E+00	1.89	AKT1,CAMK2A,EIF4E,GNB2,HSPB2,PPP3CA,PRKACA,PRKAR2A
Sirtuin Signaling Pathway	4.98E+00	1.633	AKT1,CPT1A,MT-ATP6,NQO1,PPIF,PRKAA1,SIRT2,SOD1,TIMM10
Insulin Secretion Signaling Pathway	2.74E+00	1.633	CAMK2A,EIF2S3,EIF4E,INSR,PRKACA,PRKAR2A

Energy metabolism, as described above, is intrinsically linked to the development of PH; and 2DG, being a glucose analog, is also related to energy function. Since the IPA results were along these lines, we decided to put the focus on alterations in energy metabolism. Figure 37 shows key canonical pathways for the SuHx/CTL (Figure 37A) and SuHx-2DG/SuHx (Figure 37B) comparisons. Each pathway is represented by a circle, in which the color is determined by the z-score to show the activation/inhibition pattern, and the size by the number of genes overlapping the pathway.

Among them, the sirtuin signaling pathway and the NAD signaling pathways stand out. These pathways are closely linked, as sirtuins are a large family of enzymes that use nicotine adenine dinucleotide (NAD) as a cofactor. They have a significant p-value, but opposite activation-inhibition pattern between comparisons. Sirtuin and NAD signaling pathways were inhibited in SuHx/CTL (blue) but activated in SuHx-2DG/SuHx (orange), evidencing an essential role of energetic metabolism and redox status, both in the development of PH, and in the mechanisms derived from 2DG treatment. The inhibition of glutathione redox reactions in SuHx rats, and activation with 2DG treatment, supports the involvement of redox homeostasis in PH and 2DG-

derived mechanisms. Figure 65 of the Annex displays the alterations in the sirtuin signaling pathway in the cytoplasm and mitochondria for SuHx/CTL and SuHx-2DG/SuHx comparisons. In addition, Figure 66 exposes the NAD$^+$/NADH role in regulating enzymatic deacetylation by some sirtuins.
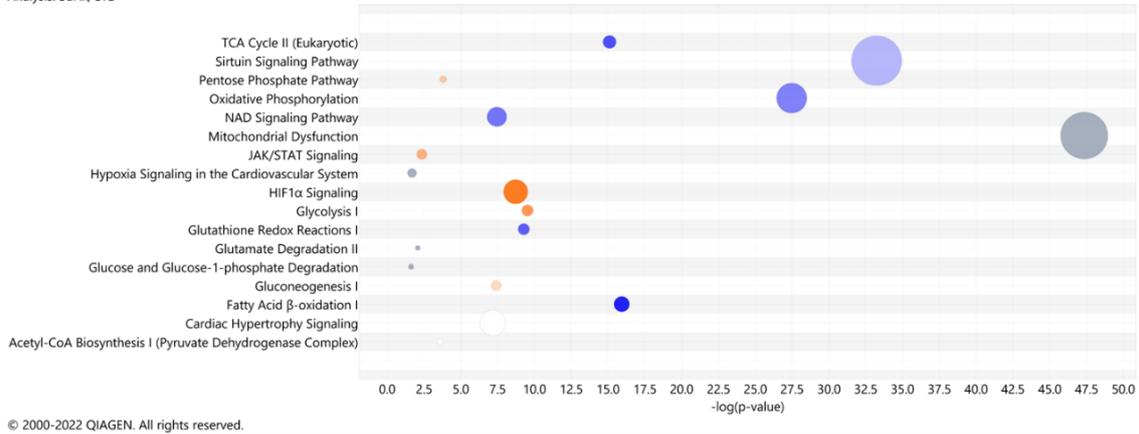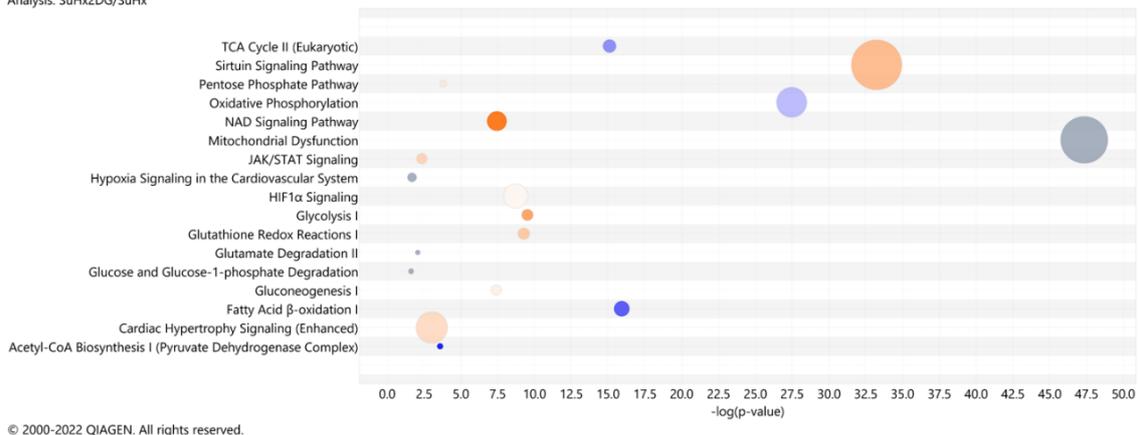
Figure 37. Adaptation of the IPA analysis of canonical pathways alterations. Representation of the main altered canonical pathways in (A) SuHx vs. CTL and (B) SuHx-2DG vs. SuHx. Differentially activated pathways appear in orange and differentially inhibited pathways appear in blue. The size of each circle is determined by the number of genes that overlap the pathway.

Figure 37 further reveals the evident activation of glycolysis and the inhibition of fatty acid β-oxidation in SuHx rats, a pattern that clearly matches the glycolytic shift associated with PH development. Glycolysis and fatty acid β-oxidation pathways are represented in Figures 64 and

65 of the Annex, respectively, for SuHx/CTL and SuHx-2DG/SuHx comparisons. A convoluted effect of 2DG on these pathways is observed. The metabolic shift after 2DG was accompanied by an amelioration of different ventricular and vascular remodeling functional and histopathological parameters, as indicated above. Although the mechanism underlying these changes is likely to be complex, our results demonstrated downregulation of SIRT2 in SuHx rats and, interestingly, upregulation after 2DG treatment (see Annex, Figure 66). This observation prompted us to further study this enzyme.

Increased SIRT2 protein expression in 2DG groups

We validated the variations in SIRT2 expression identified by proteomic analysis. For that, we performed a WB using frozen RV extracts.
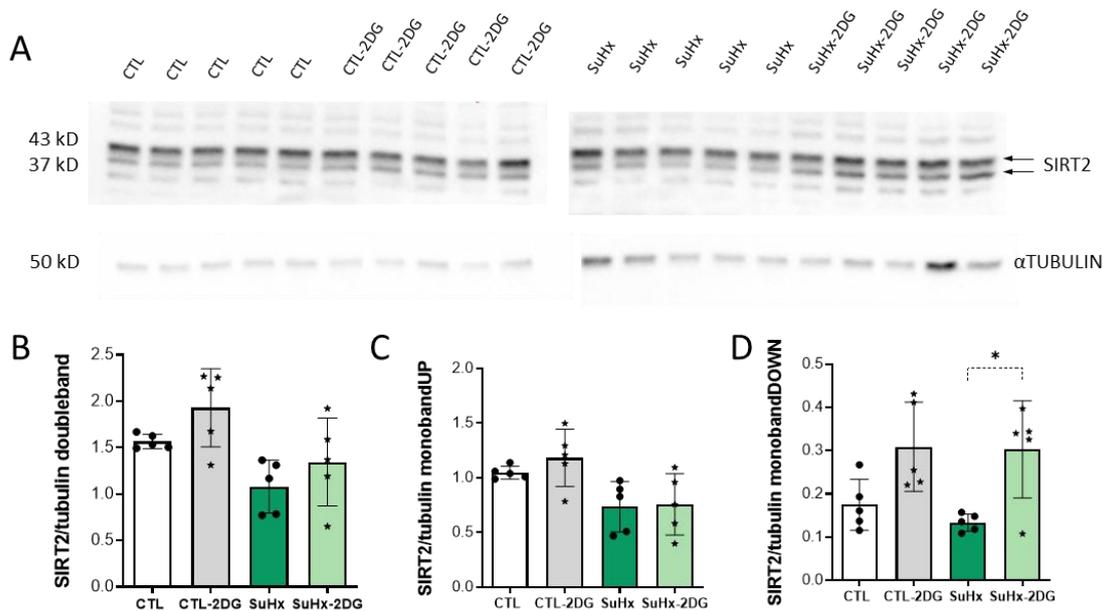
Figure 38. Expression of SIRT2 in the RV of experimental rats. (A) WB showing the bands corresponding to Sirtuin 2 as well as Tubulin, used as a loading control. (B) Quantification of SIRT2 double band (B), upper band (C) and lower band (D). Values are presented as mean ± SD, *p-value < 0.05 assessed by the One-way ANOVA test.

By quantifying the double band that appears in the membrane, since rat SIRT2 has two isoforms, we detected that the expression of the smaller isoform was slightly decreased in the SuHx group and significantly increased in SuHx-2DG compared SuHx rats (Figure 38D).

Assessment of the redox status of RV tissue

As an additional validation of our proteomic results, we aimed to investigate the redox status of the RV in the four different groups. For this purpose, we used a commercially available colorimetric kit to quantify the NAD$^+$/NADH status.
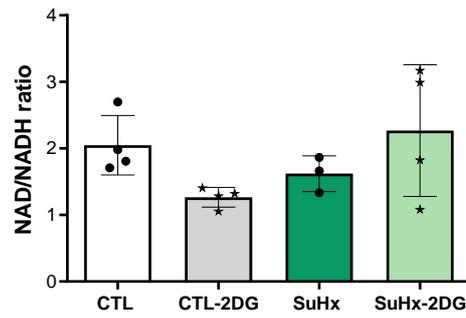
Figure 39. Representation of the NAD/NADH ratio in the different groups. Concentrations were calculated by extrapolating the data from a standard curve with known NADH concentrations A ROUT test (Q = 2%) was performed to identify outliers, which ruled out a value from the SuHx group. Values are presented as mean ± SD.

In our model, we found a tendency to decrease the NAD$^+$/NADH ratio in the SuHx group compared to CTL. This was partly reversed after treatment with 2DG.

IV.3.3 Discussion

This study explored the effect of continuous 2DG treatment for four weeks on the development of PH in a SuHx rat model. The results showed that the animals from the group suffering from PH but treated with 2DG presented a significant attenuation of the main functional, hemodynamic and histopathological parameters defining a PH phenotype, pointing to the beneficial effects of the drug in our female rat model.

PH phenotype associated with the 2DG treatment

To determine the different patterns of PH achieved in each group, RVSP was measured as described in section III of Material and Methods of this thesis. These hemodynamic results showed, as expected, that the SuHx groups presented an increase in the values compared to the animals in the control groups, but it was less pronounced in the group treated with 2DG. Additional functional and histological parameters were measured to characterize pulmonary vascular dysfunction and RV remodeling.

Short-axis images of the heart taken by CMR allowed visualization of ventricles remodeling. By segmenting all the MRI slices, the functional PH markers have been characterized in the LV and the RV. Additional systolic and diastolic parameters were obtained from the time derivative data of the ventricular volumes, particularly PER normalized to EDV to characterize the systolic function and PFR normalized to EDV to characterize the diastolic function.

LV parameters revealed no differences between the groups, indicating preserved left ventricular function. On the contrary, SuHx rats presented reduced RV PER normalized to EDV pointing to systolic dysfunction in this ventricle. Furthermore, in the RV of the SuHx group appeared a significant increase in EDVi, ESVi, and the Fulton Index, accompanied by a significant decrease in EF, which are characteristic manifestations of decompensated RV failure and RV remodeling [195]. The SuHx-2DG group presented the same trend but to a lesser degree, indicating the attenuation of RV remodeling (see Figures 33-34). Improvements in these functional parameters associated with treatment with 2DG reveal the protective function of this drug in the RV. Similar changes have been reported with other drugs that reduce metabolic change, such as DCA [77].

Lungs were dissected to measure vascular remodeling by histology. As shown in Figure 32, the increase in medial wall thickness and the medial wall areas in the SuHx groups indicate the thickening of the vessel walls. As in the case of hemodynamic data, this increase was attenuated by 2DG treatment. These results align with decreased pulmonary vascular resistance, translating into minor ventricular remodeling.

Metabolic implications of 2DG

We and others have demonstrated a metabolic rewiring associated with PH measured with ^{18}F-FDG PET. In the current experiments with rats, we did observe an ^{18}F-FDG uptake increase in the heart but not in the lungs. By measuring this radiotracer uptake in each ventricle, we obtained

a non-statistically significant trend to increase in the LV and the expected ^{18}F-FDG uptake increase in RV of both SuHx groups (see Figure 35).

Taking together all these imaging, hemodynamic and histopathological results, it seems that the 2DG had a beneficial effect on the disease evolution minimizing the risk of heart failure.

2DG modified energetic metabolism in RV cardiomyocytes

We investigated the potential beneficial effect of 2DG and the mechanisms responsible for this improvement with a proteomic analysis of RV.

The results pointed out that the effects of 2DG were exacerbated in a pathological context.

In SuHx rats, numerous metabolic pathways were altered. As described above, a metabolic rewiring characterized by an increase in glycolysis and a decrease in oxidative phosphorylation metabolism metabolic pathway is expected in PH animals [74], and this is what we found in our rats. When comparing SuHx and CTL animals, our proteomic results displayed an oxidative phosphorylation inhibition and glycolysis activation and how the effect was partly altered after treatment with 2DG. We have also confirmed these results by NMR spectroscopy of cardiac tissues (data not shown since they are part of another thesis). We found full metabolic reprogramming in SuHx rat heart tissues characterized by a shift in glucose metabolism, with higher metabolic concentrations of lactate and lower glucose. We also observed an increase in glutaminyls with higher concentrations of glutamate. We also observed an increase of glutathione, expected after seeing the predicted increased production of NADPH in glycolysis. In this thesis, we observed that NADH activation is also partly reversed in 2DG-treated animals. We also demonstrated that some changes appeared modified in the SuHx-2DG group. This suggests that the improvements in 2DG-treated rats derived from the possible harm minimization caused by this metabolic shift.

We have identified NAD and sirtuin signaling pathways as the most representative pathways in SuHx and reversed with 2DG treatment. Both pathways present alterations in the SuHx-2DG that oppose those found in SuHx animals. Sirtuins are NAD^+-dependent deacetylases that participate in the post-translational regulation of proteins by removing acetyl groups from acetyllysine-modified residues [196]. The Sirtuin family is one of the main NAD-dependent enzymes since they require NAD^+ as a co-substrate in their deacetylase activity, consuming one molecule of NAD^+ during each diacylation cycle [197]. Therefore, sirtuins activity is strongly linked to the availability of NAD^+, which is determined by the cell's energy status. Sirtuins regulate a wide variety of cellular functions, such as DNA repair process, regulators of cell defense systems, and survival in response to stress, particularly nutrient deprivation [196]. Sirtuins have been linked to cardiovascular diseases. Studies in PASMCs [198], [199] and rodents [200] have demonstrated the role of some mitochondrial sirtuins in the development of PAH.

SIRT1, the most studied protein in the context of ventricular hypertrophy, has shown a protective role [197]. SIRT2 participates in the glucose metabolism of the cardiomyocytes and

may provide protection, and it is also involved in vascular remodeling through its action on tubulin [201]. Similar to our results, SIRT2 has been shown to have a protective role against cardiac hypertrophy [201], and its deficiency promotes cardiac hypertrophy in aged mice [202]. SIRT3 prevents fibrosis and cardiac hypertrophy [203]. SIRT5 inhibition has been demonstrated that worsens cardiac infarction after an ischemia-reperfusion episode [203]. Finally, nuclear sirtuins, SIRT6 and SIRT7 [197], and mitochondrial sirtuins [204] demonstrated to have a cardioprotective effect and exert positive effects against cardiac hypertrophy.

From our proteomics data, we identified decreased expression of SIRT2 in the SuHx/CTL comparison but considerably increased levels when comparing the SuHx groups with and without 2DG. This suggests that SIRT2 may be involved in the 2DG-associated alteration of the energetic metabolism and potentially explain the cardioprotection observed. We also verified the increased expression of SIRT2 in groups treated with 2DG by WB.

Multiple SIRT2 isoforms have been reported as a result of alternative splicing [205], showing different locations and functions [206]. This is relevant since, from our data, an upward trend can be observed when the double band is quantified, but the changes are significantly different when the band with the lowest molecular weight is analyzed separately. However, further studies will be necessary since we cannot discriminate if our antibody recognizes functional differences between the two isoforms. Importantly, our proteomics and WB results confirmed increased SIRT2 expression after treatment with 2DG.

Energy metabolism is intrinsically linked to redox reactions, which function as regulators of the metabolic network [207]. NAD, a cofactor for many enzymes, can be found as NAD^+ or NADH, oxidized or reduced forms, respectively [203]. The passage from one state to other serves as a cofactor in redox reactions that regulate energy metabolism, including glycolysis, fatty acid oxidation, and the citric acid cycle [203]. Redox systems adapt and respond to changes in energy source and demand [207], and maintaining the proper NAD^+/NADH ratio is crucial for cellular homeostasis [203]. Changes in redox balance and energy metabolism might have a synergistic action leading to PH [74]. In this study, we measured this ratio in RV tissue using a colorimetric assay to support alterations in the redox state related to sirtuin activity and energetic metabolism. We found a reduction in the NAD^+/NADH ratio in the SuHx group, which appears reversed after 2DG treatment. Our data is concordant with previous reports showing that the NAD^+/NADH ratio decreases parallel to the metabolism changes that occur in the heart upon exposure to hypoxia or during the development of heart failure [208]. Besides, increased fluxes through glycolysis promote reduced NAD^+/NADH ratios since excess lactic acid fermentation under hypoxic conditions shifts the NAD cofactor balance toward accumulation of reduced equivalents [74]. Furthermore, this trend appeared reversed in animals treated with 2DG, suggesting that 2DG treatment protects against redox and metabolic changes typically associated with PH [209].

Conclusion

In conclusion, treatment with 2DG in a SuHx model in female rats attenuated PH biomarkers in the RV and pulmonary vascular remodeling measured through a comprehensive functional and proteomic study of the RV. The results revealed that an energy imbalance occurred in SuHx rats and suggested that treatment with 2DG, partly rescued myocardial energy and redox homeostasis. We found that one of the enzymes with direct action on energy metabolism, SIRT2, was downregulated in the SuHx group but recovered with 2DG. These results were verified by WB and, independently, the redox state of the RV tissue has been investigated by measuring the NAD^+/NADH ratio. These molecular changes were aligned with the structural/functional cardiac remodeling improvements observed in these animals. Thus, 2DG seems to have beneficial effects against the development of PH, potentially associated with the alterations in energy metabolism in cardiac tissue. Our results reveal this as a new target that will be studied in depth in future experiments.

IV.4 Influence of mitochondrial function in a PH mouse model

IV.4.1 Rationale

Our previous data demonstrated the beneficial effect of 2DG, blunting the glycolytic switch associated with PH, in a SuHx female rat model (as discussed in Chapter IV.3). Based on this knowledge, the present chapter aimed to explore further the consequences of modifying mitochondrial biogenesis. For this purpose, we developed two complementary strategies to alter mitochondrial function into a PH model with SuHx male mice.

On the one hand, a well-characterized 'mitochondrial DNA inhibitor' (EtBr) was chosen to study the effect of impaired mitochondrial function on the development of PH. EtBr is a DNA intercalating agent that prevents DNA replication. Cell studies have revealed that EtBr accumulates in the mitochondria and impacts mitochondrial DNA, with little or no effect on nuclear DNA [210]–[213]. The effects of EtBr are highly consistent. It decreases mitochondrial DNA replication and transcription in many contexts, invariably reducing oxidative phosphorylation and respiration [214]–[216]. Ultrastructural changes occur after the treatment with EtBr in primary human fibroblast cell cultures [213], HeLa cells [217], human breast and lung carcinoma cells [218], and Mouse L cells [219]. Such changes are characterized by mitochondria swelling, fragmentation, and reduced cristae [213], [220]. To our knowledge, there are no reports of the effects of mitochondrial function inhibition in the context of PH.

On the other hand, we wanted to corroborate the outcomes of enhanced mitochondrial function on PH development obtained in the rat model into the mouse model. As in chapter IV.3, we used 2DG for this purpose.

We characterized the phenotype associated with PH in the lung and heart in both groups to quantify the effects of each treatment. In addition to imaging, hemodynamic, histological, and molecular biology tests, we reserved one mouse from each group to characterize the effects of the treatments on the morphology of their cardiac mitochondria by TEM analysis.

Animal food, drink, and weight monitoring in EtBr and 2DG murine groups

During the experiments, animals were checked daily to monitor their food intake, water consumption, and weight. No alterations in behavior or physical appearance were associated with EtBr (in purple) or 2DG (in blue) treatments or with the SuHx exposure during the weeks of the experiments. Overall, mice maintained normal food and water intake during this period. However, one of the mice from the SuHx group and two from the SuHx-2DG group appeared dead in the last week. We could not find any final association of these casualties with the SuHx or 2DG treatments.
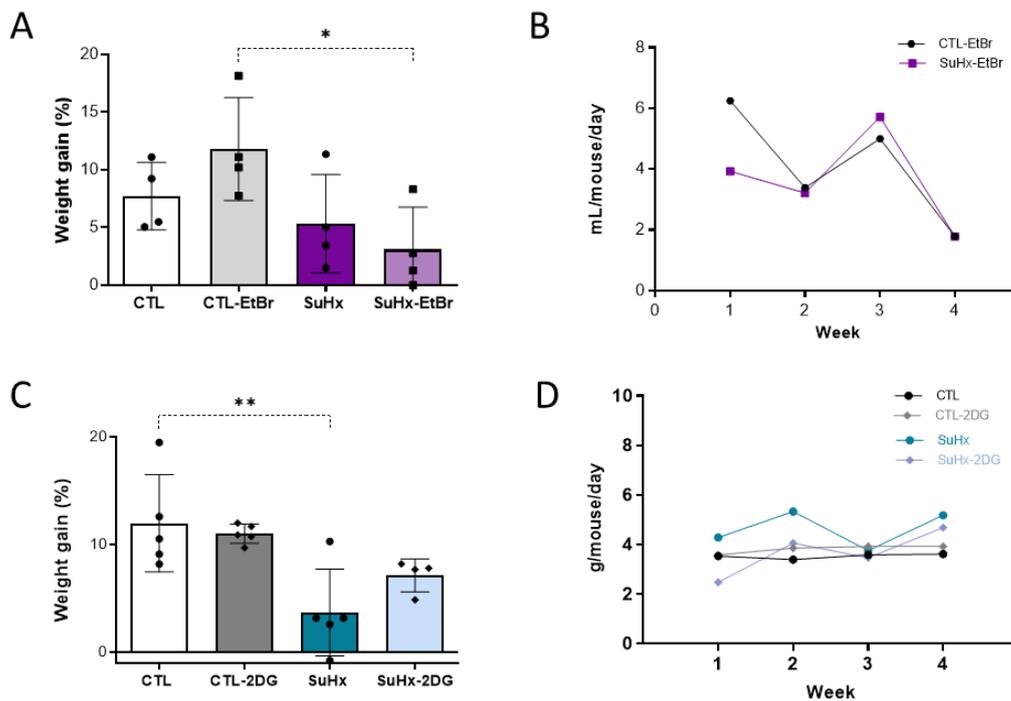
Figure 40. Food and water intake and weight monitoring along the experiment. (A&C) Graphic representation of the body weight variation throughout the EtBr and 2DG experimental approach, respectively. (B) Representation of the average water intake per mouse per day for each week for the EtBr groups. (D) Representation of the food intake per week for the 2DG cohort. Values are presented as mean ± SD, *p-value < 0.05, **p-value < 0.01 assessed by the One-way ANOVA test. CTL: control or normoxia groups. CT-EtBr: same as CTL but with ethidium bromide treatment. CT-2DG: same as CTL but with 2-deoxyglucose treatment. SuHx: Hypoxia + 1 Su5412 IP treatment. SuHx-EtBr: same as SuHx but with ethidium bromide treatment. SuHx-PhA: same as SuHx but with 2-deoxyglucose treatment.

In both models, we took advantage of the weekly cage change and IP injection of Sugen/vehicle (max. of 30 minutes – 1 h out of the hypoxia workstation) to monitor weight. As previously reported, we confirmed a smaller weight gain of mice upon SuHx (Figure 40A, C). It is worth noting that 2DG treatment seems to prevent this decrease in weight (Figure 40C), even though these animals did not eat more (Figure 40D) during the whole experiment.

Hemodynamic characterization in EtBr and 2DG mice cohorts

As a standard measure in the PH field, we measured RVSP for the final PH evaluation. The increase in RVSP values in SuHx groups was expected and evident (Figure 41), though the mean of the groups treated with EtBr was not affected, indicating that this treatment did not influence mean RVSP. In the case of 2DG, values were lower in one animal of the SuHx-2DG group.
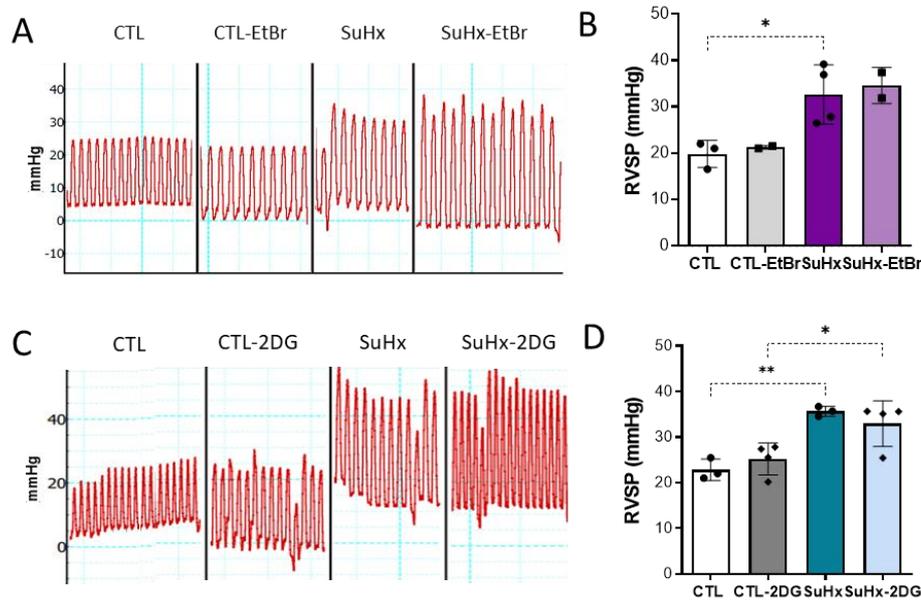
Figure 41. Tracking the RV hemodynamics. (A&C) Typical RVSP curves of each group (B&D). Box plot representation of RVSP measured at the end of the treatment. Values are presented as mean ± SD, *p-value < 0.05, **p-value < 0.01 assessed by the One-way ANOVA test between groups with n >2.

Pulmonary vascular remodeling and cell proliferation markers after EtBr and 2DG treatments

As indicated in several parts of this thesis, pulmonary vascular remodeling determined by classical histology is another classical and relevant parameter to characterize the different endophenotypes associated with PH and mitochondrial status. The animals from the SuHx model showed higher medial wall thickness and medial wall area (Figure 42), indicating remodeling of the pulmonary vessels. Like the results of RVSP, these histopathological parameters were not affected as a consequence of the treatments.
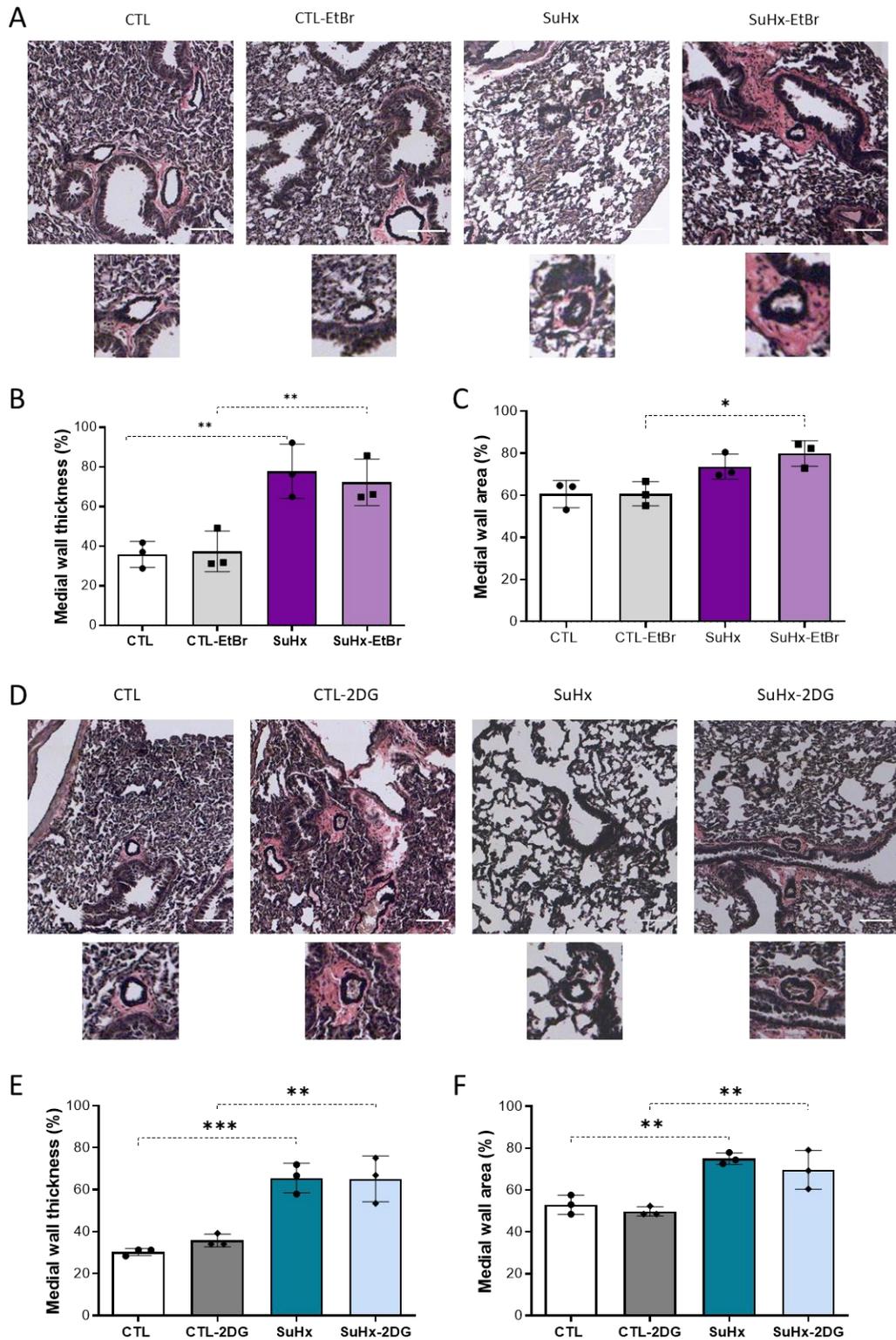
Figure 42. Assessment of pulmonary vascular remodeling. (A&D) Displayed for each lung section representative photomicrographs of the elastic staining of the whole lung (upper panel) and a pulmonary artery (bottom panel). Scale bars are 100 μm. (B&E) Quantitative analysis of the medial wall thickness and (C&F) medial wall area in the EtBr and the 2DG cohort, respectively. The graph represents the mean ± SD, *p-value < 0.05, **p-value < 0.01, ***p-value < 0.001 assessed by the One-way ANOVA test.

The increase in the sizes of pulmonary vessel walls is usually correlated to the rate of proliferation of their SMCs. Greater proliferation is linked to a higher number of cells and, therefore, greater vessel thickness. Similar to Chapter IV.1, two immunofluorescence markers were used to analyze SMC proliferation: Ki67, used as a read-out of proliferating cells, and αSMA, to locate SMCs.
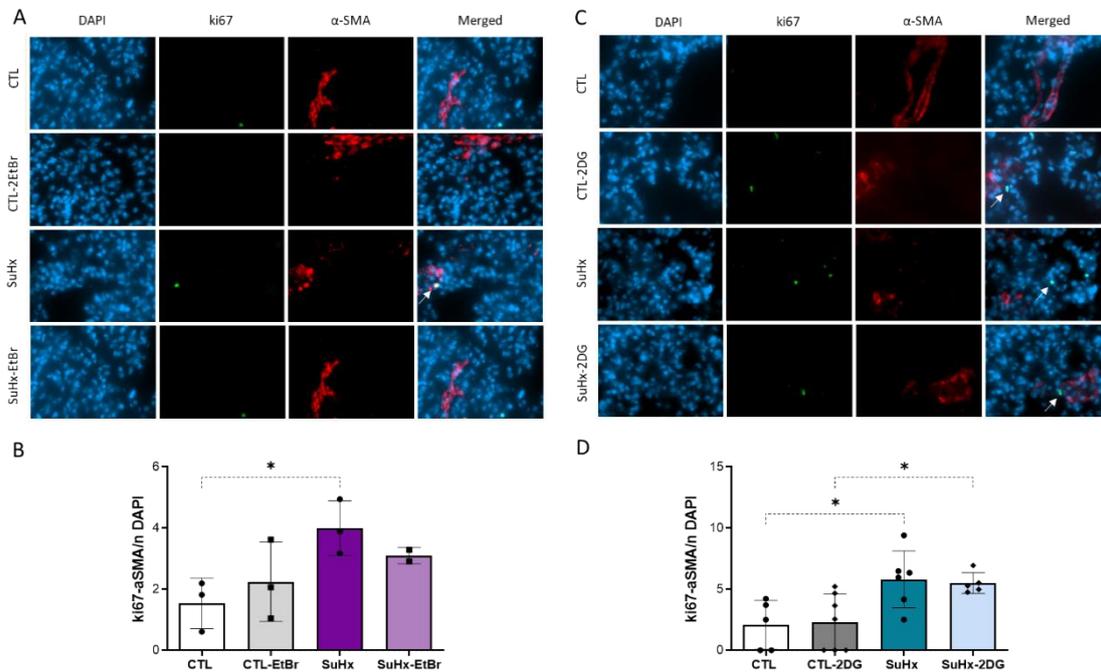
Figure 43. Immunofluorescence evaluation of Pulmonary SMCs proliferation. (A&C) Representative photomicrographs of lungs stained with Ki67, αSMA, and DAPI. (B&D) Quantification of αSMA and Ki67 positive cells in the EtBr and the 2DG cohort, respectively. Values are presented as mean ± SD, *p-value < 0.05 assessed by a One-way ANOVA test between groups with n >2.

From each slice of immune-stained lungs, a total of 10 fields for lungs were analyzed with the 63x aqueous immersion objective (Cell Axio Observer microscopy, ZEN). In line with what has been seen, a significantly higher proliferation rate in the pulmonary SMCs appeared in the SuHx groups compared to the controls (Figure 43B, D). Furthermore, our data showed decreased SMC proliferation, without statistical significance, due to EtBr or 2DG treatments.

Cardiac function characterization by MRI

To get an additional insight into cardiac remodeling *in vivo*, multi-slice short-axis cine MRI images of the heart were taken before the sacrifice of the animals. As described above, we determined the volumes of both heart chambers and calculated the corresponding functional parameters.
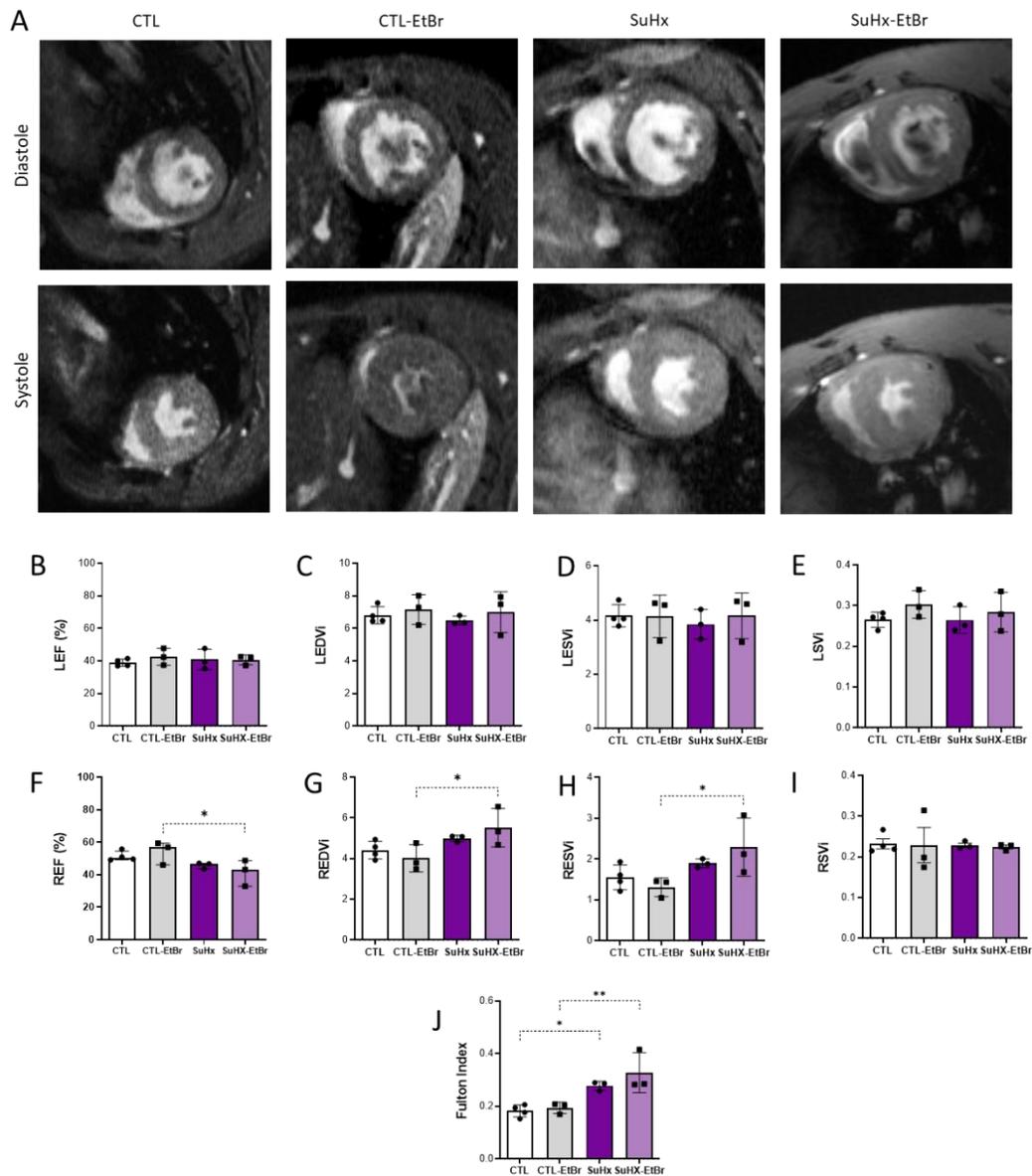
Figure 44. MRI images and quantitative analysis of cardiac remodeling of animals treated with EtBr and corresponding controls in normoxia (CTL) and hypoxia (SuHx‡). (A) Cross-sectional representative images of the heart of a representative animal of each group acquired by MRI showing the myocardium and epicardium of both ventricles in systole (bottom image) and diastole (upper image). Measurement of the Left Ejection Fraction (LEF, B), the Left-ventricle End-Diastolic Volume Index (LEDVi, C), the Left-ventricle End-Systolic Volume Index (LESVi, D), the Left-ventricle Stroke Volume index (LSVi, E), the Right-ventricle Ejection Fraction (REF, F), the Right-ventricle End-Diastolic Volume Index (REDVi, G), the Right-ventricle End-Systolic Volume Index (RESVi, H), the Right-ventricle Stroke Volume index (RSVi, I), and the right ventricular hypertrophy calculated using the Fulton index (J). Values are presented as mean ± SD, **p-value < 0.01, ***p-value < 0.001 assessed by the One-way ANOVA test. ‡ Animals in hypoxia only had one IP shot of Sugen at the beginning of the hypoxia exposure.

Figure 44 summarizes the cardiac function data for the animals treated with EtBr. We found no variations in LV. In the RV of SuHx groups, there was a tendency to increase EDVi and ESVi, an increase that was significantly changed when hypoxic animals were treated with EtBr. EF was significantly reduced in these animals compared with the control animals treated with this

mitochondrial DNA inhibitor. MRI-derived Fulton Index was augmented in both SuHx groups compared to the controls.
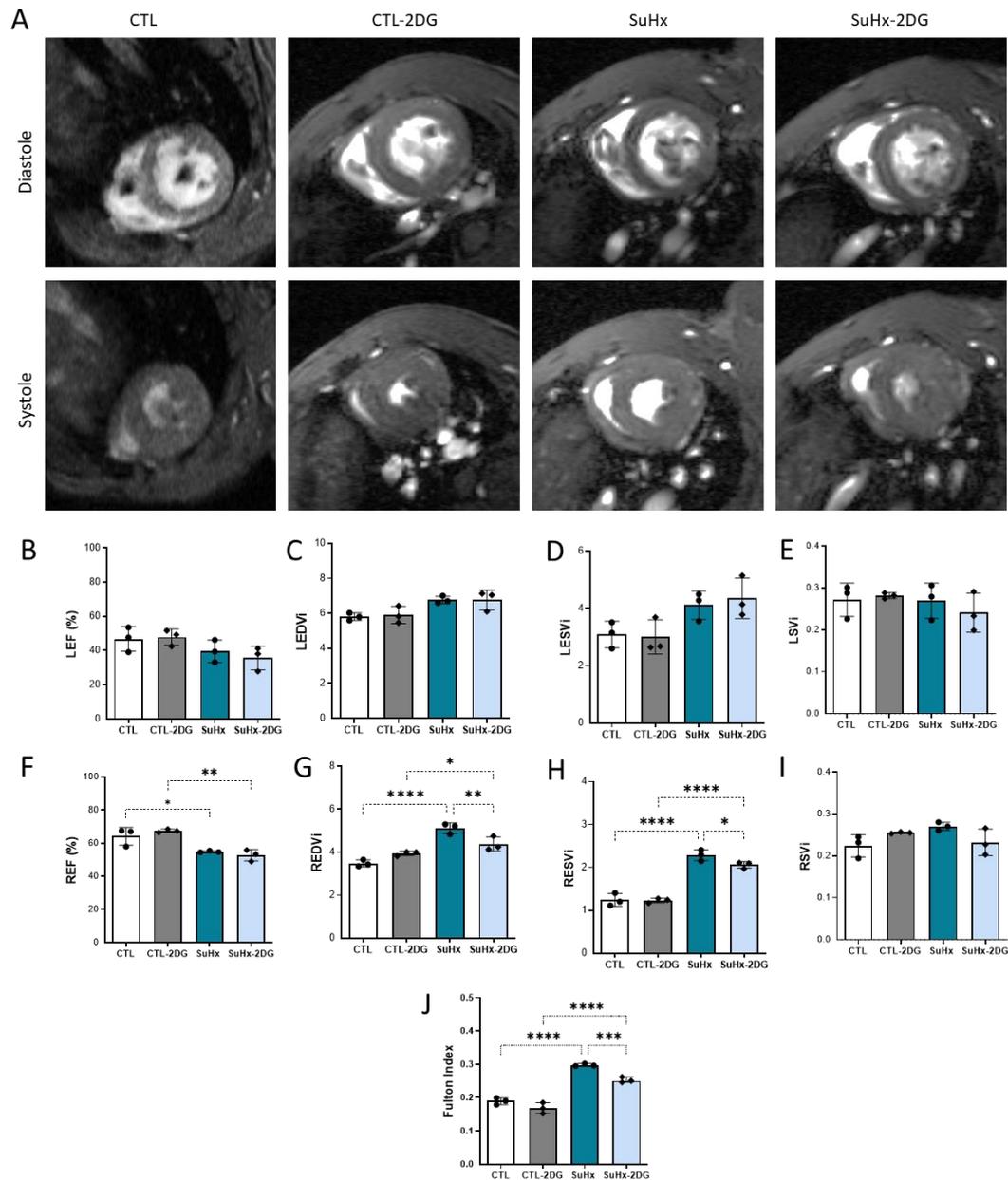
Figure 45. MRI images and quantitative analysis of cardiac remodeling of animals treated with 2DG and corresponding controls in normoxia (CTL) and hypoxia (SuHx). (A) Cross-sectional representative images of the heart of a representative animal of each group acquired by MRI showing the myocardium and epicardium of both ventricles in systole (bottom image) and diastole (upper image). Measurement of the Left Ejection Fraction (LEF, B), the Left-ventricle End-Diastolic Volume Index (LEDVi, C), the Left-ventricle End-Systolic Volume Index (LESVi, D), the Left-ventricle Stroke Volume index (LSVi, E), the Right-ventricle Ejection Fraction (REF, F), the Right-ventricle End-Diastolic Volume Index (REDVi, G), the Right-ventricle End-Systolic Volume Index (RESVi, H), the Right-ventricle Stroke Volume index (RSVi, I), and the right ventricular hypertrophy calculated using the Fulton index (J). Values are presented as mean ± SD, *p-value < 0.05, **p-value < 0.01, ***p-value < 0.001, ****p-value < 0.0001 assessed by the One-way ANOVA test.

The same cardiac function indices obtained by MRI have been calculated for animals treated with 2DG. Similar to the observation in Chapter IV.3 with rats treated with this agent, Figure 45 shows a significant increase in REDVi, RESVi and Fulton Index, as well as a reduction in EF in SuHx groups compared to the control animals. The results indicated a specific improvement produced with the 2DG treatment, as observed in rats (chapter IV.3).
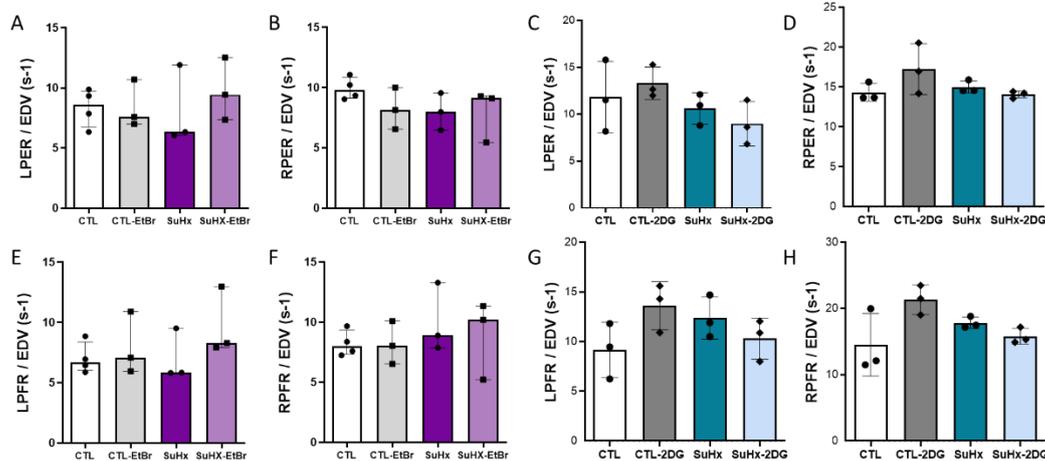
Figure 46. Analysis of the systolic and diastolic function. Measurement of the (A&C) left-ventricle peak ejection rate (PER) normalized to end-diastolic volume (EDV), (B&D) Right-ventricle PER normalized to EDV, (E&G) Left-ventricle peak filling rate (PFR) normalized to EDV, (F&H) Right-ventricle PFR normalized to EDV. Values are presented as mean ± SD assessed by the One-way ANOVA test.

Systolic and diastolic parameters described in previous chapters were calculated, but we found no differences between the groups in any ventricle (Figure 46).

Metabolic alterations measured by PET imaging

^{18}F-FDG PET allows direct glucose metabolism monitorization *in vivo* using a radiolabeled glucose analog as a radiotracer. The uptake of this radiotracer allowed us to explore the alterations in the glucose pathway or reveal the accumulation of metabolically active cells (e.g., tumoral, highly proliferative, or inflammatory cells), as has been described and used for human and animal applications. ^{18}F-FDG PET was performed in EtBr/2DG models like that presented in previous chapters.
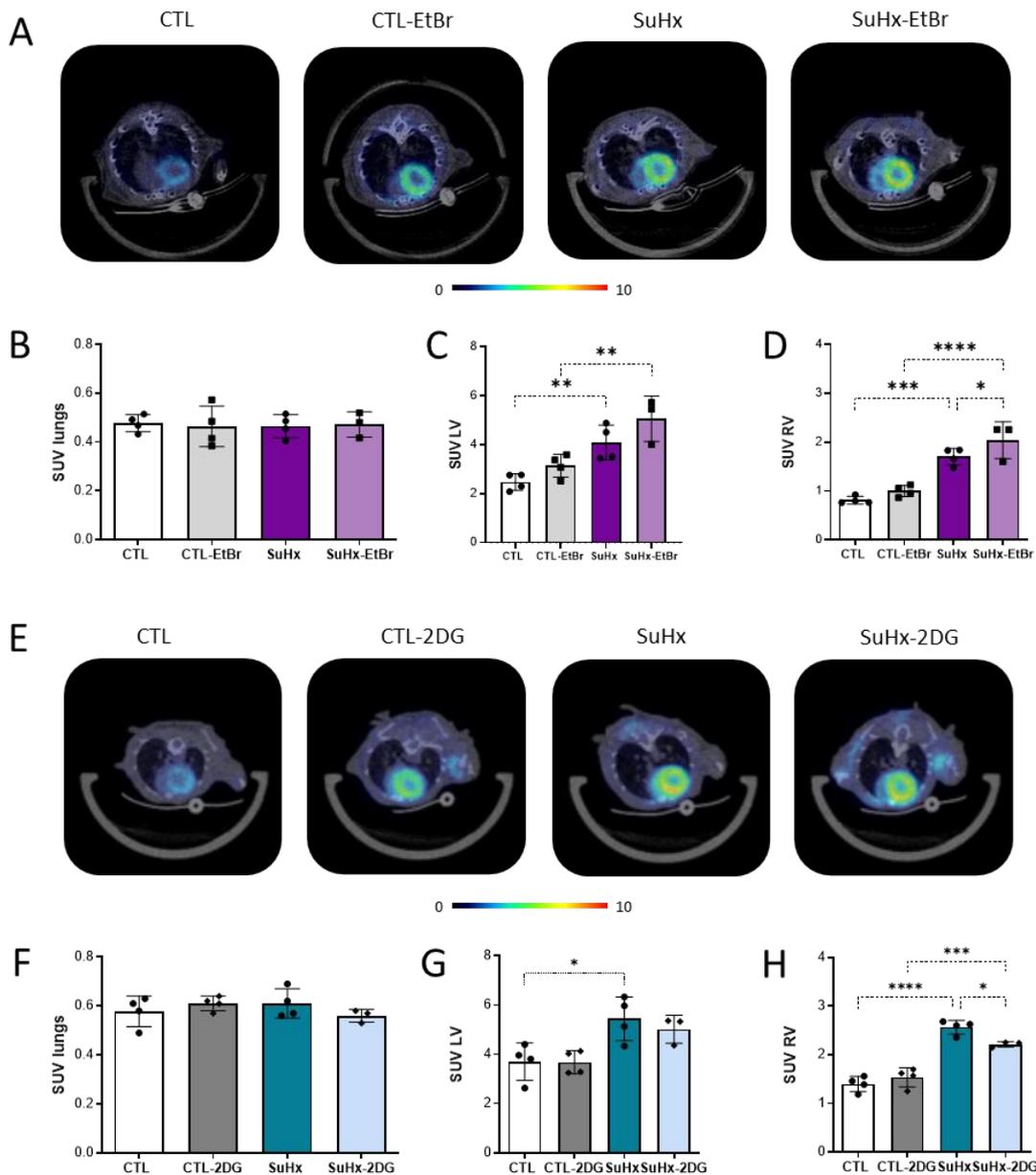
Figure 47. Evaluation of organ glucose metabolism by ^{18}F-FDG accumulation. (A) Overlay illustration of a representative image of the three-dimensional reconstructions of CT (MIP, gray scale) and PET (color scale represented over the images) images, transversal plane. Measurement of the SUV uptake in the (B) lungs, (C) LV and (D) RV. Values are presented as mean ± SD, *p-value < 0.05, **p-value < 0.01, ***p-value < 0.001, ****p-value < 0.0001 assessed by the One-way ANOVA test.

Figure 47A shows a representative midventricular thoracic CT cross-section and the corresponding PET view from each animal sub-group. From the quantification of the PET images in the lungs, we observed that ^{18}F-FDG SUV did not significantly vary in the different sub-groups (Figure 47B, F). However, both models showed a significant increase in LV and RV uptake in the SuHx groups. The RV changes have been associated with ventricle hypertrophy or the characteristic metabolic shift seen in PH patients or animal models, confirmed in our case. However, as far as we know, the glucose uptake changes in the LV have not been described before. Still, this result cannot be associated with significant functional changes in this ventricle,

as seen in MRI data summarized in figures 44 and 45. We also noticed that ^{18}F-FDG glucose uptake significantly changed in RV as a consequence of the two treatments, revealing a slight decrease in the group of SuHx-2DG mice and a higher increase in the SuHx-EtBr group, probably associated with the most severe PH phenotype in these animals.

In the EtBr group, we also investigated the role of ^{11}C-Choline, a radiolabeled version of choline, as a tracer for cellular proliferation. We used ^{11}C-Choline to evaluate the value of this technology as a potential pulmonary vascular remodeling imaging biomarker in PH.
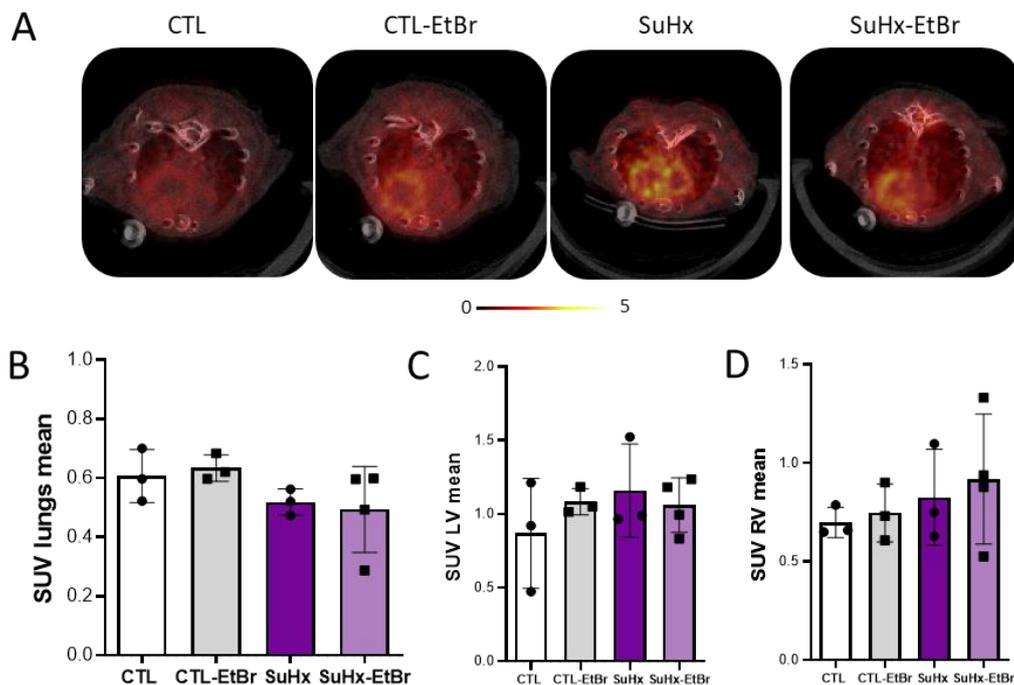
Figure 48. Analysis of choline uptake by PET imaging in the SuHx/EtBr model. (A) Reconstructed image from last 5 frames of the dynamic PET scans of ^{11}C-Choline uptake in the lungs and heart at the time of administration, in the last 10 minutes of acquisition, after 20 minutes circulation. (B) The quantification of the SUV ^{11}C-Choline uptake in lungs and heart from these averaged frames. Values are presented as mean ± SD assessed by the One-way ANOVA test.

We followed the same protocol as in Chapter IV.1, described in section III of Material and Methods. Figure 48 shows the averaged SUV from pulmonary and cardiac tissues obtained from images from the last 10 minutes of acquisition of all animals. Interestingly, although there were no statistically significant changes, RV choline uptake tended to increase after mitochondrial DNA inhibition and SuHx exposure.

Effect of 2DG treatment on the expression of glycolytic enzymes

To understand the changes in glucose uptake in heart and lung tissues, the expression of some glycolytic enzymes in the case of the 2DG-treated animals was quantified by qPCR. These results are summarized in Figure 49 (heart) and Figure 50 (lung tissues).
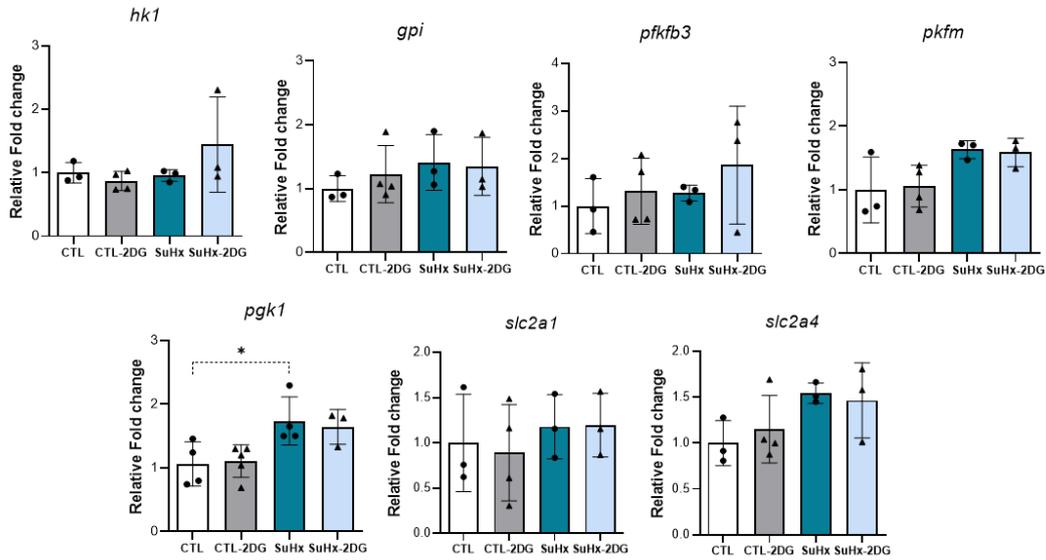
Figure 49. Expression of "glycolytic" enzymes into the heart following 2DG treatment. mRNA relative fold change of *hk1, gpi, pfkb3, pkfm, pgk1, slc2a1*, and *slc2a4* in the heart tissues of mice normalized to *rplp0*. Values are presented as mean ± SD, *p-value < 0.05 assessed by the One-way ANOVA test.

In the heart, *pkfm*, *pgk1* and solute carrier family 2, facilitated glucose transporter member 4 *(slc2a4)* demonstrated a tendency to increase in SuHx groups, which was statistically significant only for *pgk1* (Figure 49), compatible with the increase in glucose uptake observed by PET. Despite the known inhibition of glycolysis, 2DG treatment did not change the expression of these targets, although glucose uptake in this organ was significantly lower (Figure 47H).
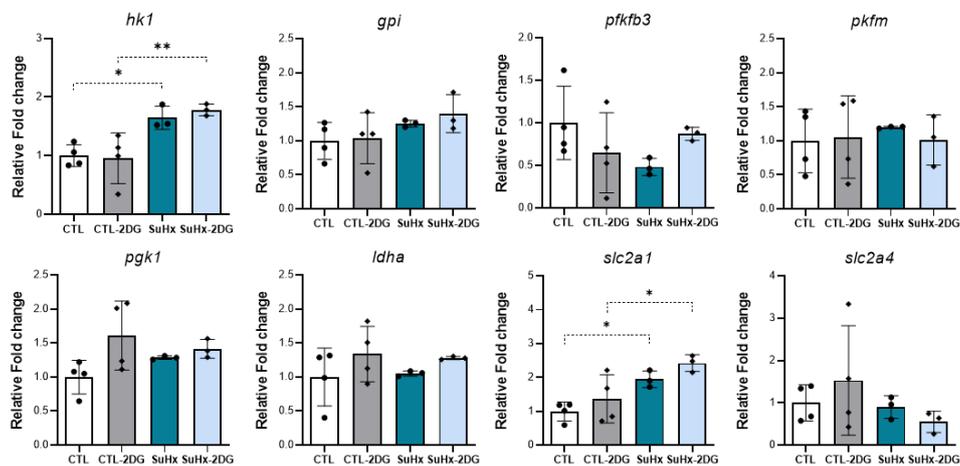
Figure 50. Expression of "glycolytic" enzymes into the lung following 2DG treatment. mRNA relative fold change of *hk1, gpi, pfkb3, pkfm, pgk1, ldha, slc2a1* and *slc2a4* in the heart tissues of mice normalized to r*plp0*. Values are presented as mean ± SD, *p-value < 0.05, **p-value < 0.01 assessed by the One-way ANOVA test.

The same glycolytic shift was observed in the lungs. Figure 50 displays that *hk1* and *slc2a1* were significantly over-expressed in the SuHx groups. These two enzymes, in addition to *pgk1*, lactate dehydrogenase A *(ldha)* and 6-phosphofructo-2-kinase 3 (*pfkfb3*) underwent a slight increase with the 2DG treatment, while *slc2a4* decreased in this group compared to the non-treated SuHx animals.

Approximation of the mitochondrial status

Translocase of the Outer Membrane of Mitochondria 20 (Tom20), a peripheral subunit of the Tom complex, is a translocase enzyme located at the outer membrane of mitochondria, responsible for the recognition and translocation of cytosolically synthesized mitochondrial pre-proteins. Tom20 is then an excellent mitochondrial marker of mitochondrial content by the quantitative analysis of the fluorescence signal.
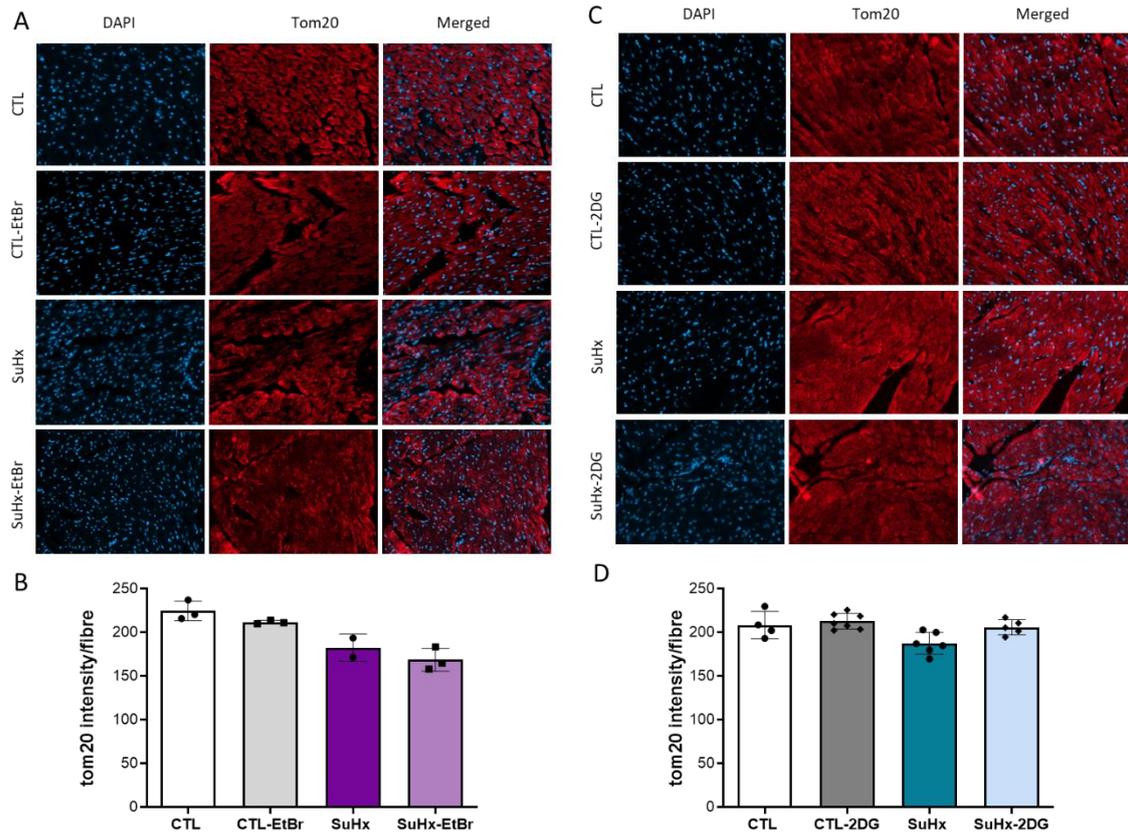
Figure 51. Analysis of the mitochondria status by immunofluorescence into the heart. (A&C) Representative photomicrographs of heart tissues stained with Tom20 and DAPI in the EtBr and 2DG models, respectively. (B&D) Quantitative representation of the Tom20 staining means intensities per cardiac fiber. Values are presented as mean ± SD assessed by the One-way ANOVA test.

In the case of PH models with EtBr or 2DG treatments, the immunofluorescence analysis with Anti-Tom20 was performed to evaluate potential differences in mitochondrial density in the different models. Panels B and D of Figure 51 compare Tom20 immunofluorescence intensity between the different groups in the heart. A tendency to decrease the signal was observed in the SuHx groups, slightly decreased with EtBr, and recovered with 2DG, in agreement with the expected mitochondrial biogenesis increases after treatment with this drug.

Characterization of mitochondria mass and morphology by electron microscopy

Finally, in order to corroborate the consequences of the treatments in the mitochondrial morphology of the animals, the RV tissues of each group were analyzed by TEM. This technique allows direct visualization of cell organelles in great detail.

CTL
CTL-EtBr
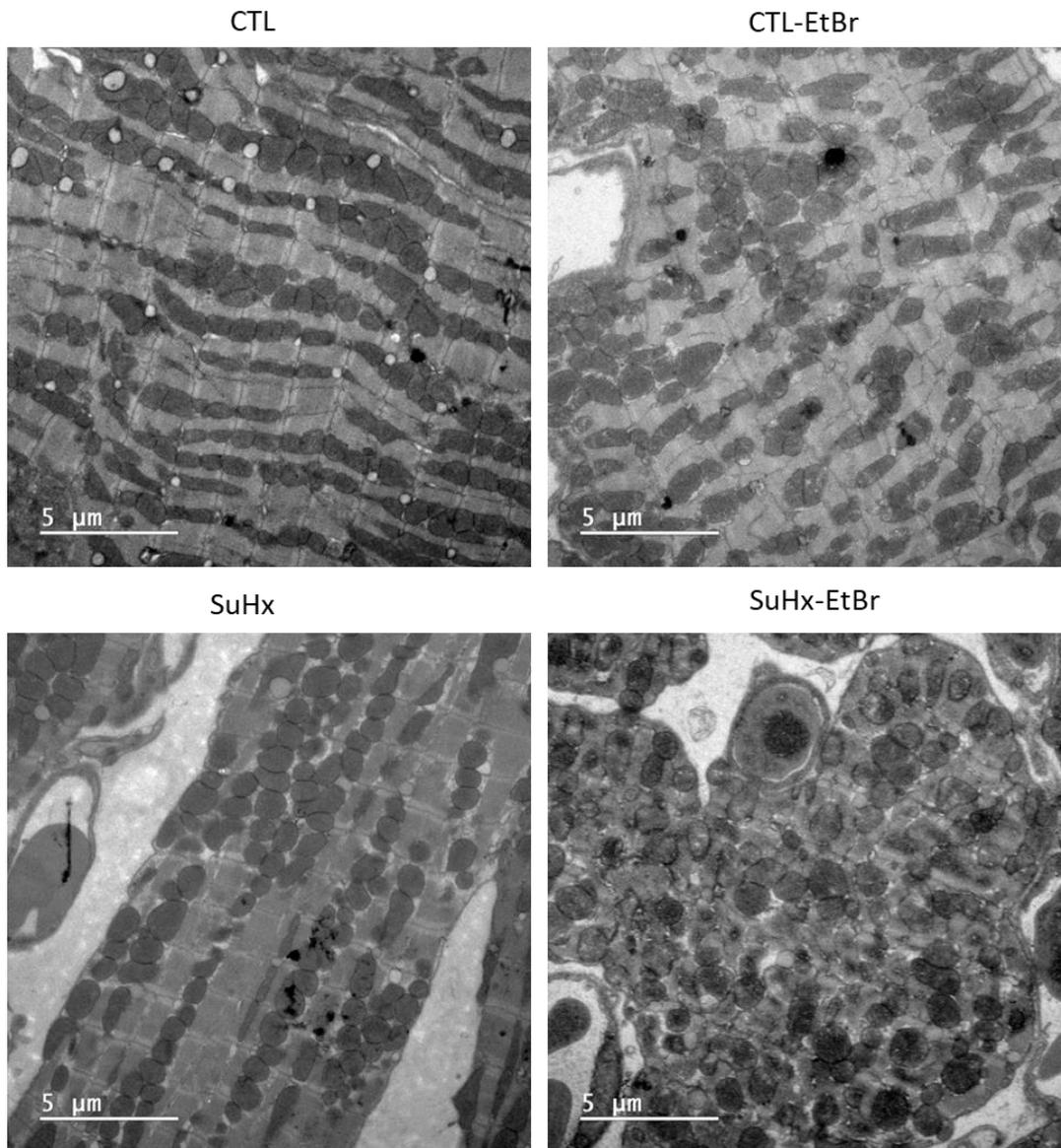
SuHx
SuHx-EtBr

Figure 52. 1000x TEM images of RV tissue of EtBr group.

The first visual inspection of these images confirmed a slight decrease in the number of mitochondria in the muscular fibers of hypoxic animals (CTL vs SuHx). Mitochondria in SuHx RV were normal in shape and size compared to the control. In the groups treated with EtBr, the mitochondrial fiber structure seems impaired with mitochondria of larger and smaller sizes and different shapes than control and SuHx group, as well as the mitochondrial density, while mitochondria in SuHx treated with EtBr exhibited a significant change in shape and presence of mitochondrial fission and fusion processes. These results are compatible with an impairment in mitochondrial homeostasis in these animals.

The interesting result will be further studied by more experiments to characterize the effect of 2DG on the structure of the mitochondria.

The mitochondrion is known to be involved in PH pathophysiology [69], [80], but the specific role in its pathogenesis of this disease remains to be determined unresolved. In this study, we aimed to elucidate whether alterations in mitochondrial biogenesis and function would affect the phenotype associated with PH in the lungs and heart of a mouse SuHx male model. Inhibition of DNA mitochondrial function was forced by EtBr supplementation in drinking water. To stimulate mitochondrial biogenesis, 2DG was added to the drinking water. 2DG is a glucose analogue that blocks the glycolytic pathway, favoring a switch from glycolytic to mitochondrial ATP production. A metabolic shift towards glycolysis in PH has been observed in human and animal models, so we wanted to further investigate the possible beneficial role of this treatment outlined in Chapter IV.3. Structural, functional, and molecular comparison of PH models after treatment with EtBr and 2DG has been performed.

The main structural manifestations of PH are vascular remodeling in the lungs, increased RVSP, and consequent RV hypertrophy. These three characteristics and associated parameters were increased in our SuHx models, as shown in Figures 41-46. However, this phenotype was less evident in the hypoxic group for the EtBr cohort due to the single injection of Sugen in these animals (as we have indicated, we only used one injection since we anticipated a more severe phenotype in the animals treated with the mitochondrial DNA inhibitor). The remodeling of the pulmonary vasculature in SuHx animals was confirmed by the increase in the histological indices (percentage of medial wall and percentage of medial wall area), and by the increase in SMCs proliferation in these groups. At this phase of the disease (three weeks in hypoxia), PH is still in an early phase, and we could not detect heart failure in any of the experimental animals and groups. Our results in any case revealed then that treatments with EtBr and 2DG affected the main structural PH phenotypes in opposite directions, more severely in animals treated with EtBr. We could also see the difference in SuHx animals after a single or a triple injection of Sugen.

Treatment with 2DG

Interestingly, as observed in rats, hemodynamic, vascular remodeling and function parameters measured by MRI indicate that 2DG treatment improved the PH phenotype in male mice after the glycolytic inhibition treatment with this glucose derivative (see Figures 41D, 42F and 45G-J, respectively). REDVi and Fulton Index, indicators of RV hypertrophy, were significantly reduced in the animals exposed to 2DG (see Figure 45).

To determine the metabolic shift, we also wanted to confirm the impact of 2DG treatment at the molecular level, including ^{18}F-FDG imaging. Previous results show that structural changes, the most prominent manifestations of PH, are normally accompanied by metabolic adaptations, mainly related to energy metabolism changes [101]. The metabolic change characteristic of PH is linked to a glycolytic shift [73] in both the lung (vascular cell status and vascular remodeling) and RV cardiomyocytes. These metabolic shifts can accelerate molecular alterations and stress the development of the pathology by promoting vascular and ventricular remodeling. Hence,

we focused on determining our models' metabolic state associated with the mitochondria's functional status.

Despite the observed increase in some of the glycolytic enzymes measured by qPCR in the lungs, our PET results showed a similar ^{18}F-FDG uptake in the different groups. The data for the lungs probably showed that ^{18}F-FDG is not sensitive enough to determine changes in glucose metabolism at early PH stages in this heterogeneous organ, neither due to the typical SuHx model nor in the group after treatment with 2DG (see Figure 47F). The lung is a very heterogenous organ with low tissue density and small mean SUV values. However, approaching the molecular expression of glycolytic enzymes increased the expression of *hk1* and *slc2a1* in the SuHx groups (see Figure 50). We recently observed this metabolic shift in the same animal model through HIF-1 [89], showing that the metabolic alteration typical of PH has occurred in these mice. Both the upregulation of *slc2a1* expression by hypoxia through HIF-1 [221] and the upregulation of HK in the lung tissue of PH animal models [71] are in concordance with previous reports.

Regarding the heart, we found an increased glucose uptake in the left and right ventricles of all hypoxic groups (see Figure 47G, H). Our data are consistent with previous observations by other authors and us with this model in the RV. Most of this bibliography has limited the discussion and provides data only on the RV and the hypertrophic adaptation of the RV as a consequence of the increased pulmonary vascular resistance [89], [94], [95]. As far as we know, nobody has described the increased ^{18}F-FDG uptake in the LV in this model or humans. Moreover, the increased expression of certain enzymes related to the glycolytic pathway in the heart of the SuHx groups supports PET results.

Treatment with EtBr

The hemodynamics measurements in the animal treated with the mitochondrial DNA inhibitor (see Figure 41) demonstrated a higher RVSP. The number of animals included in the study did not allow us to apply statistics and differentiate treated and untreated SuHx animals. However, we observed an increased trend related to a more severe PH phenotype. Furthermore, as expected, treatment with this agent did worsen RV functional parameters measured by CMR (see Figure 44) compared to control and untreated hypoxic animals. Untreated hypoxic animals also showed less RV remodeling than the similar group Sugen (for instance, compare REDVi in figures 44G and 45G). As observed in Figures 44G-J, some of these functional parameters increased with the treatment with EtBr.

Similar to the animals treated with 2DG, all the groups in this study did not display differences in the ^{18}F-FDG lung uptake (Figure 47B). Of note, despite a single Sugen IP administration, EtBr-treated animals showed statistically significant glucose uptake increases in LV and RV of the SuHx groups, and these glucose uptakes were significantly higher after EtBr treatment in the hypoxic groups. The increase in LV and RV glucose uptake of the hypoxic animals treated with the DNA inhibitor compared to the untreated hypoxic animals are consistent with the higher

severity of the PH phenotype after this treatment observed by hemodynamics and by MRI. Consequently, all imaging-derived functional, structural, and molecular parameters converge in worsening the PH phenotype after EtBr treatment and the role of mitochondria in the evolution of this disease.

To evaluate this phenotype and metabolic shift, ^{11}C-Choline PET was introduced to determine its value as a biomarker of cell proliferation. The results with this radiotracer do not support its use to identify proliferative phenotypes in PH due to the low lung uptake in small animals.

Consequences of treatment with EtBr and 2DG in mitochondria

In this chapter, we have investigated the role of mitochondrial homeostasis in PH. We have included a comprehensive evaluation of this organelle by immunofluorescence and TEM imaging in normoxic and hypoxic animals after treating them with agents that impair or enhance mitochondrial function.

The results with Tom20 for immunofluorescence, a marker related to the mitochondrial membrane and usually employed to determine mitochondria mass, confirmed that mitochondrial density was lower in the SuHx groups in the lung and heart sections. As expected, in EtBr animals, we observed a higher reduction in this signal, while 2DG tended to reverse it (see Figure 51).

Our TEM ultrastructure mitochondrial analysis results are very limited and will require additional experiments. These data are essential to understand our functional and molecular results since the morphology of the mitochondria can be related to their function [222]. During this thesis, we have optimized the fixation protocols and evaluation of these organelles by TEM, first done in our institution. For this reason, we could not dedicate many animals to the study until these protocols were finally acceptable. Unfortunately, only one animal from each group could be finally assigned to TEM (the protocol requires the exclusive use of the samples for this procedure), and we were unable to obtain data from 2DG-treated animals comparable to those from EtBr-treated mice. Although very preliminary to provide conclusions, these mitochondria from the EtBr treated groups, especially those from the SuHx-EtBr group, appeared strongly altered in structure and density.

Conclusion

EtBr treatment exacerbates the main biomarkers of the disease determined by hemodynamics, vascular remodeling, and RV hypertrophy. We also observed an increased ^{18}F-FDG uptake in the right and left heart without altering uptake in the lungs.

The 2DG-treated mice in hypoxia showed a significant improvement in cardiac functions and beneficial effects on hemodynamic parameters and pulmonary vascular remodeling. These changes were accompanied by the reversion of some cardiac functional MRI parameters and the metabolic change in the RV measured by a lower uptake of ^{18}F-FDG. This might be explained since the qPCR analysis was performed in all the heart, and the PET analysis was performed in

each ventricle separately. A proteomic study will help to elucidate the nature of the effects of 2DG, as was done in Chapter IV.3 in rats. Due to technical reasons and the limited number of animals, we were unable to characterize the state of the mitochondria after treatment with 2DG by TEM, a point of great interest and high priority in future studies.

Several improvements can be incorporated into the subsequent studies. One is to evaluate the effect on different sex (males and females), and the second is to use different concentrations and administration protocols (e.g., continuous vs discontinuous administration, such as observed in our group with healthy aging animals). It is also possible that we will prolong the stay in hypoxia (for weeks) or use multi-injections of Sugen in EtBr studies to induce a more severe PH phenotype, developing heart failure. Thus, we can improve the evaluation of mitochondrial biogenesis in the development/therapy of PH.

IV.5 Role of USP11 in the development of PH

IV.5.1 Rationale

As already outlined in the introduction, hypoxia is a critical mechanism in developing PH. The central orchestrator of the response to hypoxia is HIF [98]. HIF is tightly controlled post-transcriptionally [98]. Through the intervention of this post-transcriptional modulation, HIF activity can be regulated, thus adapting cellular response to hypoxia. Ubiquitination is a relevant process in HIF regulation and signaling mechanisms. Connected to this process, USP11 is a deubiquitinating enzyme recently discovered to stabilize *HIF-1α* mRNA [132].

We conducted a preliminary study by maintaining USP11 knockout mice (*Usp11*$^{-/-}$) under chronic hypoxia. Results revealed beneficial effects on the development of the PH-associated phenotype in the lung and heart, opening the doors to study the implications of the suppression of USP11 in the development of PH.

In this chapter, we have exposed *Usp11*$^{-/-}$ female and male mice to hypoxia, with a second hit with Sugen to exacerbate the vascular remodeling, to elucidate the effects of USP11 genetic inhibition on the PH development in these animals.

IV.5.2 Results

Preliminary results of WT and Usp11$^{-/-}$ mice in hypoxia

In a first approach to study the response of *Usp11$^{-/-}$* mice to hypoxia, we kept female and male mice in the hypoxia chamber for three weeks with WT controls. In this first experiment, we did not add any injection of the VEGF receptor inhibitor since we did not have any clue of the response to chronic hypoxia of these animals. After the three weeks of hypoxia exposure, the animals were apparently in good health. The results of parameters related to right ventricular hypertrophy, pulmonary vascular remodeling and weight gain are presented in Figure 53, compared to their respective controls in normoxia.
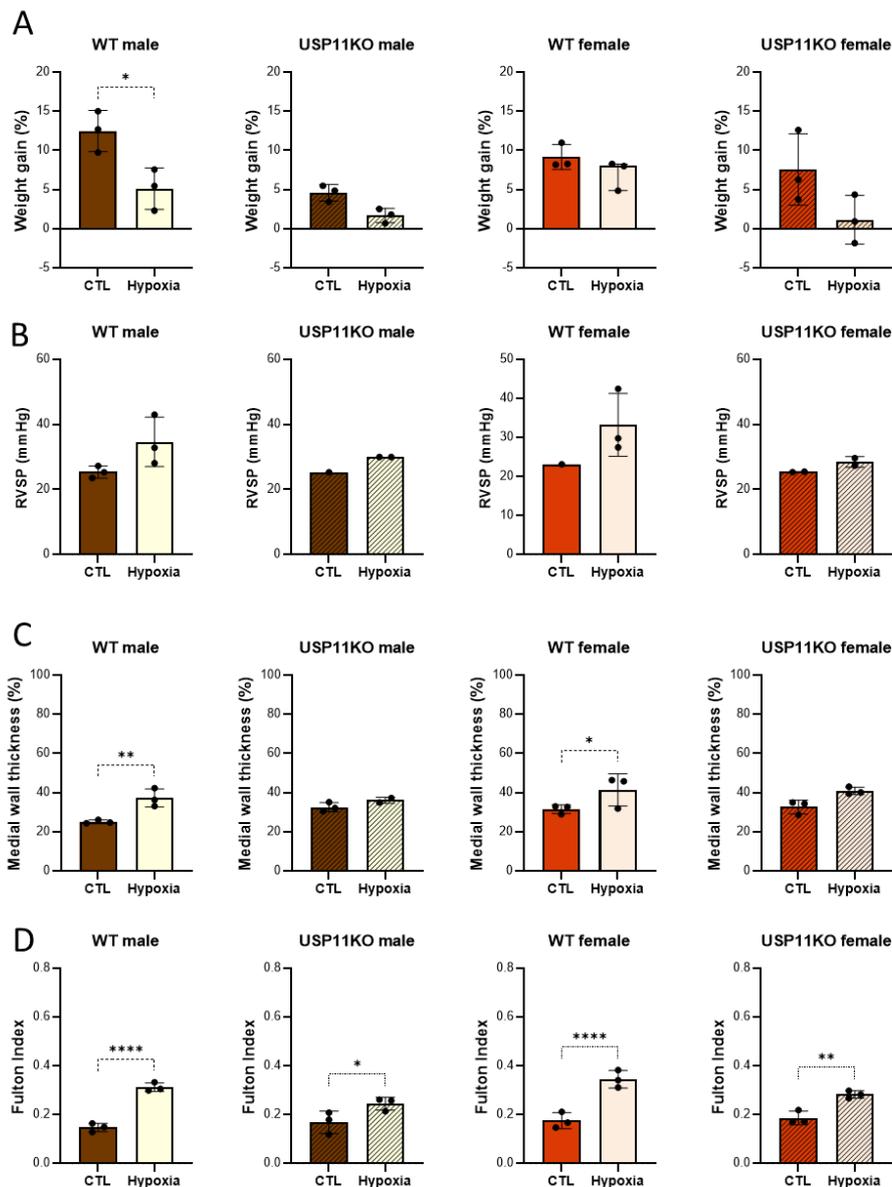
Figure 53. Preliminary results of *Usp11$^{-/-}$* mice after three weeks chronic hypoxia exposure. (A) Graphic representation of the body weight variation throughout the experimental approach. (B) Plots of hemodynamic quantification of RVSP. (C) Quantitative analysis of the pulmonary vascular remodeling medial wall thickness. (D) Fulton index measurement. . CTL: control or normoxia groups. WT: wild-type mice. USP11KO: USP11 knock-out mice.

The results of hemodynamic values (Figure 53B), vascular remodeling in the lungs (Figure 53C), as well as RV hypertrophy (Figure 53D), showed some protection in *Usp11*^{-/-} mice. Due to the mild conditions and for comparison with other results, we decided to exacerbate the phenotype in the hypoxia model with the second hit of Sugen.

Health status of WT and Usp11^{-/-} mice

We repeated the experiment with the SuHx model and added controls in normoxia. During the experiment, the mice were checked daily to monitor their health. No significant alterations in behavior or physical appearance were found, and the mice remained healthy (Figure 54). As expected, the females were smaller than the males and had a lower weight. There were no casualties during the experiment.
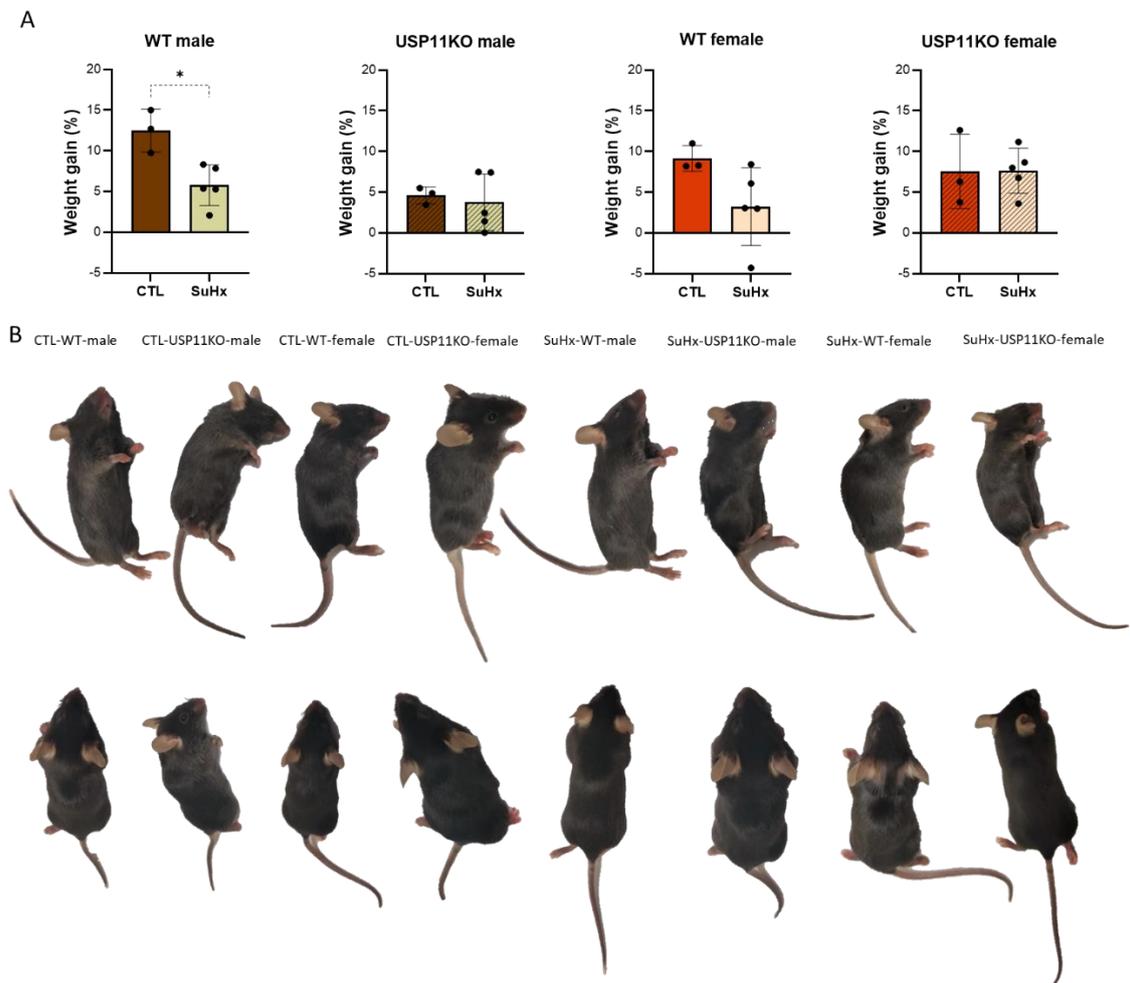
Figure 54. Tracking animal health status. (A) Graphic representation of the body weight variation throughout the experimental approach. (B) Representative images of one mouse from each group in a lateral recumbent position (top) and prone position (bottom). Values are presented as mean ± SD, *p-value < 0.05, assessed by the One-way ANOVA test. SuHx: Hypoxia + Su5412 IP treatment.

We monitored weight gain by taking advantage of the weekly cage change and IP injection of Sugen/vehicle (max. of 30 minutes – 1 h out of the hypoxia workstation). Mice increased their weight from the beginning of the experiment until sacrifice, except for one of the animals of the SuHx WT female group. In WT mice, the SuHx groups generally presented a smaller weight gain than their respective CTL, which was statistically significant in the case of males. This is an effect usually observed in this mice model. Of notice, *Usp11*$^{-/-}$ groups maintained comparable weight gain in the CTL and SuHx groups.

Hemodynamics and pulmonary vasculature remodeling changes associated with the inhibition of USP11

We measured RVSP for the final characterization of the PH phenotype. The increase in RVSP values in the SuHx groups was evident (Figure 55), except in the case of *Usp11*$^{-/-}$ females, which only presented slightly higher values than *Usp11*$^{-/-}$ CTL females.
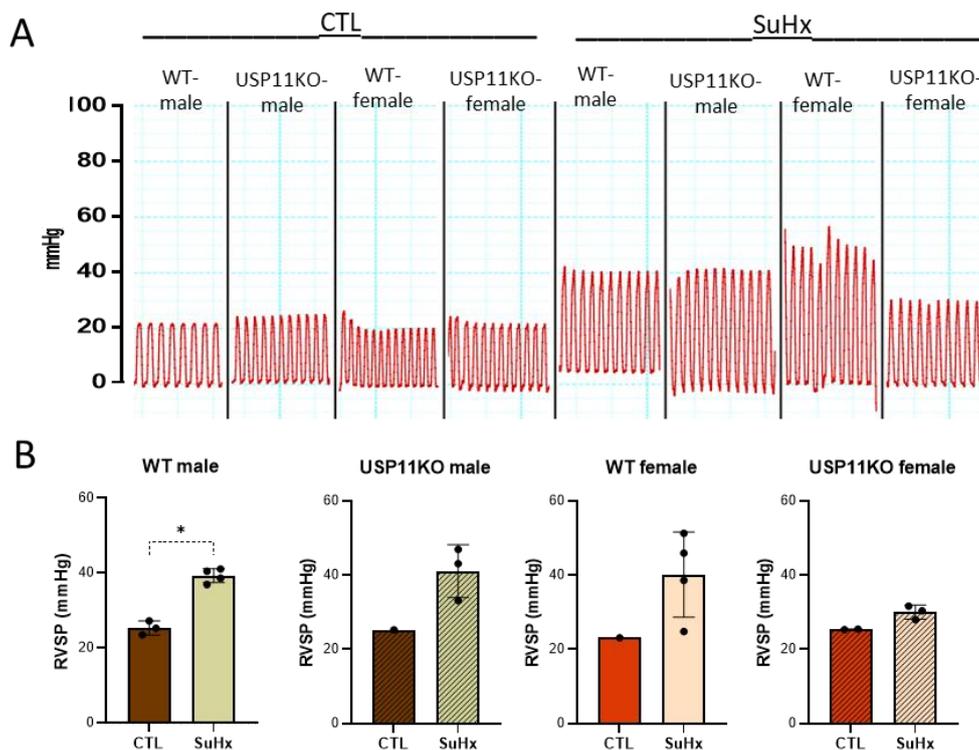
Figure 55. Tracking the RV hemodynamics. (A) Images of the invasive RVSP measurement curves of each group at the end of the treatment. (B) Quantitative analysis of RVSP. Values are presented as mean ± SD, *p-value < 0.05 assessed by the One-way ANOVA test.

Additionally, vascular remodeling determined by histopathology (Figure 56A) was evident in both male and female SuHx WT mice. Moreover, the increase in the medial wall thickness (Figure 56B) and the medial wall area (Figure 56C) was similarly reported. However, in *Usp11*$^{-/-}$ mice,

although the same trend was observed in the male SuHx group, the differences were no longer detected in the case of the female mice.
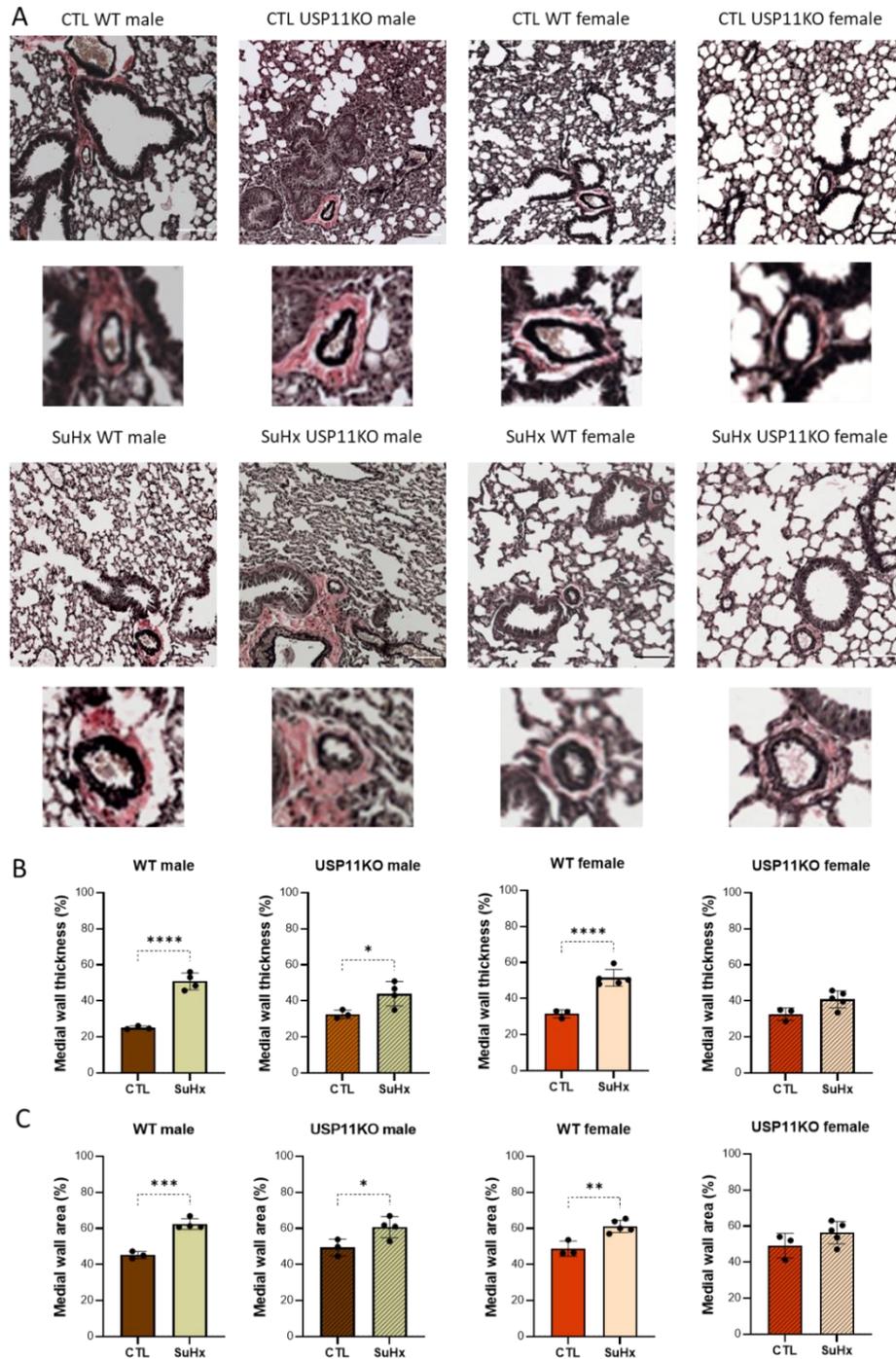
Figure 56. Assessment of pulmonary vascular remodeling. (A) Representative photomicrographs of the elastic staining of the whole lung (upper panel) and a representative pulmonary arterial (bottom panel) for each lung section. Scale bars are 100 µm. Quantitative analysis of the pulmonary vascular remodeling (B) medial wall thickness and (C) medial wall area). Values are presented as mean ± SD, *p-value < 0.05, **p-value < 0.01, ***p-value < 0.001, ****p-value < 0.0001 assessed by the One-way ANOVA test.

Cardiac function by MRI

MRI of the heart was used to gain insight into RV adaptation to hypoxic conditions and the subsequent increase of pulmonary vascular flow resistance. We estimated the ventricular volumes and the mass of the LV and RV. Using these data, we calculated the functional cardiac parameters (LEDVi, LESVi, LSVi, REDVi, RESVi, RSVi, and Fulton Index) similarly to what was done in previous chapters.

We found no alterations in LV parameters in any of the groups (see Annex, Figure 68), suggesting a preserved function of this ventricle.

Regarding RV, an increase in EDVi and ESVi (Figure 57A, B) was observed in the SuHx groups. This increase reached statistical significance in all groups except EDVi for the $Usp11^{-/-}$ female mice and ESVi for the group of WT males. As shown in Figure 57E, Fulton Index was significantly augmented in all SuHx groups, including the $Usp11^{-/-}$ female mice, indicating ventricular wall hypertrophy characteristic of this model.
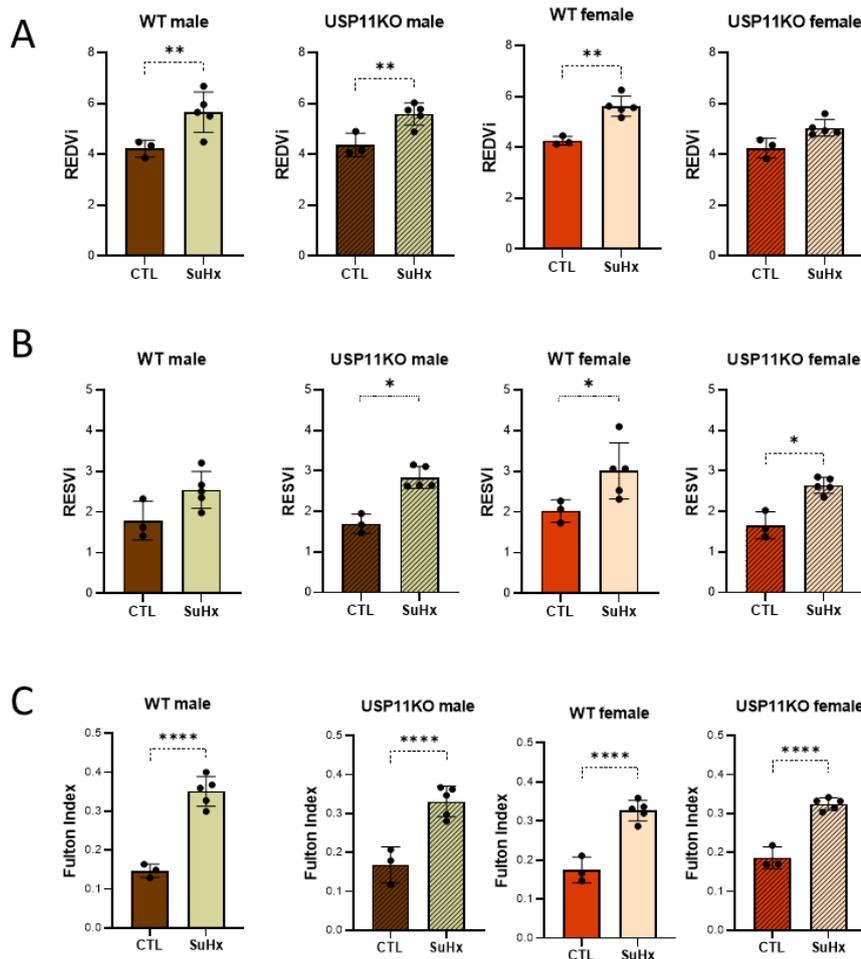
Figure 57. Analysis of RV remodeling from MRI images. Main functional parameters obtained from the analysis of the endocardial volume throughout the cardiac cycle: (A) Right ventricular end-diastolic volume index (EDVi), (B) Right ventricular stroke volume index (SVi), and (D) Fulton index. Values are presented as mean ± SD, *p-value < 0.05, **p-value < 0.01, ****p-value < 0.0001 assessed by the One-way ANOVA test.

As in previous chapters, PER/EDV and PFR/EDV, systolic and diastolic function parameters, respectively, were calculated from the curves of the time derivative of the ventricular volume. The results reveal the absence of significant systolic and diastolic alterations in any group, which is why we have not included them in this section. These parameters are represented in the Annex.

Imaging glucose metabolism

Alterations in glucose metabolism in the lung and heart were explored by ^{18}F-FDG PET *in vivo* analysis .
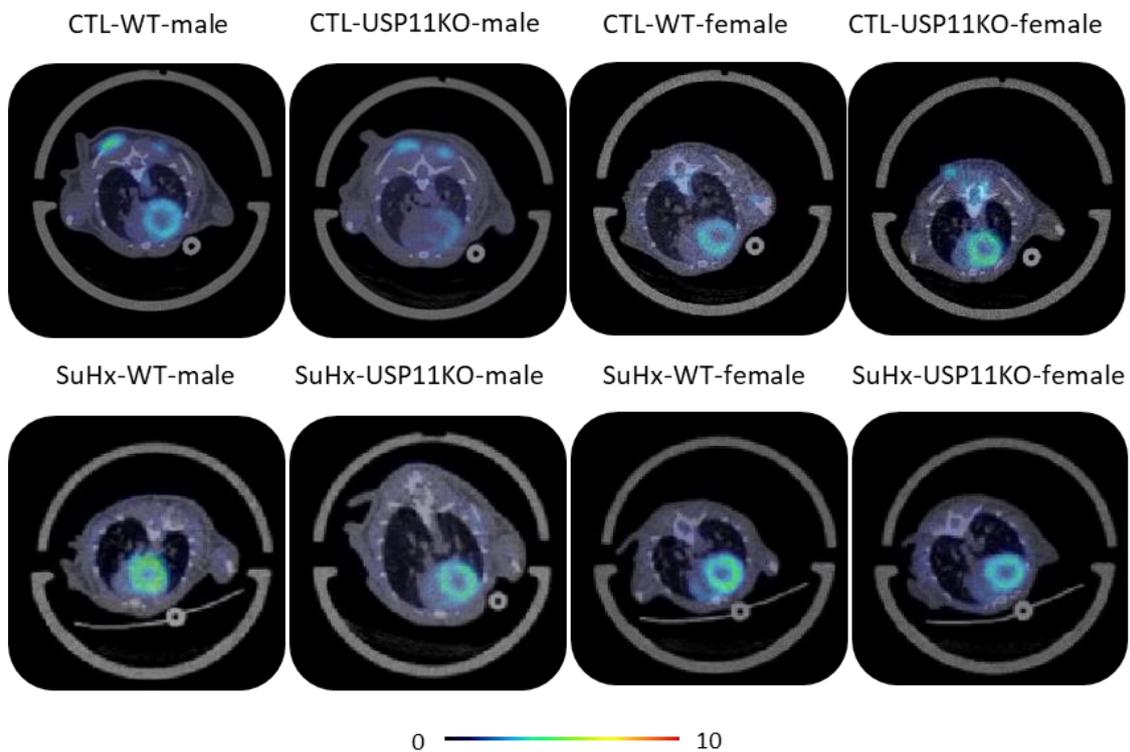
Figure 58. Representative images of the radiotracer (^{18}F-FDG) distribution in lungs and heart for each group. Overlay illustration of a representative image of the three-dimensional reconstructions of CT (MIP, gray scale) and PET (color scale represented over the images) images, transversal plane.

Representative axial images of the lungs and heart from each group are shown in Figure 58. From the quantification of these images, we observed, similar to the observations of the previous chapter, that lung ^{18}F-FDG SUV (Figure 59) did not change between groups.
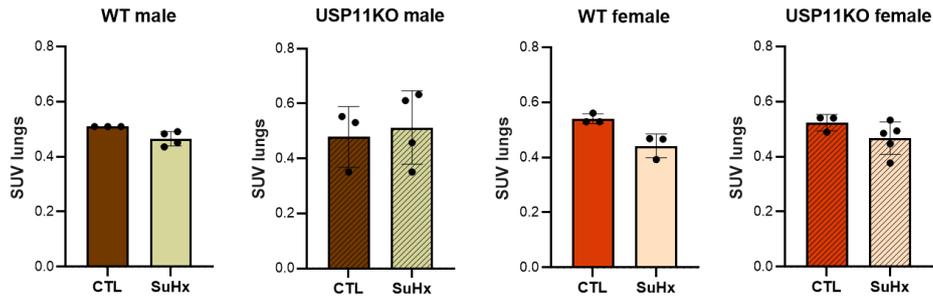
Figure 59. ¹⁸F-FDG uptake in the lungs measured by PET imaging. Quantification of the SUV ¹⁸F-FDG uptake in lungs. Data represents the mean ± SD assessed by the One-way ANOVA test. SUV: standardized uptake value.

In the heart, a tendency to increase ¹⁸F-FDG uptake after hypoxia exposure was observed in all groups, statistically significant increase in SuHx *Usp11*$^{-/-}$ male animals, both in the LV (Figure 60A) and the RV (Figure 60B).
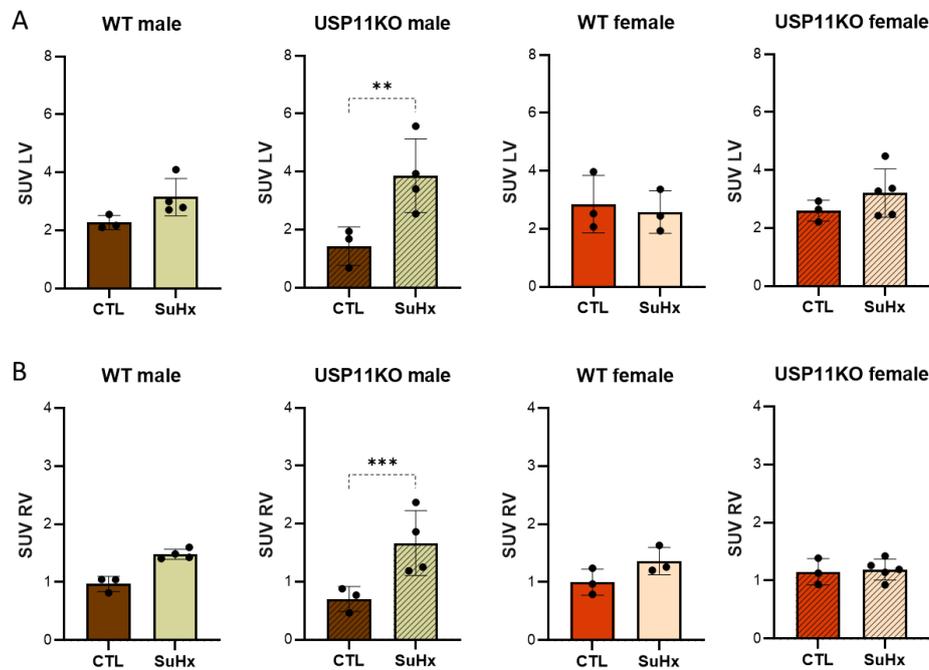
Figure 60. ¹⁸F-FDG uptake in the heart measured by PET imaging. Quantification of the SUV ¹⁸F-FDG uptake in (A) total heart, (B) left ventricle (LV), and (C) right ventricle (RV). Values are presented as mean ± SD, **p-value < 0.01, ***p-value < 0.001 assessed by the One-way ANOVA test.

IV.5.3 Discussion

In this chapter, $Usp11^{-/-}$ mice have been used to explore the effects of USP11 inhibition on the development of PH. This protein could be relevant in modulating the response to hypoxia due to its role in $HIF\text{-}1\alpha$ mRNA stabilization. $Usp11^{-/-}$ mice were fully functional. This is consistent with a study assessing cognitive function in $Usp11^{-/-}$ mice, which stated that they had normal motor activity, visual acuity, and nonspatial memory. Although the same study noted that USP11 deficiency interferes with learning profiles, memory, and anxiety [223], our mice showed no alterations in their appearance or behavior.

Characterization of PH phenotype in Usp11$^{-/-}$ mice after SuHx conditions

The mice of the SuHx groups presented alterations in the representative parameters of this model: increased RVSP, increased vascular remodeling, and altered RV cardiac parameters, specifically increased EDVi and ESVi, as well as Fulton Index.

We found different degrees of development of the PH pathology depending on the group.

In the male groups, both WT and $Usp11^{-/-}$ SuHx mice resembled the early PH phenotype, only differentiated in that the WT group achieved higher values of vascular remodeling and RVSP, while the $Usp11^{-/-}$ mice presented greater cardiac dysfunctional parameters, characterized by a higher increase in ESVi.

In the group of females, we found a significant increase in the percentage of medial wall thickness, medial wall area, and EDVi in the SuHx WT group. Female $Usp11^{-/-}$ mice showed a minor increase in all these parameters, indicating that female Usp11$^{-/-}$ mice could be protected against the development of PH (remodeling of the pulmonary vasculature, RVSP, and RV hypertrophy).

Absence of evident metabolic alterations in the heart associated with the inhibition of USP11

Analogous to what we observed in the previous chapters, ^{18}F-FDG uptake in lungs did not present significant differences in any of the groups pointing to the lack of detectable alterations in the glucose metabolism.

Regarding the heart, ^{18}F-FDG uptake tended to increase in both ventricles of SuHx male mice, significantly higher in the SuHx $Usp11^{-/-}$ male group. However, this higher tendency was not present in female groups, suggesting a different metabolic adaptation in these animals to hypoxia.

Sexual dimorphism associated SuHx mice model and USP11 inhibition

Interestingly, we have found disparities in the manifestation of PH between females and males in the $Usp11^{-/-}$ mouse model. As mentioned in the introduction, PH in humans is more prevalent in females, though the prognosis is worse in males [24].

Figure 61 shows the individualized results of MRI and ^{18}F-FDG imaging biomarkers in each group. A similar trend in all animals and groups allows us to think of a possible correlation of these two biomarkers at least in the RV, probably relating hypertrophy and higher glucose uptake. Figure 61 also highlights the apparent protection of *Usp11*$^{-/-}$ females to the development of the typical PH phenotype. Note that there is no separation between groups in this case.
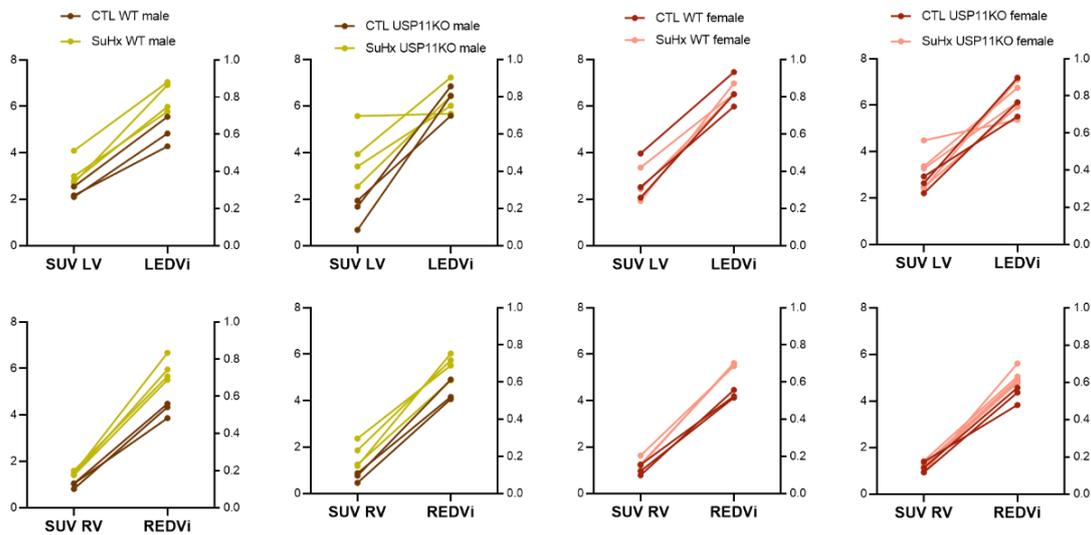
Figure 61. Left and right ventricular hypertrophy relation with ^{18}F-FDG uptake. Graphical representation of relation between ^{18}F-FDG uptake and EDVi of the LV (up) and of the RV (down), for each group.

The protective role of USP11 inhibition against the development of the PH phenotype found in female mice is in line with a recent study with a *Usp11*$^{-/-}$ tauopathy mouse model, with protection found preferentially in females [224]. This study also demonstrates sexual dimorphism in USP11 expression in the brain, with higher levels in female patients and mice than in their male referents. Interesting notes are that USP11 resides on the X chromosome in both humans and rodents, and that, only in male *Usp11*$^{-/-}$ mice, genetic deletion of USP11 triggered significant genetic compensation through positive regulation of related USPs. This may shed light on the sex-dependent effects of USP11 deletion.

Furthermore, significant differences between men and women have been reported in gene expression for cardiac adaptations to hypoxia [225]. Sex-associated disparities in HIF-1α expression may produce variations in response to hypoxia [226]. Pulmonary artery SMCs obtained from female patients showed higher levels of HIF-1α than in male patients [226]. In addition, in a rat model of myocardial ischemia due to coronary ligation, superior HIF-1α levels in the heart were reported in females at baseline and 24 h after induction [227]. Higher levels of HIF-1α in females may contribute to the increased susceptibility to developing PH and, in turn to greater protection in the *Usp11*$^{-/-}$ mice.

USP11 mechanism behind the beneficial effects against the development of PH

Our results highlight USP11 as a relevant piece in the underlying machinery PH. Recently, a study focused on prolyl hydroxylase domain-2 (PHD2) has highlighted the relevance of modifying HIF stability in mice [228]. PHD2 is the major responsible for HIF-α hydroxylation and subsequent inactivation and shows an antagonistic role to USP11. Inducible deletions of PHD2 in ECs in normoxia produced a progressive elevation in pulmonary artery pressure, pulmonary interstitial fibrosis, and compensatory RV hypertrophy without structural remodeling of the pulmonary arteries. In SMCs, PHD2 deficiency causes an elevation in RV pressure not associated with lung pathologies [228]. In line with our results, this indicates that HIF stability can modulate the PH-associated phenotype. Otherwise, USP11 deficiency mitigated pulmonary fibrosis in mice exposed to X-ray irradiation [229]. It has been reported that USP11 promotes TGFβ1 signaling through TβRII stabilization and may, also in this way, contribute to the pathogenesis of pulmonary fibrosis [229], [230]. Further studies are required in order to clarify the relevance of the USP11/HIF axis in PH development.

Conclusion

The inhibition of USP11 offers protection against the development of the phenotype associated with PH in the case of female mice. Additional studies are needed to determine the underlying mechanisms and clarify the nature of this beneficial effect.

GENERAL DISCUSSION

V) General discussion

Throughout this thesis, the influence of different factors in the development of the phenotype associated with PH (lungs and heart) has been explored. In particular, we have analyzed the impact of voluntary physical activity, the manipulation of mitochondrial content with chemical agents, and the modulation of the hypoxia response using the *usp11* KO mice. Moreover, we have evaluated the inflammatory profile of two different PH models using a newly developed PET probe to target neutrophils.

In vivo imaging techniques and hemodynamic measurements have been combined with histological and molecular biology techniques to confirm the diagnosis of the PH phenotype and understand the underlying molecular mechanisms. This comprehensive and complete study is not common in PH literature, so we think this thesis can be very valuable in identifying and characterizing different endophenotypes of the disease in relation to different environmental factors.

To complete the specific discussion included in each chapter, in this section, we aim to make a global assessment of the whole study.

V.1 Characteristics of animal models to study preclinical PH

V.1.1 PH phenotype depending on the PH induction procedure

The availability of a reliable animal model that resembles the characteristics of the human disease is an essential starting point for the preclinical study of PH. Nowadays, rodents are the most used animals in the field, as they are small, easy to maintain and breed, and are amenable to genetic manipulations [231]. In this thesis, two PH models have been used in rats, MCT and SuHx, and one in mice, SuHx, and a genetic model to investigate the role of USP11. Each model shows a specific pathological profile and exciting differences in males and females.

The MCT rat model is one of the first and best understood models of experimental PH [231]. A single exposure of rats to 60-100 mg/kg MCT reliably results in PH and death of animals within three and six-eight weeks, respectively [162]. In general, our rats (Chapter IV.2) developed a milder PH phenotype with an injection of 60 mg/kg after three weeks of exposure to this toxin. MCT model recapitulates many features of human PH, in particular PAH, and shows clear increase on mean pulmonary artery pressures [162], and muscle content [232]. Our data showed an increased RVSP and vascular remodeling, RV hypertrophy, and augmented ^{18}F-FDG heart uptake. Our results further highlight the presence of significant neutrophil recruitment in the MCT rats. The main limitation of this model is that it does not recapitulate vascular occlusions and is concurrent with many and complexes lesions affecting the vasculature and epithelium [233], and hepatic venous dysfunction [232]. Three weeks after treatment with MCT, we have detected substantial heterogeneity among subjects in our group, with significant differences according to disease severity. This heterogeneity has been also described in previous examples and was explained by the development of LV myocarditis and significant inflammatory infiltration [184]. We did not observe this particular inflammatory lesion in our histopathological samples. However, from our experience with this model, most of the histopathological observations in the lung are closer to adult respiratory distress syndrome than PAH [233], so the results in relation to PH need to be taken with extreme caution. The lungs showed the presence of Clara cells in the lumen of bronchioles and a small number of erythrocytes and macrophages in the alveoli. They also showed focal destruction of alveoli with signs of focal congestion in the right lung with a more pronounced alveolar macrophage infiltration. In some regions of different animals, we also observed (mainly in basal region of the middle segment of the right lung) the presence of small vessels with evidence of platelet and fibrin thromboembolism. This has been previously described by other authors [233].
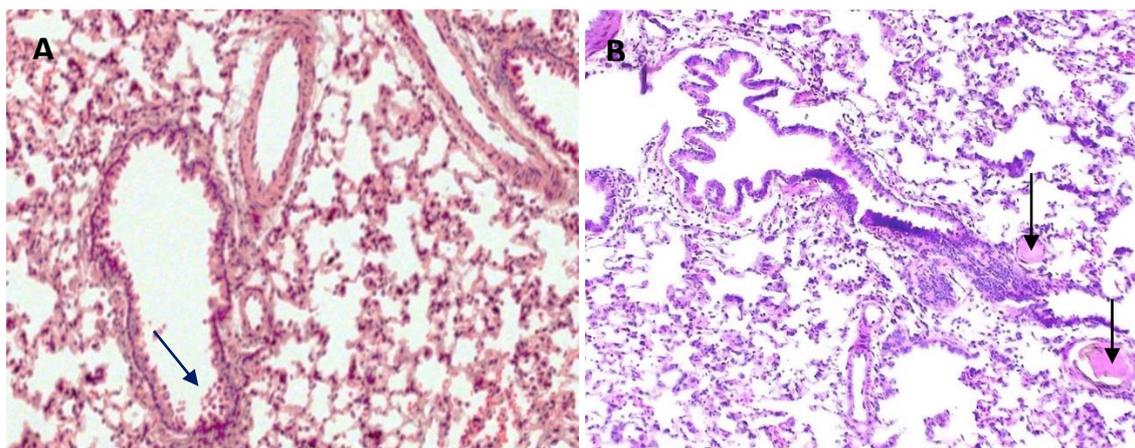
Figure 62. Preliminary results Hematoxylin-Eosin histopathological evaluation of left lung in the MCT model. Images are displayed with x20 augments. (A) Arrow points to secretory Clara cells. (B) The hematoxylin and eosin slice shows the presence of thromboembolic lesions in the pulmonary vasculature.

Another PH model classically used in rats and mice is the chronic hypoxia model. With the hypoxia exposure times used in our case, this is a model for the mild or early PH stage of group I [234], and is more severe in rats than mice. Three weeks of exposure to moderate hypoxia (10% O_2) elevates pulmonary vascular resistance and causes RV hypertrophy. The pulmonary arteries develop medial hypertrophy, but there is minimal evidence of vascular obstruction and no intimal fibrosis or plexiform lesions. In hypoxia models, the proliferation of adventitial fibroblast appears, as well as the distal extension of PASMCs and thickening of the pulmonary artery wall. Upon removal from hypoxia, the histological changes are slowly reversible [162]. In the search for an alternative that more accurately resembles human PH, we added a second hit: Sugen. Sugen blocks VEGF receptor 1, a critical modulator of endothelial signaling and angiogenesis. This receptor's inhibition initially causes EC apoptosis, and together with the hypoxia, triggers a more aggressive and apoptosis-resistant EC phenotype [231], [232]. The SuHx model, which arises as the combination of hypoxia with the injection of Sugen, recapitulates more faithfully the human pathology [231]. This model, in rats, was used in chapters IV.2 and IV.3. As expected, SuHx animals presented more advanced stages of PH than MCT, with higher RVSP, thickening of the pulmonary vessel walls, and a more severe RV hypertrophy phenotype. The importance of Sugen in the development of the disease has been seen in Chapter IV.4, by comparing SuHx groups after one or three shots of this VEGF receptor 1 inhibitor in combination with a mitochondrial DNA depletion agent.

A factor intrinsically related to the animal model is the species used since there are dissimilarities in the development of PH between different rodents. Therefore, this is the next point to be addressed.

V.1.2 Degree of PH development according to the species, rat or mouse

It is well known that PH models do not develop equally in rats and mice. The study of rats is simpler due to their specific physiological characteristics and, in general, to larger vessel sizes and ease of surgical procedures.

In the case of the MCT-induced model, despite strong effects in rats, PH does not develop in mice similarly. It has been hypothesized that mice metabolize MCT differently in the liver, although this is still not clear since some studies used the theoretical active pyrrolic derivative with varied results [235]. For this reason, the MCT model is mainly described and used in rats (Chapter IV.2). This model was demonstrated in mice after several injections of MCT but was associated with pulmonary fibrosis.

Likewise, in rats, SuHx standard protocol is commonly generated by a single injection of Sugen combined with three weeks of hypoxia (10% O_2) and followed by returning to normoxia for 1-2 weeks. The induced PH in this model is irreversible, and more extended periods in normoxia aggravate the pathology [162]. In this rat model, PH is severe and is accompanied by plexiform lesions, RV failure with reduced cardiac output, increased RV diastolic diameter, capillary rarefaction, RV fibrosis, and cardiomyocyte apoptosis [236]. Our results indicated that after three weeks of hypoxia and one week of normoxia, a severe PH phenotype was generated, but RV failure did not occur. In addition, there was a significant difference within the groups and, as in the MCT model, plexiform lesions were not detected in the animals. In the case of the mouse SuHx approach, mice require multiple (weekly) injections of Sugen. The murine model exhibits less severe vascular injuries, hemodynamic changes, and RV hypertrophy than the rat counterpart. Mice models reproduce neither obstructive nor plexogenic lesions detected in clinical PH [231]. The main reason for repeated injections in mice, but not in rats, may be due to differences in the distribution, metabolism, and excretion of Sugen between rats and mice, with a systemic and renal clearance of Sugen being much higher in mice [236]. In this thesis, if we compare the results obtained between the groups of these models in Chapters IV.2 and IV.3 (rat) and Chapters IV.4 and IV.5 (mouse), it can be determined that, although a robust PH phenotype is produced in both cases, it was more exacerbated in rats. In the heart, greater increases in RVSP and MRI-derived parameters related to cardiac hypertrophy were obtained in rats than in mice. We could also observe the differences between a single or triple IP Sugen injection in hypoxic animals.

Physiological differences in cardiac tissue between rats and mice may likely explain the difference in responses to the SuHx model. These differences are mainly characterized by a different proportion of fibroblasts and cardiomyocytes and the expression pattern of cytochrome P-450 [236]. The model mimicking the protocol in rats was followed in Chapter IV.1 and the EtBr cohort in Chapter IV.4 to protect the integrity of the mice. This mouse model denotes a milder PH phenotype. All our results reflect this slighter pathology, with less pronounced values of the main PH functional and morphological markers used in this thesis.

PH models in rats generate severe and sometimes dysfunctional RV hypertrophy. On the contrary, in mice, augmented RVSP and Fulton Index do not appear together, but rather increases in RVSP or Fulton Index have been reported, depending on the model and conditions [236]. In this thesis, although a positive correlation between RVSP and the Fulton Index was largely observed, in Chapter IV.5 a certain decoupling between these two parameters was appreciated. The increase in RVSP presented different degrees within the different groups, being very small in the case of $Usp11^{-/-}$ females.

V.1.3 Differences in the development of PH associated with the sex

Furthermore, sex is a relevant factor affecting the frequency, prognosis, and pathology of PH. As mentioned in the introduction, epidemiological data reveal a predominance in women but a worse prognosis and higher mortality in men [24]. In general, females have better RV systolic function, with higher RV EF, lower RV mass, and smaller RV volumes [234]. These data indeed account for the increased survival and heart failure prevention in women. No animal model faithfully recapitulates human disease and captures the differences between males and females [237]. As seen with the $Usp11^{-/-}$ model, our results support the paradoxically increased male susceptibility reported in classical animal models of PAH [238].

As a standard protocol that was being used in the laboratory, we used female rats and male mice, although due to the results obtained in this thesis, new experiments are ongoing to evaluate deeply these differences between sexes. When we compared to other results previously described in the literature, we conclude that sex must be one of the essential variables of any study in PH. For that reason, the last experiment presented in chapter IV.5, we included both sexes to evaluate the differences in PH development. Notably, the results revealed a marked sexual dimorphism, clearly indicating the importance of taking into account the influence of sex on these results.

Sex hormones are important factors that explain this sexual dimorphism. If we look for information about sexual dimorphism in PH in the literature, the influence of estrogens on heart-lung function is widely recognized. This impact is important in the case of PAH and is known as the "estrogen paradox" [234]. Estrogens are postulated to cause both the female bias and the better survival of women with PAH. On the one hand, the estrogens and their receptors, which are synthesized in the PASMCs of women, cause a localized proliferation of these cells [237]. On the other hand, estrogens protect against RV hypertrophy, slow the progression of the disease and make it less severe by providing cardioprotection [237]. Moreover, it has been reported a decrease in the expression of estrogen receptor α in the RV of patients with PAH-induced RV failure [239]. In this thesis we noticed, as summarized in Chapter IV.4, that the estrogen receptor signaling pathway was altered after 2DG treatment in female SuHx rats. However, although estrogen signaling may potentiate the beneficial effect of 2DG on cardiac function, we discard this as the main factor since 2DG also benefits in a male mouse model. Hence, although the

involvement of estrogens is evident, their action does not fully explain the sexual dimorphism observed in PAH.

The typical cardiac adaptive response to hypoxia between females and males is another element of particular relevance to our results [225]. HIF-1α protein expression is higher in females, which may increase susceptibility to PH development [226]. HIF-1α plays a crucial role in adaptive cardiopulmonary responses, and dysfunction of the HIF-1 pathway significantly affects transcriptional regulation in the heart [225]. In Chapter IV.5, we observed enhanced sexual dimorphism in *Usp11*$^{-/-}$ mice which may be related to this increased expression of HIF-1α in females and points to sex-dependent differences in HIF-1 signaling. USP11 encoding on the X chromosome and compensatory mechanisms against USP11 inhibition in males may be other mechanisms leading to the differential effects of Chapter IV.5 in female mice [224].

V.2 Cardiopulmonary metabolism

The relevance of metabolic alterations underlying PH has been extensively highlighted through this thesis.

As stated above, it is commonly accepted that during the development of the PH, oxidative phosphorylation is reduced in favor of glycolysis [71], [73]. PET is a technique that allows an *in vivo* assessment of such a glycolytic switch. Izquierdo et al. [89] identified a wider metabolic reprogramming in the PH mouse model after three weeks of hypoxia, characterized by the increased uptake of ^{18}F-FDG. This higher ^{18}F-FDG uptake has also been observed in human patients [94], [240]. Nevertheless, some studies contradict these observations. In human lung samples from severe PAH, the metabolomic analysis describes a change in energy use with an overall decrease in glucose metabolism characterized by downregulated glycolysis [70]. In this thesis, we aimed to investigate alterations in glucose metabolism, so at the end of each protocol, we submitted all the groups to a ^{18}F-FDG study.

^{18}F-FDG uptake in the heart was analyzed in each ventricle separately. The results generally showed a greater uptake in the RV within the SuHx groups. Regarding LV, we have detected an increase in the SuHx mouse groups (Chapters IV.1, IV.4, IV.5) that did not appear in the rats (Chapters IV.2, IV.3). In the literature, we found a similar inconsistency in ^{18}F-FDG uptake in LV [89], [183]. In human patients with end-stage lung disease, ^{18}F-FDG uptake was significantly higher in RV or RV/LV ratio, but not in LV [240]. Of note, other studies noted significant heterogeneity in RV glucose uptake among participants with PH [241]. Therefore, there is a consensus about the increase in ^{18}F-FDG uptake in the RV, but the origin of the different data reported in the LV should be further studied.

Additional tests were performed in some groups to explore glucose metabolism further. In Chapter IV.3, the RV tissue was studied by proteomics. When comparing SuHx rats with controls, PET imaging can quantify increased cellular metabolism the glycolytic pathway was found to be activated, and particularly, both HK1 and HK2 were significantly increased. The isozymes HK1 [151], [242], [243] and HK2 [244] are part of the first rate-limiting enzyme in glycolysis and proved to be increased in PH models. The increase in HK and the activity of the glycolytic pathway is consistent with the ^{18}F-FDG PET uptake results.

Moreover, in the group that performed physical activity and the 2DG group (Chapters IV.1 and IV.4), we measured the expression of certain enzymes related to the glycolytic pathway by qPCR. In both groups, it seems that the expression of these enzymes tended to increase in the SuHx group, although we observed a high intra-group disparity that prevented us from establishing a detailed pattern. Nevertheless, mRNA upregulation is in line with the increase in ^{18}F-FDG uptake, and both markers point to a glycolytic shift characterized by increased glucose utilization in RV of PH animals.

In the lungs, our results in all animal groups resulted in the absence of differences in the uptake of ^{18}F-FDG, which is different to previous reports on human patients and animal models [94], [96]. In male mice ^{18}F-FDG uptake was also increased in the lung in the SuHx, and the hypoxia models [89]. However, in this study, ten weeks old mice were used, and the PET scans were taken after one hour of incorporation instead of 30 minutes. Apart from this, it is known that factors such as anesthesia can alter glucose metabolism [245]. In patients with PH, some studies indicate an increase in ^{18}F-FDG in the lungs, though there are a few caveats and missing details to further compare (e.g. the use of overnight fasting in the studies). Moreover, instead of using the SUV directly, some studies use a semi-quantitative measurement, blood-corrected SUV [94], which is challenging to perform in mice due to their small sizes. Significant variations within patients have also been reported [246]. We believe that the discrepancies could be explained by the severity of the model as we reached the early stages of PH. Probably, differences in ^{18}F-FDG uptake in the lung may only be seen in animals with more advanced disease or other coexisting inflammatory lung or heart diseases. This was not the case with our animals, except in MCT rats. Glucose metabolism can also be influenced by sex. Differences in energy metabolism have been reported between male and female mice [247], [248]. However, in our case, Chapter IV.5 shows no sex-related differences.

The results of glycolysis-related enzyme expression levels in the 2DG cohort of Chapter IV.4, which revealed increased expression of *hk1* and *slc2a1* in SuHx mice, reflect an increase in glucose utilization characteristic of the metabolic shift. This leads to thinking that the measurement and analysis protocol is not sensitive enough to detect alterations in glucose metabolism in lung tissue at this stage of the disease. Therefore, it will probably require more prolonged hypoxia exposures or additional hits to make the PH phenotype more severe.

V.2.1 Choline

^{18}F-FDG is a very general marker of inflammation, proliferation, and pathogenic processes. We wanted to look for something more specific, so we used radioactively labeled choline analogs for *in vivo* analysis by PET imaging as markers of cell proliferation and pulmonary pathology. Preliminary results of the group in MCT-induced male rats pointed to ^{11}C-Choline as a good proliferative marker in preclinical models of PH (Figure 63). We relied on these data to propose ^{11}C-Choline as a biomarker in PH.
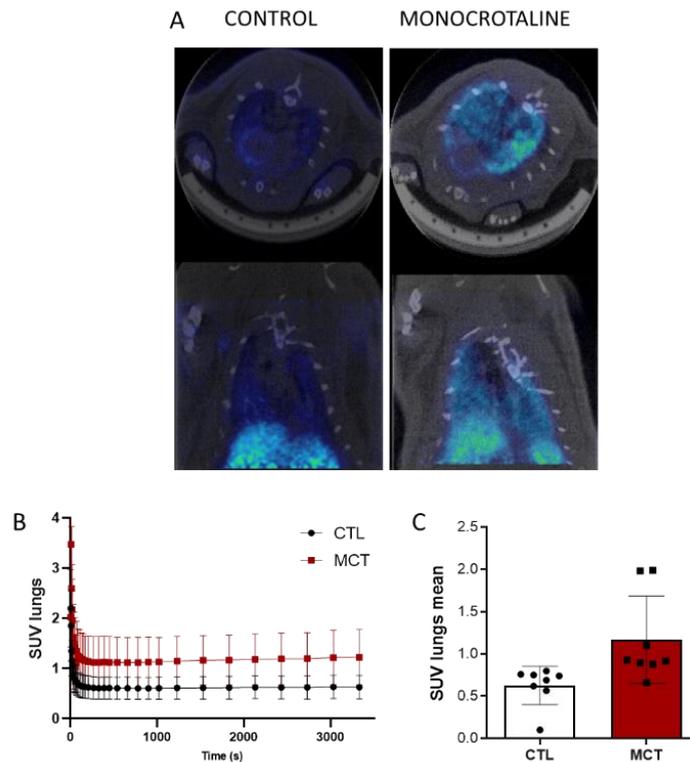
Figure 63. Preliminary results of choline uptake by PET imaging in the MCT model. (A) Reconstructed image from last frames of the dynamic PET scans of ^{11}C-Choline uptake in the lungs and heart at the time of administration. (B) Quantification of the SUV ^{11}C-Choline uptake in lungs in each frame with respect to the time. (C) SUV means in the lungs.

As the most abundant lipid in cell membranes, phosphatidylcholine is substantially required by proliferating cells to synthesize membranes. Metabolic analysis of blood and plasma samples from PH human patients found elevated choline [92] and acyl choline pathway enriched [93]. Besides, lung tissue samples from a SuHx-induced mice model of PH presented higher levels of phosphocholine and glycerophosphocholine [89]. Analogous to the results obtained with ^{18}F-FDG, the uptake in the lungs did not present differences between the different groups. It would be necessary to explore whether this is because the pulmonary metabolism of glucose and choline is not altered or to the low sensitivity of the technique or the analysis. In the heart, a slight increase in ^{11}C-Choline uptake was found in SuHx animals, reflecting that there are undoubtedly metabolic alterations related to choline metabolism underlying PH.

Therefore, the results of this thesis do not confirm ^{11}C-Choline as a specific marker of cell proliferation in PH. Future analyses will be able to clarify whether the radiotracer has a role in characterizing PH or whether, as occurred in Chapter IV.2 with the neutrophil probe, the increase in uptake is model-dependent.

In this case, we cannot conclude about the influence of species or sex, since we only performed it on male mice and, to our knowledge, there are no similar studies in other models or in patients with PH.

V.3 Open research fields

Although some of the results of the thesis are not definitive, they open the field for interesting future studies.

First, we have reported a protective effect of increased physical activity in the early stages of PH, which is associated with reducing the expression of certain glycolytic enzymes. The nature of this process needs to be further investigated, and this study must be complemented with studies including more severe PH cases.

Second, the presence of neutrophils and other inflammatory components, such as macrophages, has been evaluated in two *in vivo* PH models. In this context, this thesis has provided new tools to study further the role of inflammation in PH: unique imaging tools to monitor and to be compared with unspecific cell inflammatory tracers such as ^{18}F-FDG.

Third, the beneficial effects of 2DG in SuHx female rats have been demonstrated. Although the underlying mechanism needs to be further investigated, our data suggest a role for SIRT2-mediated rescue of energy metabolism and redox homeostasis in the process.

Fourth, the influence of two chemical agents to hinder and enhance mitochondrial activity has been analyzed and shown pernicious and beneficial responses. The thesis should be complemented with further experiments to investigate the safety and the best way of 2DG administration.

Finally, the sex-specific protective effect of USP11 inhibition against PH has been unveiled.

These last results of Chapter IV.5, which establish a relationship between USP11 and the development of PH, are noteworthy. We have continued investigating the role of USP11 in the disease. Data from transcriptomic analysis of lung tissue from PAH [249] were used to investigate USP11 expression in human samples. In line with our results, significantly higher levels were found in PAH patients, specifically in the female group. This evidence is inspiring, as it proves that the action of USP11 is not specific to the mouse model of PH but is intrinsic to the disease. Overall, the protective effect exerted by USP11 deletion, enhanced in female mice, and the increased levels of this protein in the lung tissue of female patients, supports USP11 as a promising therapeutic target.

CONCLUSIONS

VI) Conclusions

1) Early physical activity in the context of PH produces adaptations in energy metabolism and protects against remodeling of the pulmonary vasculature and cardiac fibrosis, possibly by a metabolically-related delaying RV cellular maladaptation to a permanent increase in ventricular afterloads.

2) ^{68}Ga-IONP-citrate-cFLF is able to detect the presence of neutrophils *in vivo* and therefore, we have identified a novel and interesting nanoparticle-based probe for molecular imaging that will facilitate the study of the role of neutrophilic inflammation in PH.

3) Treatment with 2DG in a female rat SuHx model attenuates pulmonary vascular remodeling and PH associated biomarkers in the RV, possibly through preservation of myocardial energy metabolism and redox homeostasis. Changes in the expression of SIRT2, a central effector in metabolism and redox systems, have been identified and will be studied in more depth.

4) Chemical alterations of mitochondria function with EtBr and 2DG treatments impact on major markers of PH in a male mouse model. EtBr produces damage to mitochondria that negatively impacts PH development. 2DG suggests some protection, but fails to reproduce the effects observed in female rats.

5) Genetic inhibition of USP11 preferentially protects females against the development of the PH-associate phenotype.

ANNEX

VII) Annex
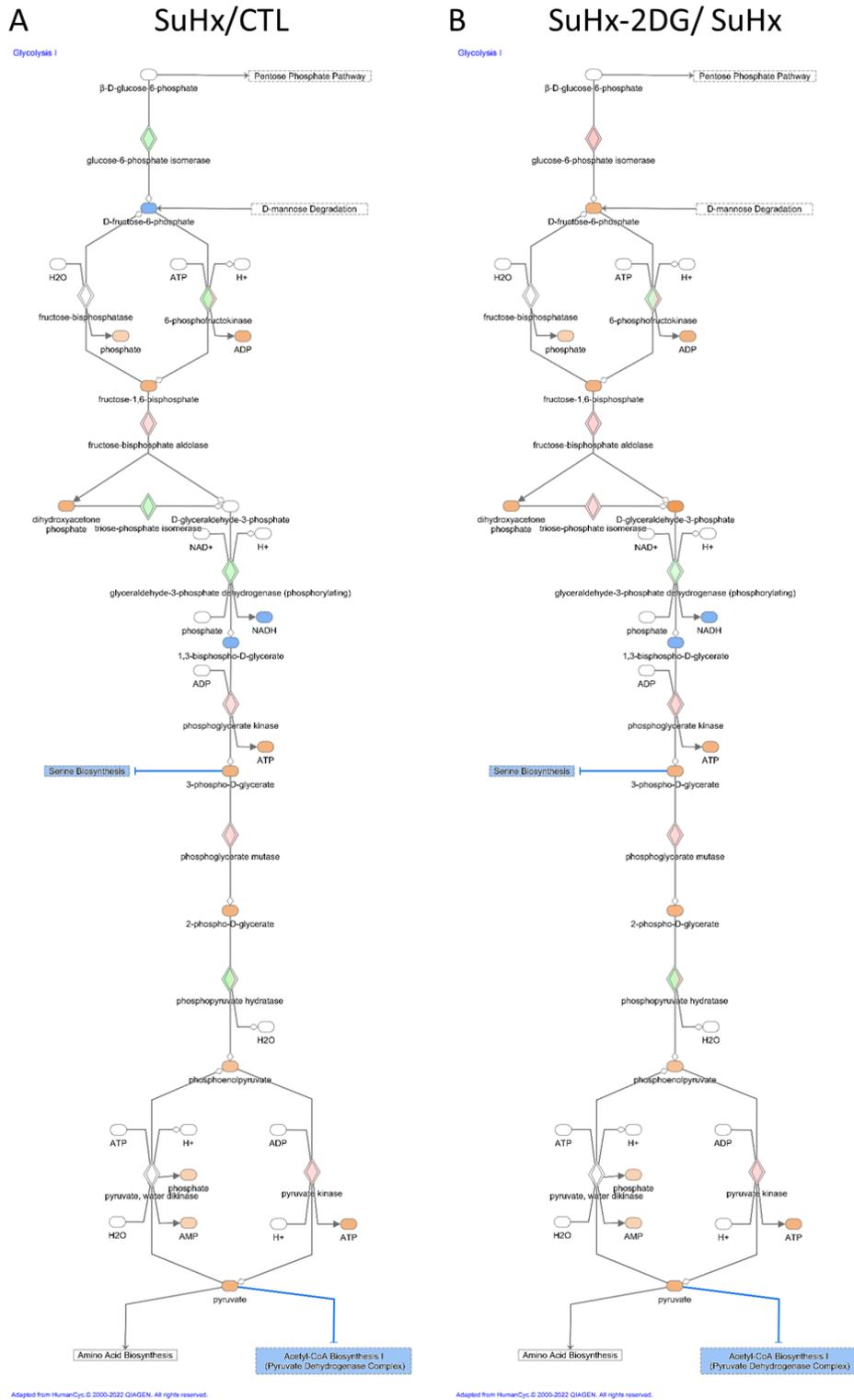
Figure 64. Adaptation of the IPA figure of the glycolysis pathway. Representation of the alterations of this pathway in (A) SuHx vs. CTL and (B) SuHx-2DG vs. SuHx. Differentially expressed upregulated proteins appear in red and differentially downregulated in green. Predicted activated molecules and routes are colored orange, while predicted inhibited molecules and routes are colored in blue.

Figure 65. Adaptation of the IPA figure of the oxidative phosphorylation pathway. Representation of the alterations of this pathway in (A) SuHx vs. CTL and (B) SuHx-2DG vs. SuHx. Differentially expressed upregulated proteins appear in red and differentially downregulated in green. Predicted activated molecules and routes are colored orange, while predicted inhibited molecules and routes are colored in blue.

A SuHx/CTL
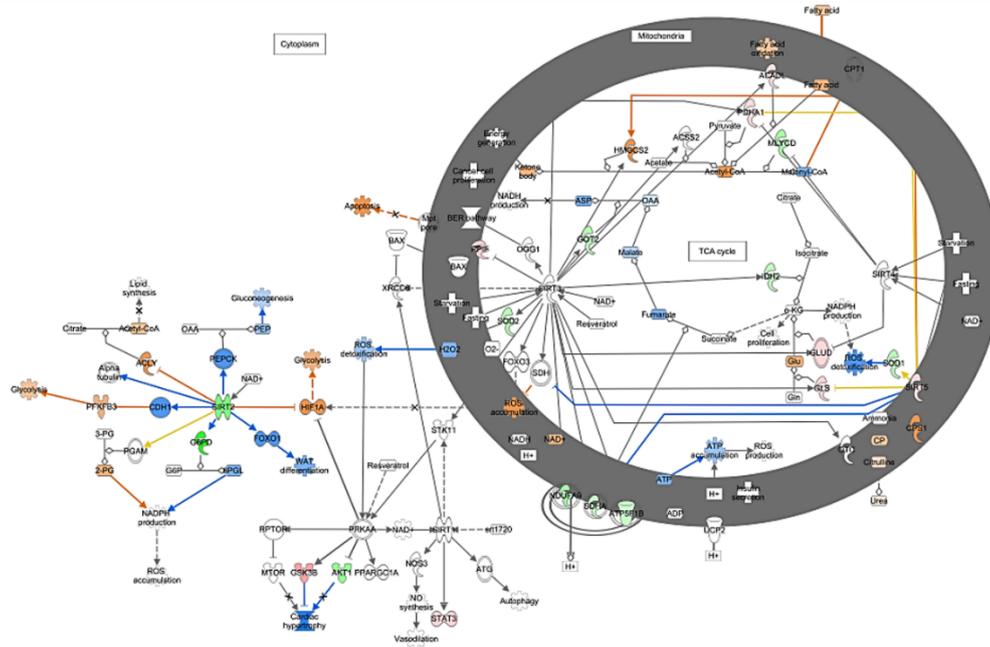
B SuHx-2DG/ SuHx
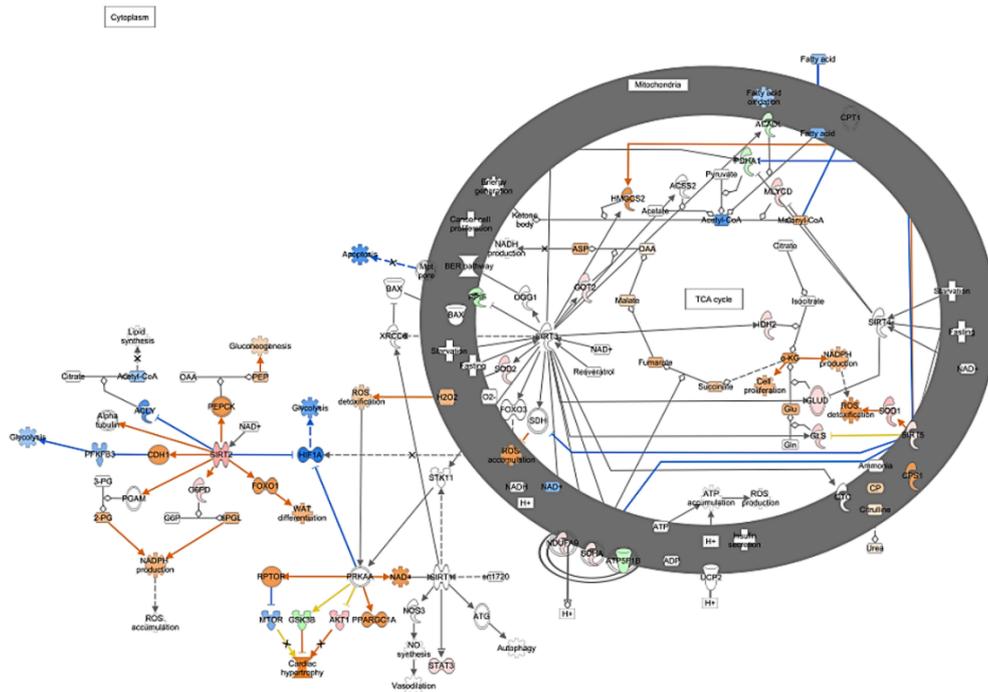
Figure 66. Adaptation of the IPA figure of the sirtuin signaling canonical pathway. Representation of the alterations of this pathway in (A) SuHx vs. CTL and (B) SuHx-2DG vs. SuHx. Differentially expressed upregulated proteins appear in red and differentially downregulated in green. Predicted activated molecules and routes are colored orange, while predicted inhibited molecules and routes are colored in blue.
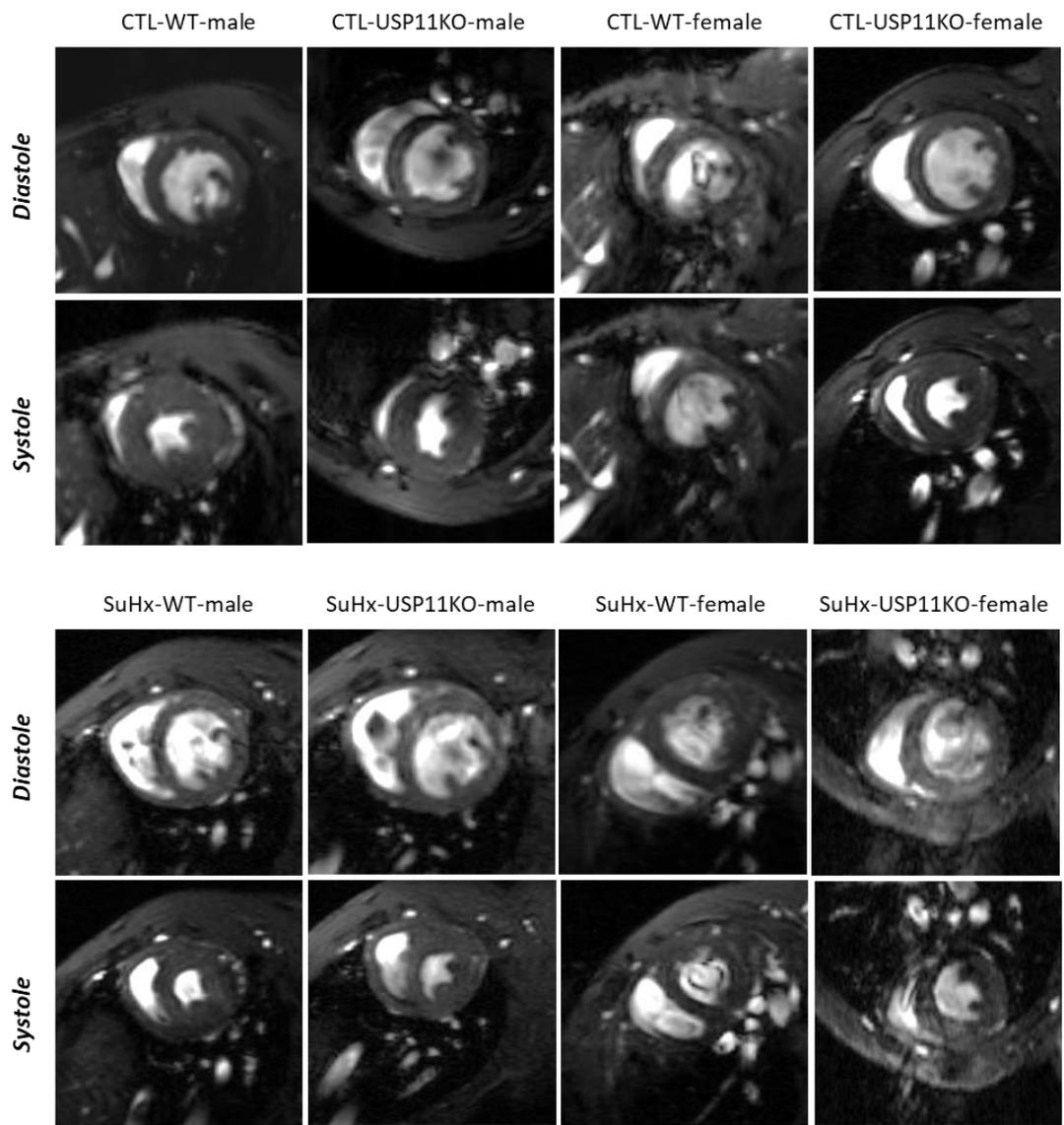
Figure 67. Representative MRI images of a midventricular axial slice in end-systolic and end-diastolic phases for each group.
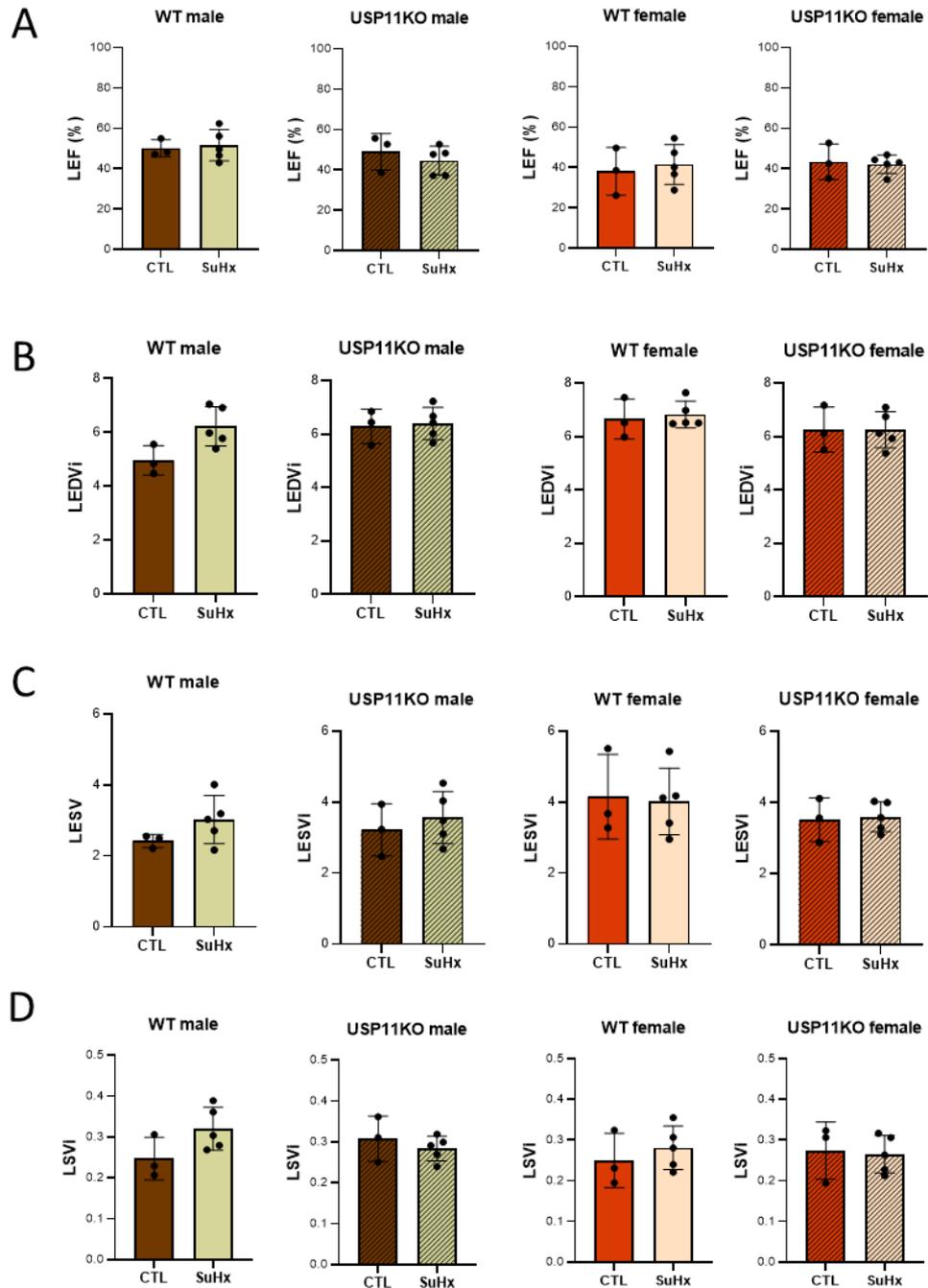
Figure 68. Quantitative analysis of LV function in each group. (A) Measurement of the Left Ejection Fraction (LEF). (B) Measurement of the Left End-Diastolic Volume Index (LEDVi). (C) Measurement of the End-Systolic Volume Index (LESVi). (D) Measurement of the left-ventricle Stroke Volume index (LSVi). Values are presented as mean ± SD. LEDVi: left-ventricle End-Diastolic Volume Index, LESVi: left-ventricle End-Systolic Volume Index, LSVi: left-ventricle Stroke Volume index, REDVi: right-ventricle End-Diastolic Volume Index, RESVi: right-ventricle End-Systolic Volume Index, RSVi: right-ventricle Stroke Volume index.
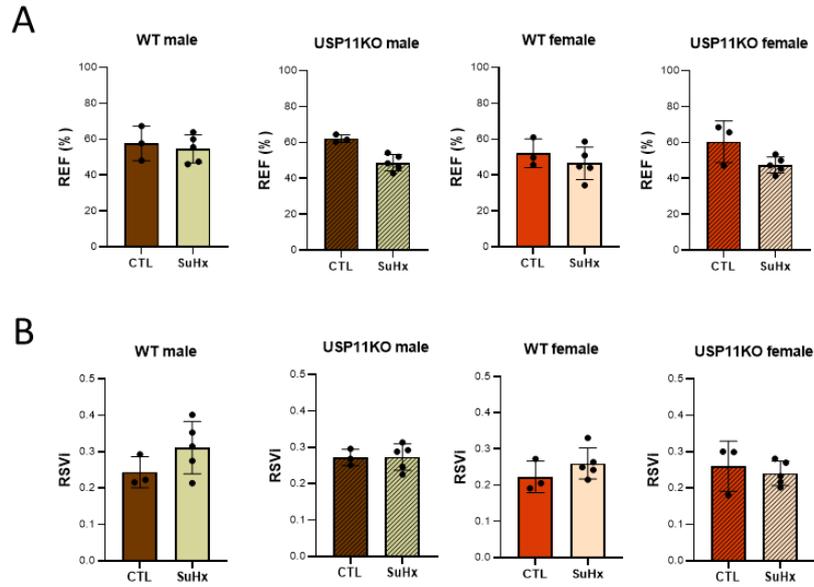
Figure 69. Quantitative analysis of EF and Svi of RV in each group. (A) Measurement of the Right Ejection Fraction (REF). (B) Measurement of the Right Stroke Volume Index (RSVi). Values are presented as mean ± SD.
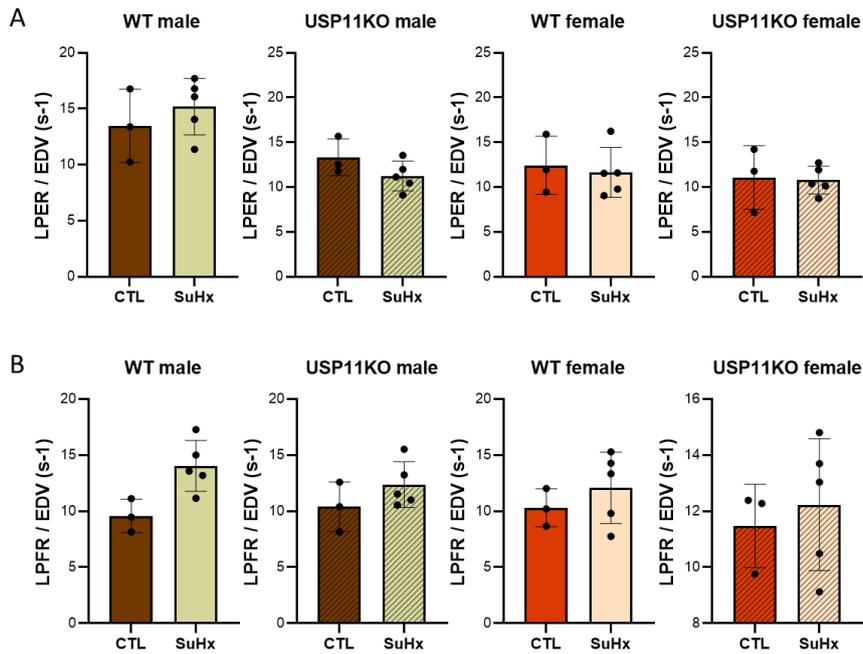
Figure 70. Analysis of the left ventricular systolic and diastolic function. Measurement of the (A) left-ventricle Peak Ejection Rate (PER) normalized to End-Diastolic Volume (EDV), and (B) left-ventricle Peak Filling Rate (PFR) normalized to EDV. Values are presented as mean ± SD assessed by the One-way ANOVA test.
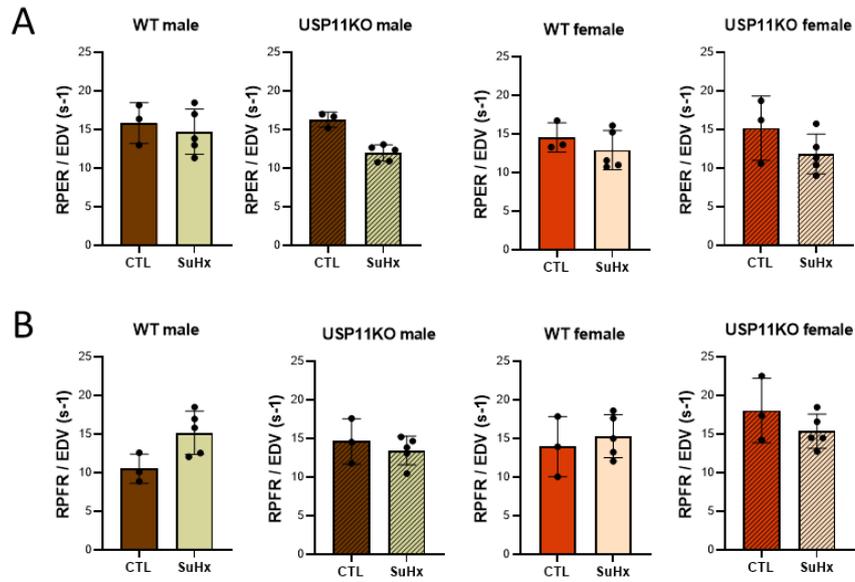
Figure 71. Analysis of the right ventricular systolic and diastolic function. Measurement of the (A) Right-ventricle Peak Ejection Rate (PER) normalized to End-Diastolic Volume (EDV), and (B) right-ventricle Peak Filling Rate (PFR) normalized to EDV. Values are presented as mean ± SD assessed by the One-way ANOVA test.

BIBLIOGRAPHY

Bibliography

[1]   G. Simonneau *et al.*, "Haemodynamic definitions and updated clinical classification of pulmonary hypertension," *European Respiratory Journal*, vol. 53, no. 1, Jan. 2019, doi: 10.1183/13993003.01913-2018.

[2]   R. Nair and N. Lamaa, "Pulmonary Capillary Wedge Pressure," *StatPearls*, Apr. 2022, Accessed: Jun. 03, 2022. [Online]. Available: https://www.ncbi.nlm.nih.gov/books/NBK557748/

[3]   J. Deng, "Clinical application of pulmonary vascular resistance in patients with pulmonary arterial hypertension," *J Cardiothorac Surg*, vol. 16, no. 1, p. 311, Dec. 2021, doi: 10.1186/S13019-021-01696-4.

[4]   R. Naeije and K. Chin, "Differentiating Precapillary from Postcapillary Pulmonary Hypertension: Pulmonary Artery Wedge Pressure Versus Left Ventricular End-Diastolic Pressure," *Circulation*, vol. 140, no. 9, pp. 712–714, Aug. 2019, doi: 10.1161/CIRCULATIONAHA.119.040295.

[5]   V. v. McLaughlin *et al.*, "A report of the american college of cardiology foundation task force on expert consensus documents and the american heart association," *Circulation*, vol. 119, no. 16. Circulation, pp. 2250–2294, Apr. 28, 2009. doi: 10.1161/CIRCULATIONAHA.109.192230.

[6]   M. M. Hoeper *et al.*, "A global view of pulmonary hypertension," *Lancet Respir Med*, vol. 4, no. 4, pp. 306–322, Apr. 2016, doi: 10.1016/S2213-2600(15)00543-3.

[7]   G. Strange *et al.*, "Pulmonary hypertension: prevalence and mortality in the Armadale echocardiography cohort," *Heart*, vol. 98, no. 24, p. 1805, Dec. 2012, doi: 10.1136/HEARTJNL-2012-301992.

[8]   Y. Ling *et al.*, "Changing Demographics, Epidemiology, and Survival of Incident Pulmonary Arterial Hypertension," *https://doi.org/10.1164/rccm.201203-0383OC*, vol. 186, no. 8, pp. 790–796, Nov. 2012, doi: 10.1164/RCCM.201203-0383OC.

[9]   A. J. Peacock, N. F. Murphy, J. J. V. McMurrey, L. Caballero, and S. Stewart, "An epidemiological study of pulmonary arterial hypertension," *European Respiratory Journal*, vol. 30, no. 1, pp. 104–109, Jul. 2007, doi: 10.1183/09031936.00092306.

[10]   M. Humbert *et al.*, "Pulmonary arterial hypertension in France: results from a national registry," *Am J Respir Crit Care Med*, vol. 173, no. 9, pp. 1023–1030, May 2006, doi: 10.1164/RCCM.200510-1668OC.

[11]   A. Groenewegen, F. H. Rutten, A. Mosterd, and A. W. Hoes, "Epidemiology of heart failure," *Eur J Heart Fail*, vol. 22, no. 8, p. 1342, Aug. 2020, doi: 10.1002/EJHF.1858.

[12] M. Delcroix *et al.*, "ERS statement on chronic thromboembolic pulmonary hypertension," *European Respiratory Journal*, vol. 57, no. 6, p. 29, Jun. 2021, doi: 10.1183/13993003.02828-2020.

[13] C. S. P. Lam, V. L. Roger, R. J. Rodeheffer, B. A. Borlaug, F. T. Enders, and M. M. Redfield, "Pulmonary Hypertension in Heart Failure with Preserved Ejection Fraction: A Community-Based Study," *J Am Coll Cardiol*, vol. 53, no. 13, p. 1119, Mar. 2009, doi: 10.1016/J.JACC.2008.11.051.

[14] S. Bhogal, D. Mukherjee, S. Banerjee, A. M. Islam, R. Daggubati, and T. K. Paul, "Current Trends and Future Perspectives in the Treatment of Pulmonary Hypertension: WHO Group II-V," *Curr Probl Cardiol*, vol. 43, no. 5, pp. 217–231, May 2018, doi: 10.1016/J.CPCARDIOL.2017.10.003.

[15] J. R. Klinger, "Group III Pulmonary Hypertension: Pulmonary Hypertension Associated with Lung Disease: Epidemiology, Pathophysiology, and Treatments," *Cardiol Clin*, vol. 34, no. 3, pp. 413–433, Aug. 2016, doi: 10.1016/J.CCL.2016.04.003.

[16] T. M. Maher *et al.*, "Global incidence and prevalence of idiopathic pulmonary fibrosis," *Respir Res*, vol. 22, no. 1, p. 197, Dec. 2021, doi: 10.1186/S12931-021-01791-Z.

[17] B. A. Maron *et al.*, "Pulmonary arterial hypertension: Diagnosis, treatment, and novel advances," *Am J Respir Crit Care Med*, vol. 203, no. 12, pp. 1472–1487, Jun. 2021, doi: 10.1164/RCCM.202012-4317SO.

[18] C. Orem, "Epidemiology of pulmonary hypertension in the elderly," *Journal of Geriatric Cardiology : JGC*, vol. 14, no. 1, Institute of Geriatric Cardiology, Chinese PLA General Hospital, p. 11, 2017. doi: 10.11909/J.ISSN.1671-5411.2017.01.001.

[19] M. D. McGoon and D. P. Miller, "REVEAL: a contemporary US pulmonary arterial hypertension registry," *European Respiratory Review*, vol. 21, no. 123, pp. 8–18, Mar. 2012, doi: 10.1183/09059180.00008211.

[20] V. Khou *et al.*, "Diagnostic delay in pulmonary arterial hypertension: Insights from the Australian and New Zealand pulmonary hypertension registry," *Respirology*, vol. 25, no. 8, pp. 863–871, Aug. 2020, doi: 10.1111/RESP.13768.

[21] P. Santer *et al.*, "Intravenous iron and chronic obstructive pulmonary disease: a randomised controlled trial," *BMJ Open Respir Res*, vol. 7, no. 1, Jun. 2020, doi: 10.1136/BMJRESP-2020-000577.

[22] M. M. Madani *et al.*, "Pulmonary Endarterectomy: Recent Changes in a Single Institution's Experience of More Than 2,700 Patients," *Ann Thorac Surg*, vol. 94, no. 1, pp. 97–103, Jul. 2012, doi: 10.1016/J.ATHORACSUR.2012.04.004.

[23]   Y. Sakurai *et al.*, "Predictors of Outcomes After Surgery for Chronic Thromboembolic Pulmonary Hypertension," *Ann Thorac Surg*, vol. 108, no. 4, pp. 1154–1161, Oct. 2019, doi: 10.1016/J.ATHORACSUR.2019.03.100.

[24]   C. Cheron *et al.*, "Sex and gender in pulmonary arterial hypertension," *European Respiratory Review*, vol. 30, no. 162, Dec. 2021, doi: 10.1183/16000617.0330-2020.

[25]   A. Frost *et al.*, "Diagnosis of pulmonary hypertension," *European Respiratory Journal*, vol. 53, no. 1, Jan. 2019, doi: 10.1183/13993003.01904-2018.

[26]   J. Bylica, M. Waligóra, I. Owsianka, J. Król, P. Podolec, and G. Kopeć, "Time from symptom onset to final diagnosis of pulmonary arterial hypertension in Polish patients," *Kardiologia Polska (Polish Heart Journal)*, vol. 78, no. 7–8, pp. 750–752, May 2020, doi: 10.33963/KP.15344.

[27]   J. Pepke-Zaba *et al.*, "Chronic thromboembolic pulmonary hypertension (CTEPH): Results from an international prospective registry," *Circulation*, vol. 124, no. 18, pp. 1973–1981, Nov. 2011, doi: 10.1161/CIRCULATIONAHA.110.015008.

[28]   S. A. Mandras, H. S. Mehta, and A. Vaidya, "Pulmonary Hypertension: A Brief Guide for Clinicians," *Mayo Clin Proc*, vol. 95, no. 9, pp. 1978–1988, Sep. 2020, doi: 10.1016/J.MAYOCP.2020.04.039.

[29]   C. Liu, J. Chen, Y. Gao, B. Deng, and K. Liu, "Endothelin receptor antagonists for pulmonary arterial hypertension," *Cochrane Database Syst Rev*, vol. 2021, no. 3, Mar. 2021, doi: 10.1002/14651858.CD004434.PUB6.

[30]   S. Saxer, M. Lichtblau, C. Berlier, E. D. Hasler, E. I. Schwarz, and S. Ulrich, "Physical activity in incident patients with pulmonary arterial and chronic thromboembolic hypertension," *Lung 2019 197:5*, vol. 197, no. 5, pp. 617–625, Jul. 2019, doi: 10.1007/S00408-019-00248-X.

[31]   L. Waller, K. Krüger, K. Conrad, A. Weiss, and K. Alack, "Effects of Different Types of Exercise Training on Pulmonary Arterial Hypertension: A Systematic Review," *J Clin Med*, vol. 9, no. 6, Jun. 2020, doi: 10.3390/JCM9061689.

[32]   L. Yan *et al.*, "The benefit of exercise-based rehabilitation programs in patients with pulmonary hypertension: a systematic review and meta-analysis of randomized controlled trials," *Pulmonary Circulation*, vol. 11, no. 2, pp. 1–8, Jun. 2021. doi: 10.1177/20458940211007810.

[33]   E. Grünig *et al.*, "Standardized exercise training is feasible, safe, and effective in pulmonary arterial and chronic thromboembolic pulmonary hypertension: results from a large European multicentre randomized controlled trial," *Eur Heart J*, vol. 42, no. 23, pp. 2284–2295, Jun. 2021, doi: 10.1093/EURHEARTJ/EHAA696.

[34] J. Marvin-Peek *et al.*, "Daily Step Counts Are Associated with Hospitalization Risk in Pulmonary Arterial Hypertension," *Am J Respir Crit Care Med*, vol. 204, no. 11, pp. 1338–1340, Dec. 2021, doi: 10.1164/RCCM.202104-1035LE.

[35] S. Ulrich, M. Fischler, R. Speich, and K. E. Bloch, "Wrist Actigraphy Predicts Outcome in Patients with Pulmonary Hypertension," *Respiration*, vol. 86, no. 1, pp. 45–51, Jul. 2013, doi: 10.1159/000342351.

[36] J. S. Vieira *et al.*, "Exercise intolerance establishment in pulmonary hypertension: Preventive effect of aerobic exercise training," *Life Sci*, vol. 261, no. 6, p. 118298, 2020, doi: 10.1016/j.lfs.2020.118298.

[37] E. Hassel, A. M. Berre, A. J. Skjulsvik, and S. Steinshamn, "Effects of exercise training on pulmonary vessel muscularization and right ventricular function in an animal model of COPD," *Respiratory Research*, vol. 15, no. 1, p. 117, Sep. 2014. doi: 10.1186/s12931-014-0117-y.

[38] F. L. Pacagnelli *et al.*, "Preventive aerobic training exerts a cardioprotective effect on rats treated with monocrotaline," *International Journal of Experimental Pathology*, vol. 97, no. 3, pp. 238–247, Jun. 2016. doi: 10.1111/iep.12166.

[39] R. Colombo *et al.*, "Effects of exercise on monocrotaline-induced changes in right heart function and pulmonary artery remodeling in rats," *Can J Physiol Pharmacol*, vol. 91, no. 1, pp. 38–44, Jan. 2013, doi: 10.1139/CJPP-2012-0261.

[40] M. P. Souza-Rabbo, L. F. F. Silva, J. A. S. Auzani, M. Picoral, N. Khaper, and A. Belló-Klein, "Effects of a chronic exercise training protocol on oxidative stress and right ventricular hypertrophy in monocrotaline-treated rats," *Clin Exp Pharmacol Physiol*, vol. 35, no. 8, pp. 944–948, Aug. 2008, doi: 10.1111/J.1440-1681.2008.04936.X.

[41] R. Nogueira-Ferreira *et al.*, "Exercise preconditioning prevents MCT-induced right ventricle remodeling through the regulation of TNF superfamily cytokines," *Int J Cardiol*, vol. 203, pp. 858–866, Jan. 2016, doi: 10.1016/J.IJCARD.2015.11.066.

[42] M. L. Handoko *et al.*, "Opposite effects of training in rats with stable and progressive pulmonary hypertension," *Circulation*, vol. 120, no. 1, pp. 42–49, Jul. 2009, doi: 10.1161/CIRCULATIONAHA.108.829713.

[43] R. Humar, T. Resink, and E. J. Battegay, "Vascular remodeling in hypertension: roles of apoptosis, inflammation, and fibrosis," *Hypertension*, vol. 38, no. 3 Pt 2, pp. 85–98, Jan. 2001, doi: 10.1161/HY09T1.096249.

[44] T. Thenappan, S. Y. Chan, and E. K. Weir, "Role of extracellular matrix in the pathogenesis of pulmonary arterial hypertension," *Am J Physiol Heart Circ Physiol*, vol. 315, no. 5, pp. H1322–H1331, Oct. 2018, doi: 10.1152/AJPHEART.00136.2018.

[45]   C. Guignabert and P. Dorfmuller, "Pathology and pathobiology of pulmonary hypertension," *Semin Respir Crit Care Med*, vol. 34, no. 5, pp. 551–559, 2013, doi: 10.1055/S-0033-1356496.

[46]   A. Zaiman, I. Fijalkowska, P. M. Hassoun, and R. M. Tuder, "One hundred years of research in the pathogenesis of pulmonary hypertension," *Am J Respir Cell Mol Biol*, vol. 33, no. 5, pp. 425–431, Nov. 2005, doi: 10.1165/RCMB.F307.

[47]   W. Xu and S. C. Erzurum, "Endothelial cell energy metabolism, proliferation, and apoptosis in pulmonary hypertension," *Compr Physiol*, vol. 1, no. 1, pp. 357–372, Nov. 2011, doi: 10.1002/CPHY.C090005.

[48]   K. R. Stenmark, B. Meyrick, N. Galie, W. J. Mooi, and I. F. McMurtry, "Animal models of pulmonary arterial hypertension: the hope for etiological discovery and pharmacological cure," *Am J Physiol Lung Cell Mol Physiol*, vol. 297, no. 6, 2009, doi: 10.1152/AJPLUNG.00217.2009.

[49]   R. Medzhitov, "Origin and physiological roles of inflammation," *Nature*, vol. 454, no. 7203, pp. 428–435, Jul. 2008, doi: 10.1038/NATURE07201.

[50]   A. I. Fernández *et al.*, "The Biological Bases of Group 2 Pulmonary Hypertension," *Int J Mol Sci*, vol. 20, no. 23, Dec. 2019, doi: 10.3390/IJMS20235884.

[51]   G. Simonneau, A. Torbicki, P. Dorfmüller, and N. Kim, "The pathophysiology of chronic thromboembolic pulmonary hypertension," *Eur Respir Rev*, vol. 26, no. 143, Mar. 2017, doi: 10.1183/16000617.0112-2016.

[52]   V. I. Peinado *et al.*, "Inflammatory reaction in pulmonary muscular arteries of patients with mild chronic obstructive pulmonary disease," *Am J Respir Crit Care Med*, vol. 159, no. 5 Pt 1, pp. 1605–1611, 1999, doi: 10.1164/AJRCCM.159.5.9807059.

[53]   Y. Hu, L. Chi, W. M. Kuebler, and N. M. Goldenberg, "Perivascular Inflammation in Pulmonary Arterial Hypertension," *Cells*, vol. 9, no. 11, Oct. 2020, doi: 10.3390/CELLS9112338.

[54]   M. Humbert *et al.*, "Increased interleukin-1 and interleukin-6 serum concentrations in severe primary pulmonary hypertension," *Am J Respir Crit Care Med*, vol. 151, no. 5, pp. 1628–1631, 1995, doi: 10.1164/AJRCCM.151.5.7735624.

[55]   E. Soon *et al.*, "Elevated levels of inflammatory cytokines predict survival in idiopathic and familial pulmonary arterial hypertension," *Circulation*, vol. 122, no. 9, pp. 920–927, Aug. 2010, doi: 10.1161/CIRCULATIONAHA.109.933762.

[56]   E. Hsu, H. Shi, R. M. Jordan, J. Lyons-Weiler, J. M. Pilewski, and C. A. Feghali-Bostwick, "Lung tissues in patients with systemic sclerosis have gene expression patterns unique to pulmonary fibrosis and pulmonary hypertension," *Arthritis Rheum*, vol. 63, no. 3, pp. 783–794, Mar. 2011, doi: 10.1002/ART.30159.

[57] S. Mumby *et al.*, "Bromodomain and extra-terminal protein mimic JQ1 decreases inflammation in human vascular endothelial cells: Implications for pulmonary arterial hypertension," *Respirology*, vol. 22, no. 1, pp. 157–164, Jan. 2017, doi: 10.1111/RESP.12872.

[58] M. Sakuma, S. Toyoda, T. Inoue, and K. Node, "Inflammation in pulmonary artery hypertension," *Vascul Pharmacol*, vol. 118–119, p. 106562, Jul. 2019, doi: 10.1016/J.VPH.2019.05.002.

[59] M. le Hiress *et al.*, "Proinflammatory Signature of the Dysfunctional Endothelium in Pulmonary Hypertension. Role of the Macrophage Migration Inhibitory Factor/CD74 Complex," *Am J Respir Crit Care Med*, vol. 192, no. 8, pp. 983–997, Oct. 2015, doi: 10.1164/RCCM.201402-0322OC.

[60] R. Kumar and B. Graham, "How does inflammation contribute to pulmonary hypertension?," *The European respiratory journal*, vol. 51, no. 1, NIH Public Access, 2018. doi: 10.1183/13993003.02403-2017.

[61] M. G. Frid *et al.*, "Hypoxia-induced pulmonary vascular remodeling requires recruitment of circulating mesenchymal precursors of a monocyte/macrophage lineage," *American Journal of Pathology*, vol. 168, no. 2, American Society for Investigative Pathology, p. 659, Feb. 2006. doi: 10.2353/ajpath.2006.050599.

[62] K. Kim and J.-H. Choi, "Involvement of immune responses in pulmonary arterial hypertension; lessons from rodent models," *Lab Anim Res*, vol. 35, no. 1, Dec. 2019, doi: 10.1186/S42826-019-0021-1.

[63] S. Taylor, O. Dirir, R. T. Zamanian, M. Rabinovitch, and A. A. R. Thompson, "The Role of Neutrophils and Neutrophil Elastase in Pulmonary Arterial Hypertension," *Front Med (Lausanne)*, vol. 5, no. AUG, pp. 1–1, 2018, doi: 10.3389/FMED.2018.00217.

[64] E. M. Berghausen, L. Feik, M. Zierden, M. Vantler, and S. Rosenkranz, "Key inflammatory pathways underlying vascular remodeling in pulmonary hypertension," *Herz*, vol. 44, no. 2, pp. 130–137, Apr. 2019, doi: 10.1007/s00059-019-4795-6.

[65] S.-C. Yang *et al.*, "Propofol inhibits superoxide production, elastase release, and chemotaxis in formyl peptide-activated human neutrophils by blocking formyl peptide receptor 1," *J Immunol*, vol. 190, no. 12, pp. 6511–6519, Jun. 2013, doi: 10.4049/JIMMUNOL.1202215.

[66] C. Taggart *et al.*, "Protean proteases: at the cutting edge of lung diseases," *Eur Respir J*, vol. 49, no. 2, Feb. 2017, doi: 10.1183/13993003.01200-2015.

[67] G. Ndrepepa, "Myeloperoxidase - A bridge linking inflammation and oxidative stress with cardiovascular disease," *Clin Chim Acta*, vol. 493, pp. 36–51, Jun. 2019, doi: 10.1016/J.CCA.2019.02.022.

[68] A. C. Oliveira, E. M. Richards, and M. K. Raizada, "Pulmonary Hypertension: Pathophysiology Beyond the Lung," *Pharmacol Res*, vol. 151, p. 104518, Jan. 2020, doi: 10.1016/J.PHRS.2019.104518.

[69] M. K. Culley and S. Y. Chan, "Mitochondrial metabolism in pulmonary hypertension: beyond mountains there are mountains," *J Clin Invest*, vol. 128, no. 9, p. 3704, Aug. 2018, doi: 10.1172/JCI120847.

[70] Y. Zhao *et al.*, "Metabolomic Heterogeneity of Pulmonary Arterial Hypertension," *PLoS One*, vol. 9, no. 2, p. 88727, Feb. 2014, doi: 10.1371/JOURNAL.PONE.0088727.

[71] Y. L. Zhang *et al.*, "3-Bromopyruvate Attenuates Experimental Pulmonary Hypertension via Inhibition of Glycolysis," *Am J Hypertens*, vol. 32, no. 4, pp. 426–432, Mar. 2019, doi: 10.1093/AJH/HPY191.

[72] J. J. Ryan and S. L. Archer, "Emerging concepts in the molecular basis of pulmonary arterial hypertension: part I: metabolic plasticity and mitochondrial dynamics in the pulmonary circulation and right ventricle in pulmonary arterial hypertension," *Circulation*, vol. 131, no. 19, Circulation, pp. 1691–1702, May 2015. doi: 10.1161/CIRCULATIONAHA.114.006979.

[73] H. Peng, Y. Xiao, X. Deng, J. Luo, C. Hong, and X. Qin, "The Warburg effect: A new story in pulmonary arterial hypertension," vol. 461, pp. 53–58, Oct. 2016, doi: 10.1016/J.CCA.2016.07.017.

[74] L. Plecitá-Hlavatá *et al.*, "Metabolic reprogramming and redox signaling in pulmonary hypertension," *Advances in Experimental Medicine and Biology*, vol. 967, Springer New York LLC, pp. 241–260, Oct. 2017. doi: 10.1007/978-3-319-63245-2_14.

[75] L. Piao *et al.*, "FOXO1-mediated upregulation of pyruvate dehydrogenase kinase-4 (PDK4) decreases glucose oxidation and impairs right ventricular function in pulmonary hypertension: therapeutic benefits of dichloroacetate," *Journal of Molecular Medicine 2012 91:3*, vol. 91, no. 3, pp. 333–346, Dec. 2012, doi: 10.1007/S00109-012-0982-0.

[76] E. D. Michelakis *et al.*, "Inhibition of pyruvate dehydrogenase kinase improves pulmonary arterial hypertension in genetically susceptible patients," *Sci Transl Med*, vol. 9, no. 413, Oct. 2017, doi: 10.1126/SCITRANSLMED.AAO4583.

[77] M. S. McMurtry *et al.*, "Dichloroacetate Prevents and Reverses Pulmonary Hypertension by Inducing Pulmonary Artery Smooth Muscle Cell Apoptosis," *Circ Res*, vol. 95, no. 8, pp. 830–840, Oct. 2004, doi: 10.1161/01.RES.0000145360.16770.9F.

[78] S. G. Wolf *et al.*, "3D visualization of mitochondrial solid-phase calcium stores in whole cells," *Elife*, vol. 6, Nov. 2017, doi: 10.7554/ELIFE.29929.

[79] N. S. Chandel, "Evolution of Mitochondria as Signaling Organelles," *Cell Metab*, vol. 22, no. 2, pp. 204–206, Aug. 2015, doi: 10.1016/J.CMET.2015.05.013.

[80] V. Freund-Michel, N. Khoyrattee, J. P. Savineau, B. Muller, and C. Guibert, "Mitochondria: roles in pulmonary hypertension," *Int J Biochem Cell Biol*, vol. 55, pp. 93–97, 2014, doi: 10.1016/J.BIOCEL.2014.08.012.

[81] J. D. Marshall, I. Bazan, Y. Zhang, W. H. Fares, and P. J. Lee, "Mitochondrial dysfunction and pulmonary hypertension: cause, effect, or both," *Am J Physiol Lung Cell Mol Physiol*, vol. 314, no. 5, pp. L782–L796, May 2018, doi: 10.1152/AJPLUNG.00331.2017.

[82] O. Pak *et al.*, "Mitochondrial hyperpolarization in pulmonary vascular remodeling. Mitochondrial uncoupling protein deficiency as disease model," *Am J Respir Cell Mol Biol*, vol. 49, no. 3, pp. 348–357, Sep. 2013, doi: 10.1165/RCMB.2012-0361OC.

[83] H. B. Suliman and E. Nozik-Grayck, "Mitochondrial Dysfunction: Metabolic Drivers of Pulmonary Hypertension," *Antioxid Redox Signal*, vol. 31, no. 12, pp. 843–857, Oct. 2019, doi: 10.1089/ARS.2018.7705.

[84] G. W. Dorn, "Mitochondrial dynamics in heart disease," *Biochimica et Biophysica Acta (BBA) - Molecular Cell Research*, vol. 1833, no. 1, pp. 233–241, Jan. 2013, doi: 10.1016/J.BBAMCR.2012.03.008.

[85] G. Sutendra *et al.*, "A metabolic remodeling in right ventricular hypertrophy is associated with decreased angiogenesis and a transition from a compensated to a decompensated state in pulmonary hypertension," *J Mol Med (Berl)*, vol. 91, no. 11, pp. 1315–1327, Nov. 2013, doi: 10.1007/S00109-013-1059-4.

[86] C. Sotomayor-Flores *et al.*, "Angiotensin-(1–9) prevents cardiomyocyte hypertrophy by controlling mitochondrial dynamics via miR-129-3p/PKIA pathway," *Cell Death Differ*, vol. 27, no. 9, p. 2586, Sep. 2020, doi: 10.1038/S41418-020-0522-3.

[87] J. Gomez-Arroyo *et al.*, "Metabolic gene remodeling and mitochondrial dysfunction in failing right ventricular hypertrophy secondary to pulmonary arterial hypertension," *Circ Heart Fail*, vol. 6, no. 1, pp. 136–144, Jan. 2013, doi: 10.1161/CIRCHEARTFAILURE.111.966127/-/DC1.

[88] L. Piao, G. Marsboom, and S. L. Archer, "Mitochondrial metabolic adaptation in right ventricular hypertrophy and failure," *Journal of Molecular Medicine 2010 88:10*, vol. 88, no. 10, pp. 1011–1020, Sep. 2010, doi: 10.1007/S00109-010-0679-1.

[89] J. L. Izquierdo-Garcia *et al.*, "Metabolic Reprogramming in the Heart and Lung in a Murine Model of Pulmonary Arterial Hypertension," *Front Cardiovasc Med*, vol. 5, Aug. 2018, doi: 10.3389/FCVM.2018.00110.

[90] V. Cuccurullo, G. D. di Stasio, L. Evangelista, G. Castoria, and L. Mansi, "Biochemical and Pathophysiological Premises to Positron Emission Tomography With Choline Radiotracers," *J Cell Physiol*, vol. 232, no. 2, pp. 270–275, Feb. 2017, doi: 10.1002/JCP.25478.

[91] F. O. Onono and A. J. Morris, "Phospholipase D and Choline Metabolism," *Handbook of experimental pharmacology*, vol. 259, Handb Exp Pharmacol, pp. 205–218, 2020. doi: 10.1007/164_2019_320.

[92] M. R. la Frano *et al.*, "Umbilical cord blood metabolomics reveal distinct signatures of dyslipidemia prior to bronchopulmonary dysplasia and pulmonary hypertension," *Am J Physiol Lung Cell Mol Physiol*, vol. 315, no. 5, pp. L870–L881, Nov. 2018, doi: 10.1152/AJPLUNG.00283.2017.

[93] G. A. Heresi *et al.*, "Plasma metabolomic profile in chronic thromboembolic pulmonary hypertension," *Pulm Circ*, vol. 10, no. 1, Jan. 2020, doi: 10.1177/2045894019890553.

[94] G. Hagan *et al.*, "18FDG PET imaging can quantify increased cellular metabolism in pulmonary arterial hypertension: A proof-of-principle study," *Pulmonary Circulation*, vol. 1, no. 4, Wiley-Blackwell, p. 448, 2011. doi: 10.4103/2045-8932.93543.

[95] M. M. Can *et al.*, "Increased right ventricular glucose metabolism in patients with pulmonary arterial hypertension," *Clin Nucl Med*, vol. 36, no. 9, pp. 743–748, Sep. 2011, doi: 10.1097/RLU.0B013E3182177389.

[96] G. Marsboom *et al.*, "Lung 18F-fluorodeoxyglucose positron emission tomography for diagnosis and monitoring of pulmonary arterial hypertension," *Am J Respir Crit Care Med*, vol. 185, no. 6, p. 670, Mar. 2012, doi: 10.1164/rccm.201108-1562OC.

[97] J. P. Richalet, "The invention of hypoxia," *J Appl Physiol*, vol. 130, no. 5, pp. 1573–1582, May 2021, doi: 10.1152/JAPPLPHYSIOL.00936.2020.

[98] H. Choudhry and A. L. Harris, "Advances in Hypoxia-Inducible Factor Biology," *Cell Metab*, vol. 27, no. 2, pp. 281–298, Feb. 2018, doi: 10.1016/J.CMET.2017.10.005.

[99] A. A. Tirpe, D. Gulei, S. M. Ciortea, C. Crivii, and I. Berindan-Neagoe, "Hypoxia: Overview on Hypoxia-Mediated Mechanisms with a Focus on the Role of HIF Genes," *Int J Mol Sci*, vol. 20, no. 24, Dec. 2019, doi: 10.3390/IJMS20246140.

[100] S. J. Kierans and C. T. Taylor, "Regulation of glycolysis by the hypoxia-inducible factor (HIF): implications for cellular physiology," *J Physiol*, vol. 599, no. 1, pp. 23–37, Jan. 2021, doi: 10.1113/JP280572.

[101] G. Sutendra and E. D. Michelakis, "The Metabolic Basis of Pulmonary Arterial Hypertension," *Cell Metab*, vol. 19, no. 4, pp. 558–573, Apr. 2014, doi: 10.1016/J.CMET.2014.01.004.

[102] K. R. Stenmark, K. A. Fagan, and M. G. Frid, "Hypoxia-Induced Pulmonary Vascular Remodeling," *Circ Res*, vol. 99, no. 7, pp. 675–691, Sep. 2006, doi: 10.1161/01.RES.0000243584.45145.3F.

[103] Y.-L. Lai and T. C. Law, "Chronic hypoxia- and monocrotaline-induced elevation of hypoxia-inducible factor-1 alpha levels and pulmonary hypertension," *J Biomed Sci*, vol. 11, no. 3, pp. 315–321, May 2004, doi: 10.1007/BF02254435.

[104] H. Kojima *et al.*, "Hypoxia-inducible factor-1 α deletion in myeloid lineage attenuates hypoxia-induced pulmonary hypertension," *Physiol Rep*, vol. 7, no. 7, Apr. 2019, doi: 10.14814/PHY2.14025.

[105] L. A. Shimoda, "Cellular pathways promoting pulmonary vascular remodeling by hypoxia," *Physiology*, vol. 35, no. 4, pp. 222–233, Jul. 2020, doi: 10.1152/PHYSIOL.00039.2019.

[106] W. Wu, Y. Li, and D. Xu, "Role of ROS/Kv/HIF Axis in the Development of Hypoxia-Induced Pulmonary Hypertension," *Chin Med Sci J*, vol. 32, no. 4, pp. 253–259, Dec. 2017, doi: 10.24920/J1001-9294.2017.037.

[107] K. R. Stenmark *et al.*, "The Adventitia: Essential Regulator of Vascular Wall Structure and Function," *Annu Rev Physiol*, vol. 75, p. 23, Feb. 2013, doi: 10.1146/ANNUREV-PHYSIOL-030212-183802.

[108] K. R. Stenmark, N. Davie, M. Frid, E. Gerasimovskaya, and M. Das, "Role of the adventitia in pulmonary vascular remodeling," *Physiology*, vol. 21, no. 2, pp. 134–145, Apr. 2006, doi: 10.1152/PHYSIOL.00053.2005.

[109] Y. Li *et al.*, "Suppression of the expression of hypoxia-inducible factor-1α by RNA interference alleviates hypoxia-induced pulmonary hypertension in adult rats," *Int J Mol Med*, vol. 38, no. 6, pp. 1786–1794, Dec. 2016, doi: 10.3892/IJMM.2016.2773.

[110] K. A. Cottrill and S. Y. Chan, "Metabolic Dysfunction in Pulmonary Hypertension: The Expanding Relevance of the Warburg Effect," *Eur J Clin Invest*, vol. 43, no. 8, pp. 855–865, Aug. 2013, doi: 10.1111/ECI.12104.

[111] R. Naeije and C. Dedobbeleer, "Pulmonary hypertension and the right ventricle in hypoxia," *Exp Physiol*, vol. 98, no. 8, pp. 1247–1256, Aug. 2013, doi: 10.1113/EXPPHYSIOL.2012.069112.

[112] G. L. Semenza, "HIF-1 and mechanisms of hypoxia sensing," *Curr Opin Cell Biol*, vol. 13, no. 2, pp. 167–171, Apr. 2001, doi: 10.1016/S0955-0674(00)00194-0.

[113] A. Y. Yu *et al.*, "Impaired physiological responses to chronic hypoxia in mice partially deficient for hypoxia-inducible factor 1α," *J Clin Invest*, vol. 103, no. 5, pp. 691–696, Mar. 1999, doi: 10.1172/JCI5912.

[114] L. A. Shimoda, D. J. Manalo, J. S. K. Sham, G. L. Semenza, and J. T. Sylvester, "Partial HIF-1alpha deficiency impairs pulmonary arterial myocyte electrophysiological responses to hypoxia," *American journal of physiology. Lung cellular and molecular physiology*, vol.

281, no. 1, Am J Physiol Lung Cell Mol Physiol, pp. L202-210, Jul. 2001. doi: 10.1152/AJPLUNG.2001.281.1.L202.

[115] K. Brusselmans *et al.*, "Heterozygous deficiency of hypoxia-inducible factor-2alpha protects mice against pulmonary hypertension and right ventricular dysfunction during prolonged hypoxia," *The Journal of clinical investigation*, vol. 111, no. 10, J Clin Invest, pp. 1519–1527, May 2003. doi: 10.1172/JCI15496.

[116] C. J. Hu *et al.*, "Suppression of HIF2 signalling attenuates the initiation of hypoxia-induced pulmonary hypertension," *Eur Respir J*, vol. 54, no. 6, Dec. 2019, doi: 10.1183/13993003.00378-2019.

[117] A. S. Cowburn *et al.*, "HIF2α-arginase axis is essential for the development of pulmonary hypertension," *Proc Natl Acad Sci U S A*, vol. 113, no. 31, pp. 8801–8806, Aug. 2016, doi: 10.1073/PNAS.1602978113.

[118] M. K. Ball *et al.*, "Regulation of hypoxia-induced pulmonary hypertension by vascular smooth muscle hypoxia-inducible factor-1α," *Am J Respir Crit Care Med*, vol. 189, no. 3, pp. 314–324, Feb. 2014, doi: 10.1164/RCCM.201302-0302OC.

[119] D. Wang *et al.*, "Phosphorylated E2F1 is stabilized by nuclear USP11 to drive Peg10 gene expression and activate lung epithelial cells," *J Mol Cell Biol*, vol. 10, no. 1, pp. 60–73, Feb. 2018, doi: 10.1093/JMCB/MJX034.

[120] A. S. Schober and E. Berra, "DUBs, New Members in the Hypoxia Signaling clUb," *Front Oncol*, vol. 6, no. MAR, 2016, doi: 10.3389/FONC.2016.00053.

[121] Z. Zhou *et al.*, "Regulation of XIAP Turnover Reveals a Role for USP11 in Promotion of Tumorigenesis," *EBioMedicine*, vol. 15, pp. 48–61, Feb. 2017, doi: 10.1016/J.EBIOM.2016.12.014.

[122] M. A. Al-Salihi, L. Herhaus, T. MacArtney, and G. P. Sapkota, "USP11 augments TGFβ signalling by deubiquitylating ALK5," *Open Biology*, vol. 2, no. 6, The Royal Society, Jun. 2012. doi: 10.1098/RSOB.120063.

[123] C. Meng *et al.*, "The deubiquitinase USP11 regulates cell proliferation and ferroptotic cell death via stabilization of NRF2 USP11 deubiquitinates and stabilizes NRF2," *Oncogene 2021 40:9*, vol. 40, no. 9, pp. 1706–1720, Feb. 2021, doi: 10.1038/s41388-021-01660-5.

[124] H. Sun *et al.*, "USP11 promotes growth and metastasis of colorectal cancer via PPP1CA-mediated activation of ERK/MAPK signaling pathway," *EBioMedicine*, vol. 48, pp. 236–247, Oct. 2019, doi: 10.1016/J.EBIOM.2019.08.061.

[125] H. C. Wu *et al.*, "USP11 regulates PML stability to control Notch-induced malignancy in brain tumours," *Nat Commun*, vol. 5, Feb. 2014, doi: 10.1038/NCOMMS4214.

[126] X. Ting *et al.*, "USP11 acts as a histone deubiquitinase functioning in chromatin reorganization during DNA repair," *Nucleic Acids Res*, vol. 47, no. 18, pp. 9721–9740, Oct. 2019, doi: 10.1093/NAR/GKZ726.

[127] I. A. Hendriks, J. Schimmel, K. Eifler, J. v. Olsen, and A. C. O. Vertegaal, "Ubiquitin-specific Protease 11 (USP11) Deubiquitinates Hybrid Small Ubiquitin-like Modifier (SUMO)-Ubiquitin Chains to Counteract RING Finger Protein 4 (RNF4)," *J Biol Chem*, vol. 290, no. 25, pp. 15526–15537, Jun. 2015, doi: 10.1074/JBC.M114.618132.

[128] M. Jurga, A. A. Abugable, A. S. H. Goldman, and S. F. El-Khamisy, "USP11 controls R-loops by regulating senataxin proteostasis," *Nature Communications 2021 12:1*, vol. 12, no. 1, pp. 1–18, Sep. 2021, doi: 10.1038/s41467-021-25459-w.

[129] T. Deng *et al.*, "Deubiquitylation and stabilization of p21 by USP11 is critical for cell-cycle progression and DNA damage responses," *Proc Natl Acad Sci U S A*, vol. 115, no. 18, pp. 4678–4683, May 2018, doi: 10.1073/PNAS.1714938115.

[130] W. Sun *et al.*, "USP11 Negatively Regulates TNFα-Induced NF-κB Activation by Targeting on IκBα," *Cell Signal*, vol. 22, no. 3, p. 386, Mar. 2010, doi: 10.1016/J.CELLSIG.2009.10.008.

[131] T. Yamaguchi, J. Kimura, Y. Miki, and K. Yoshida, "The deubiquitinating enzyme USP11 controls an IkappaB kinase alpha (IKKalpha)-p53 signaling pathway in response to tumor necrosis factor alpha (TNFalpha)," *J Biol Chem*, vol. 282, no. 47, pp. 33943–33948, Nov. 2007, doi: 10.1074/JBC.M706282200.

[132] "Characterization of USP11 as a novel regulator of Hypoxia inducible factor a." https://addi.ehu.es/handle/10810/42834 (accessed May 04, 2022).

[133] B. L. Carman, D. N. Predescu, R. Machado, and S. A. Predescu, "Plexiform Arteriopathy in Rodent Models of Pulmonary Arterial Hypertension," *Am J Pathol*, vol. 189, no. 6, pp. 1133–1144, Jun. 2019, doi: 10.1016/J.AJPATH.2019.02.005.

[134] L. Ciuclan *et al.*, "A novel murine model of severe pulmonary arterial hypertension," *Am J Respir Crit Care Med*, vol. 184, no. 10, pp. 1171–1182, Nov. 2011, doi: 10.1164/RCCM.201103-0412OC.

[135] E. Gouma, Y. Simos, I. Verginadis, E. Lykoudis, A. Evangelou, and S. Karkabounas, "A simple procedure for estimation of total body surface area and determination of a new value of Meeh's constant in rats," *Lab Anim*, vol. 46, no. 1, pp. 40–45, Jan. 2012, doi: 10.1258/la.2011.011021.

[136] N. J. Dawson, "The Surface-Area/Body-Weight Relationship in Mice," *Aust J Biol Sci*, vol. 20, no. 3, pp. 687–690, 1967, doi: 10.1071/BI9670687.

[137] B. Kojonazarov *et al.*, "Evaluating Systolic and Diastolic Cardiac Function in Rodents Using Microscopic Computed Tomography," *Circ Cardiovasc Imaging*, vol. 11, no. 12, p. e007653, Dec. 2018, doi: 10.1161/CIRCIMAGING.118.007653.

[138] J. R. Wiśniewski, A. Zougman, N. Nagaraj, and M. Mann, "Universal sample preparation method for proteome analysis," *Nat Methods*, vol. 6, no. 5, pp. 359–362, 2009, doi: 10.1038/NMETH.1322.

[139] J. Cox and M. Mann, "MaxQuant enables high peptide identification rates, individualized p.p.b.-range mass accuracies and proteome-wide protein quantification," *Nat Biotechnol*, vol. 26, no. 12, pp. 1367–1372, Dec. 2008, doi: 10.1038/NBT.1511.

[140] S. Tyanova *et al.*, "The Perseus computational platform for comprehensive analysis of (prote)omics data," *Nat Methods*, vol. 13, no. 9, pp. 731–740, Aug. 2016, doi: 10.1038/NMETH.3901.

[141] G. Manzanares, G. Brito-Da-Silva, and P. G. Gandra, "Voluntary wheel running: patterns and physiological effects in mice," *Brazilian Journal of Medical and Biological Research*, vol. 52, no. 1, 2019, doi: 10.1590/1414-431X20187830.

[142] A. J. Natali, E. D. Fowler, S. C. Calaghan, and E. White, "Voluntary exercise delays heart failure onset in rats with pulmonary artery hypertension," *Am J Physiol Heart Circ Physiol*, vol. 309, no. 3, pp. H421–H424, Aug. 2015, doi: 10.1152/AJPHEART.00262.2015.

[143] A. A. Gibb *et al.*, "Exercise-Induced Changes in Glucose Metabolism Promote Physiological Cardiac Growth," *Circulation*, vol. 136, no. 22, pp. 2144–2157, Nov. 2017, doi: 10.1161/CIRCULATIONAHA.117.028274/-/DC1.

[144] O. Mirea, O. M. Corîci, O. Istrătoaie, I. Donoiu, M. Iancău, and C. Militaru, "Left and right ventricular morphology and function in athletes with elevated pulmonary systolic arterial pressure," *Echocardiography*, vol. 35, no. 6, pp. 769–776, Jun. 2018, doi: 10.1111/ECHO.14016.

[145] A. Decloedt, D. de Clercq, S. Ven, L. Vera, and G. van Loon, "Right ventricular function during pharmacological and exercise stress testing in horses," *The Veterinary Journal*, vol. 227, pp. 8–14, Sep. 2017, doi: 10.1016/J.TVJL.2017.08.001.

[146] A. la Gerche *et al.*, "Exercise-induced right ventricular dysfunction is associated with ventricular arrhythmias in endurance athletes," *Eur Heart J*, vol. 36, no. 30, pp. 1998–2010, Aug. 2015, doi: 10.1093/EURHEARTJ/EHV202.

[147] R. Naeije, "Physiological Adaptation of the Cardiovascular System to High Altitude," *Prog Cardiovasc Dis*, vol. 52, no. 6, pp. 456–466, May 2010, doi: 10.1016/J.PCAD.2010.03.004.

[148] L. Piao *et al.*, "The inhibition of pyruvate dehydrogenase kinase improves impaired cardiac function and electrical remodeling in two models of right ventricular

hypertrophy: Resuscitating the hibernating right ventricle," *J Mol Med*, vol. 88, no. 1, pp. 47–60, Jan. 2010, doi: 10.1007/S00109-009-0524-6.

[149] M. Oikawa *et al.*, "Increased [18F]fluorodeoxyglucose accumulation in right ventricular free wall in patients with pulmonary hypertension and the effect of epoprostenol," *J Am Coll Cardiol*, vol. 45, no. 11, pp. 1849–1855, Jun. 2005, doi: 10.1016/J.JACC.2005.02.065.

[150] H. Xia *et al.*, "Hypoxia-induced modulation of glucose transporter expression impacts 18F-fluorodeoxyglucose PET-CT imaging in hepatocellular carcinoma," *Eur J Nucl Med Mol Imaging*, vol. 47, no. 4, pp. 787–797, Apr. 2020, doi: 10.1007/S00259-019-04638-4.

[151] A. C. Koop *et al.*, "Metabolic Remodeling in the Pressure-Loaded Right Ventricle: Shifts in Glucose and Fatty Acid Metabolism—A Systematic Review and Meta-Analysis," *J Am Heart Assoc*, vol. 8, no. 21, Nov. 2019, doi: 10.1161/JAHA.119.012086.

[152] J.-Z. Zhang, A. Behrooz, and F. Ismail-Beigi, "Regulation of glucose transport by hypoxia," *American Journal of Kidney Diseases*, vol. 34, no. 1, pp. 189–202, Jul. 1999, doi: 10.1016/S0272-6386(99)70131-9.

[153] I. S. Wood, B. Wang, S. Lorente-Cebrián, and P. Trayhurn, "Hypoxia increases expression of selective facilitative glucose transporters (GLUT) and 2-deoxy-d-glucose uptake in human adipocytes," *Biochem Biophys Res Commun*, vol. 361, no. 2–2, p. 468, Sep. 2007, doi: 10.1016/J.BBRC.2007.07.032.

[154] A. al Mamun, H. Hayashi, A. Yamamura, M. J. Nayeem, and M. Sato, "Hypoxia induces the translocation of glucose transporter 1 to the plasma membrane in vascular endothelial cells," *J Physiol Sci*, vol. 70, no. 1, Sep. 2020, doi: 10.1186/S12576-020-00773-Y.

[155] M. A. Chowdhury *et al.*, "Exercise and Cardioprotection: A Natural Defense Against Lethal Myocardial Ischemia-Reperfusion Injury and Potential Guide to Cardiovascular Prophylaxis," *J Cardiovasc Pharmacol Ther*, vol. 24, no. 1, pp. 18–30, Jan. 2019, doi: 10.1177/1074248418788575.

[156] B. Egemnazarov, S. Crnkovic, B. M. Nagy, H. Olschewski, and G. Kwapiszewska, "Right ventricular fibrosis and dysfunction: Actual concepts and common misconceptions," *Matrix Biol*, vol. 68–69, pp. 507–521, Aug. 2018, doi: 10.1016/J.MATBIO.2018.01.010.

[157] M. Connolly, B. E. Garfield, A. Crosby, N. W. Morrell, S. J. Wort, and P. R. Kemp, "miR-1-5p targets TGF-βR1 and is suppressed in the hypertrophying hearts of rats with pulmonary arterial hypertension," *PLoS ONE*, vol. 15, no. 2, Public Library of Science, p. e0229409, Feb. 2020. doi: 10.1371/JOURNAL.PONE.0229409.

[158] K. Okumura *et al.*, "Carvedilol improves biventricular fibrosis and function in experimental pulmonary hypertension," *J Mol Med (Berl)*, vol. 93, no. 6, pp. 663–674, Jun. 2015, doi: 10.1007/S00109-015-1251-9.

[159] O. Rafikova *et al.*, "Early progression of pulmonary hypertension in the monocrotaline model in males is associated with increased lung permeability," *Biol Sex Differ*, vol. 11, no. 1, pp. 1–9, Mar. 2020, doi: 10.1186/s13293-020-00289-5.

[160] R. Nogueira-Ferreira, R. Vitorino, R. Ferreira, and T. Henriques-Coelho, "Exploring the monocrotaline animal model for the study of pulmonary arterial hypertension: A network approach," *Pulm Pharmacol Ther*, vol. 35, pp. 8–16, 2015, doi: 10.1016/J.PUPT.2015.09.007.

[161] R. J. White *et al.*, "Plexiform-like lesions and increased tissue factor expression in a rat model of severe pulmonary arterial hypertension," *Am J Physiol Lung Cell Mol Physiol*, vol. 293, no. 3, Sep. 2007, doi: 10.1152/AJPLUNG.00321.2006.

[162] J. Ryan, K. Bloch, and S. L. Archer, "Rodent models of pulmonary hypertension: harmonisation with the world health organisation's categorisation of human PH," *Int J Clin Pract Suppl*, vol. 65, no. 172, pp. 15–34, 2011, doi: 10.1111/J.1742-1241.2011.02710.X.

[163] K. Abe *et al.*, "Formation of plexiform lesions in experimental severe pulmonary arterial hypertension," *Circulation*, vol. 121, no. 25, pp. 2747–2754, Jun. 2010, doi: 10.1161/CIRCULATIONAHA.109.927681.

[164] O. Rafikova, R. Rafikov, M. L. Meadows, A. Kangath, D. Jonigk, and S. M. Black, "The sexual dimorphism associated with pulmonary hypertension corresponds to a fibrotic phenotype," *Pulm Circ*, vol. 5, no. 1, p. 184, Mar. 2015, doi: 10.1086/679724.

[165] J. H. Zhao *et al.*, "Circulating Plasma Metabolomic Profiles Differentiate Rodent Models of Pulmonary Hypertension and Idiopathic Pulmonary Arterial Hypertension Patients," *Am J Hypertens*, vol. 32, no. 11, pp. 1109–1117, Oct. 2019, doi: 10.1093/AJH/HPZ121.

[166] M. Kircher and C. Lapa, "Infection and Inflammation Imaging: Beyond FDG," *PET Clin*, vol. 15, no. 2, pp. 215–229, Apr. 2020, doi: 10.1016/J.CPET.2019.11.004.

[167] M. T. Parisi, J. P. Otjen, A. L. Stanescu, and B. L. Shulkin, "Radionuclide Imaging of Infection and Inflammation in Children: a Review," *Semin Nucl Med*, vol. 48, no. 2, pp. 148–165, Mar. 2018, doi: 10.1053/J.SEMNUCLMED.2017.11.002.

[168] M. Gotthardt, C. P. Bleeker-Rovers, O. C. Boerman, and W. J. G. Oyen, "Imaging of inflammation by PET, conventional scintigraphy, and other imaging techniques," *J Nucl Med Technol*, vol. 41, no. 3, pp. 157–169, 2013, doi: 10.2967/jnumed.110.076232.

[169] C. Wu, F. Li, G. Niu, and X. Chen, "PET imaging of inflammation biomarkers," *Theranostics*, vol. 3, no. 7, Theranostics, pp. 448–466, Jun. 2013. doi: 10.7150/thno.6592.

[170] N. Ageyama *et al.*, "Successful Inflammation Imaging of Non-Human Primate Hearts Using an Antibody Specific for Tenascin-C," *Int Heart J*, vol. 60, no. 1, pp. 151–158, 2019, doi: 10.1536/IHJ.17-734.

[171] J. M. Tarkin *et al.*, "Detection of Atherosclerotic Inflammation by 68Ga-DOTATATE PET Compared to [18F]FDG PET Imaging," *J Am Coll Cardiol*, vol. 69, no. 14, pp. 1774–1791, Apr. 2017, doi: 10.1016/J.JACC.2017.01.060.

[172] J. B. Park *et al.*, "Assessment of Inflammation in Pulmonary Artery Hypertension by 68Ga-Mannosylated Human Serum Albumin," *Am J Respir Crit Care Med*, vol. 201, no. 1, pp. 95–106, Jan. 2020, doi: 10.1164/RCCM.201903-0639OC.

[173] D. A. Dorward, C. D. Lucas, G. B. Chapman, C. Haslett, K. Dhaliwal, and A. G. Rossi, "The role of formylated peptides and formyl peptide receptor 1 in governing neutrophil function during acute inflammation," *Am J Pathol*, vol. 185, no. 5, pp. 1172–1184, May 2015, doi: 10.1016/J.AJPATH.2015.01.020.

[174] H. Carp, "Mitochondrial N-formylmethionyl proteins as chemoattractants for neutrophils," *J Exp Med*, vol. 155, no. 1, pp. 264–275, 1982, doi: 10.1084/JEM.155.1.264.

[175] J. Chen *et al.*, "[99mTc]cFLFLF for Early Diagnosis and Therapeutic Evaluation in a Rat Model of Acute Osteomyelitis," *Mol Imaging Biol*, vol. 17, no. 3, pp. 337–344, Jun. 2015, doi: 10.1007/S11307-014-0787-3.

[176] X. Yang *et al.*, "Targeting formyl peptide receptor 1 of activated macrophages to monitor inflammation of experimental osteoarthritis in rat," *J Orthop Res*, vol. 34, no. 9, pp. 1529–1538, Sep. 2016, doi: 10.1002/JOR.23148.

[177] E. J. Charles *et al.*, "SPECT imaging of lung ischemia-reperfusion injury using [99mTc]cFLFLF for molecular targeting of formyl peptide receptor 1," *Am J Physiol Lung Cell Mol Physiol*, vol. 318, no. 2, pp. L304–L313, Feb. 2020, doi: 10.1152/AJPLUNG.00220.2018.

[178] L. Xiao *et al.*, "A Novel Modality for Functional Imaging in Acute Intervertebral Disk Herniation via Tracking Leukocyte Infiltration," *Mol Imaging Biol*, vol. 19, no. 5, pp. 703–713, Oct. 2017, doi: 10.1007/S11307-016-1038-6.

[179] Y. Zhang *et al.*, "PET imaging detection of macrophages with a formyl peptide receptor antagonist," *Nucl Med Biol*, vol. 42, no. 4, pp. 381–386, Apr. 2015, doi: 10.1016/J.NUCMEDBIO.2014.12.001.

[180] A. H. Shannon *et al.*, "Single-Photon Emission Computed Tomography Imaging Using Formyl Peptide Receptor 1 Ligand Can Diagnose Aortic Aneurysms in a Mouse Model," *J Surg Res*, vol. 251, pp. 239–247, Jul. 2020, doi: 10.1016/J.JSS.2020.01.028.

[181] J. Pellico *et al.*, "In vivo imaging of lung inflammation with neutrophil-specific 68Ga nano-radiotracer," *Sci Rep*, vol. 7, no. 1, Dec. 2017, doi: 10.1038/S41598-017-12829-Y.

[182] J. Pellico *et al.*, "Fast synthesis and bioconjugation of 68Ga core-doped extremely small iron oxide nanoparticles for PET/MR imaging," *Contrast Media Mol Imaging*, vol. 11, no. 3, pp. 203–210, May 2016, doi: 10.1002/CMMI.1681.

[183] K. Drozd *et al.*, "Effects of an endothelin receptor antagonist, Macitentan, on right ventricular substrate utilization and function in a Sugen 5416/hypoxia rat model of severe pulmonary arterial hypertension," *Journal of Nuclear Cardiology*, vol. 24, no. 6, pp. 1979–1989, Sep. 2017, doi: 10.1007/s12350-016-0663-4.

[184] M. K. Hołda *et al.*, "Changes in heart morphometric parameters over the course of a monocrotaline-induced pulmonary arterial hypertension rat model," *J Transl Med*, vol. 18, no. 1, Jun. 2020, doi: 10.1186/S12967-020-02440-7.

[185] D. Vélez-Rendón, X. Zhang, J. Gerringer, and D. Valdez-Jasso, "Compensated right ventricular function of the onset of pulmonary hypertension in a rat model depends on chamber remodeling and contractile augmentation," *Pulm Circ*, vol. 8, no. 4, pp. 1–13, Oct. 2018, doi: 10.1177/2045894018800439.

[186] F. Farahmand, M. F. Hill, and P. K. Singal, "Antioxidant and oxidative stress changes in experimental cor pulmonale," *Mol Cell Biochem*, vol. 260, no. 1–2, pp. 21–29, May 2004, doi: 10.1023/B:MCBI.0000026047.48534.50.

[187] A. Vonk Noordegraaf, B. E. Westerhof, and N. Westerhof, "The Relationship Between the Right Ventricle and its Load in Pulmonary Hypertension," *J Am Coll Cardiol*, vol. 69, no. 2, pp. 236–243, 2017. doi: 10.1016/j.jacc.2016.10.047.

[188] M. Casali *et al.*, "State of the art of 18F-FDG PET/CT application in inflammation and infection: a guide for image acquisition and interpretation," *Clin Transl Imaging*, vol. 9, no. 4, p. 299, Aug. 2021, doi: 10.1007/S40336-021-00445-W.

[189] R. L. Wahl, V. Dilsizian, and C. J. Palestro, "At Last, 18F-FDG for Inflammation and Infection!," *Journal of Nuclear Medicine*, vol. 62, no. 8, pp. 1048–1049, Aug. 2021, doi: 10.2967/JNUMED.121.262446.

[190] S. Greulich *et al.*, "Hybrid Cardiac Magnetic Resonance/Fluorodeoxyglucose Positron Emission Tomography to Differentiate Active From Chronic Cardiac Sarcoidosis," *JACC Cardiovasc Imaging*, vol. 15, no. 3, pp. 445–456, Mar. 2022, doi: 10.1016/J.JCMG.2021.08.018.

[191] R. Dumitrascu *et al.*, "Acute lung injury induced by the pyrrolizidine alkaloid monocrotaline in mice," *Pneumologie*, vol. 60, no. S 1, Apr. 2006, doi: 10.1055/S-2006-934026.

[192] O. Rafikova, A. Srivastava, A. A. Desai, R. Rafikov, and S. P. Tofovic, "Recurrent inhibition of mitochondrial complex III induces chronic pulmonary vasoconstriction and glycolytic switch in the rat lung," *Respir Res*, vol. 19, no. 1, Apr. 2018, doi: 10.1186/S12931-018-0776-1.

[193] H. Xiao, S. Li, D. Zhang, T. Liu, M. Yu, and F. Wang, "Separate and concurrent use of 2-deoxy-D-glucose and 3-bromopyruvate in pancreatic cancer cells," *Oncol Rep*, vol. 29, no. 1, pp. 329–334, Jan. 2013, doi: 10.3892/OR.2012.2085.

[194] K. Chen, X. Xu, S. Kobayashi, D. Timm, T. Jepperson, and Q. Liang, "Caloric restriction mimetic 2-deoxyglucose antagonizes doxorubicin-induced cardiomyocyte death by multiple mechanisms," *J Biol Chem*, vol. 286, no. 25, pp. 21993–22006, Jun. 2011, doi: 10.1074/JBC.M111.225805.

[195] A. Andersen, D. E. van der Feen, S. Andersen, J. G. Schultz, G. Hansmann, and H. J. Bogaard, "Animal models of right heart failure," *Cardiovasc Diagn Ther*, vol. 10, no. 5, pp. 1561–1579, Oct. 2020, doi: 10.21037/CDT-20-400.

[196] T. Yang and A. A. Sauve, "NAD metabolism and sirtuins: Metabolic regulation of protein deacetylation in stress and toxicity," *AAPS J*, vol. 8, no. 4, Oct. 2006, doi: 10.1208/AAPSJ080472.

[197] H. C. Chang and L. Guarente, "SIRT1 and other sirtuins in Metabolism," *Trends Endocrinol Metab*, vol. 25, no. 3, p. 138, Mar. 2014, doi: 10.1016/J.TEM.2013.12.001.

[198] G. Zurlo *et al.*, "Sirtuin 1 regulates pulmonary artery smooth muscle cell proliferation: role in pulmonary arterial hypertension," *J Hypertens*, vol. 36, no. 5, pp. 1164–1177, May 2018, doi: 10.1097/HJH.0000000000001676.

[199] C. X. Huang, Z. X. Jiang, D. Y. Du, Z. M. Zhang, Y. Liu, and Y. T. Li, "The MFF-SIRT1/3 axis, regulated by miR-340-5p, restores mitochondrial homeostasis of hypoxia-induced pulmonary artery smooth muscle cells," *Laboratory Investigation 2022*, pp. 1–9, Jan. 2022, doi: 10.1038/s41374-022-00730-w.

[200] R. Paulin *et al.*, "Sirtuin 3 deficiency is associated with inhibited mitochondrial function and pulmonary arterial hypertension in rodents and humans," *Cell Metab*, vol. 20, no. 5, pp. 827–839, Nov. 2014, doi: 10.1016/J.CMET.2014.08.011.

[201] B. Wu *et al.*, "The role of SIRT2 in vascular-related and heart-related diseases: A review," *J Cell Mol Med*, vol. 25, no. 14, pp. 6470–6478, Jul. 2021, doi: 10.1111/JCMM.16618.

[202] X. Tang *et al.*, "SIRT2 acts as a cardioprotective deacetylase in pathological cardiac hypertrophy," *Circulation*, vol. 136, no. 21, pp. 2051–2067, Nov. 2017, doi: 10.1161/CIRCULATIONAHA.117.028728.

[203] N. Xie *et al.*, "NAD+ metabolism: pathophysiologic mechanisms and therapeutic potential," *Signal Transduction and Targeted Therapy 2020 5:1*, vol. 5, no. 1, pp. 1–37, Oct. 2020, doi: 10.1038/s41392-020-00311-7.

[204] X. Tang, X. F. Chen, H. Z. Chen, and D. P. Liu, "Mitochondrial Sirtuins in cardiometabolic diseases," *Clin Sci*, vol. 131, no. 16, pp. 2063–2078, Aug. 2017, doi: 10.1042/CS20160685.

[205] M. M. Maxwell *et al.*, "The Sirtuin 2 microtubule deacetylase is an abundant neuronal protein that accumulates in the aging CNS," *Hum Mol Genet*, vol. 20, no. 20, pp. 3986–3996, Oct. 2011, doi: 10.1093/HMG/DDR326.

[206] J. M. Pereira *et al.*, "Infection Reveals a Modification of SIRT2 Critical for Chromatin Association," *Cell Rep*, vol. 23, no. 4, pp. 1124–1137, Apr. 2018, doi: 10.1016/J.CELREP.2018.03.116.

[207] B. E. Corkey and J. T. Deeney, "The Redox Communication Network as a Regulator of Metabolism," *Front Physiol*, vol. 11, p. 1310, Oct. 2020, doi: 10.3389/FPHYS.2020.567796/BIBTEX.

[208] D. S. Matasic, C. Brenner, and B. London, "Emerging potential benefits of modulating NAD+ metabolism in cardiovascular disease," *Am J Physiol Heart Circ Physiol*, vol. 314, no. 4, pp. H839–H852, Apr. 2018, doi: 10.1152/AJPHEART.00409.2017.

[209] V. G. DeMarco, A. T. Whaley-Connell, J. R. Sowers, J. Habibi, and K. C. Dellsperger, "Contribution of oxidative stress to pulmonary arterial hypertension," *World J Cardiol*, vol. 2, no. 10, p. 316, Oct. 2010, doi: 10.4330/WJC.V2.I10.316.

[210] D. P, F. E, and M. R, "Ethidium bromide-induced loss of mitochondrial DNA from primary chicken embryo fibroblasts," *Mol Cell Biol*, vol. 5, no. 5, pp. 1163–1169, May 1985, doi: 10.1128/MCB.5.5.1163-1169.1985.

[211] M. M. K. Nass, "Differential effects of ethidium bromide on mitochondrial and nuclear DNA synthesis in vivo in cultured mammalian cells," *Exp Cell Res*, vol. 72, no. 1, pp. 211–222, 1972, doi: 10.1016/0014-4827(72)90583-6.

[212] Y. G. Yoon, Y. J. Oh, and Y. H. Yoo, "Rapid Isolation of Mitochondrial DNA-Depleted Mammalian Cells by Ethidium Bromide and Dideoxycytidine Treatments," *undefined*, vol. 57, no. 3, pp. 259–265, Sep. 2014, doi: 10.3839/JABC.2014.042.

[213] L. P. Kao, D. Ovchinnikov, and E. Wolvetang, "The effect of ethidium bromide and chloramphenicol on mitochondrial biogenesis in primary human fibroblasts," *Toxicol Appl Pharmacol*, vol. 261, no. 1, pp. 42–49, May 2012, doi: 10.1016/J.TAAP.2012.03.009.

[214] R. M. Hall, M. K. Trembath, A. W. Linnane, L. Wheelis, and R. S. Criddle, "Factors affecting petite induction and the recovery of respiratory competence in yeast cells exposed to ethidium bromide," *Mol Gen Genet*, vol. 144, no. 3, pp. 253–262, Jan. 1976, doi: 10.1007/BF00341723.

[215] M. R. Chiaratti *et al.*, "Ooplast-mediated developmental rescue of bovine oocytes exposed to ethidium bromide," *Reprod Biomed Online*, vol. 22, no. 2, pp. 172–183, Feb. 2011, doi: 10.1016/J.RBMO.2010.10.011.

[216] R. N. Stuchell, B. I. Weinstein, and D. S. Beattie, "Effects of Ethidium Bromide on the Respiratory Chain and Oligomycin-sensitive Adenosine Triphosphatase in Purified

Mitochondria from the Cellular Slime Mold Dictyostelium discoideum*," *Journal of Biological Chemistry*, vol. 250, no. 2, pp. 570–576, 1975, doi: 10.1016/S0021-9258(19)41935-2.

[217] J. Röding, A. Naujok, and H. W. Zimmermann, "Effects of ethidium bromide, tetramethylethidium bromide and betaine B on the ultrastructure of HeLa cell mitochondria in situ. A comparative binding study," *Histochemistry*, vol. 85, no. 3, pp. 215–222, May 1986, doi: 10.1007/BF00494807.

[218] A. M. Villa and S. M. Doglia, "Ethidium bromide as a vital probe of mitochondrial DNA in carcinoma cells," *Eur J Cancer*, vol. 45, no. 14, pp. 2588–2597, Sep. 2009, doi: 10.1016/J.EJCA.2009.06.022.

[219] G. Soslau and M. M. K. Nass, "Effects of ethidium bromide on the cytochrome content and ultrastructure of L cell mitochondria," *J Cell Biol*, vol. 51, no. 21, pp. 514–524, Nov. 1971, doi: 10.1083/JCB.51.2.514.

[220] E. B. Warren, A. E. Aicher, J. P. Fessel, and C. Konradi, "Mitochondrial DNA depletion by ethidium bromide decreases neuronal mitochondrial creatine kinase: Implications for striatal energy metabolism," *PLoS One*, vol. 12, no. 12, Dec. 2017, doi: 10.1371/JOURNAL.PONE.0190456.

[221] V. Lauer *et al.*, "Hypoxia drives glucose transporter 3 expression through hypoxia-inducible transcription factor (HIF)–mediated induction of the long noncoding RNA NICI," *Journal of Biological Chemistry*, vol. 295, no. 13, pp. 4065–4078, Mar. 2020, doi: 10.1074/JBC.RA119.009827.

[222] S. B. Kalkhoran *et al.*, "Unique morphological characteristics of mitochondrial subtypes in the heart: the effect of ischemia and ischemic preconditioning," *Discoveries (Craiova)*, vol. 5, no. 1, p. e71, Mar. 2017, doi: 10.15190/D.2017.1.

[223] S. Y. Chiang *et al.*, "Usp11 controls cortical neurogenesis and neuronal migration through Sox11 stabilization," *Sci Adv*, vol. 7, no. 7, pp. 6093–6105, Feb. 2021, doi: 10.1126/SCIADV.ABC6093.

[224] Y. Yan *et al.*, "X-linked ubiquitin-specific peptidase 11 increases tauopathy vulnerability in women," *Cell*, vol. 185, no. 21, pp. 3913-3930.e19, Oct. 2022, doi: 10.1016/J.CELL.2022.09.002.

[225] R. Bohuslavová, F. Kolář, L. Kuthanová, J. Neckář, A. Tichopád, and G. Pavlinkova, "Gene expression profiling of sex differences in HIF1-dependent adaptive cardiac responses to chronic hypoxia," *J Appl Physiol*, vol. 109, no. 4, pp. 1195–1202, Oct. 2010, doi: 10.1152/JAPPLPHYSIOL.00366.2010.

[226] C. K. Docherty, M. Nilsen, and M. R. MacLean, "Influence of 2-Methoxyestradiol and Sex on Hypoxia-Induced Pulmonary Hypertension and Hypoxia-Inducible Factor-1-α," *Journal*

of the American Heart Association: Cardiovascular and Cerebrovascular Disease, vol. 8, no. 5, Mar. 2019, doi: 10.1161/JAHA.118.011628.

[227] M. Zampino *et al.*, "Sex-related dimorphic response of HIF-1α expression in myocardial ischemia," *American Journal of Physiology - Heart and Circulatory Physiology*, vol. 291, no. 2, pp. 957–964, 2006. doi: 10.1152/AJPHEART.00580.2005.

[228] H. Elamaa *et al.*, "PHD2 deletion in endothelial or arterial smooth muscle cells reveals vascular cell type-specific responses in pulmonary hypertension and fibrosis.," *Angiogenesis*, vol. 25, no. 2, pp. 259–274, Jan. 2022, doi: 10.1007/S10456-021-09828-Z.

[229] Y. Tang *et al.*, "Targeting USP11 may alleviate radiation-induced pulmonary fibrosis by regulating endothelium tight junction," *Int J Radiat Biol*, vol. 98, no. 1, pp. 30–40, 2022, doi: 10.1080/09553002.2022.1998711.

[230] A. M. Jacko *et al.*, "De-ubiquitinating enzyme, USP11, promotes transforming growth factor β-1 signaling through stabilization of transforming growth factor β receptor II," *Cell Death Dis*, vol. 7, no. 11, p. e2474, 2016, doi: 10.1038/CDDIS.2016.371.

[231] V. A. de Jesus Perez, "Molecular pathogenesis and current pathology of pulmonary hypertension," *Heart Fail Rev*, vol. 21, no. 3, pp. 239–257, May 2016, doi: 10.1007/S10741-015-9519-2.

[232] L. A. Shimoda and S. S. Laurie, "Vascular Remodeling in Pulmonary Hypertension," *J Mol Med (Berl)*, vol. 91, no. 3, p. 297, Mar. 2013, doi: 10.1007/S00109-013-0998-0.

[233] A. E. Schultze and R. A. Roth, "Chronic pulmonary hypertension--the monocrotaline model and involvement of the hemostatic system," *J Toxicol Environ Health B Crit Rev*, vol. 1, no. 4, pp. 271–346, Jan. 1998, doi: 10.1080/10937409809524557.

[234] J. Hester, C. Ventetuolo, and T. Lahm, "Sex, Gender, and Sex Hormones in Pulmonary Hypertension and Right Ventricular Failure," *Compr Physiol*, vol. 10, no. 1, p. 125, Dec. 2019, doi: 10.1002/CPHY.C190011.

[235] R. Dumitrascu *et al.*, "Characterization of a murine model of monocrotaline pyrrole-induced acute lung injury," *BMC Pulm Med*, vol. 8, p. 25, 2008, doi: 10.1186/1471-2466-8-25.

[236] J. Gomez-Arroyo *et al.*, "A brief overview of mouse models of pulmonary arterial hypertension: Problems and prospects," *Am J Physiol Lung Cell Mol Physiol*, vol. 302, no. 10, May 2012, doi: 10.1152/AJPLUNG.00362.2011.

[237] T. Hye *et al.*, "Newer insights into the pathobiological and pharmacological basis of the sex disparity in patients with pulmonary arterial hypertension," *Am J Physiol Lung Cell Mol Physiol*, vol. 320, no. 6, p. L1025, Jun. 2021, doi: 10.1152/AJPLUNG.00559.2020.

[238] Y. Dempsie and M. R. Maclean, "The influence of gender on the development of pulmonary arterial hypertension," *Exp Physiol*, vol. 98, no. 8, pp. 1257–1261, Aug. 2013, doi: 10.1113/EXPPHYSIOL.2012.069120.

[239] A. L. Frump *et al.*, "17β-Estradiol and estrogen receptor α protect right ventricular function in pulmonary hypertension via BMPR2 and apelin," *J Clin Invest*, vol. 131, no. 6, Mar. 2021, doi: 10.1172/JCI129433.

[240] A. Frille *et al.*, "Thoracic [18F]fluorodeoxyglucose uptake measured by positron emission tomography/computed tomography in pulmonary hypertension," *Medicine*, vol. 95, no. 25, pp. 25–3976, Jun. 2016, doi: 10.1097/MD.0000000000003976.

[241] S. Farha *et al.*, "Metabolic endophenotype associated with right ventricular glucose uptake in pulmonary hypertension," *Pulm Circ*, vol. 11, no. 4, pp. 1–12, Nov. 2021, doi: 10.1177/20458940211054325.

[242] Z. WH, Q. MH, W. XJ, S. K, Z. Y, and J. ZC, "Up-regulation of hexokinase1 in the right ventricle of monocrotaline induced pulmonary hypertension," *Respir Res*, vol. 15, no. 1, Oct. 2014, doi: 10.1186/S12931-014-0119-9.

[243] D. H. Tran and Z. v. Wang, "Glucose Metabolism in Cardiac Hypertrophy and Heart Failure," *J Am Heart Assoc*, vol. 8, no. 12, Jun. 2019, doi: 10.1161/JAHA.119.012673.

[244] L. Luo, L. Xiao, G. Lian, H. Wang, and L. Xie, "miR-125a-5p inhibits glycolysis by targeting hexokinase-II to improve pulmonary arterial hypertension," *Aging (Albany NY)*, vol. 12, no. 10, p. 9014, May 2020, doi: 10.18632/AGING.103163.

[245] C. J. Zuurbier, A. Koeman, S. M. Houten, M. W. Hollmann, and W. J. Florijn, "Optimizing anesthetic regimen for surgery in mice through minimization of hemodynamic, metabolic, and inflammatory perturbations," *Exp Biol Med (Maywood)*, vol. 239, no. 6, pp. 737–746, 2014, doi: 10.1177/1535370214524877.

[246] L. Zhao *et al.*, "Heterogeneity in Lung 18FDG Uptake in pulmonary arterial hypertension: Potential of dynamic 18FDG Positron emission tomography with kinetic analysis as a bridging biomarker for pulmonary vascular remodeling targeted treatments," *Circulation*, vol. 128, no. 11, pp. 1214–1224, Sep. 2013, doi: 10.1161/CIRCULATIONAHA.113.004136.

[247] Y. Macotela, J. Boucher, T. T. Tran, and C. R. Kahn, "Sex and Depot Differences in Adipocyte Insulin Sensitivity and Glucose Metabolism," *Diabetes*, vol. 58, no. 4, pp. 803–812, Apr. 2009, doi: 10.2337/DB08-1054.

[248] H. Shi, A. D. Strader, J. E. Sorrell, J. B. Chambers, S. C. Woods, and R. J. Seeley, "Sexually different actions of leptin in proopiomelanocortin neurons to regulate glucose homeostasis," *Am J Physiol Endocrinol Metab*, vol. 294, no. 3, pp. 630–639, Mar. 2008, doi: 10.1152/AJPENDO.00704.2007.

[249] R. S. Stearman *et al.*, "Systems analysis of the human pulmonary arterial hypertension lung transcriptome," *Am J Respir Cell Mol Biol*, vol. 60, no. 6, pp. 637–649, Jun. 2019, doi: 10.1165/RCMB.2018-0368OC.